NORTHWESTERN UNIVERSITY

Modular Carbon and Gold Nanoparticles for High Field MR Imaging and Theranostics

A DISSERTATION

SUBMITTED TO THE GRADUATE SCHOOL

IN PARTIAL FULFILLMENT OF THE REQUIREMENTS

for the degree

DOCTOR OF PHILOSOPHY

Field of Interdisciplinary Biological Sciences

By

Nikhil Rammohan

EVANSTON, ILLINOIS

December 2016

Abstract

Modular Carbon and Gold Nanoparticles for High Field MR Imaging and Theranostics

Nikhil Rammohan

The ability to track labeled cancer cells *in vivo* would allow researchers to study their distribution, growth and metastatic potential within the intact organism. Magnetic Resonance (MR) imaging is invaluable for tracking cancer cells *in vivo* as it benefits from high spatial resolution and absence of ionizing radiation. However, many MR contrast agents (CAs) required to label cells either do not significantly accumulate in cells or are not biologically compatible for translational studies. Accordingly, we have developed carbon- and gold-nanoparticles coupled to gadolinium(III) [Gd(III)] chelates for T_1-weighted MR imaging that demonstrated remarkable properties for cell tracking *in vitro* and *in vivo*.

We created nanodiamond-Gd(III) aggregates (NDG) by peptide coupling Gd(III) chelates to aminated nanodiamonds. NDG had high relaxivity *independent of field strength* (unprecedented for Gd(III)-nanoparticle conjugates), and demonstrated a *300-fold increase* in cellular delivery of Gd(III) compared to clinical Gd(III) chelates. Further, we were able to monitor the tumor growth of NDG-labeled flank tumors by T_1-weighted MRI for *26 days in vivo*, longer than reported for other MR CAs or nuclear agents. Further, theranostic nanodiamond-gadolinium(III)-doxorubicin (ND-Gd-Dox) aggregates were generated by conjugating doxorubicin (ND-Gd-Dox), which enabled efficient cancer chemotherapy in breast cancer cells.

Further, we synthesized Gd(III)-gold nanoconjugates (Gd@AuNPs) with varied chelate structure and nanoparticle-chelate linker length. Significantly enhanced cell labeling was demonstrated compared to previous gadolinium-gold-DNA nanoconstructs. Differences in Gd(III) loading, surface packing and cell uptake were observed between four different Gd@AuNP formulations suggesting that linker length and surface charge play an important role in cell labeling. The best performing Gd@AuNPs afforded 23.6 ± 3.6 fmol of Gd(III) per cell at an incubation concentration of 27.5 μM. This efficiency of Gd(III) payload delivery (Gd(III)/cell normalized to dose) exceeds that of previously Gd(III)-Au conjugates and most other Gd(III)-nanoparticle formulations. Finally, Gd@AuNPs were the first MR CAs of any type to effectively image the pancreas *in vivo*.

In summary, both Gd@AuNPs and NDG support future MR-mediated cell tracking and theranostic applications in whole-animal models.

Acknowledgement

There was once a time I thought I would never be able to write these words of gratitude to all those who helped me reach this defining moment in my academic career. When I started my PhD, I was neither a chemist, nor a biologist nor an engineer but I had just chosen to spend the next several years on scientific endeavors that involved elements of three disciplines. As a student in the Medical Scientist Training Program, I wanted to expand on my training as an applied statistician to pursue translational research in a laboratory well-versed in several different research areas, to become a physician-scientist with a broad training base and widely applicable skills. I would not have accomplished this goal without the support of the individuals mentioned herein.

First, I would like to thank my advisor Prof. Thomas J. Meade for accepting me into his lab. Not many professors would have been gracious enough to want a student with limited background in their primary research areas. However, Tom believed in my scientific potential and always backed me even in my early years even when I was finding the learning curve a little too steep. I would also like to thank Tom for giving me the freedom to set the trajectory for my projects, and for supporting me even when we disagreed or when progress had stalled. Finally I am grateful to Tom for creating a wonderful environment to perform scientific research, and fostering a lab ethos comprised of curiosity, optimism and collaboration.

I would like to thank my undergraduate advisor at Johns Hopkins University, Prof. Carey E. Priebe. As my first research advisor, he embodied what it meant to be scholar, teacher, mentor and friend, and it was his unwavering support that led me to pursue a career in science, apply to graduate school and medical school, and be where I am today. I would like to also thank Dr.

Youngser Park who, along with Carey, taught me all I know about applied statistics which served me well even as I branched out to different fields of research.

I would next like to thank my committee members, Professors Thomas V O'Halloran (chair), Lonnie Shea, Guillermo Ameer and Ming Zhao. Over the years, Prof. O'Halloran has always been able to troubleshoot my experimental design and provide suggestions to overcome roadblocks along the way. I would like to acknowledge the valuable input of Prof. Lonnie Shea during my first year of PhD before unfortunately leaving the university. I would like to thank Prof. Ameer for agreeing to serve on my committee after Prof. Shea's departure, and always providing useful feedback on materials chemistry. I first met Prof. Zhao during a class on biological imaging techniques and he inspired several of my thesis ideas involving theranostics and mouse model design, and I am very grateful to him for his support and advice over the years.

I would next like to thank my colleagues in the Meade lab. Dr. Keith MacRenaris played a huge role in nearly every major experiment I undertook, from helping me design my studies to assisting with MR imaging and running hundreds of ICP-MS samples, he was there with me every step of the way. Dr. Lisa Manus, Dr. Andy Hung and Dr. Marie Heffern were my first mentors when I joined the lab and their advice certainly got me through the early years. Drs. Matthew Rotz and Robert Holbrook took me under their wing for the gold nanoparticles project and I owe them for adding an extra dimension to my dissertation work. Dr. Christiane Carney and Luke Vistain were instrumental in teaching me tissue culture techniques and biological study design, and played a huge role in my success during grad school. My office mates Laura Lilley and Dr. Adam Preslar were not only there to collaborate and offer chemistry advice but we also shared YouTube videos, music and fun that got me through my PhD. I would also like to thank Shaunna McLeod for taking

over some of my unfinished work and I wish her the very best for graduate school. I would like to show my appreciation to my undergrad Abigail Filicko, who was a quick learner and made significant contributions to the nanodiamonds project. Finally, I would like to thank Mrs. Sophie Tidd, who was a friend, confidante and invaluable guide navigating grant submissions and graduate school in general.

Next I would like to highlight the outstanding contributions of my collaborators. Prof. Dean Ho has supported me throughout my PhD and always made available his vast expertise on the nanodiamonds project. Likewise, Dr. Laura Moore from Prof. Ho's lab was an excellent mentor when I started out and taught me the basics of nanodiamonds research that set the course for the rest of my PhD. I would also like to thank Profs. Giacomo Parigi and Claudio Luchinat from University of Florence in Italy, whose expertise in nuclear magnetic relaxation dispersion played a major role in my dissertation work.

I would next like to mention the support I received from Northwestern University core facilities and related personnel who made substantial contributions towards my various projects. First, I would like to Dr. Alex Waters and Dr. Chad Haney from the Center for Advanced Molecular Imaging whose assistance with *in vivo* MR imaging was invaluable. Secondly, I would like to thank Dr. Irawati Kandela for her assistance with tumor inoculation and agent administration without whom I could not have completed mouse studies. Lastly, I would like to acknowledge Dr. Reiner Bleher from the Quantitative Bioelemental Imaging Center and Ms. Charlene Wilke from the Biological Imaging Facility for Transmission Electron Microscopy and Energy Dispersive X-ray Spectroscopy experiments.

Of course, I would like to acknowledge my family, without whom my achievements would not have been possible. I married my wife, Malini, right around the time I started my PhD and she has been an incredible pillar of support to get me to the finish line. Being a graduate student herself, she always understood my stress, was always there to keep me strong, lift my spirits, and maintain a life beyond school. My mom, Kamal, and dad, Rammohan, who have made extraordinary sacrifices to make my life and education their highest priority – I would not have made it through college, medical school and now my PhD without their support and guidance. Even though she was thousands of miles and several time zones away, my mom always took my calls over phone and Skype no matter what the time. I would also like to thank my older brother, Nitin, as he believed in my abilities even when I barely believed in my own. I would like to acknowledge my parents-in-law Latha and Suresh, brother-in-law Krishna and sister-in-law Vidya, who have supported me throughout, valued my educational pursuits, and celebrated my success as though no different than their own. I am proud to share this day with my wonderful family and friends.

List of Abbreviations

Acronyms

CA .....contrast agent
CNR .....contrast-to-noise ratio
CT .....computed tomography
EA .....elemental analysis
EM.....electromagnetic
ESI.....electrospray ionization
FI.....fluorescence imaging
Gd@AuNPs .....gadolinium(III)-gold nanoconjugates
HPLC .....high performance liquid chromatography
ICP-MS .....inductively coupled plasma mass spectrometry
IR.....infrared
IS .....inner-sphere
IVIS.....*in vivo* imaging system
LC-MS .....liquid chromatography-mass spectrometry
MALDI-TOF.....matrix assisted laser desorption ionization - time of flight
MR .....magnetic resonance
MRI.....magnetic resonance imaging
MS.....mass spectrometry
NIR.....near-infrared
NMR .....nuclear magnetic resonance
NMRD.....nuclear magnetic resonance dispersion
OATP .....organic anion transporting polypeptide
OS .....outer-sphere
PET .....positron emission tomography
QDs .....quantum dots
RF.....radiofrequency
SBM .....Solomon, Bloembergen, and Morgan
SPECT.....single-photon emission computed tomography
SPIO.....super-paramagnetic iron oxide
TLC.....thin layer chromatography
US .....ultrasound
UV.....ultraviolet
Z .....atomic number

Chemicals

AAZTA .....6-amino-6-methylperhydro-1,4-diazepinetetraacetic acid
BSP .....bromosulfopthalein
$CDCl_3$.....deuterated chloroform
$CHCl_3$.....chloroform

D_2O .....deuterated water
DCM .....dichloromethane
DIC.....N,N'-diisopropylcarbodiimide
DIPEA.....N,N-diisopropylethylamine
DMF.....dimethylformamide
DMSO.....dimethyl sulfoxide
DMT.....dimethoxytrityl
DOTA .....1,4,7,10-tetraazacyclododecanetetraacetic acid
DO3A.....1,4,7-tetraazacyclododecanetriacetic acid
DTPA .....diethylene triaminepentaacetic acid
DTT.....dithiothreitol
DTTA.....diethylenetriamine N, N, N', N'-tetraacetate
EDC.....1-ethyl-3-[3-dimethylaminopropyl]carbodiimide hydrochloride
EtOAc .....ethyl acetate
EtOH .....ethanol
Et_2O.....diethylether
Eu(III) .....europium (III)
FITC.....fluorescein isothiocyanate
Gd(III) .....gadoilinium (III)
$GdCl_3$.....gadolinium (III) chloride
$Gd(OAc)_3$ .....gadolinium (III) acetate
HCl.....hydrochloric acid
HNO_3.....nitric acid
H_2O .....water
K_2CO_3 .....potassium carbonate
MeCN.....acetonitrile
MeOD .....deuterated methanol
MeOH .....methanol
$MgSO_4$.....magnesium sulfate
MOPS.....3-(N-morpholino-propansulfonic acid)
NaOH .....sodium hydroxide
NHS.....n-hydroxy succinimide
NH_4OH.....ammonium hydroxide
NaN_3.....sodium azide
PBS .....phosphate buffered saline
PEG.....poly(ethylene glycol)
PPh_3.....triphenylphosphine
PEG.....polyethylene glycol
TBTA .....tris[(1-benzyl-1*H*-1,2,3-triazol-4-yl)methyl]amine
t-Bu .....tert-butyl
TEA.....triethylamine
TFA.....trifluoroacetic acid
THF.....tetrahydrofuran
TIPS .....triisopropylsilane

TMS .....trimethylsilyl
t-BuOH.....*tert*-butanol

Units

°C .....degrees Celsius
AU.....absorbance units
Å.....angstroms
cm.....centimeters
g.....grams
hrs.....hours
K.....Kelvin
M.....molar
mg .....milligrams
MHz .....megahertz
min .....minutes
mM.....millimolar
mm .....millimeters
mmol .....millimoles
mol .....moles
ms.....milliseconds
nm .....nanometers
nmol .....nanomoles
ns.....nanoseconds
ppm .....parts per a million
ps.....picoseconds
s.....seconds
T .....Tesla
μL.....microliters
μM.....micromolar
μm .....micrometers
μmol .....micromoles
μs.....microseconds

Symbols

B_0.....external magnetic field
B_1.....temporary magnetic field
γ.....gyromagnetic ratio
K_d .....dissociation constant
k_B.....Boltzmann constant
λ_{em} .....emission wavelength
λ_{ex} .....excitation wavelength
m .....mass

N_A.....Avogadro's number
ϕ .....quantum yield
q.....water coordination number
τ_M.....residence lifetime of water
τ_R .....rotational correlation time
ω_o.....Larmor frequency
r_1.....longitudinal relaxivity
r_2.....transverse relaxaivity
T .....temperature
T_1.....longitudinal (spin-lattice) relaxation time
T_{1e}.....longitudinal extronic spin relaxation time
T_2.....transverse (spin-spin) relaxation time
V_0 .....initial volume
ΔA .....change in absorbance
ΔA_{500}.....change in absorbance at 500 nm
ΔG.....Gibbs free energy
$\Delta G^{\ddagger}$ .....activation energy
ΔH.....enthalpy
ΔS.....entropy
ε.....molar extinction coefficient

Table of Contents

List of Figures and Tables

Chapter 1:

Introduction and Background

1.1. Introduction: Molecular Imaging of Cancer.

Wilhelm Roentgen's discovery of X-rays in 1896 enabled the visualization of internal anatomical structures within a live, intact subject for the first time.[1] The discovery transformed the capabilities of biology and medicine, for opaque subjects had become transparent for diagnosis, treatment and research. Over the years, diagnostic imaging and radiology have evolved into a complex multidisciplinary field involving physicists, chemists, biologists and engineers to advance Roentgen's vision to "see through" living organisms.

Imaging is grounded in the use of electromagnetic (EM) radiation to pass through a subject and process the emitted radiation into a signal that can be interpreted. In that context, while the use of EM radiation is a centuries-old concept, engineering advances have enabled a revolution in diagnostic imaging utilizing a wide range of the EM spectrum (***Figure 1.1***).[2] The advent of modern medical imaging has allowed accurate diagnosis, detailed study of anatomy, improved therapeutic outcomes, all at a scale not previously possible.[3-6] While anatomical imaging can be thought of as the visualization of STRUCTURE, "molecular imaging" refers to the study of FUNCTION - biological processes ranging from variations in gene expression within a particular tissue type to visualization of stem cell translocation and differentiation *in vivo*.[7,8] Molecular imaging modalities include computed tomography (CT),[9-11] positron emission tomography (PET),[12-14] single photon emission computed tomography (SPECT),[15-17] ultrasound (US)[18,19], optical imaging,[20-23] and magnetic resonance imaging (MRI).[24-26] Each modality has several advantages and disadvantages depending on the application. For example, PET and SPECT have the highest sensitivity but limited spatial resolution. On the other hand, CT and MRI enable high spatiotemporal resolution but their sensitivity usually needs to be augmented by the use of contrast agents.

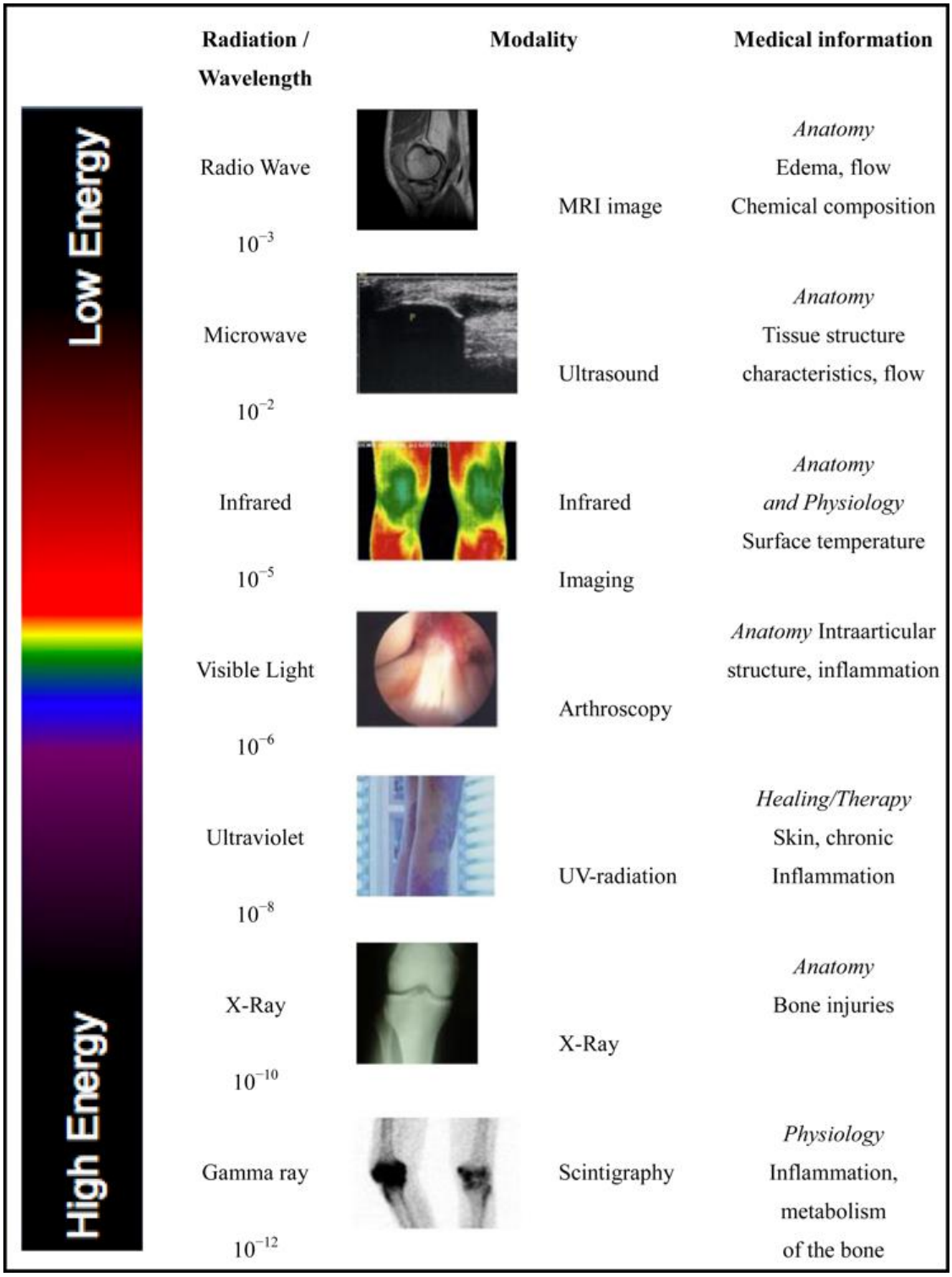

Figure 1.1. Typical imaging modalities within the electromagnetic spectrum.[2]

The Meade Lab focusses on the development of MRI contrast agents, specifically on improving the sensitivity, specificity, and target-specific accumulation of Gadolinium(III) [Gd(III)]-based agents. One of the strategies employed for addressing these goals is the utilization of nanomaterials as delivery vehicles of small molecule Gd(III) contrast agents.

An important application of molecular imaging is towards the effective diagnosis and treatment of cancer. Cancer is the second leading cause of mortality in the United States and worldwide.[27] Modern clinical cancer treatments require tremendous precision and knowledge of tumor environment, including location, size, nodal spread and extra-organ involvement.[28,29] To be able to answer these questions, mainstay imaging tools such as CT, MRI and US need to be supplemented by the acquisition of molecular and physiological information using emerging molecular imaging technologies.[3,7,29] As summarized by Weissleder, it is expected that "clinical molecular imaging will one day be used to achieve the following: (i) the detection of molecular or physiological alterations that signal the presence of cancer when it is still at a curable stage, (ii) the ability to evaluate and adjust treatment protocols in real time, and (iii) the ability to streamline the cancer drug development process."[29]

MRI is commonly employed to track tumor size, location, and metastatic burden because of its high resolution and ability to produce images of entire organs/organisms with exquisite soft-tissue contrast and without the use of ionizing radiation.[4,30-32] In particular, the ability to localize transplanted cancer cells *in vivo* and monitor their tissue biodistribution would be valuable to understand cellular migration after transplantation.[33] One of the most promising areas of investigation that will benefit from the ability to noninvasively monitor cell migration and function over time is monitoring cancer growth and cancer cell metastasis.[28,29,33]

1.2. Scope of Thesis.

The focus of my research efforts over the course of my PhD was the utilization of carbon and gold nanoparticles for amplification of Gd(III)-based contrast agent delivery and performance towards *in vivo* MRI of cancer growth. Nanomaterials not only provide a scaffold for contrast agent conjugation, they also improve their performance and allow superior cellular penetration and labeling.[34-37]

Carbon nanomaterials such as buckminsterfullerenes, nanodiamonds, carbon nanotubes, graphenes and graphene oxides have all been utilized as MRI contrast agents.[36,38-40] Among these, nanodiamonds are particularly useful due to their facile production, biocompatibility, and ease of functionalization.[38,41-43] Previously, the Meade and Ho labs developed Gd(III)-nanodiamond conjugates, whose relaxivity (ability to decrease T_1 relaxation time) exceeded nearly all other Gd(III)-based agents.[38]

In chapter 2, nanodiamond-Gd(III) (NDG) conjugates are used to label cancer cells *ex vivo*, and follow the growth of a labeled tumor *in vivo* over 26 days. The synthesis of NDG was modified from previous methods to increase the Gd(III) loading. The newly synthesized NDG were biocompatible and afforded *300-fold increased cell uptake* compared to unmodified and clinical Gd(III) agents. Further, the relaxivity of NDG was shown to be *field-independent*, a first for nanoparticle-Gd(III) conjugates. Finally, by quantifying relaxation times within the tumor, we were able to demonstrate dual T_1-T_2 contrast and describe tumor morphology and heterogeneity. This work resulted in a *first-author publication currently under review* (Nano Letters, 2016).

In chapter 3, nanodiamond-Gd(III)-doxorubicin (ND-G-D) theranostic nanoconjugates were developed for chemotherapy that can be fate-mapped by MRI. Previously, doxorubicin (Dox)

was adsorbed onto the faceted surface of NDs and was used to treat drug-resistant breast cancer & liver cancer.[44,45] This sequestration of Dox onto the ND surface produced a delayed release profile, which in turn decreased systemic toxicity and the capacity of the tumors to expel Dox; furthermore, it increased the circulation half-time 10-fold over unmodified Dox and allowed for higher dosages of Dox in mice without affecting survivability. Given the success of NDs in both imaging and therapy applications, a significant advance would be the simultaneous ND-mediated delivery of both MRI contrast agents and chemotherapy. ND-G-D enabled two-fold more potent chemotherapy of breast cancer cells *in vitro* which could be tracked by Gd(III) content within cells. *A first-author manuscript describing this work is currently in preparation*.

Apart from carbon nanomaterials, I also utilized gold nanoparticles conjugated to Gd(III) chelates for MRI. Gold nanoparticles of different shapes, sizes, and surface chemistries have been coupled to Gd(III) chelates to produce high efficiency MRI contrast agents.[37,46-49] While spherical nanoparticles of varying size are the predominant form of gold nanoparticle used in nanoconjugate CAs, some groups have investigated the use of other shapes, including nanorods[50,51] and nanostars.[46] The robustness of gold-thiol conjugation chemistry has enabled Gd(III)-gold nanoconjugate CAs bearing ligands of DNA,[37,49] peptides,[52,53] PEG,[54,55] saccharides,[56,57] polymers[58-60] and various combinations of the above. In 2009, the Meade and Mirkin labs conceived of a new Gd(III)-DNA-gold nanoconjugate contrast agent. A 3' thiolated poly-deoxythymidine (dT) DNA, covalently modified with Gd(III) at five positions and containing a 5' Cyanine3 fluorophore, was conjugated to the surface of 13.1 nm gold nanoparticles.[49] This construct, termed DNA-Gd^{III}@AuNP was also utilized to track the migration of neural stem cells

in vivo.[61] However, apart from being a carrier for the Gd(III) chelates and optical dyes, it is likely that the presence of DNA limits the amount of Gd(III) that can be loaded onto the AuNP surface.

In chapter 4, the last and final chapter, we synthesized DNA-free Gd(III)-gold nanoconjugates for highly efficient cell labeling and for targeting the mouse pancreas *in vivo*. For these new constructs, a series of Gd(III) chelates were modified with lipoic acid and directly coupled to the particle surface. This approach to Gd(III) conjugation demonstrated superior Gd(III) loading, better particle stability, better relaxivity, and upto twenty-fold better Gd(III) uptake compared to the previous generation DNA-Gd^{III}@AuNPs. Besides the improvement in performance, this new design enabled exceptional contrast of labeled cells at 7 T, and was also the first MRI contrast agent of any type to accumulate in the pancreas of wild type mice. This work resulted in *one first-author publication (Bioconjugate Chemistry, 2016) and one second author publication (Nano Letters, 2016).*

1.3. Background

1.3.1. X-ray Computed Tomography (CT)

Since their discovery in 1895, X-rays still remain one of the widely used imaging modalities diagnostic radiology today, in the guise of X-ray radiography and computed tomography.[62] X-ray radiography involves a source transmitting X-ray beams towards the subject, where the subject's inherent tissue composition results in differential absorption and transmittance of the X-rays, which form an image when they come in contact with a detector.[1] CT scanning is a modification of this concept, which involves rotation of the X-ray source and detectors about the subject in a spiral trajectory, acquiring images in several different planes, and assembling these tomographic images into a three dimensional (3D) reconstruction of the subject.[63] CT is beneficial

because images with high spatial resolution can be acquired quickly, at relatively low cost, particularly with the use of contrast media. CT scans are first-line diagnostic techniques for head and abdominal trauma, pulmonary embolism, cardiac angiography and other routine and emergent examinations. However, like X-ray radiography, CT does suffer from the use of ionizing radiation, which can preclude frequent imaging, especially in susceptible patients (e.g. cancer-afflicted or pregnant patients).[64]

CT is often augmented by contrast agents for increased signal-to-noise ratios (SNR). Most clinical CT contrast agents are composed of iodine or barium, as these elements benefit from large X-ray absorption cross sections.[64] CT contrast agent development in a research setting has utilized various gold nanoparticle formulations, which have often provided better contrast with lower required doses of radiation.[65-67] For example, Hainfeld *et al.* used 15 nm gold nanoparticles coated with polyethylene glycol (PEG) and functionalized with an anti-Her2 antibody to detect tumors as small as 1 mm, and demonstrated effective molecular targeting to Her2+ tumors (compared to Her2- controls).[68]

1.3.2. Positron Emission Tomography (PET).

PET is a tomographic technique where a positron emitting radionuclide is the basis for the signal generation.[69] A radioactive tracer (e.g. ^{18}F-fludeoxyglucose (FDG)) undergoes β-decay yielding a positron, which travels a nucleus-specific distance before coming in contact with an electron – this results in an annihilation event, generating two gamma photons, traveling in opposite directions, that collide with a detector.[70] As a result, PET suffers from poor spatial resolution (in the order of multi-mm), and images are typically co-registered by other anatomical imaging techniques, such as CT (PET-CT). PET provides a highly sensitive, zero background

signal for the detection of injected materials. In the context of molecular imaging, relevant molecules can be targeted by PET-responsive nuclei, radiolabeled and quantified.[71] The disadvantages of PET imaging, include poor spatial resolution, high cost of production of radionuclides, and time-limited study durations depending on half-life of isotopes. Furthermore, PET usually requires advanced infrastructure (e.g. a cyclotron to generate radioactive isotopes, corresponding transport mechanisms etc.) which many clinical and research facilities do not have access to.[69]

The most common radioisotopes for PET include ^{11}Carbon, ^{13}Nitrogen, ^{15}Oxygen and ^{18}Flourine. These atoms are ideal since they can be easily incorporated into existing organic molecules of interest, and immediately injected for efficient image acquisition. For example, ^{18}F-FDG is often used for cancer detection, since tumors have higher metabolic rate than surrounding tissue thereby preferentially taking up the radiolabeled glucose. Since the glucose is fluorinated, it accumulates within the tumor without undergoing further metabolism, and is a highly sensitive marker of cancerous tissue.[72,73]

Isotopes such as ^{67}Gallium and ^{64}Copper can be chelated to organic ligands and can enable longer time-course studies.[74-78] These radionuclide inorganic metal complexes can be further conjugated with biological ligands for efficient molecular targeting.[75,76] Efficiency can further be amplified by conjugation of chelated radioisotopes to the surface of nanoparticles. This permits increased local concentration of radionuclide, and inclusion of PEG coatings can enable longer circulation times. Nanoparticle scaffolds allow conjugation of targeting groups for specificity, or other imaging agents to generate targeted multi-modal agents.[14] For example, Luehmann *et al.* synthesized nanoparticles composed of a poly(methyl methacrylate) core surrounded by a PEG

shell bearing ^{64}Cu chelated by DOTA ligands, and targeted using the D-Ala-peptide T-amide peptide to the chemokine 5 receptor.[79] This nanoparticle platform demonstrated significant accumulation and targeted PET signal.

1.3.3. Single Photon Emission Computed Tomography (SPECT)

Like PET, SPECT is a radionuclide-based 3D tomographic technique but utilizes gamma decay as opposed to β-decay. The radioisotopes involved include ^{99m}Tc, ^{111}In and ^{123}I, and can be measured directly. The corresponding single photon emission limits spatial resolution to sub-centimeter, and like PET benefits from co-registration with CT or MRI. SPECT also enables sensitive, quantitative imaging of injected species for targeted molecular imaging applications. The half-lives of ^{99m}Tc, ^{111}In and ^{123}I are considerably longer than PET radioisotopes, and permits longer studies. Common clinical applications of SPECT include myocardial perfusion imaging, functional brain imaging and tumor detection.[80,81] SPECT agents can also be amplified by conjugating radioisotopes to nanoparticles. For example, dual-radiolabeled gold nanoparticle SPECT probes were developed for imaging MMP-9 activity, a marker of tumor metastasis.[82]

1.3.4. Ultrasound Imaging (US)

US utilizes high frequency sound waves to generate images, and produces excellent soft tissue contrast. Inherent variations in tissue density will cause sound waves to be deflected in different directions before reaching the detector, producing native contrast.[83] US is widely used because of its portability, low cost, and short acquisition times. Clinically, it is used in maternal-fetal medicine, rapid assessment of abdominal or testicular pathologies, and breast cancer screening.[84] US is not without its disadvantages, which includes low resolution, limited depth penetration, and poor sensitivity.

US contrast agents have been developed, which are comprised of micron-sized gas bubbles ("microbubbles").[85] Mice bearing xenografts of human ovarian adenocarcinoma were imaged using targeted microbubbles, and significantly higher tissue contrast was observed compared to control injections or untargeted microbubbles.[86]

1.3.5. Optical Imaging

Optical imaging is reliant on signal generated by bioluminescent and fluorescent probes. These probes are frequently used in cellular imaging as they are versatile and require only an excitation source, but application in whole animal models have been limited due to poor depth penetration of visible light through intact tissue.[28] To address this, near-infrared (NIR) dyes have been used, which affords superior tissue penetration.[87] Optical imaging techniques still allow molecular imaging of a variety of targets. However, apart from depth penetration, quantification of signal is difficult due to wide scattering of emitted radiation, which can vary greatly depending on region of tissue being imaged.

Nanotechnology offers a method for targeted delivery of fluorophores. For example, a NIR dye-nanoparticle formulation composed block co-polymer PEG nanovesicles bearing docetaxel and BODIPY fluorophores was used for theranostics of mice with hepatocellular carcinoma xenografts. The agent enabled tumor regression and fluorescence imaging of the xenograft over a period of eight days.[88]

Bioluminescent probes are analogous to fluorescent ones, except signal is from genetic modification to create an endogenous probe. Specifically, the gene of interest can be linked to the firefly luciferase gene, which can now be probed in the presence of the luciferin substrate.[89] In this context, bioluminescense is thus far used in research settings since it requires extensive genetic

modification. Bioluminescence is particularly useful for monitoring long term response to cancer therapy in transgenic animals. For example, Zhao *et al.* used bioluminescence to monitor the acute effects of the vascular disrupting agent combretastatin A4 phosphate (CA4P) on luciferase-expressing MDA-MBA-231 human breast cancer tumor cell xenografts. A 50 – 90% decrease in luciferase signal was observed in the tumors, confirming the therapeutic efficacy of the CA4P at restricting blood perfusion to the tumor.[90]

1.3.6. Magnetic Resonance Imaging (MRI)

The foundation for MRI as a potential imaging modality can be largely attributed to the work of two pioneering scientists, Raymond Damadian and Paul Lauterbur. In his seminal Nature paper in 1973, Paul Lauterbur suggests "a new class of image generated, by taking advantage of induced local interactions".[91] Up until that time, the prevalent theory was that the generation of an image required the object to interact with matter or radiation with a wavelength equal or less than the smallest feature to be delineated. Lauterbur's idea was to use the principles of nuclear magnetic resonance (NMR); his solution was place the object in a secondary magnetic field such that the object's interaction with the primary magnetic field would be restricted to a particular region, thereby making the image measurement independent of wavelength. He described this new technique as "NMR zeugmatography"[91] for general purpose imaging not specific to medicine.

Two years prior, in 1971, Raymond Damadian published in *Science* that tumors could potentially be detected by their vastly different NMR relaxation times as compared to healthy tissue.[92] While he did not provide a technique for how an image of a patient or portion of a patient could be obtained, it was perhaps the first indication the principles of NMR could be used in *medical* imaging. To this day it remains a major point of contention that Raymond Damadian was

denied the 2003 Nobel Prize in Physiology/Medicine while it was given jointly to Paul Lauterbur and Peter Mansfield.

MRI offers several advantages over the other imaging techniques described previously. Compared to X-ray radiography, CT, PET and SPECT, MRI provides exceptional soft tissue contrast, has no limits to depth penetration, does not utilize nor produce ionizing radiation, and enables imaging in three dimensions.[93-97] Compared to US or optical modalities, it has far superior spatial resolution (as low as 50 μm depending on field strength of the magnet).[31,95,98]

While a detailed explanation of relaxation theory can be found in a number of excellent articles[99-102], a brief overview is presented here. The signal-to-noise ratios in MRI depend on the density of water protons (the human body is roughly 80% water) present in the region of interest and the degree of polarization of the nuclear spin states. When placed in a magnetic field, some protons will orient in the direction of the magnetic field and precess at a characteristic frequency (known as the Larmor frequency) related to the strength of the magnetic field. Upon application of an external radiofrequency pulse, the proton spins are perturbed; once the pulse is removed, the protons return ("relax") back to their ground state. Relaxation is measured in two directions, longitudinal and transverse. Longitudinal or spin-lattice relaxation is defined by the time constant T_1 and occurs in the direction of the main magnetic field. Transverse or spin-spin relaxation corresponds to vector dephasing in the plane perpendicular to the main magnetic field and is characterized by T_2. T_2 is always equal to or shorter than T_1. Inhomogeneity in the static magnetic field and spin-spin relaxation has an effect on the transverse magnetization, and T_2^* is the time constant that takes these into account. Overall, the time constants always adhere to the following relation: $T_2^* < T_2 < T_1$. Signals received from spin vectors are used to produce images by

superimposing magnetic gradients which define the spatial location of the signal. Tissue types vary in their relaxation properties, and thus MRI is used to reconstruct images to evaluate anatomical, perfusion and flow-related abnormalities.[99-102]

1.3.7. MRI Contrast Agents.

MRI contrast agents are used in clinical and research settings to augment the sensitivity of MRI, particularly for the differentiation of magnetically similar but histologically distinct tissues.[95,98,103] A majority of MRI contrast agents use paramagnetic or superparamagnetic species that alter the relaxation rates of surrounding water protons to produce positive (bright) or negative (dark) contrast. Thus it is important to note that MR contrast agents are themselves not a source of a signal and are not directly visualized but rather affect the surrounding water molecules that in turn directly influence the received signal. Today, contrast agents are administered in approximately 40-50% of the 7-10 million MR examinations per year.[102] The purpose of these agents is to add significant morphological and functional information to unenhanced MR images, thereby allowing for better-than-native tissue contrast, characterization of lesions, and evaluation of perfusion and flow-related abnormalities.

Although gadolinium based agents are by far are the most commonly used class of MR contrast agents to date, several other types have emerged. The different classes of contrast agents can be classified according to 1) the magnetic property of the agent, 2) the dominant effect of the agent on the signal intensity and 3) the biodistribution of the agent. ***Figure 1.2*** summarizes different classes of MRI agents according to these properties.[100]

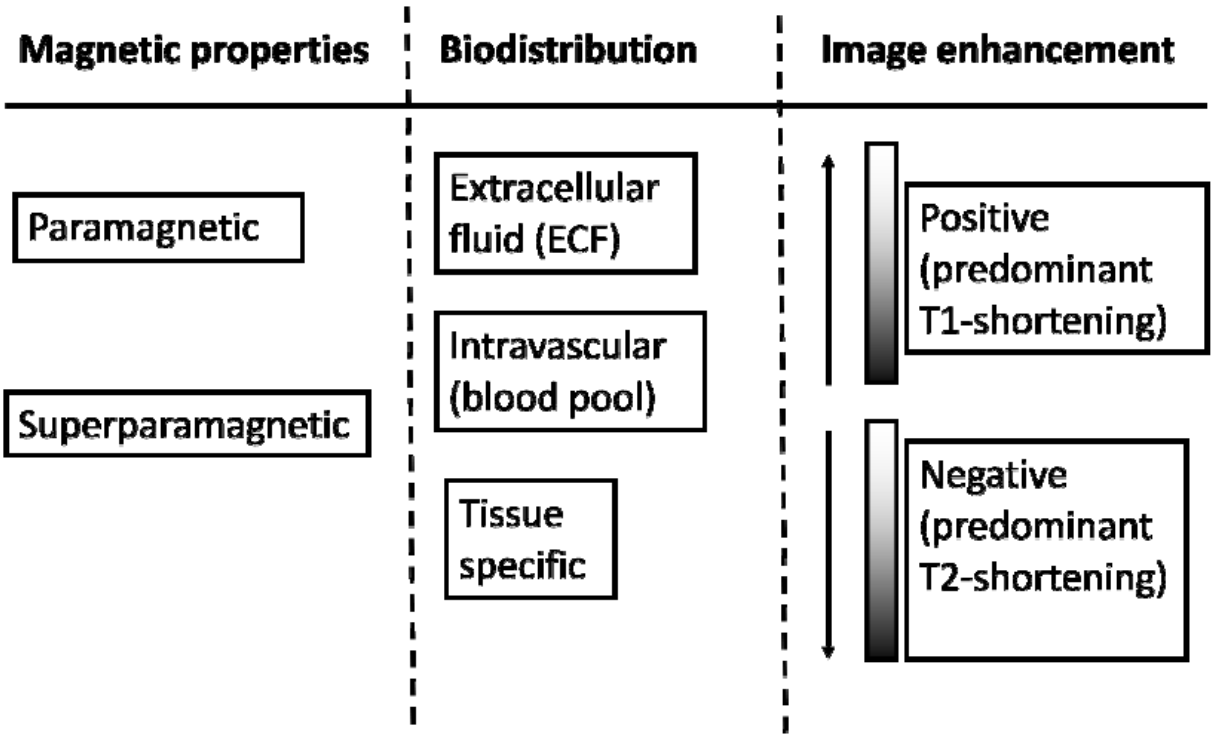

Figure 1.2. Classification of MRI contrast agents based on magnetic properties, image enhancement and biodistribution.[100]

(a) Paramagnetic vs Supermagnetic species[100]: Most MR contrast agents in clinical use to date are based on paramagnetic metal ions. *Paramagnetic* materials are metals with unpaired electrons in the outer orbital shells (most transition and lanthanide metals), giving rise to magnetic dipoles when exposed to a magnetic field. Since the magnetic moment of an electron is about 700 times larger than that of a proton (due to smaller mass), the paramagnetic ions induce large fluctuating magnetic fields experienced by nearby protons. If the frequency of this fluctuation has a component close to the Larmor frequency, it will result in a significant enhancement of proton relaxation, particularly T_1 relaxation. There are many paramagnetic metal ions that could potentially be used as MR contrast agents but the transition metal *gadolinium* (Gd(III)) is by far the most commonly used. This is due to a favorable combination of many (seven) unpaired electrons combined with a long electron spin relaxation time which makes this metal a very efficient relaxation enhancing agent.

Superparamagnetic agents are most commonly based on magnetite (Fe_3O_4) or maghemite (γ- Fe_2O_3) insoluble iron oxide nanoparticles. These particles, termed *superparagmagnetic iron oxide nanoparticles* (SPIO), have a core diameter between 5-10 nm, where each nanoparticle contains several thousand paramagnetic Fe ions (Fe^{2+} and Fe^{3+}), resulting in a net magnetic moment (only in the presence of an external magnetic field) that is significantly larger than that of paramagnetic species. Other formulations of superparamagnetic nanoparticles include Manganese-based nanoparticles which have similar properties to SPIO. Superparamagnetic agents also produce strong enhancement of T_1 relaxation of water (depending on size and composition), but their dominant effect is on T_2/T_2* relaxation.

(b) Biodistribution[100]: The biodistribution of a contrast agent describes how the agent is distributed *in vivo* after intravenous administration. *ECF agents* are typically small molecular weight (MW) paramagnetic agents that are capable of diffusing from the plasma into the interstitium and be distributed to the extracellular fluid. They are not taken up by cells and are therefore eliminated by renal excretion with a half-life determined by the glomerular filtration rate. *Intravascular agents* are contrast agents with a MW large enough to prevent leakage from the vascular to the intravascular space. All SPIO nanoparticles are intravascular agents, with a half-life in blood ranging from a few minutes to several hours. They are eventually eliminated from the blood by the reticuloendothelial system, via phagocytosis by the Kupffer cells of the liver, and macrophages from the spleen and lymphatic system. Other types of intravascular agents exist which are based on macromolecular gadolinium compounds. Such agents are designed either by linking Gd(III) ions to a macromolecular polymer during synthesis or by making the Gd(III) complex bind to plasma proteins after injection and thus forming macromolecules in blood. *Tissue specific agents* have been specifically designed to accumulate in a given organ or tissue type (e.g. molecular targeting via antibodies or ligand-receptor interactions).

(c) Image enhancement[100]: The effect of the contrast agent on the signal intensity can either be positive (increase in signal or T_1-enhancement) or negative (signal reduction or T_2-enhancement). In general, Gd(III)-based, paramagnetic agents predominantly behave as T_1-enhancing agents, and SPIO/Manganese oxide superparamagnetic nanoparticles behave

as T_2/T_2*-enhancing agents. However, it is important to note that almost all MRI contrast agents will affect *both* T_1- and T_2-relaxation times and the distinction between T_1- and T_2-enhancing agents is therefore somewhat artificial that will depend on several parameters as well as contrast agent dose.

1.3.8. The Concept of Relaxivity

Relaxivity theory, presented in extensive detail in several books and review papers[99,100,102], is abridged and summarized in this section. The ability of a contrast agent to enhance the proton relaxation rate is defined as *relaxivity.* The observed solvent relaxation, $(1/Ti)_{obs}$, is the sum of the intrinsic diamagnetic solvent relaxation rate in the absence of the paramagnetic species, $(1/Ti)_{d}$, and the additional paramagnetic contribution, $(1/Ti)_{p}$, that is:

$$\frac{1}{T_{i,obs}} = \frac{1}{T_{i,d}} + \frac{1}{T_{i,p}}; i = 1,2$$

Equation 1.1.

In the absence of solute-solute interactions, the solvent relaxation rate is linearly dependent on the concentration of the paramagnetic ion, c_{agent}:

$$\frac{1}{T_{i,obs}} = \frac{1}{T_{i,d}} + r_i c_{agent}\ ; i = 1,2$$

Equation 1.2.

where r_i agent is the *relaxivity* of the paramagnetic agent, typically defined in units of $mM^{-1}\ s^{-1}$. The effect of the agent is dependent on the distance from the ion and the diffusion of solvent molecules. Water interaction with the metal ion is classified into three types: (1) primary coordination sphere, (2) hydrogen-bonded molecules in the secondary coordination sphere, and (3) bulk water that translates and diffuses past the metal. These interactions are shown in ***Figure 1.3***, with Gd(III) as the model paramagnetic ion.

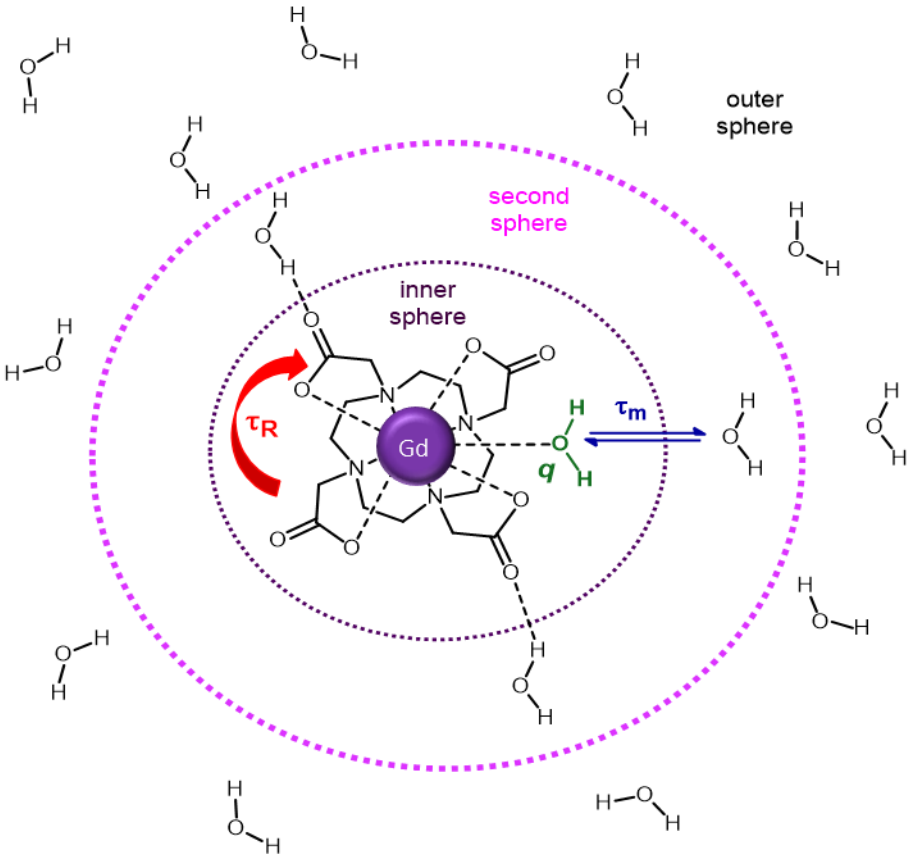

Figure 1.3. Relaxation coordination spheres of water: inner-sphere, outer-sphere and bulk water. Also shown are the Solomon-Bloembergen-Morgan parameters: (i) τ_R, which is the rotational tumbling or correlation time of the entire metal-water complex, (ii) τ_M, which is the water residence time in the metal center and (iii) q, which is the hydration number or the number of water molecules bound to the metal center. Image adapted from: Villaraza *et al*. *Chem Rev* 2010, *110*, 2921-59

Inner-sphere relaxation is the enhancement found in the first coordination sphere. If the time of interaction is long compared to the time of diffusion, second coordination sphere water molecules demonstrate similar relaxation to the first sphere. However, typically enhancement in the second coordination sphere and bulk water is grouped together as outer-sphere relaxation. Thus, the total paramagnetic relaxation enhancement is the sum of the inner-sphere and outer-sphere relaxation.

While outer-sphere relaxivity is difficult to quantify, there are several parameters that govern inner-sphere relaxivity as modeled by the Solomon-Bloembergen-Morgan equations. These parameters can be optimized to improve the efficiency of a contrast agent. The three most important parameters that govern inner-sphere relaxivity are: (i) τ_R, which is the rotational tumbling or correlation time of the entire metal-water complex, (ii) τ_M, which is the water residence time in the metal center and (iii) q, which is the hydration number or the number of water molecules bound to the metal center (see ***Figure 1.3*** for more detail). In order to maximize relaxivity per water molecule (q=1), τ_R must increase and τ_M must decrease i.e. longer tumbling time of the entire water-metal complex and shorter mean residence lifetime of the water molecular at the metal center would both enhance relaxivity. τ_R can be increased by using an agent with higher molecular weight (tumbles longer in solution) and τ_M can be decreased by changing the chemistry of the molecule (e.g. inclusion of a back-binding arm that limits water coordination of the water molecule to the metal center).

The mechanism presented above is valid for all paramagnetic metal ions; however, it must be noted superparamagnetic species such as SPIO nanoparticles have a mechanism for relaxation enhancement that is not fully known and is currently being extensively studied[100,104,105]

For safe use of Gd(III) in biological systems, the paramagnetic ion must be chelated by an organic ligand. This is due to the ionic radius of Gd(III) being similar to that of Ca(II) and Zn(II) which can interfere with endogenous calcium and zinc signaling. For example, unchelated Gd(III) can be permanently retained within bone when taken up in place of calcium. Accordingly, Gd(III) is often chelated into macrocyclic and linear ligands, which provides adequate stability for clinical use. Clinically used Gd(III) chelates are shown in ***Figure 1.4***. These agents show incredibly high values of thermodynamic stability, with formation constants (log K_{eq}) of up to 25.8 for Dotarem.[96] The agents shown in ***Figure 1.4*** generate relaxivities between 3.5 – 5.5 mM^{-1} s^{-1}, values which represent only 10% of the maximum achievable relaxivity predicted for clinical field strength MR instruments (most commonly 1.5 T).[95]

Experimental manipulations of the variables presented in ***Figure 1.3*** are often implemented towards optimization of Gd(III)-based contrast agents. The number of bound waters, the inner-sphere water exchange rate, and the molecular reorientation time, however, are more readily accessible by synthetic modification of the ligand, and can be measured by straightforward chemical techniques.[106] For this reason, these are the most commonly used strategies for contrast agent optimization.

1.3.9. High-Field MRI

Optimizing r_1 in practice is difficult. There are several variables which define relaxivity, like the electronic relaxation time and the molecular reorientation time, which have different optimized values at different magnetic field strengths.[107] Therefore, no single agent can perform at the highest level across all magnetic field strengths. As research grade MRI magnets shift toward higher and higher magnetic fields strengths (for the purposes of increased spatial resolution and

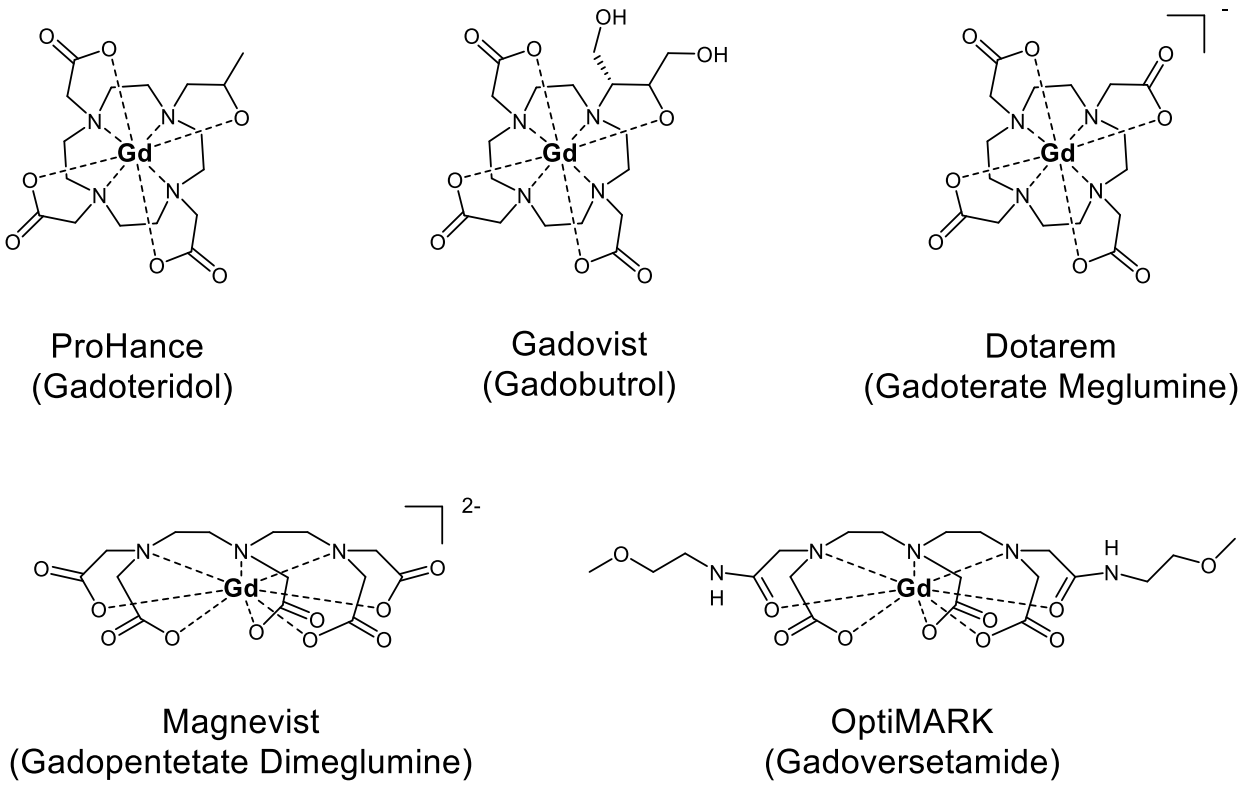

Figure 1.4. Linear and macrocyclic varieties of clinically approved Gd(III) contrast agents and their trade names. When coordinated into octadentate ligands which allow for dynamic chemical exchange of one water molecule, these complexes exhibit thermodynamic stability constants between 22.1 – 25.8.[96]

decreased scan times), the beneficial effects of SBM parametric optimization decrease, because the maximum values of r_1 which are possible at increasingly high fields strengths diminish rapidly.[107] Specific strategies which address modulation of these parameters are described in more detail below.

(a) Varying the Quantity of Inner-Sphere Water Molecules. As shown in ***Figure 1.4***, small clinical agents are chelated such that they allow coordination of one inner sphere water molecule (q = 1). This prioritizes safety over performance, provides adequate thermodynamic stability constants for clinical use. However, based on the equations that govern inner-sphere contributions to r_1, the addition of a second or third inner sphere water can double or triple relaxivity. For example, alternate ligand designs include variations of diethylenetriamine N, N, N', N'-tetraacetate (DTTA, q = 2), 6-amino-6-methylperhydro-1,4-diazepinetetraacetic acid (AAZTA, q = 2) and a number of chemistries associated with the dihydroxypyridone (HOPO, q = 2, 3) ligand.[98,108-113]

(b) Modulating the Rotational Correlation Time.

Changing the molecular reorientation of the Gd(III) complex is known to produce large changes in r_1 relaxivity, particularly at field strengths between 0.5 – 1.5 T. In practice, this strategy is implemented by increasing the molecular weight of the Gd(III)-ligand complex, or restricting the rotational motion of the complex by coupling its local rotation to the global rotation of a larger molecule, macromolecule, protein or nanoparticle. For example, using a multiplexing approach multiple Gd(III) complexes can be immobilized about a barycenter, simultaneously increasing the number of Gd(III) complexes and the total molecular size and making τ_r longer. Alternately, using bifunctional Gd(III) complexes, linear or dendrimeric polymers can be made to both restrict

motion and bear multiple Gd(III) centers per polymer.[96,111,114-117] By the simple addition of long hydrophobic tails or amphiphilic peptide sequences to Gd(III) complexes, a self-assembly process provides the formation of spherical micelles, lamellar bilayers or even high aspect ratio cylindrical fibers, which in each case is shown to slow the local rotation of the Gd(III) complex.[35,118-121] Another strategy where the molecules themselves are not providing the increased molar mass is the attachment of the Gd(III) complex (covalently or non-covalently) to a biomacromolecule like human serum albumin or viral capsids.[122-128] Recently, viral capsids were shown to provide a nanometer sized substrate onto which the Gd(III) complexes were bound, not only increasing the relaxivity per Gd(III), providing a large payload of Gd(III) per capsid, increasing the local concentration of CA significantly.

1.4. Nanoparticle Contrast Agents for Amplification of MR Signal.

Despite its numerous advantages as an *in vivo* imaging modality, the principal shortcoming of MRI for applications in molecular imaging is low agent sensitivity.[129] The limit of detection for MR contrast agents *in vivo* is between millimolar and tens of micromolar in concentration, whereas much of the mammalian transcriptome is expressed at concentrations of low micromolar through picomolar in concentration.[31,103] Therefore, it is nearly impossible to design a Gd(III)-based targeted contrast agent to produce contrast in 1:1 ligand:receptor ratios.[130,131] This limitation can be partially overcome by relaxivity enhancements per ion upon target binding (e.g. by τ_r or inner/outer/second sphere modulation) but this strategy still requires target expression levels be among the highest known (like HSA targeted agents for angiography), or additional significant signal amplification.[122,123,132-142] Multiplexing Gd(III) agents is another strategy for relaxivity enhancement but this provides only a few-fold improvement at best.

Nanotechnology is a viable alternative to overcome some of the shortcomings mentioned above. Nanoparticle-contrast agent conjugates provide several advantages. Firstly, agents immobilized to a particle surface will benefit from a boost in relaxivity by restricted rotational freedom (which can be modulated by linker length and chemistry). Secondly, nanoparticle scaffolds can be conjugated to hundreds or more Gd(III) complexes per particle. Finally, nanoparticles can be combined with a variety of conjugation chemistries and provide the capacity for multi-modal imaging, delivery of chemotherapeutic payload, and molecular targeting, all while continuing to display the unique features of the nanomaterial of choice.[143] The subsequent sections of this chapter will provide a brief overview of the different types of Gd(III)-nanoparticle designs.

1.4.1. Silica-Based Gd(III) Nanoparticle CAs.

Silica–based nanomaterials provide a number of interesting features for use as MR contrast agents. They are readily synthesized, can be controlled for size, shape, porosity and surface area, and be designed to coat the exterior surface of nanomaterials of other types.[144,145] The porosity and hydrophilic surface of Si-Gd(III) nanoparticles have been shown to produce high relaxivity at high magnetic field strengths. For example, Rieter *et al.* synthesized ruthenium core-silica shell mesoporous particles functionalized with two versions of Gd(III)-DTPA complexes.[146] These constructs achieved as high as 20 mM^{-1} s^{-1} at 3 T, with particle loading of 10,200 Gd(III) per particle.[147] Other groups investigating silica-based nanoparticles have used relatively large mesoporous particles, all of which have r_1 high values – this indicates Si-Gd(III) nanoparticles provide a unique enhancement to relaxivity not demonstrated by other nanoparticle-immobilized Gd(III) complexes.[148,149]

1.4.2. Polymeric Nanoparticle and Dendrimer Gd(III) CAs.

Biocompatible polymers have been shown to provide high Gd(III) payload and high performance. Research is largely split between spherical polymer particles (though there are some examples of alternate shapes), and dendrimeric polymers. Some recent examples include covalent attachment of Gd(III)-DTPA and Gd(III)-DOTA to poly(D,L-lactide-co-glycolide) nanoparticles, Anti-VEGF targeted triblock poly-lactic acid-polyethylene glycol-poly-L-Lysine functionalized particles with Gd(III)-DTPA, and non-covalent dissolution of Dotarem into a co-polymer of hyaluronic acid and chitosan, which displayed some of the highest values of r_1 ever reported for a chelated Gd(III) – approximately 110 mM^{-1} s^{-1} at 0.47T.[150,151,152] Though this area of research presents interesting work, there are relatively few examples in the literature, and of these, the most often reported sizes of particle are around 100 nm, which limits their utility for *in vivo* applications.

Dendrimers are controlled growth polymers which are synthesized from a central core in successive rounds of chemical reaction (to create layers of monomers that grow outward exponentially, known as generations, by the strategy of divergent synthesis) or the linkage of discretely synthesized branched units which are later bound to a central core (convergent synthesis).[96] They differ from spherical particles because they tend to be small, growing outward approximately 1 nm per generation, and are reported to become unstable past the tenth generation (G10). This characteristic limits the available size range, but based on the discrete chemistry used to add each generation, dendrimers feature extremely low polydispersity indices (PDI).[153,154] Monomers and the chemistries used to create dendrimers are diverse, but the most common of these use Poly(amido amines), known as PAMAM, and the earliest examples of these dendrimeric CAs incorporated Gd(III)-DOTA, Gd(III)-DTPA or other synthetic variants of Gd(III)-DO3A.[155-

[159] More recent work has explored different chemistries for better biocompatibility and have utilized the HOPO ligand for increased relaxivities.[160,161]

1.4.3. Micellar and Liposomal Gd(III) Loaded Nanoparticle CAs.

The use of micelles and liposomes are some of the most commonly used nanoformulations due to ease of synthesis, scalability, and size selection capacity. Specifically, these constructs are made from amphiphilic molecules which display a hydrophobic tail and a polar head group, and can be assembled in such a way as they form either solvent-excluded hydrophobic cores between 5 and 50 nm (micelles), or larger, spherical bilayers which range in size from 50 – 800 nm in size (liposomes). Importantly, because these structures are assembled from monomeric amphiphiles, other molecules with differently functionalized head groups can be doped into the formulation to create mixed monolayers of different surface functionality.[162-164] Application of this premise has allowed the addition of targeting groups, additional charge stabilization, pharmaceuticals or imaging agents like Gd(III).[165-167] In addition, the hydrophobic core of micelles, and the intralayer space of liposomes can be used to solubilize hydrophobic molecules like chemotherapeutics.[168] In recent work by Gianolio and Briley-Szabo, micelles were assembled using a lipophilic Gd(III)-AAZTA complex, and displayed relaxivities of 30 mM^{-1} s^{-1} using only the Gd(III) complex in 5.5 nm micelles.[169] However, when the lipophilic contrast agent was co-assembled with high density lipoproteins (HDL), the 10-15 nm nanoconstructs displayed a relaxivity which improved to 36 mM^{-1} s^{-1} with loading of 80 Gd(III) per particle.[170]

1.4.4. Carbon Based Gd(III) Nanomaterials.

Carbon nanomaterials come in numerous sizes and shapes, from spherical buckminsterfullerenes, truncated octahedral nanodiamonds, cylindrical single- and double-walled

carbon nanotubes and single atomic layer graphenes and graphene oxides. These materials have generated excitement in many fields for their remarkable properties of mechanical strength, electronic and phonon conduction capacities, unmatched surface area per weight and unique optical properties. [42,171-173]

By placing a single Gd(III) ion inside the volume of a C_{60} buckminsterfullerene, researchers observed remarkably high relaxivities, due to the Gd(III) interaction with the carbon material, and that it contained no organic ligand, and so could complex up to 9 water molecules at a time.[39,174-176] However, these materials showed pH-dependent behavior, and highly variable colloidal stability which may limit their use for *in vivo* applications in the short term. Similarly, carbon nanotubes can be loaded with unchelated Gd(III) and generate relaxivities up to 170 $mM^{-1}\,s^{-1}$ at 60 MHz.[177,178] Using chelated Gd(III) with long hydrocarbon tails, multi-walled carbon nanotubes provided a non-covalent substrate, and proof-of-concept *in vivo* imaging was successfully performed.[40]

Hung *et al.* studied the non-covalent interaction of variably functionalized Gd(III) complexes, examining colloidal stability, relaxivity and cell transfection ability of graphene and graphene oxide. In addition to generating remarkably high relaxivities, the constructs were incorporated into a cellular incubation process for efficient intracellular delivery of Gd(III) for cell labeling purposes.[36,179]

1.4.5. Nanodiamonds

Nanoscale diamond particles, or nanodiamonds (NDs), represent one of several classes of carbon nanoparticles that have great potential for a variety of biological applications.[38,180-189] Originally discovered in the 1960's, their value in materials science was not explored till the

1980's. Today, nanodiamonds are commercially produced from detonation of explosives, which provide both a source of carbon and energy for the conversion. The detonation takes place in a closed chamber filled with an inert gas ('dry synthesis') or ice coolant ('wet synthesis').[183] The product — detonation soot — is a mixture of diamond particles 4–5 nm in diameter with other carbon allotropes and impurities. Detonation soot contains up to 75 wt% of diamond and the carbon yield is 4–10% of the weight of the explosive, depending on cooling media. The detonation soot is then purified by oxidation to remove non-diamond carbon. Oxidation in air is robust, cost-effective and the most environmentally benign purification technique, and increases the diamond content from ~25 wt% (detonation soot) to >95 wt%. Oxidation also transforms functional groups present on the nanodiamond surface to oxygen-containing species (mainly anhydrides and carboxylic acids), thereby creating a product with a high content of diamond and a unified surface chemistry.[183] In order to further homogenize the ND surface, various ketones, esters, carboxylic acids, and aldehydes are reduced to hydroxyl and hydroxymethyl groups using lithium aluminum hydride or borane in THF. This hydroxylated ND can be used as a starting material for a wide variety of subsequent functionalizations of the ND, allowing for greater control of the NDs chemical and physical properties, as well as the development of related applications.[190] Individual nanodiamonds have diameters of 4–5 nm, but they tend to aggregate when dispersed as a colloidal suspension. Small aggregates are actually useful for the purpose of drug delivery and chromatography, but individual nanodiamonds in a colloidal suspension can be generated by milling with ceramic microbeads or by microbead-assisted ultrasonic disintegration.[183]

ND-based constructs have provided numerous breakthroughs for molecular imaging.[191-198] Through advances in covalent and noncovalent modification of the ND surface, imaging of ND

particles has largely centered on optical imaging with fluorescence spectroscopy. Ion beam irradiation has been used to form fluorescent centers with red and green emission visible at the cellular level.[180,199] Blue fluorescent nanodiamonds (5 nm in diameter) have been produced by covalent attachment of octadecylamine (ODA) to the carboxylate groups of the nanodiamond surface.[180,199] These fluorescent nanodiamonds provide an alternative to toxic quantum dots. Recently, a novel biocompatible ND for MRI was synthesized in the Meade lab by covalently coupling a Gd(III) chelate to the ND surface.[38] ND-Gd(III) complexes decreased the average longitudinal relaxation time of environmental water protons 10-fold with respect to NDs that were not functionalized, and 12-fold with respect to the free Gd(III) chelate. The relaxivity of ND-Gd(III) complexes was among the highest ever reported in the literature.

1.4.6. Gold nanoparticle Gd(III) Nanoconjugates.

In the area of nanoconjugate contrast agents, gold nanoparticles boast the largest variety, with examples of different combinations of particle shapes, sizes, Gd(III) complexes, and variations in surface stabilization strategies, targeting, and multi-modality. In fact, in a number of cases Gd(III) bearing particles have used as multimodal agents by the generation of CT contrast using the ability of gold to attenuate X-Rays.[47,65-68,200] In the simplest case of Gd(III) gold nanoparticle conjugates, thiolated metal complexes were added directly to the nanoparticle surface as either monomeric complexes,[201,202] or bifunctional thiolated adducts of Gd(III)-DTPA. For example, Tillement and co-workers describe a nanoconjugate CA where the particle surface was functionalized with loops of Gd(III)-DTPA complexes linked end to end by disulfide linkages. [48] In a second example, Moriggi *et al.* functionalized 2.3 nm gold spherical gold nanoparticles with a Gd(III) complex bearing a thiophenol modification off the backbone of a DTTA ligand. Despite

the very small size of the gold core, loading of Gd(III) was 56 complexes per particle, and showed 30 MHz relaxivities up to 60 mM^{-1} s^{-1}, due to strong coupling of the local motion of the Gd(III) to the global rotation of the particle.[202] In these cases the Gd(III) complexes were acting as both a contrast agent and stabilizing ligand for the colloidal stability of the nanoparticle.

While spherical nanoparticles of varying size are the predominant form of gold nanoparticle used in nanoconjugate CAs, some groups have investigated the use of other shapes, including nanorods[50,51] and nanostars.[46] Due to the robustness of gold-thiol conjugation chemistry, the availability of ligands for particle stabilization and attachment of Gd(III) is vast. The literature of nanoconjugate CAs boasts gold particles bearing ligands of DNA,[37,49] peptides,[52,53] PEG,[54,55] saccharides,[56,57] polymers[58-60] and combinations thereof. Besides the use of the gold core for generation of CT contrast, the modular nature of nanoparticle assembly and the ease of gold-thiol chemistry allows the addition of other imaging modalities, including optical imaging and PET/SPECT probes.

3’ thiolated deoxyribonucleic acid (DNA), and the subsequent product of its conjugation to gold nanoparticles, is termed the ‘spherical nucleic acid’ (SNA).[203] In 2009, the Mirkin and Meade labs conceived of a new Gd(III) DNA gold nanoconjugate contrast agent design. The construct was composed of a 3’ thiolated 24-mer poly deoxythymidine (dT) DNA strand containing modified dT bases at five positions, which was covalently modified with Gd(III) and which contained a 5’ Cyanine3 fluorophore, and which is then conjugated to the surface of 13.1 nm gold nanoparticles.[204] After publication of this work, the DNA-Gd^{III}@AuNP particle construct was immediately considered for work in a long standing collaboration between the Modo and Meade labs for the tracking of labeled human Neural Stem Cells (hNSCs).[61]

A large portion of this thesis was devoted to the synthesis of next-generation gadolinium(III)-gold nanoconjugates. These constructs, termed Gd@AuNPs, were synthesized to be devoid of DNA, yet bear significantly greater Gd(III) loading and long-term cell labeling. This new construct was also the first MRI contrast agent of any type to accumulate in the pancreas, which shows tremendous promise for preclinical imaging of pancreatic diseases. Chapter 4 of this thesis is devoted to this work.

1.5. Nanoparticle MRI Contrast Agents for Cancer Cell Tracking.

Metastatic brain tumors are a leading cause of cancer-related death worldwide. Several cancer subtypes have propensity for brain metastases, including melanoma, colon, kidney, lung and breast cancer. Patients typically survive only twelve to seventeen months after metastatic onset.[205-207] Elucidating the mechanism of brain metastasis may enable early diagnosis and therapy.

The current limits of spatial resolution from preclinical scanners and the efficiency of the best Gd(III)-based cell labeling agents affords a detection limit of only 1000 Gd(III)-labeled cells *in vivo*.[208] In comparison, polysaccharide-coated iron oxide nanoparticles have been used to label cells *ex vivo* and enables up to single cell detection due to a blooming T_2^* susceptibility artifact.[32,208,209]

Superparamagnetic iron oxide nanoparticles (SPIONs) are the only contrast agents approved for clinical use.[210,211] Lumirem® (silicon-coated iron oxide particles with a diameter of 300 nm) and Endorem® (magnetite nanoparticles of 150 nm in diameter, coated with dextran) are commercial names of SPIONs available on the market, used for imaging the gastro-intestinal tract and for the detection of liver and spleen diseases including cancer.[210,211] Endorem® exploits its

uptake by Kupffer cells, which produces significant contrast between healthy and diseased tissues devoid of Kupffer cells (e.g. tumors or metastases).

However, T_2 CAs for cell tracking are plagued by several disadvantages. Firstly, T_2 CAs cause signal loss (negative contrast) as opposed signal gain (positive contrast). Negative contrast can be confused with *in vivo* phenomena such as hemorrhage, blood flow, air pockets, or regions of native high iron content such as liver or spleen.[209,212,213] Secondly, blooming susceptibility artifacts, while enabling more sensitivity, also overestimates the size of a cell cluster as determined by imaging. This will severely hamper interpretation of surrounding anatomical structures in a cell graft. Thirdly, iron oxide particles are susceptible to clearance by macrophages which can lead to high transplanted cell death rates. Finally, T_2 CAs are best visualized by T_2-weighted sequences, which have an inherently lower signal-to-noise ratio than T_1-weighted images.

More recently, Gd(III) chelates have been receiving increasing interest as an intracellular imaging probe.[61,209,214,215] One of the main advantages of Gd(III) chelates over T_2 CAs is their predominant positive contrast effect due to T_1 shortening. Furthermore, as a result of its low molecular weight, the Gd(III) chelate can escape macrophage reuptake after cellular release due to, for example, cell death. This is a highly important advantage in the in vivo setting as it contributes to a high specificity of the MRI signal, aiding the assessment of overall cell viability after cell transplantation. A major focus of Chapters 2 and 3 of this thesis is the development of Gd(III)-based nanoparticle conjugates (specifically using carbon nanodiamonds) for MRI of cancer growth *in vivo*.

1.6. Theranostic Nanoparticle Constructs for Cancer Imaging and Therapy.

Results of gene expression studies have confirmed that cancer of a specific organ is not a single disease with variable morphologic features and biomarkers but a group of molecularly distinct neoplastic disorders.[216-219] For example, molecular classes of non-hereditary breast cancer have been distinguished using gene-expression profiles. In particular, the estrogen receptor (ER)-positive, progesterone receptor (PR)-positive, and Human Epidermal Growth Factor Receptor 2 (HER2)-positive subtypes have been used to design targeted therapies; for example, Tamoxifen is a selective ER modulator (SERM) that is used in ER+ breast cancer, and trastuzumab is a monoclonal antibody used in HER2+ breast cancer.[220] However, triple-negative breast cancer (TNBC) – no ER, PR or HER2 expression – is particularly challenging to treat since targeted or hormonal therapies are not available. Furthermore, the intrinsic molecular heterogeneity TNBC makes active targeting particularly difficult. In terms of treatment, primary breast tumors are largely managed with surgery and radiation therapy; however, systemic disease often requires adjuvant chemotherapy.[220] Since a multitude of plastic phenotypes exist within a single TN tumor, treatment resistance is becoming a significant challenge. Resistance to chemotherapeutics is believed to be responsible for treatment failure in more than 90% of patients with metastatic cancer, including metastatic breast cancer.[45] In order to combat resistance, large chemotherapeutic doses are utilized that result in significant systemic toxicity.[220-223] Nearly all current adjuvant chemotherapy protocols for breast cancer, regardless of hormone receptor status, include an anthracycline agent like doxorubicin (Dox).[220,221] Like other drugs of its class, Dox intercalates DNA causing cell death in rapidly-dividing cells. However, at high doses, Dox can cause fatal dilated cardiomyopathy, hepatic failure and severe myelosuppression.[224-228] Therefore, in order for

selective delivery of cytotoxic agents like Dox, a single delivery system that combines molecular targeting and chemotherapy is highly desirable.

A "theranostic" system is one that combines diagnostic imaging and therapeutic delivery into a single platform. Such a system overcomes undesirable differences in biodistribution and selectivity from having two distinct agents.[168,210,229-231] The ultimate goal of the theranostic field is to image the diseased tissue, evaluate delivery kinetics, and assess drug efficacy in the course of a single treatment. In the long-term, theranostics allow for tuning of therapy and dose for a more effective and personalized treatment approach.[168,210,229-231]

The most promising aspect of utilizing nanoparticles as therapeutics, diagnostics, and theranostics is their potential to localize to the site of disease, thereby reducing numerous side effects.[190,229,232-235] The nanometric size of these materials precludes them from being readily cleared through the kidneys and extends their circulation in the blood pool. In the context of cancer treatment, blood vessels in many tumor types are irregular in shape, dilated, and "leaky" with a greater number of fenestrations between endothelial cells. Therefore, nanoparticles can more easily extravasate from the blood pool into tumor tissues, and be retained due to poor lymphatic drainage. This phenomenon of selective accumulation of nanoparticles near tumor tissues is termed the enhanced permeability and retention (or EPR) effect, and is often exploited as a form of passive targeting of nanoparticles to tumors.[168,210,230,231]

Additionally, nanoparticles have high surface area-to volume ratios, yielding high loading capacities. Thus, nanoparticles can be loaded with therapeutic drugs and imaging agents; they may also be surface functionalized with targeting ligands and cloaking agents like PEG. Introduction of targeting ligands may help to increase the target-to-background contrast in imaging and improve

the local concentration of the therapeutic at the target of interest, thereby reducing systemic toxicity.[210,231]

Nanodiamonds described earlier meet the requirements for being an efficient drug delivery platform: they are biocompatible, can carry a broad range of therapeutics, are dispersible in water and allow uniform, scalable production. A range of other cargos have been delivered using NDs, including covalently attached drugs[182,189,236,237], proteins[237,238], small molecules under acidic conditions (which are commonly observed in tumors)[187,237,239] and siRNA for specific cancers.[186,188,189]

Our collaborator, Prof. Dean Ho, developed Nanodiamond–doxorubicin complexes (ND–Dox) to treat drug-resistant breast cancer (4T1) and liver cancer (LT2-M).[44,45] NDs, by sequestering Dox onto its surface and producing a delayed release profile, reduced the capacity of the tumors to expel Dox. Further, the circulation half-time of ND–Dox complexes was found to be 10 times that of unmodified doxorubicin. Other advantages of ND–Dox were the absence of myelosuppression (which is high when free Dox molecules are used), the absence of mortality when high doses are delivered (high doses of free Dox generally kill the mice in these experiments) and significant reductions in the sizes of the tumors.[44] The breakthroughs using ND-Gd(III) for MRI and ND-Dox for chemotherapy can be exploited to create theranostic ND-Gd(III)-Dox, which is a major focus of chapter 3 of this thesis.

Chapter 2:

Nanodiamond-Gadolinium(III) Aggregates for Tracking Cancer Growth *In Vivo* at High Field

Rammohan, N.; MacRenaris, K.; Moore, L.; Parigi, G; Mastarone, D; Manus, L.; Lilley L; Preslar, A.T.; Waters, E.A.; Filicko, A; Luchinat, C; Ho, D.; Meade, T.J. Nanodiamond-Gadolinium(III) Aggregates for Tracking Cancer Growth *In Vivo* at High Field. *Nano Letters*. **2016**. *Under Revision.*

2.1. Introduction

Magnetic Resonance (MR) imaging is a non-invasive technique to image live organisms in three dimensions with high spatiotemporal resolution.[1-6] MR imaging is reliant on intrinsic proton relaxation times of tissue, and is widely used in clinical settings as an alternative to X-ray radiography, computed tomography and nuclear modalities since it requires no ionizing radiation. To enhance tissue contrast, paramagnetic gadolinium(III) [Gd(III)] chelates are commonly utilized as contrast agents (CAs).[7-9] These agents shorten the relaxation time of water protons in the region of CA accumulation to generate contrast in tissue.[7-9] Gd(III)-based agents at clinically-relevant concentrations produce positive contrast by shortening the longitudinal (T_1) proton relaxation time. In regions of very high CA accumulation, these agents can produce negative contrast by decreasing the transverse (T_2) proton relaxation time. The efficiency with which CAs decrease relaxation time is termed relaxivity (r_1 or r_2 for longitudinal and transverse relaxivities respectively). One application of MR imaging is cellular labeling, which can be harnessed to track transplanted cells and tissues *in vivo.* MR imaging is advantageous due to absence of ionizing radiation and better spatiotemporal resolution than optical and nuclear techniques.[10-13] Information on cellular localization and movement would enhance our understanding of numerous disease processes, including immune cells homing to sites of inflammation, invasion and metastasis of cancer cells, and stem cell differentiation and migration.[10,14,15]

In the context of cancer, the ability to noninvasively track cancer cells *in vivo* would permit researchers to study cellular distribution, growth and metastatic potential in pre-clinical models. Cancer cells can be labeled *ex vivo* with CAs, implanted into a small-animal model system, and longitudinally monitored for tumor growth. Unlike stem cells and immune cells, cancer cells

present a unique challenge for CA development because their growth and proliferation dilutes the concentration of CA in the cell. Therefore, an ideal CA for tracking cancer cells should possess the following properties: substantial intracellular accumulation and retention, biocompatibility, congruence with cellular function, performance at clinically relevant field strengths, and enable imaging over long periods of time.[14,15]

Unfortunately, clinically-utilized Gd(III) chelates such as Dotarem®, Magnevist®, and ProHance® do not effectively accumulate in cells.[11,16] In contrast, nanoparticle CAs composed of iron oxide or manganese have been utilized to label cell populations.[12,17-19] Although these particles benefit from high labeling efficiencies, they produce non-tunable negative contrast, suffer from susceptibility artifacts and clearance by macrophages.[11] If Gd(III)-based CAs can be designed for high cell accumulation, labeled cancer cells can produce tunable T_1-T_2 contrast according to CA concentration within the cell.

A popular strategy to improve cell labeling efficiency of Gd(III)-based agents is conjugation to nanoparticles. There are numerous reports of Gd(III)-nanoparticle formulations with high cell labeling efficiency and imaging efficacy.[1,2,5,10,20-23] In particular, carbon-based nanomaterials bearing Gd(III) ions such as gadographene, gadofullerene and gadonanotubes have been explored.[21,24-27] However, a majority of these constructs have not enabled long-term cell labeling and fate-mapping *in vivo* due to limited stability in biological media.[28,29] In contrast to other carbon-based nanomaterials, detonation nanodiamonds (NDs) have great potential for a variety of *in vivo* applications.[30-35] NDs are 4-6nm carbon particles with a diamond crystal structure.[30,36,37] NDs are biocompatible, can carry a broad range of therapeutics, are dispersible in water and allow uniform, scalable production.[30,35,38] Nanodiamonds were recently analyzed for

biocompatibility in rats and non-human primates, and shown to be non-toxic over 6 months by comprehensive analysis of serum, urine, histology and body weight.[35]

We previously developed NDs for MR imaging by covalently coupling Gd(III)-based contrast agents to the ND surface.[39] These ND-Gd(III) conjugates provided approximately 10-fold enhancement in relaxivity with respect to the uncoupled Gd(III) CA and clinical Gd(III) CAs.

Herein we report the synthesis, characterization, *in vitro* and *in vivo* testing of a new class of ND-Gd(III) conjugates (NDG) for MR imaging of cancer growth (***Figure 2.1***). To increase Gd(III) loading, we functionalized the nanostructure with amines by silanization of the ND surface, and peptide-coupled the aminated NDs to a carboxylated Gd(III) chelate. NDG aggregates were evaluated for relaxivity across a wide range of field strengths, biocompatibility, cell labeling efficacy, and tracking long-term tumor growth *in vivo* using T_1- and T_2-weighted MR imaging at 7 T.

2.2. Results and Discussion

2.2.1. Synthesis and characterization of ND-Gd(III) conjugates (NDG):

NDs were reduced using borane in tetrahydrofuran, followed by silanization with (3-aminopropyl)-trimethoxysilane as previously described.[40] Silanization provided additional primary amine groups on the ND surface to create aminated NDs (NDA). A Gd(III) chelate composed of a tetraazacyclododecanetriacetic acid with a six-carbon linker terminating in a carboxylic acid (Gd-C5-COOH) was synthesized (***Figures 2.2-2.3***). Gd-C5-COOH was peptide-coupled to NDA in the presence of 1-Ethyl-3-[3-dimethylaminopropyl] carbodiimide hydrochloride (EDC) and N-hydroxysuccinimide (NHS), yielding ND-Gd(III) conjugates (NDG) (***Figure 2.1)***.

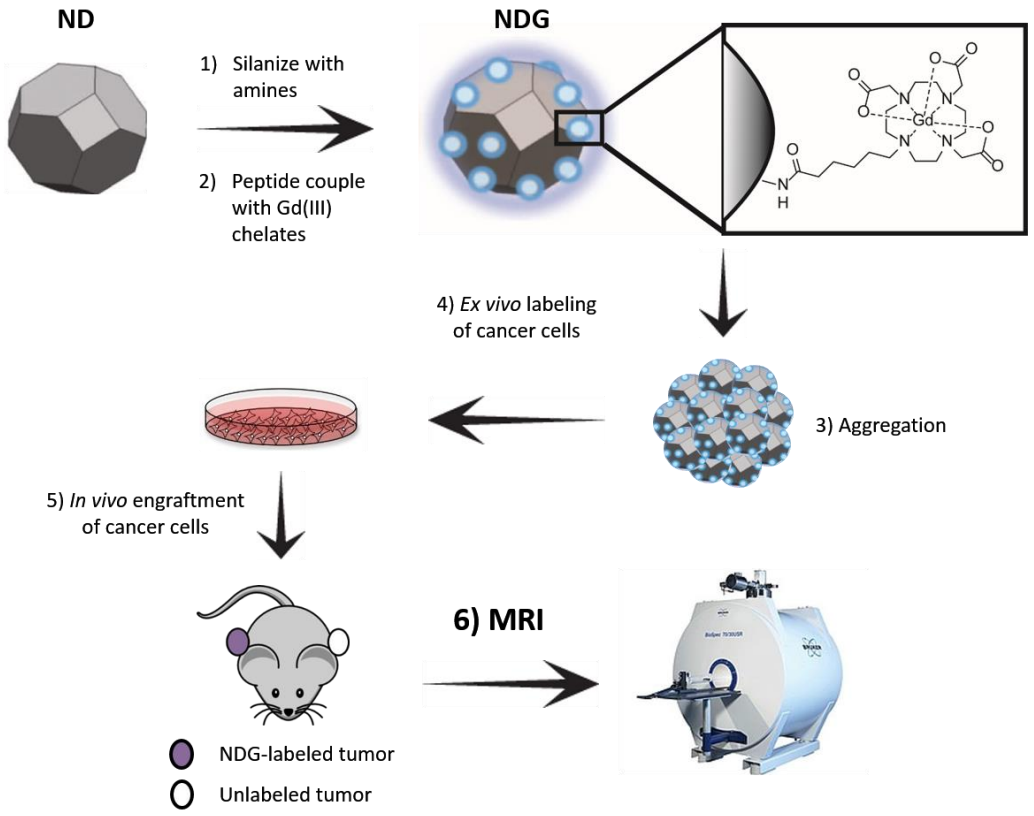

Figure 2.1. Nanodiamond-Gadolinium(III) aggregates (NDG) for tracking cancer cell growth in vivo. 1) A colloidal suspension of detonation nanodiamonds (NDs) is reduced using borane in tetrahydrofuran, followed by silanization with (3-aminopropyl)-trimethoxysilane to increase primary amines on the ND surface (NDA).[40] 2) NDA is peptide-coupled to Gd(III) chelates bearing a carboxylate with a six-carbon linker arm using EDC/NHS chemistry. 3) NDG spontaneously aggregates but maintains colloidal stability in water, saline and serum-supplemented media. 4) MDA-MB-231 m-Cherry human breast cancer cells are labeled with NDG. 5) NDG-labeled cells are engrafted on the flank of immunocompromised SCID beige mice; on the other flank is engrafted an unlabeled xenograft of the same cells as a control. 6) Mice are serially imaged by MRI at 7 T to visualize tumor growth and morphology.

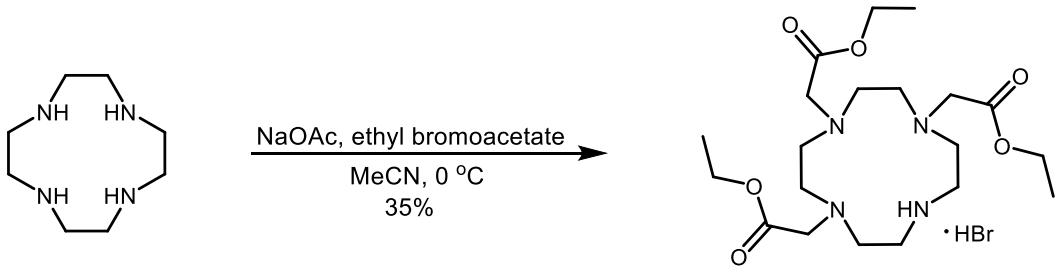

Figure 2.2. Synthesis of ethyl protected DO3A macrocycle (1,4,7-TRIS(ETHYL ACETATE)-1,4,7,10-TETRAAZACYCLODODECANE·HBr.

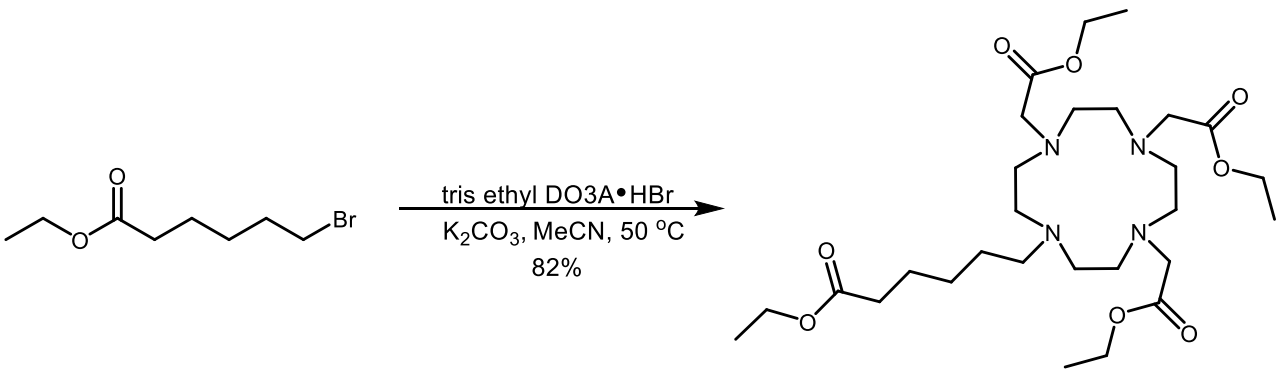

Figure 2.3. Synthesis of 1-(ETHYL HEXANOATE)-4,7,10-TRIS[(TERT-ETHYLCARBONYL)METHYL]-1,4,7,10-TETRAAZACLYCODODECANE.

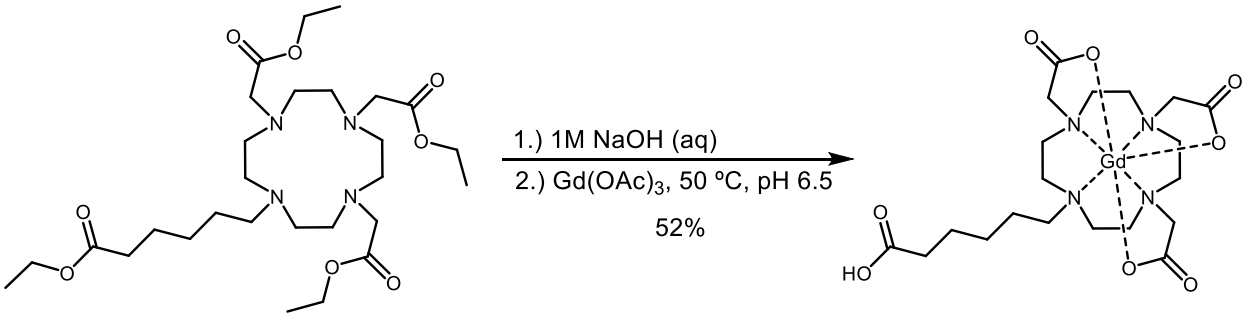

Figure 2.4. Synthesis of Gd-C5-COOH.

The resulting NDG and NDA aggregates were analyzed using a number of physical and chemical characterization methods. Transmission electron microscopy (TEM) was used to visualize particle structure, and revealed NDA and NDG to be heterogeneous particle aggregates (*Figure 2.5**a-d***). Energy-dispersive X-ray (EDX) spectroscopy was employed to compare the chemical composition of NDG and NDA. The EDX spectrum of NDG exhibited characteristic Gd(III) peaks while the spectrum of NDA did not (*Figure 2.5***e**). Gd(III) content of NDG was additionally confirmed and quantified by inductively-coupled plasma-mass spectroscopy (ICP-MS) (***Table 2.1***). The Gd(III) content of NDG was 1.5 ± 0.2 μmol/mg and exceeded that of the first-generation ND-Gd(III) conjugates by two orders of magnitude.[39] Amide bond formation was assessed by Fourier-transform infrared spectroscopy (FTIR), where an amide stretch was visualized in the IR spectrum of NDG, but not in the spectra of NDA or Gd-C5-COOH (*Figure 2.6*). Therefore, the conversion of amines to amides was assessed by a modified Kaiser test[41] (***Table 2.1,*** *Figure 2.7*). The number of primary amines in NDG was significantly lower than that of NDA, suggesting that a majority of the Gd(III) is covalently coupled to the ND surface by amide bonds. Finally, the hydrodynamic size of NDG aggregates in water was measured by dynamic light scattering (DLS), while the surrogate surface charge was assessed by measuring zeta potentials (*Figure 2.8*, ***Figure 2.9***, ***Figure 2.10***). NDA aggregates were 75.6 ± 8.6 nm with a zeta potential of +50.8 ± 1.8 mV. The strong positive potential observed is attributed to the large number of free amines on the NDA surface. Hydrodynamic size increases while zeta potential did not change significantly as peptide-coupling ratios of Gd-C5-COOH:ND increased from 0.1:1, 1:1 to 5:1. As more Gd(III) is coupled to NDG aggregates, there is greater hydration as more water molecules coordinate with Gd(III).

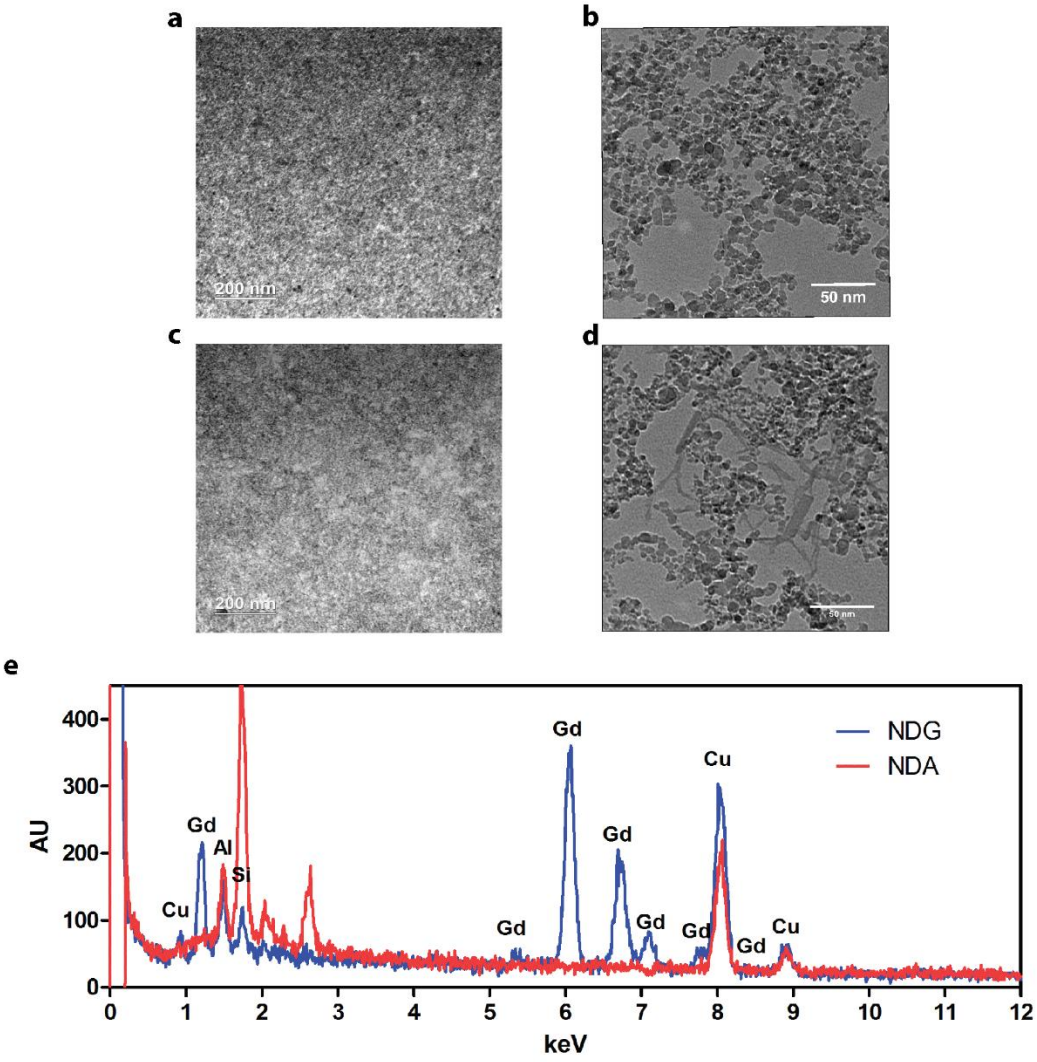

Figure 2.5. Transmission Electron Microscopy with EDX spectroscopy of NDA and NDG. (**a)** NDA images at low magnification, and (**b**) high magnification show a granular appearance with dense aggregates of particles, where individual particles are approximately 5 nm. (**c-d)** Low- and high-magnification images of NDG retain a similar appearance but also includes the presence of enhancing bridging structures. (**e**) EDX spectroscopy of NDG and NDA – the $L\alpha_1$ and $L\alpha_2$ peaks of gadolinium are clearly observed in the NDG spectrum and not in the NDA spectrum. Present in both spectra are Cu, Al, and Si (from sample preparation).

	NDG	NDA	Gd-C5-COOH
Gd(III) content (μmol mg^{-1})	1.5 ± 0.2	*n.a.*	*n.a.*
Primary amines (μmol mg^{-1})	0.2 ± 0.1	1.6 ± 0.3	*n.a.*
r_1 @ 1.4 T (mM^{-1}s^{-1})	11.1 ± 0.9	*n.a.*	6.4 ± 0.8
r_2 @ 1.4 T (mM^{-1}s^{-1})	16.1 ± 0.9	*n.a.*	10.4 ± 0.8
r_1/r_2 @ 1.4 T	0.69	*n.a*	0.61
r_1 @ 7 T (mM^{-1}s^{-1})	11.5 ± 0.8	*n.a*	4.8 ± 0.7
r_2 @ 7 T (mM^{-1}s^{-1})	15.5 ± 0.8	*n.a.*	8.1 ± 0.7
r_1/r_2 @ 7 T	0.74	*n.a*	0.59

Table 2.1. Chemical characterization of NDG. Gd(III) content of NDG is quantified by ICP-MS. Peptide coupling is verified by comparing primary amine content in NDA (pre-coupling) and NDG (post-coupling). Primary amine content is assessed using a modified Kaiser test[41] (see Figure S6). The number of primary amines is lower in NDG compared to NDA as a majority of surface amines are modified to amides post-chelate coupling. r_1 for NDG is two-fold greater, and r_2 is 1.5-fold greater, than Gd-C5-COOH at 1.4 T. Unlike other nanoformulations bearing Gd(III) that suffer from less efficient relaxation kinetics at higher field strengths, the longitudinal relaxivity of NDG and r_1/r_2 ratio are maintained at 7 T. n.a. = not applicable.

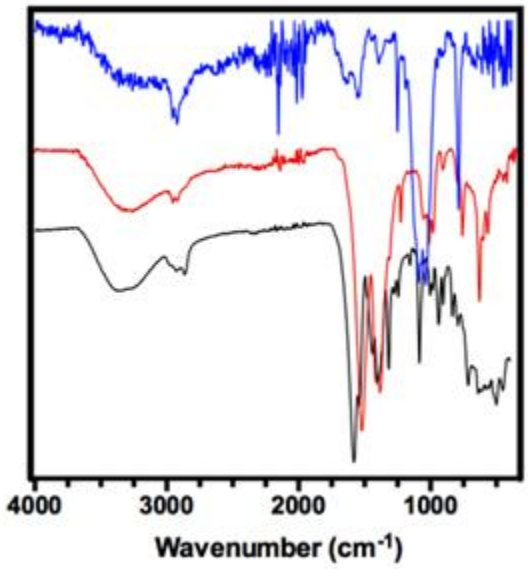

Figure 2.6. FTIR spectra of NDA (blue), NDG (red), and Gd-C5-COOH (black), where an amide stretch is visualized in NDG but not in NDA or Gd-C5-COOH.

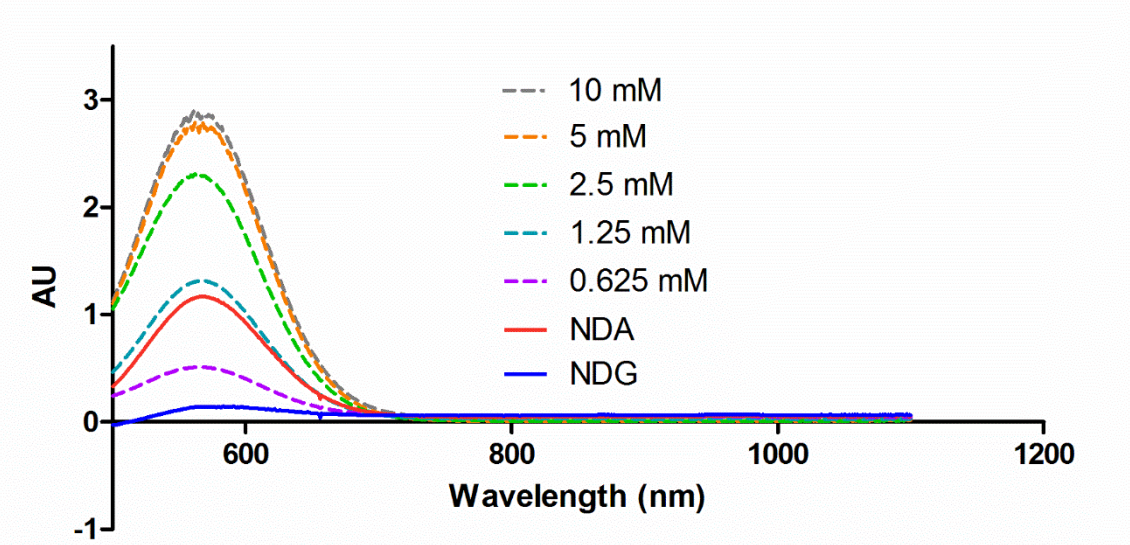

Figure 2.7. Primary amines are quantified based on absorbance at 570 nm. Spectra are shown for different concentrations of benzylamine, along with the spectra for 1 mg/ml solutions of NDA and NDG.

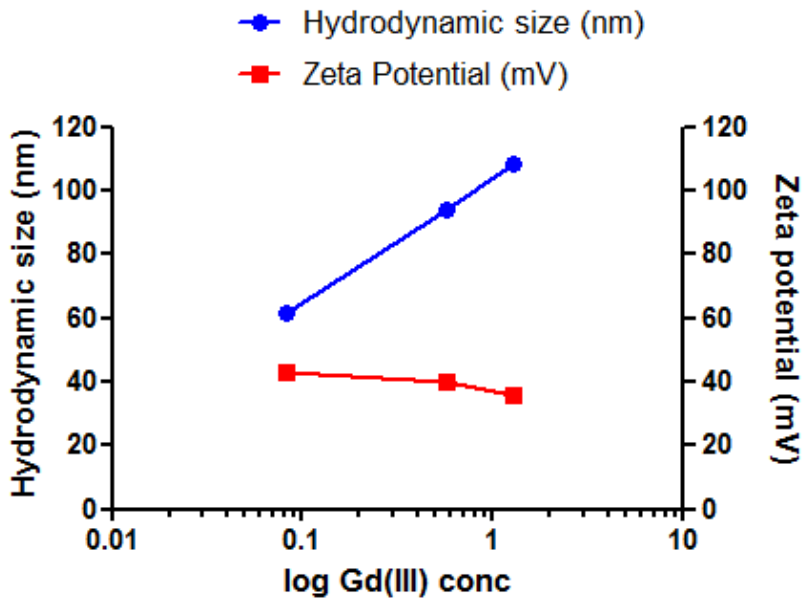

Figure 2.8. Hydrodynamic size and zeta potential for increasing Gd:ND coupling ratios.

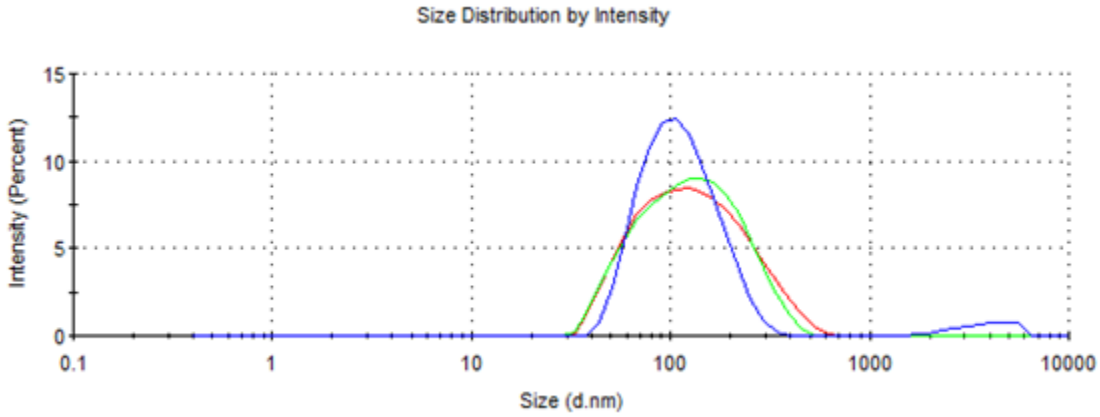

Figure 2.9. Histograms of DLS intensity spectra of three batches of NDG aggregates bearing 1.4 μmol Gd/mg of ND.

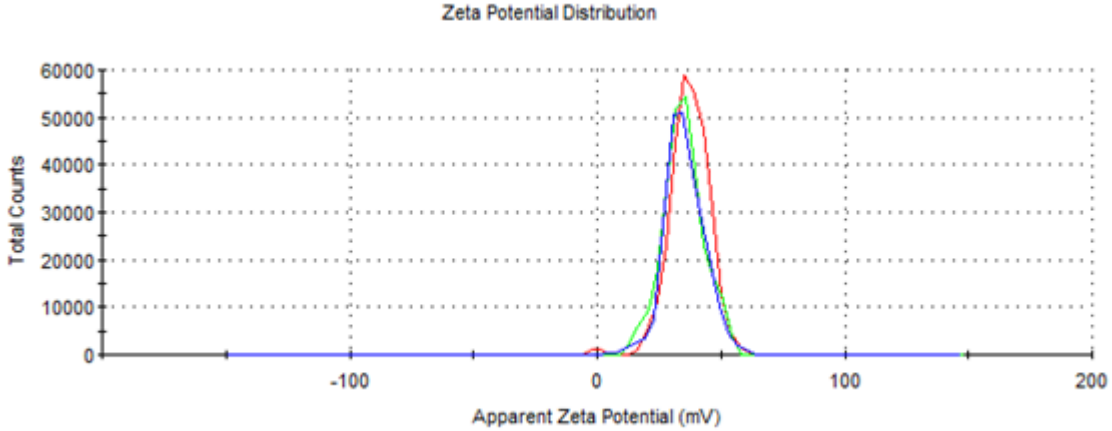

Figure 2.10. Histograms of zeta potential spectra of three batches of NDG aggregates bearing 1.4 μmol Gd/mg of ND.

To evaluate CA performance, the r_1 and r_2 relaxivities of NDG aggregates and Gd-C5-COOH were measured (**Table 2.1**). At 1.4 T, the r_1 relaxivity of NDG aggregates was 11.1 ± 0.9 $mM^{-1}s^{-1}$, about two-fold greater than the r_1 of Gd-C5-COOH. The r_2 relaxivity of NDG aggregates was 16.1 ± 0.9 $mM^{-1}s^{-1}$, about 1.5-fold greater than the r_2 of Gd-C5-COOH. Compared to the first-generation ND-Gd(III) conjugates, the relaxivities of NDG aggregates was 5-fold lower. One explanation for lower r_1 relaxivity is that the silanization of the ND surface alters the coordination network of Gd(III) compared to the previously un-silanized surface. Remarkably, the r_1 and r_2 relaxivity of NDG aggregates at 7 T was 11.5 ± 0.8 $mM^{-1}s^{-1}$ and 15.5 ± 0.8 $mM^{-1}s^{-1}$ and comparable to the relaxivities at 1.4 T. The r_1/r_2 ratio of 0.74 at 7 T is among the highest for dual T_1-T_2 agents and favors tunable contrast. Further, other nanoconstructs bearing Gd(III) experience a significant drop in r_1 relaxivity as a result of increasing field strength and altered relaxation kinetics.[7,8,42] Therefore, the magnetic field-independence of NDG r_1 relaxivity required further exploration.

2.2.2. Nuclear Magnetic Relaxation Dispersion (NMRD) profile of NDG aggregates:

The parameters influencing r_1 relaxivity of Gd(III)-based chelates are described by the Solomon-Bloembergen-Morgan (SBM) theory. SBM theory outlines three primary ways to optimize the relaxation kinetics of Gd(III) chelates: (i) changing the rotational correlation time, τ_r; (ii) increasing the rate of water exchange in the inner-sphere, τ_m; and (iii) increasing the number of coordinated water molecules, q.[7,9] Of these parameters, modulation of τ_r by slowing the reorientation time (e.g. by conjugation to a nanoparticle) is commonly used to increase r_1 relaxivity.[9,42] This method is most effective at field strengths up to 1.5 T, but at higher field strengths, long τ_r times can result in up to 90% decrease in r_1 relaxivity. NDG aggregates, like other nanoparticle constructs, would be expected to benefit from a τ_r-mediated increase ≤ 1.5 T

and a τ_r-mediated decrease at higher field strengths. However, we have observed a *unique phenomenon where r_1 relaxivity of NDG at 7 T was actually comparable to that measured at 1.4 T*. This finding suggests different mechanisms of relaxation kinetics are involved.

To explore which parameters gave rise to high-field performance of NDG, we obtained nuclear magnetic relaxation dispersion (NMRD) profiles of NDG aggregates and Gd-C5-COOH where the r_1 relaxivity was measured across field strengths ranging from 0.01 - 300 MHz (2.3 x 10^{-4} – 7 T) (**Figure 2.11**). We observed that the pattern of relaxivity changes across field strengths was similar between NDG aggregates and the small-molecule chelate Gd-C5-COOH, except NDG aggregates had higher relaxivity at all field strengths (relaxivity decreased at higher temperature due to greater molecular tumbling rates). This is in agreement with the expected fast exchange regime[43-45] of the coordinated water molecules, indicating optimized τ_m values both for the NDG aggregates and Gd-C5-COOH. There was no increase in relaxivity between 0.5 – 2 T typically seen when τ_r of the underlying construct is long. The best fit parameters of the NMRD profiles[43,45-47] revealed that the τ_r values of NDG aggregates and Gd-C5-COOH were not significantly different. This suggests that the Gd(III) chelate retained rotational freedom even after attachment to NDs and that the major contributor for high-field performance was the high number of "coordinated" water molecules, *q* (**Figures 2.11-2.12,** and **Table 2.2**).

As expected for a chelate bearing a seven-coordinate gadolinium ion, the NMRD fits of aqueous Gd-C5-COOH indicate that there are 2 water molecules coordinated to Gd(III) in the first coordination sphere (approximately 3.1 Å).[8,9] The NMRD profiles reported on $\sum_i q_i/r_i^6$, where *r* is the metal-hydrogen distance of the i^{th} water molecules.

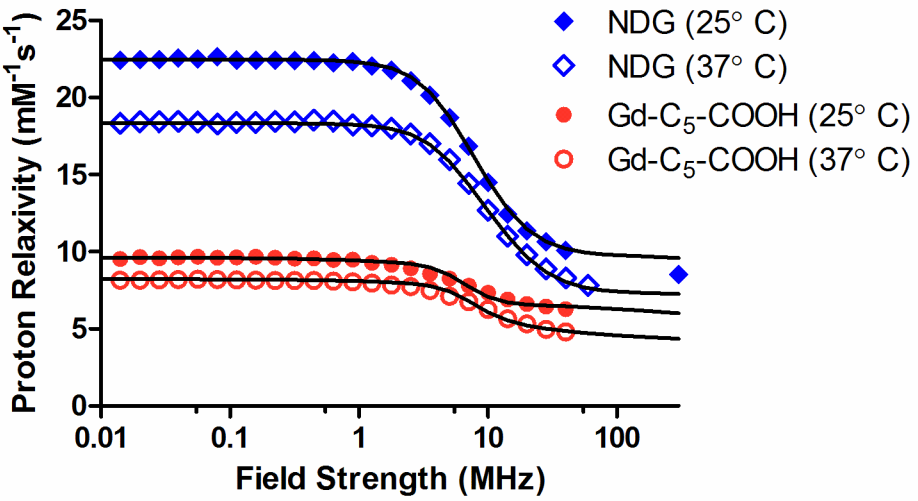

Figure 2.11. Nuclear Magnetic Relaxation Dispersion (NMRD) profiles of NDG and Gd-C5-COOH. Longitudinal proton relaxivities of NDG and Gd-C5-COOH decrease with increasing magnetic field strength, but remain stable at field strengths greater than 60 MHz. The r_1 of NDG is higher than that of Gd-C5-COOH at all field strengths. Unlike most other Gd(III)-nanoparticle constructs, NDG does not benefit from a τ_R-mediated increase between 10-100 MHz, nor does it suffer from a decrease in relaxivity between 60-300 MHz. This is likely due to ND aggregates in solution providing a loose framework for Gd(III) conjugation that does not hinder the rotational freedom of the chelates. For parameter values, see **Table 2.2**.

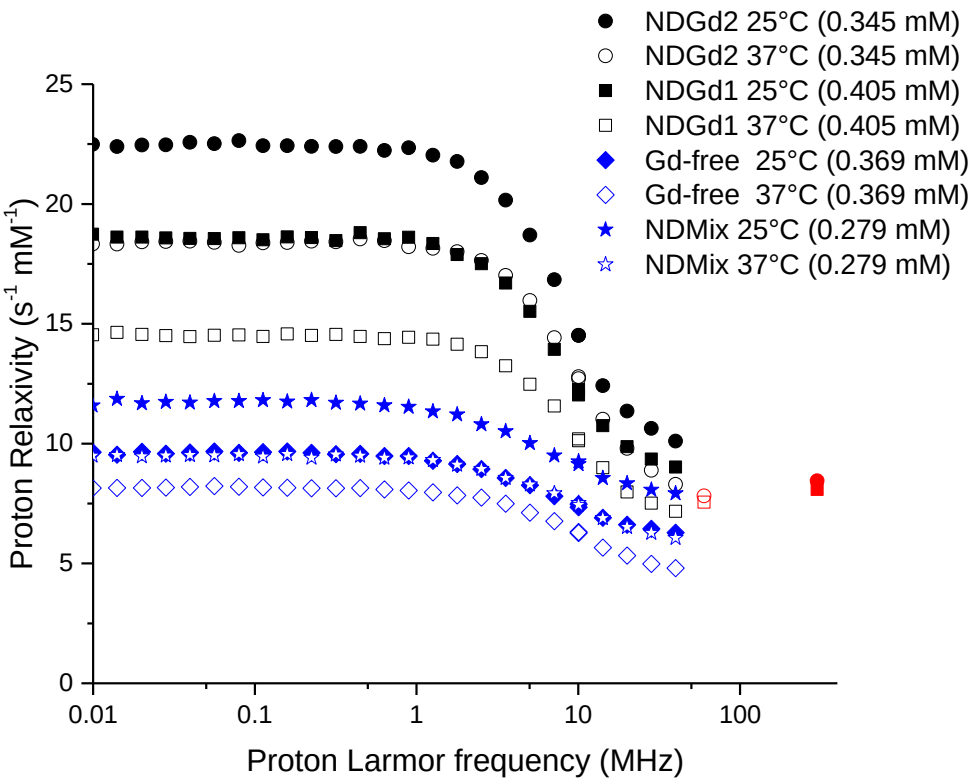

Figure 2.12. NMRD profiles at 25°C and 37°C of two different batches of NDG ("NDGd 1" and "NDGd 2"), Gd-C5-COOH ("Gd-free") and an uncoupled mix of NDA and Gd-C5-COOH ("NDMix"). Measurements in red were acquired separately, as detailed in Materials & Methods, sections 2.4.7.

	NDG @ 25°C	NDG @ 37°C	Gd-C5-COOH @ 25°C	Gd-C5-COOH @ 37°C
τ_R (ps)	77	62	78	56
$q_{1st\ sphere}$ (#)	2[1]		1.6[2]	
$r_{1st\ sphere}$ (Å)[1]	3.05		3.05[2]	
$\tau_{m\ (1st\ sphere)}$ (ns)[1]	36	25	36	25
$q_{2nd\ sphere}$ (#)	13.4		-	
$r_{2nd\ sphere/outer}$ (Å)[1]	3.6		3.6[3]	
$\tau_{m\ (2st\ sphere)}$ (ps)	38	26	-	-

Table 2.2. Parameter estimates for NMRD fits of NDG and Gd-C5-COOH at 25°C and 37°C.

[1]Values kept fixed in the best fit minimization

[2]$q_{1st\ sphere} = 2$ with $r_{1st\ sphere} = 3.16$ Å

[3]Outer-sphere relaxation calculated with a distance of closest approach fixed to 3.6 Å and diffusion coefficients fixed to $2.3 \cdot 10^{-9}$ and $3.3 \cdot 10^{-9}$ m^2/s at 25 and 37°C, respectively.

For NDG aggregates, the two water molecules in the first coordination sphere must be supplemented by a relatively large number of water molecules in what is termed the "second coordination sphere". Assuming a second-sphere radius of 3.6 Å, approximately 13 water molecules would need to coordinate with the Gd(III) ion with a lifetime τ_m of tens of picoseconds. The presence of this large network of water molecules close to the Gd(III) ion may explain the high-field performance of NDG aggregates.

There are previous reports of carbon-based nanomaterials, particularly gadonanotubes, having unique NMRD profiles in solution, especially at low field strengths (< 0.1 MHz), attributed to geometric confinement of Gd(III) and high water coordination numbers.[24,48] A plausible explanation for the relaxometric behavior of NDG may be related to the hydrophilic, amidated NDG being able to form robust and continuous hydration layers near the surface.[39,49] In this scenario, the Gd(III) ions would increase the relaxation rates of the water protons in these hydration layers as in the case of water molecules in the second coordination sphere.[45]

2.2.3. Labeling cancer cells using NDG:

The MDA-MB-231 m-Cherry human triple-negative breast cancer cell line was used as the model system for cellular studies using NDG. Cellular tolerance of NDG was evaluated by cell viability measurements across ND concentrations ranging from 31.25 – 1000 μg/ml, where NDG maintained colloidal stability in serum-supplemented media at all concentrations. We observed that NDG was well tolerated with a range of doses (**Figure 2.13a**). The cell labeling efficiency of NDG was compared with that of Gd-C5-COOH and Gd-DOTA, a clinically used chelate. Cells were incubated with different Gd(III)-equivalent doses of NDG, Gd-C5-COOH and Gd-DOTA for 24 hours, after which the agents were washed and cells harvested for analysis of Gd(III) content.

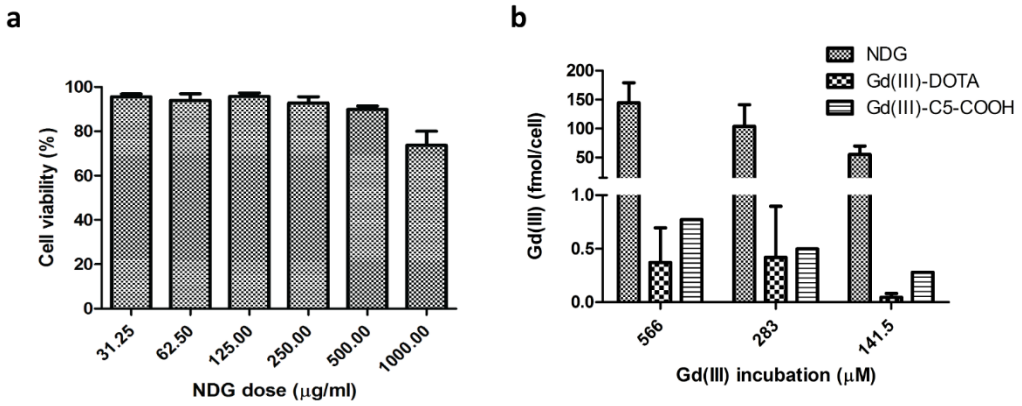

Figure 2.13. Labeling MDA-MB-231 m-Cherry cells with NDG. (**a**) Cell viability shows that NDG is well-tolerated across a wide dose range. (**b**) Cells are incubated with NDG, Gd(III)-DOTA or Gd-C5-COOH for 24 hours, after which they are harvested for analysis of Gd(III) content. NDG confers 300-fold improvement in cellular delivery of Gd(III) compared to Gd(III)-DOTA and Gd-C5-COOH.

NDG delivered in excess of 160 fmol of Gd(III) per cancer cell, which was 300-fold greater than the amount delivered by the two free chelates (**Figure 2.13b**). The detection limit of cells labeled with Gd(III) by MR imaging is known to be approximately 0.1 fmol/cell *in vitro* and 1 fmol/cell *in vivo*.[50,51]

In order to confirm that cells internalized NDG aggregates, individual cells were visualized using scanning-transmission electron microscopy (STEM). The resulting images showed NDG clusters within the cell and being engulfed by membrane-associated vesicles at the cell periphery (**Figure 2.14a**). Two regions-of-interest (ROIs) were delineated in the higher magnification STEM image of the cell: one with apparent NDG aggregates and the other a vacant region of cytoplasm (**Figure 2.14b**). EDX spectroscopy of the two ROIs revealed the characteristic Gd(III) X-ray spectrum only in the ROI bearing NDG aggregates and not in the region of vacant cytoplasm (**Figure 2.14c**). Collectively, we have shown that NDG aggregates are one of the most efficient delivery vehicles of Gd(III) to cells compared to other Gd(III)-nanoparticle formulations. Furthermore, the cell labeling efficacy of NDG compares favorably to other carbon-based nanomaterials such as gadographene[21], gadonanotubes[52] and gadofullerenes[26] without sacrificing biocompatibility.

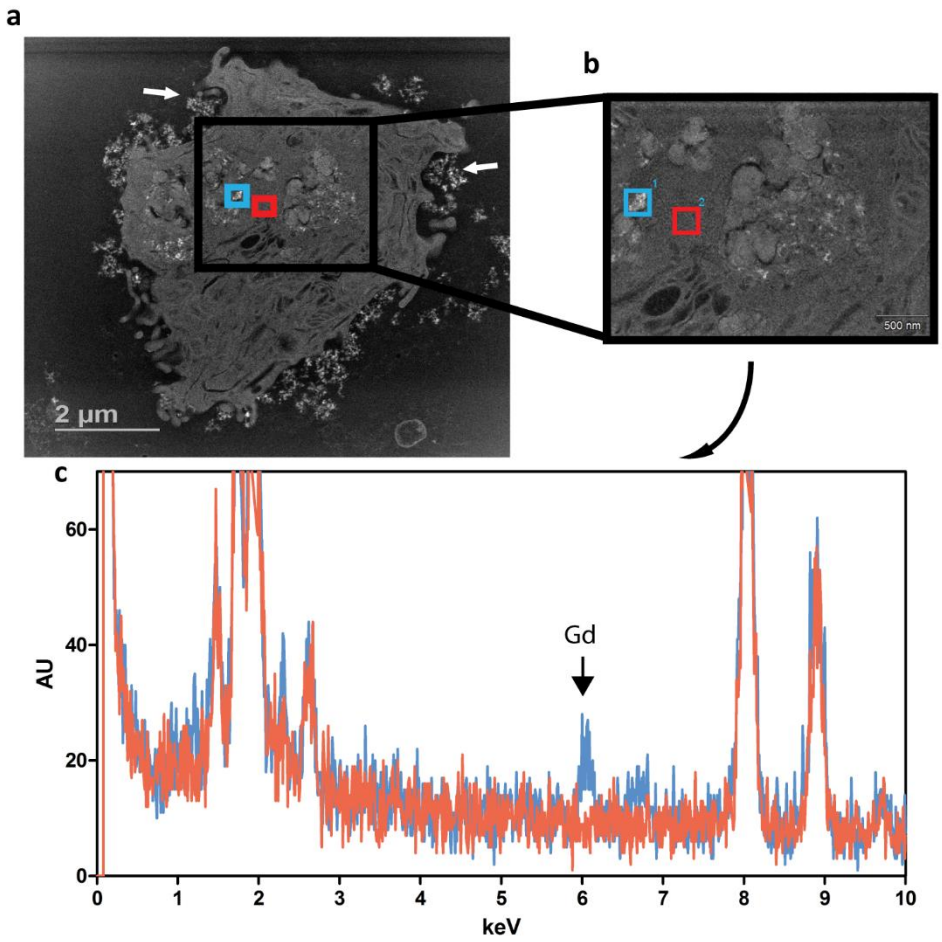

Figure 2.14. Labeling MDA-MB-231 m-Cherry cells with NDG. (**a**) STEM image of single cell after 24-hour incubation with NDG. Enhancing NDG aggregates are seen inside the cell and also being engulfed near the plasma membrane (white arrows). (**b**) STEM image at greater magnification showing two highlighted areas – one with apparent NDG aggregates (teal) and another without (red). (**c**) EDX spectroscopy of the two regions highlighted in (**b) –** the $L\alpha_1$ peak of gadolinium is clearly observed in the spectrum for the region bearing NDG aggregates (teal) and not in the region of vacant cytoplasm (red). The $L\alpha_2$ peak of gadolinium is also seen.

2.2.4. High field MR imaging of cells labeled with NDG:

In order to determine if the high cellular Gd(III) loading conferred by NDG translates into contrast, cellular phantoms were imaged using MR. Cells were labeled with increasing dose of NDG, spun down to a pellet, and imaged by MRI at 7 T (**Figure 2.15**). As expected, when cellular concentration of Gd(III) exceeds a certain threshold, positive contrast diminishes to yield negative contrast even in a T_1-weighted sequence. At the highest dose (Figure 2.15, (iv)), T_2- and T_2^*-relaxation times are shorter than the "short" echo time of a T_1-weighted sequence, resulting in a predominant T_2 effect over T_1.

We sought to demonstrate this "T_2-shortening" is concentration-dependent, and can be exploited for dual T_1-T_2 imaging. Instead of being spun down to a pellet, cells labeled with highest dose of NDG were diluted in an agarose:media suspension. Specifically, cylindrical cavities were created in an agarose gel and were filled with NDG-labeled (110 fmol Gd(III)/cell) or unlabeled cells suspended in 1:1 agarose:media (Figure 2.16**a**). The cavity containing the NDG-labeled cells exhibited positive contrast while the cavity containing unlabeled cells could not be differentiated from agarose background (Figure 2.16**b**). In addition, cells incubated with NDA (equal ND concentration but no Gd(III)) could not be differentiated from background (**Figure 2.17.**). In the T_2-weighted sequence, the cavity containing the NDG-labeled cells appeared dark and the outline of the cavity containing the unlabeled cells is visible (**Figure 2.18.**). This vial was imaged using the IVIS® Lumina optical imaging system and m-Cherry fluorescence showed the presence of cells in both cavities (**Figure 2.16c**). These findings suggest that NDG aggregates are efficiently able to deliver a Gd(III) payload to cells, and labeled cells can produce both positive and negative contrast.

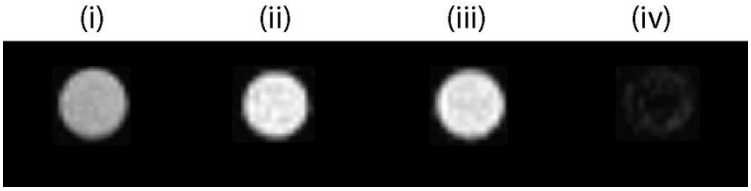

Figure 2.15. MR imaging at 7 T of MDA-MB-231 m-Cherry cells labeled with NDG. (a) Axial MRI section of cell pellets having 0 (i), 0.6 (ii), 6.4 (iii) and 117.6 (iv) fmol/cell of Gd(III) after labeling with increasing concentrations of NDG for 24 hours. (ii) yields significantly greater contrast than (i). As cellular concentration of Gd(III) increases, positive contrast diminishes to yield negative contrast. At these higher concentrations, T_2-relaxation times are even shorter than the "short" echo time TE of a T_1-weighted sequence, resulting in a predominant T_2 effect over T_1.

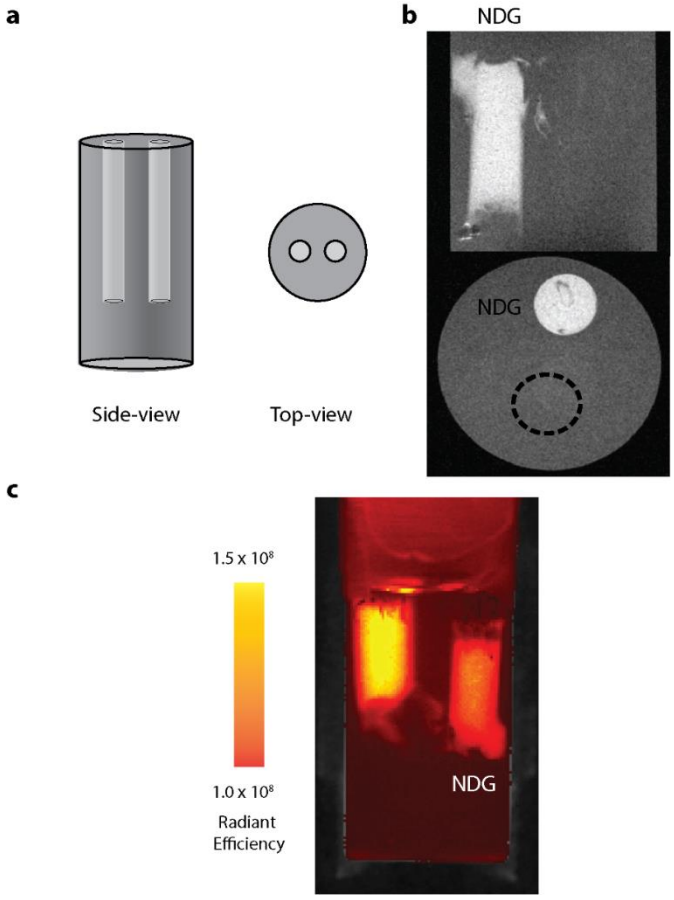

Figure 2.16. (a) Experimental setup for imaging cells suspended in agarose. Two 5-mm cylindrical cavities are created in a vial containing a 1:1 agarose:media gel. Each cavity is gelled with either NDG-labeled or unlabeled cells suspended in a 1:1 agarose:media mixture. (**b**) Coronal (top) and axial (bottom) section of vial described in (a), containing cells suspended in agarose:media. "NDG" indicates the cavity containing NDG-labeled cells, where significant contrast enhancement is observed, while the cavity containing unlabeled cells is indiscernible (location indicated by dotted circle in axial section). (**c**) Same vial imaged in an IVIS® Lumina optical imaging system detecting m-Cherry fluorescence, measured as radiant efficiency with units of $[(p/sec/cm^2/sr)/(\mu W/cm^2)]$. "NDG" indicates the cavity containing NDG-labeled cells. m-Cherry readouts indicate the presence of cells in both cavities.

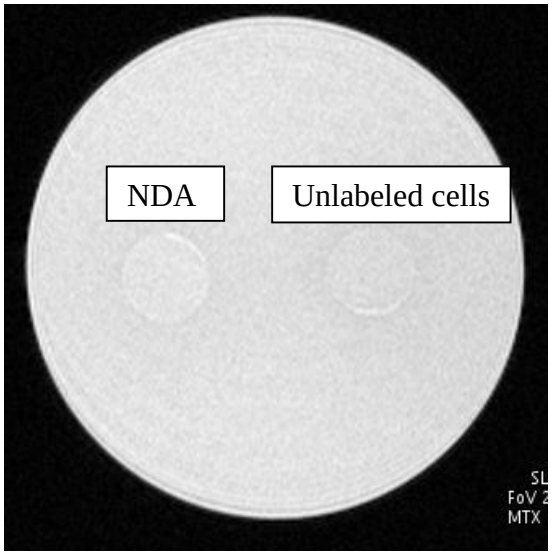

Figure 2.17. T_1-weighted MRI of NDA-labeled or unlabeled cells suspended in 1:1 agarose:media

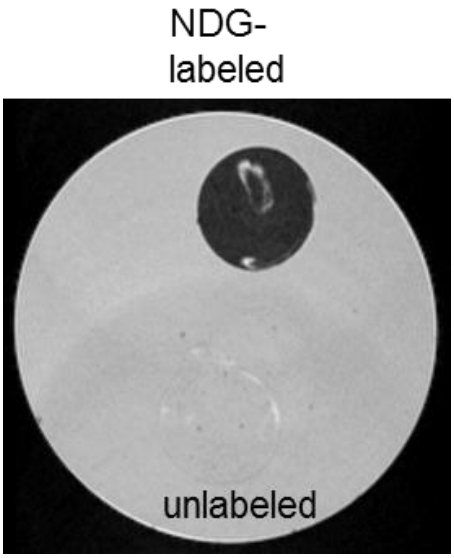

Figure 2.18. T_2-weighted MRI of NDG-labeled or unlabeled cells suspended in 1:1 agarose:media

2.2.5. High field MR imaging of NDG-labeled xenografts in immunocompromised mice for tracking cancer growth in vivo:

Immunocompromised mice were inoculated with two tumors, one composed of NDG-labeled cells (right flank) and one composed of unlabeled cells (left flank). Mice were imaged at several time points over 26 days. Tumor growth was quantified over time by m-Cherry fluorescence readouts using an IVIS® Lumina optical system (**Figure 2.19**).

To demonstrate tunability of contrast, cells were treated with maximum NDG dose at inoculation, where it was expected that high initial cellular NDG concentration would translate to negative contrast in T_1-weighted sequences. T_2-shortening is expected to dissipate as the tumor grows, where dilution of cellular NDG concentration would result in T_1-weighted positive contrast.

As early as day 2 NDG-labeled cells were visible, providing negative contrast in the T_1-weighted sequence, as expected (**Figure 2.20a**). The unlabeled cells displayed similar signal as surrounding muscle. The T_2-weighted images showed the location of the unlabeled cells on the left flank more clearly (**Figure 2.20b**). By day 14, the NDG tumor was enlarged, and still displayed T_2-shortening. The unlabeled tumor grew and continued to exhibit as much signal as surrounding muscle. However, by day 26 there was significant variance in contrast enhancement in different parts of the NDG tumor, with some regions showing positive contrast with others showing negative contrast. This suggests that Gd(III) was heterogeneously distributed. This profile was further validated by the T_2-weighted images that showed a contrast differential within the tumor (as expected, regions which appeared bright in the T_1-weighted image were dark in the T_2-weighted image). This transition from negative to positive contrast is helpful for determining tissue distribution of agent.

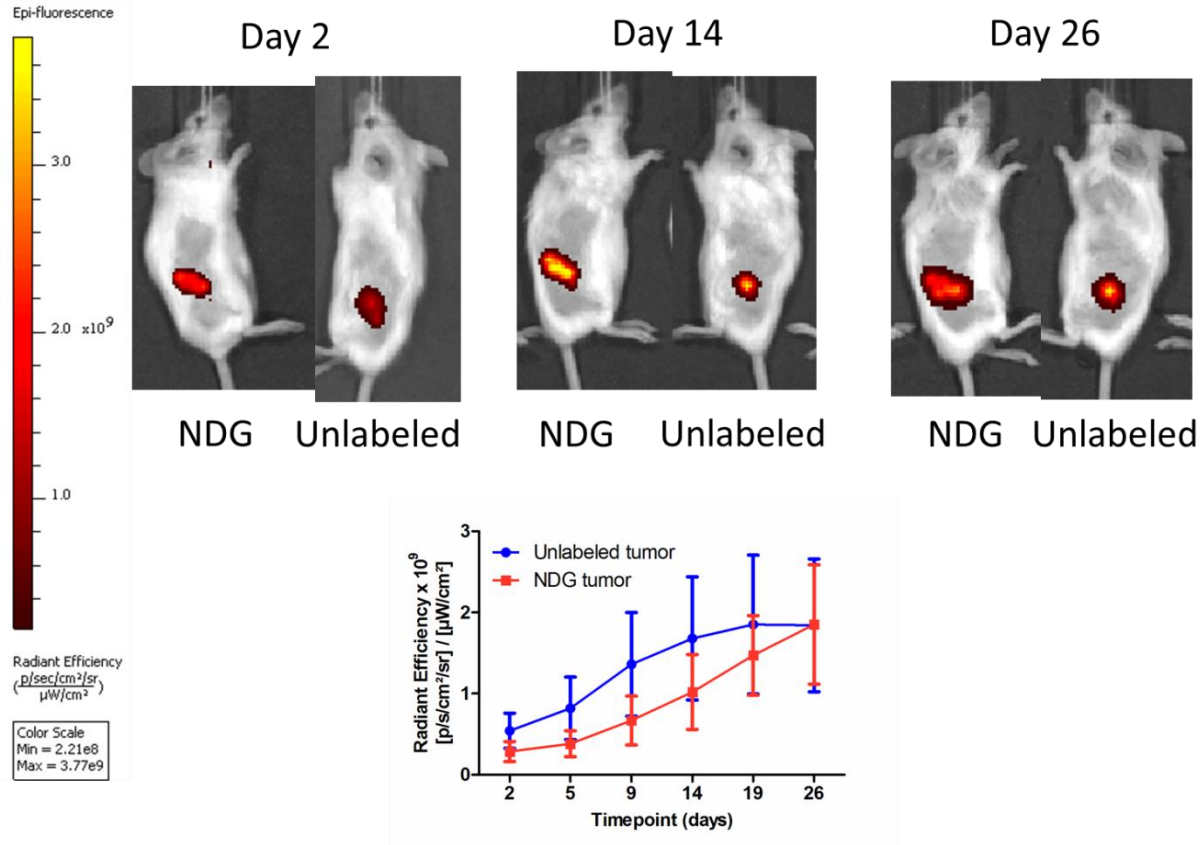

Figure 2.19. Top Row - NDG tumor (right flank) and unlabeled tumor (left flank) of representative mouse imaged at 2-, 14- and 26-days post-inoculation imaged by an IVIS Lumina optical system detecting m-Cherry fluorescence. Bottom Row – m-Cherry fluorophore-mediated radiant efficiency of each tumor at each timepoint. Images are from same mouse whose MR images are shown in Figure 6 of manuscript.

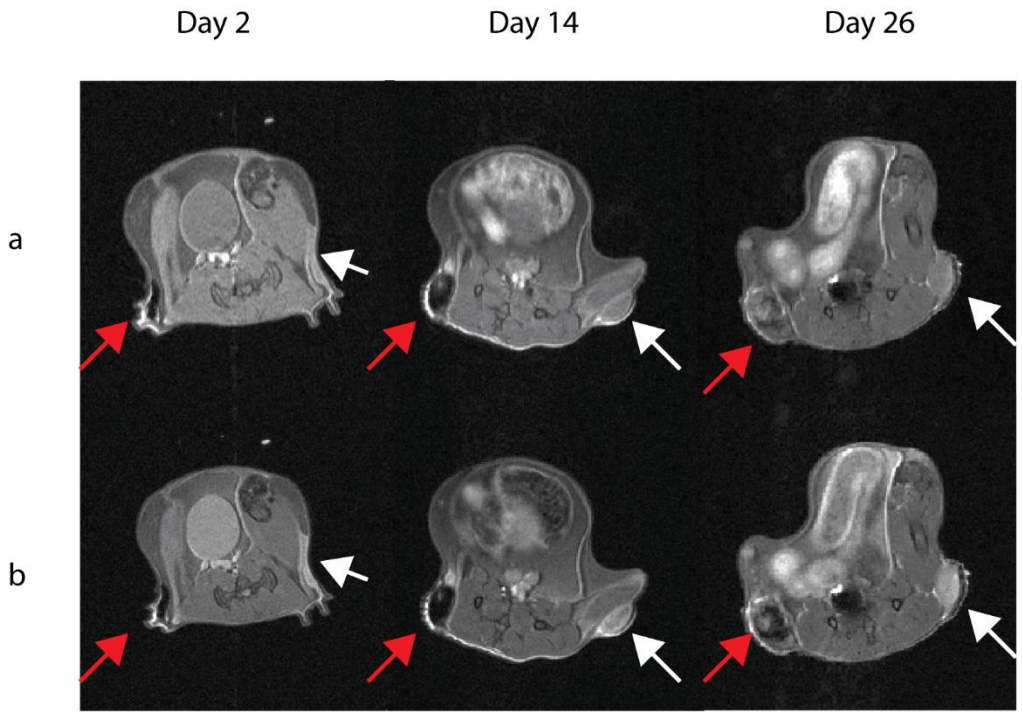

Figure 2.20. 7 T MR images of a SCID-beige mouse bearing a NDG-labeled xenograft and an unlabeled xenograft of MDA-MB-231 m-Cherry cells (n = 5, representative mouse shown). Images are shown 2, 14 and 26 days after engraftment. NDG tumor = right flank (left in page, red arrows), Unlabeled tumor = left flank (right in page, white arrows). (a) T_1-weighted images, where the NDG tumor is clearly visualized as a dark mass on the right flank, while the unlabeled tumor shows similar signal as compared to surrounding muscle. As the NDG tumor enlarges, there is a progressive increase in signal brightness as Gd(III) dilutes within the tumor to limit the T_2-shortening effect. (b) T_2-weighted images, where the NDG appears dark and the unlabeled tumor appears bright relative to surrounding tissue. This sequence of images validates the positions of the tumors in the T_1-weighted sequence, particularly of the unlabeled tumor in the left flank.

At each MR imaging time point, the T_1- and T_2-relaxation times within each tumor and surrounding muscle was measured. However, during early time points (up to 19 days), the T_1- or T_2-relaxation times could not be quantified due to high cellular NDG concentration causing T_2-shortening. At Day 26, a quantitative T_1-map was overlaid on the T_2-weighted anatomical image (**Figure 2.21, left panel**). The T_1-relaxation time for a representative ROI defined within the NDG tumor 26 days post-engraftment was 844 ms, compared to T_1 times of 2225 ms and 1999 ms in ROIs defined in the unlabeled tumor and muscle respectively. Within the NDG tumor the T_1 times ranged from 0 – 2500 ms. T_1 values have previously been correlated with tissue properties, where short T_1 values are associated with fat or Gd(III)-mediated contrast enhancement, long T_1 values are associated with fluid (blood, lymph, or edema) and intermediate values are associated with soft tissue.[8,9,53] Accordingly, in the NDG tumor, T_1-times < 100 ms likely corresponded to areas of high Gd(III) concentration (e.g. necrotic regions where Gd(III) has pooled), intermediate T_1 times between 500 – 800 ms corresponded to actively dividing NDG-labeled cells, while long T_1 times > 2500 ms were likely due to edema within the tumor.

To further quantify MR signal in the tumors, ROIs were delineated within each tumor and one within surrounding muscle. The saturation recovery of longitudinal magnetization was plotted against time for each of the ROIs (**Figure 2.21, right panel**). We observed that the unlabeled tumor and muscle have typical T_1-signal recovery profiles while the signal is not completely recovered in the NDG tumor, suggestive of T_2-shortening. Overall, by dilution of Gd(III) across time and a quantitative T_1 map within the NDG-labeled tumor, we are able to describe tumor morphology and heterogeneity.

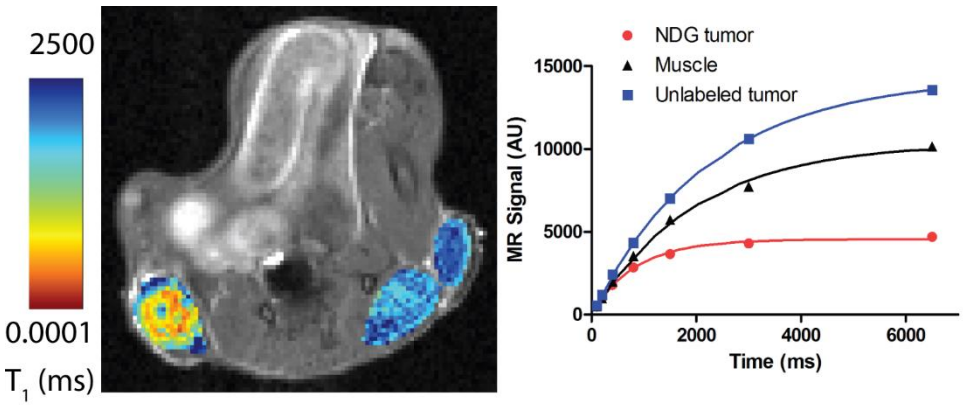

Figure 2.21. 7 T MR images of a SCID-beige mouse bearing a NDG-labeled xenograft and an unlabeled xenograft of MDA-MB-231 m-Cherry cells (n = 5, representative mouse shown). A quantitative heat map of T_1 relaxation times in the NDG tumor, unlabeled tumor and muscle is overlaid on the T_2-weighted anatomical image of the mouse at Day 26. Shorter T_1 times in the NDG tumor likely indicate high levels of Gd(III) within the tumor core, while longer T_1 times at the tumor edge likely indicate edema. The saturation-recovery plots of longitudinal relaxation (right panel) demonstrate the T_2-shortening effect in the NDG tumor, while showing the longer relaxation time of the unlabeled tumor compared with surrounding muscle.

The regional contrast variance used to describe tissue features would not be possible with other MR CAs, since T_2-agents (e.g. iron oxide nanoparticles) display negative contrast only and other Gd(III) agents suffer from low sensitivity.

2.2.6. Biodistribution of NDG aggregates in recipient mice and within tumor xenografts:

At the end of the 26-day time point three mice were euthanized, and both tumors, proximal leg muscles, kidneys, liver, spleen, stomach and bowel were harvested for analysis of Gd(III) content. On average the NDG tumors had 971 ± 534 μg of Gd(III) per g of tissue, where proximal leg muscle and unlabeled tumors had < 1 μg/g of tissue (**Figure 2.22a**). The Gd(III) content detected in the other clearance organs was also < 1 μg/g of tissue (Figure S16). The NDG tumors at the end of day 26 retained approximately 95% of the Gd(III) inoculated at day 0 (**Figure 2.22b**), indicating that NDG aggregates are well-retained within the tumor nearly one month post-engraftment. This level of retention would not be possible with iron oxide nanoparticles due to metabolism by the innate immune system.

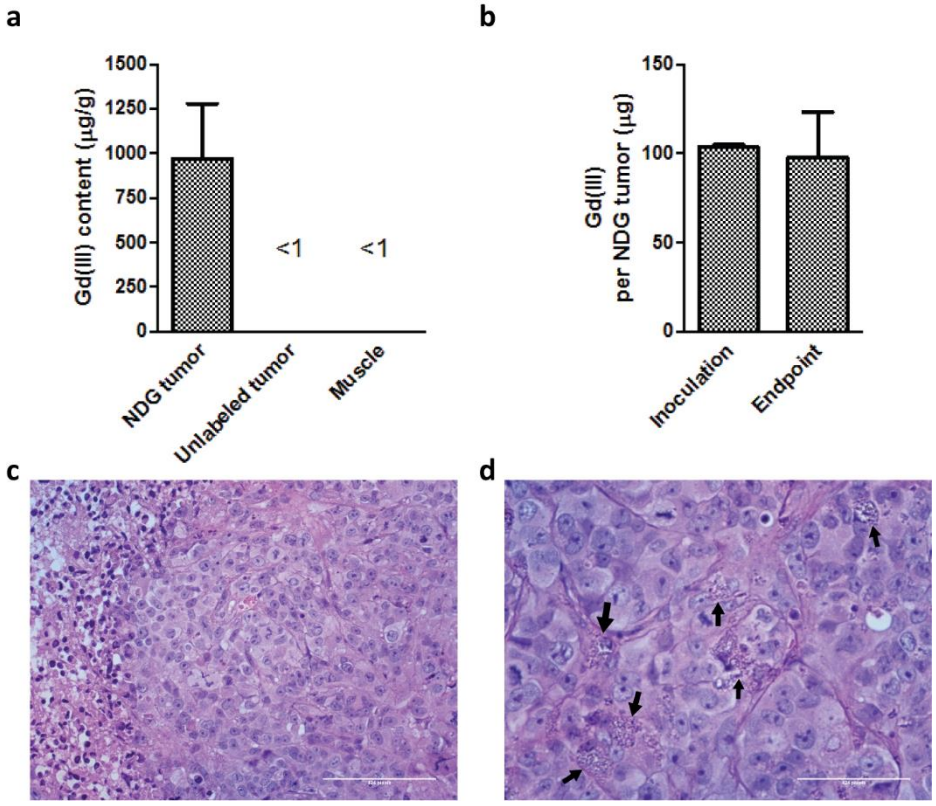

Figure 2.22. (a) Gd(III) content of tumors harvested at the 26-day endpoint (n = 3) – the NDG tumors have high Gd(III) content of approximately 1 mg per g of tissue, while unlabeled tumors and muscle has negligible quantities of Gd(III). (b) Gd(III) content in NDG tumors was compared between the inoculation timepoint and the 26-day endpoint, and on average, 95% of the Gd(III) remained within the tumor. (c) H&E section of unlabeled tumor (40x magnification) showing uniform, invasive neoplastic cells along with a region of central clearing indicative of necrosis, along with showing several mitoses indicative of high proliferative rate. (d) H&E section of NDG tumor (60x magnification) showing a similar morphology to the unlabeled tumor but containing visible NDG aggregates within neoplastic cells and in the interstitial space (black arrows). The number of mitoses visible is comparable to the unlabeled tumor. An enlarged image is shown in Figure 2.23 for greater detail.

The remaining two mice were euthanized for histological analysis of the NDG tumor and unlabeled tumor. In H&E sections, we observed invasive tumor cells with high mitotic rate, along with diffuse regions of necrosis and edema in both the unlabeled and NDG tumors (**Figure 2.22c-d**). We noted that the NDG tumor section contained several granular masses which were most likely NDG aggregates (**Figure 2.22d – black arrows**, **Figure 2.23**). Laser-ablation ICP-MS of an approximately 12 mm x 6 mm NDG tumor cross-section showed that Gd(III) was distributed throughout the tumor with highest concentrations in the center (**Figure 2.24**). Similar analysis of the unlabeled tumor showed absence of Gd(III) as expected. These findings correspond to the morphological changes described based on the T_1-maps of the tumors. Collectively, these findings serve as evidence that NDG aggregates can be visualized within the tumor by light microscopy and that they accumulate significantly within the tumor without affecting negatively affecting tumor architecture.

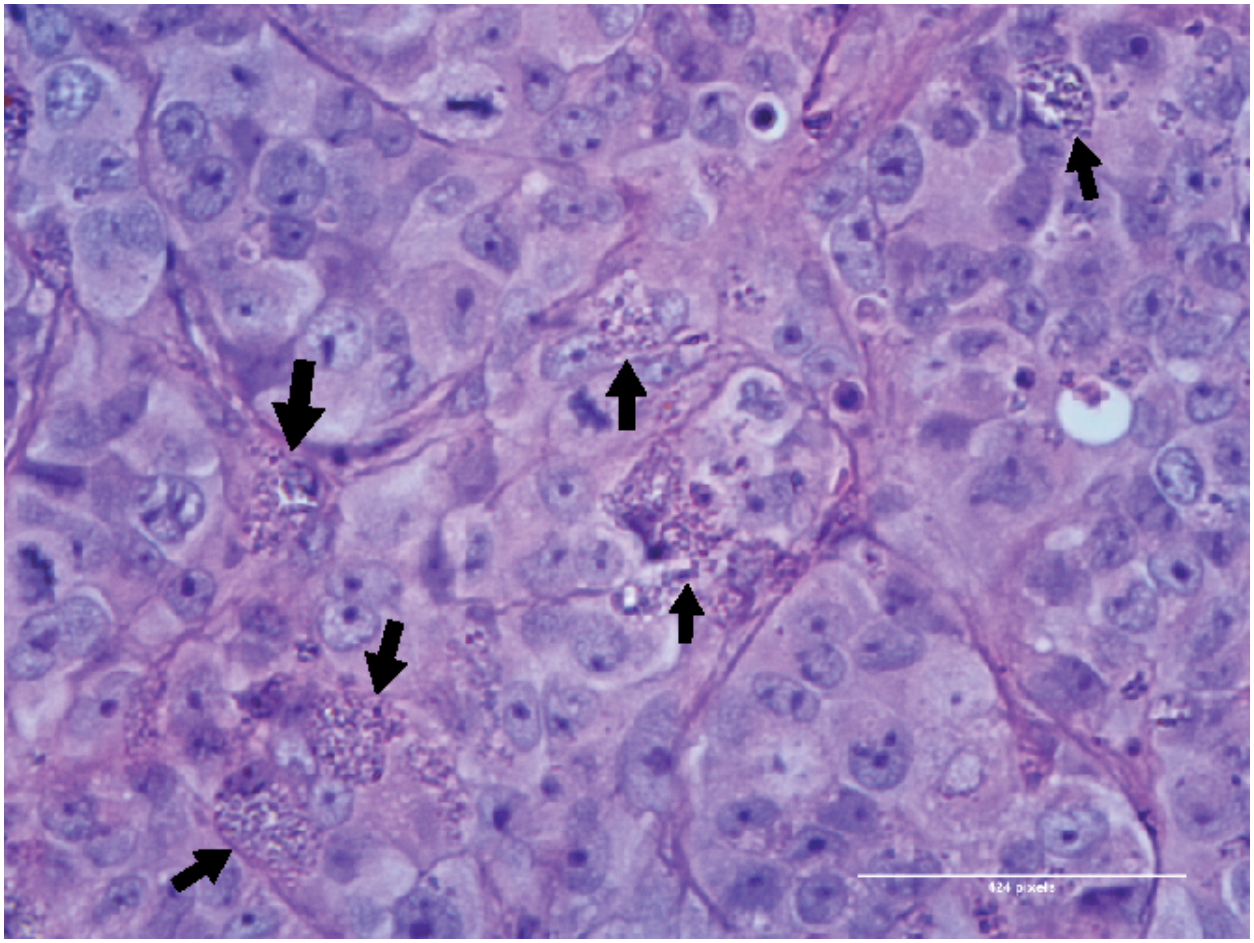

Figure 2.23. Figure 2.22d enlarged to show greater detail. H&E section of NDG tumor (60x magnification) showing a similar morphology to the unlabeled tumor but containing visible NDG aggregates within neoplastic cells and in the interstitial space (black arrows).

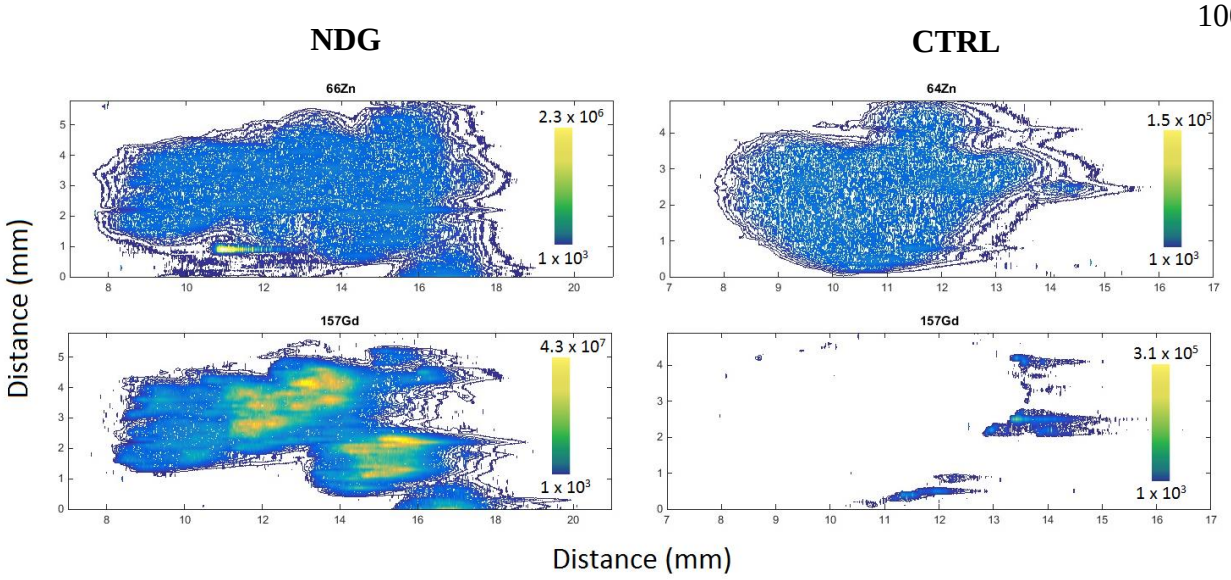

Figure 2.24. Laser Ablation ICP-MS for spatial distribution of Gd(III) content in tumor sections. Both ^{66}Zn and ^{157}Gd values are reported for each of the NDG and unlabeled tumor sections. ^{66}Zn is uniformly distributed in the tumor sections corresponding closely with the tumor section boundaries. Only the NDG tumor has Gd(III) distributed throughout the tissue with highest concentrations in the center.

2.3. Conclusions

In summary, we present a new class of nanodiamond-gadolinium(III) conjugates for MR imaging of cancer growth *in vivo*. NDG aggregates fulfill nearly all the criteria for a highly effective T_1-weighted MR contrast agent: high relaxivity at *high* field strengths, significant Gd(III) payload delivery to cells, biocompatibility, no adverse effects on the behavior or function of recipient cells, retention over time, and long-term imaging capability up to one month. While other carbon nanomaterials such as graphene, fullerenes and nanotubes have all been conjugated to Gd(III) and have been shown to label cells with high efficiency, few of these constructs have been translated toward *in vivo* biological applications.[21,26,28,54]

The ability to track the pattern of cancer growth *in vivo* is highly valuable to determine tumor properties such as growth potential and invasiveness.[4,10,55,56] We have shown that cancer cells pre-labeled with NDG aggregates enable longitudinal monitoring of cancer growth from engraftment to growth and differentiation. We have presented a new method to describe tumor morphology and regional variance in tumor architecture on the basis of T_1 relaxation. While we used flank xenografts as a proof-of-concept, our findings can be extended to orthotopic tumor xenografts within the brain, thorax, abdomen, and pelvis – locations that can only be imaged non-invasively via a modality that provides high spatial resolution, unlimited depth penetration and three-dimensional imaging.

The long-term retention of NDG aggregates within cancer cells without inducing cytotoxicity can be applied towards tracking other types of therapeutic cells such as pluripotent stem cells and immune cells. Cell-based therapies often fail because injected or implanted cells cannot be fate-mapped for long time periods, and their biodistribution within the recipient

organism becomes untraceable.[10,13-15] Studies are underway to label pluripotent stem cells with NDG aggregates, where the biocompatibility and inertness of NDG aggregates can be especially useful since these cells are particularly sensitive to *ex vivo* treatments. NDG-labeled stem cells can potentially be used to evaluate and monitor the regeneration of bone, fat, cartilage and even cardiac tissue. NDG aggregates can be used to label immune cells such as T-cells or macrophages. For example, chimeric antigen receptor (CAR) T-cells which have shown tremendous promise for targeted cancer therapy[57,58], can be pre-labeled with NDG and mapped to tumor locations to monitor treatment response rates. Similarly, adoptive transfer of NDG-labeled macrophages may further the understanding of the innate immune system, particularly macrophage phenotype activation and switching during infection, inflammation, and cancer.

It is clear that nanodiamond-gadolinium(III) aggregates are a promising class of MR contrast agents for imaging cancer *in vivo* and can potentially be utilized for labeling, imaging and tracking a variety of cells towards advanced therapeutic benefits.

2.4. Materials and Methods

2.4.1. General Synthetic Methods and Characterization: Reagents and solvents were purchased from Sigma Aldrich Chemical Co. (St. Louis, MO, USA), unless specified otherwise. Synthetic procedures were performed under ambient conditions unless described explicitly. Initial purification of Gd(III) chelates and precursors was accomplished by flash chromatography using standard grade silica gel (Sorbent Technologies, Norcross, GA, USA). A Varian 500 MHz Avance III NMR spectrometer and a Bruker Amazon X LC-MS Ion Trap Mass Spectrometer (Billerica, MA, USA) were used for chemical characterization. Final purification was achieved using a Varian Prostar 500 HPLC using a Waters 4.6 × 250 mm 5 µm Atlantis C18 column and mobile phases of

Millipore water, 0.05% trifluoroacetic acid in Millipore water, and acetonitrile. Dynamic light scattering for NDG characterization was performed on a Malvern ZetasizerNano (Malvern Instruments Ltd., Malvern, United Kingdom) particle size and zeta potential analyzer.

2.4.2. Synthesis of ethyl protected DO3A macrocycle (1,4,7-TRIS(ETHYL ACETATE)-1,4,7,10-TETRAAZACYCLODODECANE·HBr: Cyclen (Strem Chemicals Inc., 2.202 g, 12.8 mmol), sodium acetate (3.158 g, 38.5 mmol), and acetonitrile (40 mL) were added sequentially into a 250 mL round bottom flask equipped with a magnetic stir bar and a digital thermometer. The reaction vessel was cooled in an ice bath and stirred at 0 ºC for 10 minutes. In a separate 150 mL Erlenmeyer flask, ethyl bromoacetate (4.20 mL, 37.9 mmol) was diluted into acetonitrile (20 mL). The dissolved ethyl bromoacetate was transferred into an addition funnel and added dropwise to the reaction vessel containing cyclen and sodium acetate in acetonitrile over 30 minutes while maintaining a temperature below 5 ºC. The reaction was stirred under these conditions for an additional 15 minutes before removing the ice bath, and then allowed to warm to room temperature and continue stirring overnight. After stirring 18 hours, the solids were separated by filtration and rinsed with acetonitrile. The organic solution was concentrated to a clear oil and dissolved in methanol (5 mL, required heat/sonication). Upon complete dissolution, diethyl ether (25 mL) was slowly added. The resultant suspension was cooled at -20 °C for 12 hours. The white precipitate was collected and dried by lyophilization. Yield: 2.505 g (35%). ^{1}H NMR (500 MHz, $CDCl_3$) δ 10.01 (s, 1H), 4.17 (qd, *J* = 7.2, 1.2 Hz, 6H), 3.75 – 2.41 (m, 22H), 1.28 (td, *J* = 7.2, 1.2 Hz, 9H). ^{13}C NMR (126 MHz, $CDCl_3$) δ 171.15, 170.31, 61.31, 60.78, 57.27, 55.17, 51.38, 49.25, 48.22, 47.43, 14.31. ESI-MS (*m/*z): observed: 431.3, calculated: 431.3 $[M + H]^+$.

2.4.3. Synthesis of 1-(ETHYL HEXANOATE)-4,7,10-TRIS[(TERT-ETHYLCARBONYL)METHYL]-1,4,7,10-TETRAAZACLYCODODECANE: To a 50 mL round bottom flask was added 1,4,7-tris(ethyl acetate)-1,4,7,10-tetraazacyclododecane·HBr (0.550 g, 1.1 mmol) and potassium carbonate (0.375 g, 2.7 mmol) followed by dissolution in acetonitrile (10 mL). To the cloudy suspension was added ethyl 6-bromohexanoate (0.29 mL, 1.6 mmol). The reaction mixture was heated to 50 °C and allowed to stir under nitrogen for 18 hours. Reaction progress was monitored by thin layer chromatography with 1:9 methanol:dichloromethane and iodoplatinate stain. Upon completion of the reaction, the solution was filtered using a Büchner funnel to remove excess salts and the residual solids were washed with acetonitrile. The product-containing filtrate was concentrated under vacuum and the crude material was purified using flash column chromatography with a gradient of 5:95 to 10:90 methanol:dichloromethane. Elution of product was monitored by TLC using iodoplatinate stain. ^{13}C NMR analysis of purified product contained peaks which suggest partial deprotection or transesterification of ethyl esters during column chromatography. Therefore, primary product characterization was achieved by ESI-MS. Combined fractions were collected, concentrated by rotary evaporation and stored under vacuum overnight. Yield: 0.501 g (82%). ESI-MS (m/z) observed: 572.5, Calculated 572.7 $[M + H]^+$.

2.4.4. Synthesis of Gd-C5-COOH: To a 50 mL round bottom flask was added the tetra-ethyl protected chelate (0.279 g, 0.5 mmol) dissolved in aqueous 1 M sodium hydroxide (10 mL) for saponification of the chelate ethyl esters. The reaction was stirred at room temperature for 4 hours, at which time complete deprotection was observed by ESI-MS. The pH of the stirring solution was adjusted to 7.2 using 1 M hydrochloric acid. Gadolinium(III) acetate hydrate (0.242 g, 0.6 mmol) was added, followed by an observed drop in pH to 4.7. The mildly acidic conditions

required for metalation were achieved by addition of 1 M sodium hydroxide to pH 6.5. The metalation reaction was stirred at room temperature for 24 hours. The crude mixture was purified by semipreparative reverse phase HPLC using the following conditions: 0 min 0 % solvent B, 17 min 31 % solvent B, 21-26 min 100% solvent B, and 31-34 min 0 % solvent B. The desired product, Gd-C5-COOH, elutes from 15.0 to 15.9 minutes as monitored by UV-vis at 201/210 nm and was collected and lyophilized. Yield: 0.156 g (52%). ESI-MS (m/z) observed: 616.1618, calculated 616.16166 $[M + H]^+$. Anal. Calcd. for $K[C_{20}H_{32}GdN_4O_8] \bullet 5H_2O$, C:31.57 H:5.83 N:7.36 ; Found: C:31.22 H:5.69 N:7.12.

2.4.5. Nanodiamonds (NDs), Aminated nanodiamonds (NDA) and Nanodiamond-Gadolinium(III) aggregates (NDG): Nanodiamond (ND) powders were acquired from the Nanocarbon Research Institute (Nagano, Japan). Amine modified NDs were produced according to the protocols from Kruger *et al*[59], Zhang *et al*[60] and Chow *et al*[32]. Briefly, after reduction of the ND surface (2.5g) with BH3•THF (25mL, 1M) for 3 days, the ND surface (1g) was functionalized with (3-aminopropyl)trimethoxysilane (100mL, 5%), purified by centrifugation and dried by lyophlization. NDA powder was then re-suspended to a concentration of 10 mg/ml in 0.2% w/v acetic acid. 1 mL of this NDA suspension (10 mg of NDA) was dissolved in 0.5 mL of diisopropylethyl amine and 3.5 mL of DMSO, following by vigorous sonication. In a separate vessel, 0.5, 5 or 50 mg of Gd-C5-COOH (see Figures S1-S3 for synthetic details) was combined with five equivalents of NHS and EDC in 5 mL of 3:1 DMSO:Millipore water and vigorously sonicated. NDA and Gd-C5-COOH mixtures were combined in a 15 mL Falcon tube and shaken overnight at room temperature. The mixture was purified first by 3 rounds of centrifugation with milli-Q water at 10000 x g for 20 minutes. At the end of the third round, the pellet was resuspended

in 1 mL of milli-Q water and transferred to a 1.5 mL eppendorf tube. This mixture is purified by a further 3 rounds of centrifugation at 21000 x g for 20 minutes. The final pellet is re-suspended in 1 mL of 0.2% w/v acetic acid resulting in the NDG aggregates at 10 mg/mL.

2.4.6. Low-field relaxivity (r_1 and r_2): A stock suspension of NDG was made by suspending 10 mg of NDG in 1 ml of 0.2% w/v acetic acid as explained in section (b). Then, between 50-100 μL was taken from the stock and dissolved in Millipore water to total volume of 1 mL. This sample was serially diluted four times generating 5 samples each of 500 μL volume. Solutions were heated to 37 °C and 500 uL of each concentration was placed into a Bruker minispec mq60 60 MHz (1.41 T) NMR spectrometer (Billerica, MA, USA) for measurement of T_1 and T_2 relaxation time. Data were collected using an inversion recovery pulse sequence using 4 averages, a 15-second repetition time and 10 data points. The remaining volumes of each solution were utilized for ICP analysis of Gd(III) concentration. The inverse of the relaxation time ($1/T_1$ or $1/T_2$, s^{-1}) was plotted against the Gd(III) concentration (mM) determined by ICP-MS of each of the five samples. By applying a linear fit to this data, the slope that was generated was defined as the relaxivity of the agent in units of $mM^{-1}\ s^{-1}$.

2.4.7. High Field Relaxivity (7 T): A stock suspension of NDG at 10 mg/mL was made as described in section (b). 10-, 7.5-, 5-, and 2.5 μL of the stock suspension was added to Millipore water to a total volume of 500 μL. Each solution was added to a 5¾″ flame-sealed Pasteur pipet, and centrifuged at 100 x *g* at 4.0 °C for 5 minutes. The bottom sections of the pipets were scored with a glass scribe to make small capillaries, which were imaged on a Bruker Pharmscan 7 T imaging spectrometer fitted with a RF RES 300 1H 089/023 quadrature transmit receive 23-mm volume coil (Bruker BioSpin, Billerica, MA, USA). T_1 relaxation times were measured using a

rapid-acquisition rapid-echo (RARE-VTR) T_1-map pulse sequence, with static echo time (11 ms) and variable repetition time (150, 250, 500, 750, 1000, 2000, 4000, 6000, 8000, and 10000 ms) values. Imaging parameters were as follows: field of view (FOV) = 25 × 25 mm^2, matrix size (MTX) = 256 × 256, number of axial slices = 4, slice thickness (SI) = 1.0 mm, and averages (NEX) = 3 (total scan time = 2 h 36 min). T_1 analysis was carried out using the image sequence analysis tool in Paravision 6.0 software (Bruker, Billerica, MA, USA) with monoexponential curve-fitting of image intensities of selected regions of interest (ROIs) for each axial slice. Spin-spin relaxation times (T_2) were measured using a multi-slice multi-echo (MSME) T_2-map pulse sequence, with static TR (5000 ms) and 32 fitted echoes in 11 ms intervals (11, 22,..., 352 ms). Imaging parameters were as follows: field of view (FOV) = 25 × 25 mm^2, matrix size (MTX) = 256 × 256, number of axial slices = 4, slice thickness (SI) = 1.0 mm, and averages (NEX) = 3 (Total scan time = 48 min). T_2 analysis was carried out using the image sequence analysis tool in Paravision 6.0 software (Bruker, Billerica, MA, USA) with mono-exponential curve-fitting of image intensities of selected ROIs for each axial slice.

2.4.8. Metals Analysis by ICP-MS: ICP-MS was performed on a computer-controlled (QTEGA v. 2.6) Thermo (Thermo Fisher Scientific, Waltham, MA) iCapQ ICP-MS equipped with an ESI SC-2DX autosampler/autodilution system (Elemental Scientific Inc., Omaha, NE). Quantitation of metal concentration was performed by acid digestion of nanoconjugate samples, followed by ICP-MS analysis. Specifically, for NDG aggregates, Gd(III) content was measured by addition of 5 ul of NDG sample into 300 μL of concentrated nitric acid (BDH AristarPlus Nitric acid, 70%). The mixture was heated at 65 °C for at least 2 hours. This was followed by addition of ultra-pure H_2O (18.2 Ω·m) up to 10 mL total sample volume. For cells labeled with NDG, 20 –

150 μL of NDG-labeled cells suspended in PBS or media were added to 100 μL 70% nitric acid and heated at 65 °C for at least 4 hours. Following digestion, ultra-pure H_2O water was added for a final sample volume of 3 mL. Individual Gd elemental standards were prepared at 0, 0.78125, 1.5625, 3.125, 6.25, 12.5, 25.0, 50.0, 100, and 200 ng/mL concentrations with 2% nitric acid (v/v), 2% HCl (v/v) and 5.0 ng/mL internal standards (6Li, Sc, Y, In, Ho, Bi) up to a total sample volume of 5 mL. Each sample was acquired using 1 survey run (1 sweeps) and 3 main (peak jumping) runs (100 sweeps). The isotopes selected were ^{156,157}Gd using ^{115}In and ^{165}Ho as internal standards for data interpolation and machine stability. Instrument performance was optimized daily by means of manufacturer's autotune and Thermo TuneA solution.

2.4.9. FTIR: NDG, NDA, and Gd-C5-COOH, were dried *in vacuo*. Infrared spectra were obtained with a Bruker Alpha FTIR spectrometer equipped with an attenuated total reflectance accessory. Approximately 3 mg of each sample was analyzed with the anvil depressed.

2.4.10. Primary Amine Quantification: A modified Kaiser test was used to quantify primary amines and is based on a procedure previously reported by Jarre *et al.*[41] The following reagents are utilized.

i. Acetate buffer at pH 5.5
ii. 5% Ninhydrin solution
iii. KCN-pyridine reagent: 2 mL of 30 mM KCN dissolved in 98 mL of pyridine
iv. Phenol solution: 40 g of phenol dissolved in 10 mL of ethanol.
v. Ethanol solution: 30 mL of reagent alcohol is dissolved in 20 mL of DI water.

For the standard curve, 1 mL of known concentrations of benzylamine (10-, 5-, 2.5-, 1.25-, 0.625-mM) were used. For NDG or NDA, 1 mg of dried sample was vigorously sonicated in 1 mL of DI water. To this 1 mL solution of NDG, NDA or benzylamine was added 1 mL of reagent (i) followed by sonication for 15 minutes. Next, 1 mL of reagent (iii) and 1 mL of reagent (iv) were added and the suspension was heated in an oil bath @ 120° C for 10 minutes. Then 1 mL of reagent (ii) was added and heated for another 10 minutes. The solution was then cooled to room temperature within 30 minutes and 5 mL of ethanol solution was added. The solids were separated by centrifugation, and a UV-vis spectrum was recorded from the supernatants. The peak at 570 nm indicated presence of primary amines. Unknown amine concentrations were determined from a standard curve.

2.4.11. STEM and EDX spectroscopic analysis: NDG and NDA samples were dried and placed on gold slot grids with a carbon coated Formvar support film, and analyzed in a STEM (HD2300-A, Hitachi) with a dual detector EDX system (Energy Dispersive X-ray Spectroscopy, Thermo Scientific, MA). System settings were as follows: 200 kV acceleration voltage, objective aperture of 75 µm in diameter, and 2 minutes spectrum recording time per area. The NSS Noran System Seven software was used for EDX analysis. Resin embedding of cells for STEM and EDX spectroscopic analysis: Cells were labeled with 1 mg/ml NDG in media for 24 hours. Cells were washed, harvested and fixed in 2.5 % glutaraldehyde (25 % aqueous stock solution), 2 % formaldehyde (16 % aqueous stock solution) (EMS, Electron Microscopy Sciences) in DPBS (Dulbecco's Phosphate-Buffered Saline, Cellgro Mediatech, Inc., VA), pH 7.4. After fixation overnight at 4° C, the samples were rinsed in PBS and in ddH_2O for 15 minutes each and post-fixed in aqueous 2% osmium tetroxide (EMS) for one hour. After two rinses in ddH_2O for 15 minutes each, the specimens were dehydrated in 25%, 50%, 75%, 90% ethanol for 20 minutes

each, and two times for 10 minutes each in 100 % ethanol. After infiltration with a 1:1 mixture of Spurr resin (EMS) and ethanol for 3 hours, the samples were infiltrated overnight in pure resin. For polymerization, the samples were transferred into fresh resin in flat embedding molds and polymerized at 60°C for 48 hours. The blocks were sectioned using a diamond knife (Diatome) with an ultramicrotome (UC7, Leica) at a nominal thickness of 70 nm, and the sections were collected on 200 mesh copper grids, dried and observed in a STEM (HD2300-A, Hitachi) with an acceleration voltage of 80 kV. The NSS Noran System Seven software was used for EDX analysis.

2.4.12. NMRD profiles and analysis: Water proton relaxation rates of solutions containing NDG, Gd-C5-COOH, or Gd-C5-COOH mixed with NDA were measured from 0.01 to 40 MHz proton Larmor frequency using a fast field cycling Stelar relaxometer. The relaxivity profiles of NDG were obtained after the subtraction of the diamagnetic NDA relaxation rates and normalized to 1 mM Gd(III) concentration.

2.4.13. General Cell Culture: DPBS, media, and dissociation reagents were purchased from Life Technologies (Carlsbad, CA). CorningBrand® cell culture consumables (flasks, plates, etc.) and sera were purchased from VWR Scientific (Radnor, PA). MDA-MB-231 m-Cherry (ATCC® HTB-26TM) cells were purchased from the American Type Culture Collection (ATCC, Manassas, VA) and cultured in phenol red-free minimum essential media-alpha (α-MEM) supplemented with 10% fetal bovine serum (FBS), 1% non-essential amino acids, 1% sodium pyruvate, and 1% 100mM L-glutamate. Cells were confirmed free of mycoplasma contamination by MycoAlert™ Mycoplasma Detection Kit (Lonza Group Ltd., Switzerland). Prior to all experiments, cells were plated and allowed to incubate for 24 hours before dosing. Cells were

harvested with 0.25% TrypLE for 5 minutes at 37 °C in a 5.0% CO2 incubator. Cells were grown in a humidified incubator operating at 37°C and 5.0% CO_2.

2.4.14. Guava ViaCount Assay for Cell Counting: Cell counting was conducted using a Guava EasyCyte Mini Personal Cell Analyzer (EMD Millipore, Billerica, MA). After cell harvesting, an aliquot (50 μL) of the cell suspensions was mixed with Guava ViaCount reagent (150 μL) and allowed to stain at room temperature for at least 5 minutes (dilution factor of 4 and cell density between 20-150 cells/μL). After gently vortexing for 10 seconds, stained cells were counted using a Guava EasyCyte Mini Personal Cell Analyzer (PCA) using the ViaCount software module. For each sample, 500-1000 events were acquired. Gating of live/dead and cell/debris classifications were performed manually by the operator. Instrument performance was validated biweekly using GuavaCheck Beads following the software module "Daily Check".

2.4.15. Cellular Delivery Studies. Cellular delivery studies were performed with MDA-MB-231 m-Cherry cells. MDA-MB-231 m-Cherry cells were plated at a cell density of approximately 25,000 per well for 24-hour uptake in a 24-well plate as counted by a hemocytometer. Stock solutions of NDG were prepared by resuspending a pellet of known mass of NDG in fresh media. Gd(III) concentration ranged from 5 – 1500 μM (0.005 – 1 mg/ml diamond concentration). To harvest, cells were rinsed in-plate three times with 500 μL PBS and trypsinized using 100 μL 0.25% TrypLE. Following trypsin treatment, 150 μL of media was added to each well and mixed by a pipette to ensure that all cells were lifted into suspension. The cellular suspensions were centrifuged at 1000 x *g* for 5 minutes at 4 °C, after which the supernatant was discarded and the pellet was re-suspended in fresh media. This process was repeated twice. From

the final cell suspension, 50 μL was used for cell counting and 150 μL was used for Gd content analysis via ICP-MS.

2.4.16. Cell Pellet MRI: Approximately 7.5 × 10^5 MDA-MB-231 m-Cherry cells were incubated in 25-cm^2 T-flasks with NDG aggregates (Gd(III) concentrations of 500-, 50- and 5-μM) suspended in media for 24 h, rinsed with DPBS (2 × 1 mL/flask), and harvested with 500 μL of trypsin. After addition of 500 μL of fresh complete media, cells were transferred to 1.5-mL microcentrifuge tubes and centrifuged at 1000 x *g* at 4.0 °C for 5 minutes. The supernatant was removed; the cell pellets were re-suspended in 1 mL of complete media, added to 5¾″ flame-sealed Pasteur pipets, and centrifuged at 100 x *g* at 4.0 °C for 5 minutes. The bottom sections of the flame-sealed pipets were then scored with a glass scribe, broken into small capillaries, and imaged using a RF RES 300 1H 089/023 quadrature transmit receive 23-mm volume coil (Bruker BioSpin, Billerica, MA, USA). T_1 and T_2 relaxation times were measured as described in section 2.4.7.

2.4.17. Agarose cell phantoms: A 2% w/v low melting temperature agarose solution was mixed in equal parts with serum supplemented media at 37°C to create a 1% agarose/media mixture. A 10-mL glass vial was gelled with 5-mL of the agarose/media mixture around two 5 mm O.D. NMR tubes placed approximately 3 mm apart and about 1 cm from the bottom of the vial. The tubes were then removed to create cylindrical cavities within the gel. One cavity was filled with 250 μL of cells labeled with 0.5 mg/ml NDG for 24 hours, suspended in warm agarose/media mixture at a cell density of 30,000 cells/μL. The other cavity was filled with unlabeled cells suspended in warm agarose/media mixture at the same cell density. The vial was placed on ice for 15 minutes for gelling to take place.

The vial was filled with media, capped, and sealed with parafilm. The vial was imaged in a Bruker Pharmscan 7 T imaging spectrometer fitted with RF RES 300 1H 089/023 quadrature transmit receive 23-mm volume coil (Bruker BioSpin, Billerica, MA, USA) at 25 °C. A rapid acquisition with refocused echoes (RARE) pulse sequence was used. For T_1-weighting, the following parameters were used: TR = 208.7 ms, TE =10.8 ms, flip angle = 180°, NEX = 1, FOV = 25 x 25 mm^2, slice thickness = 1 mm, and matrix size = 256 x 256. For T_2-weighting, the following parameters were used: TR = 4000 ms, TE = 40 ms, flip angle = 180°, NEX = 1, FOV = 25 x 25 mm^2, slice thickness = 1 mm, and matrix size = 256 x 256. The same vial was also imaged in an IVIS Spectrum (PerkinElmer, Waltham, MA, U.S.A.) for m-Cherry fluorescence. An excitation wavelength of 580 nm and an emission wavelength of 620 nm were used.

2.4.18. In vivo studies. All mice were handled and processed according to a protocol approved by Northwestern University Animal Care and Use Committee in accordance with current guidelines from the National Institutes of Health Model Procedure of Animal Care and Use. Female, SCID-beige mice aged 6-8 weeks at initiation were used for the length of the study. Mice were imaged by MRI on a Bruker PharmaScan 7 T magnet (Bruker Biospin, Billerica, MA, U.S.A.). Five flasks containing approximately 5 x 10^6 MDA-MB-231 m-Cherry cells were labeled with NDG at 500 μM Gd(III) concentration (0.5 mg/ml diamond concentration) for 24 hours. Cells from each flask were washed repeatedly, re-suspended in sterile phosphate buffered saline to a volume of 0.1 mL, and injected into the right rear flank of the mice (n = 5).

Similarly, unlabeled cells were injected into the left rear flank of the same mice. Mice were then imaged at 2-, 5-, 9-, 14-, 19- and 26-days post-engraftment using both T_1- and T_2-weighted sequences. During imaging, mice were held under 1−2% inhaled isoflurane anesthesia and

respiration was monitored using an SA Instruments MR compatible monitoring system (SA Instruments, Stonybrook, NY, U.S.A.). T_1-weighted images were acquired using a rapid acquisition rapid echo (T_1-RARE) sequence with imaging parameters as follows: RARE factor = 4, repetition time (TR)/echo time (TE) = 750 ms/6.2 ms, field of view (FOV) = 30 x 30 mm^2, matrix size (MTX) = 200 x 200, number of axial slices (NS) = 3, slice thickness (SI) = 0.7 mm, and averages (NEX) = 1. T_2-weighted images were acquired using an accelerated TurboRARE sequence with imaging parameters as follows: RARE factor = 4, TR/TE = 800 ms/17 ms, NEX=4, and identical geometry to the T_1-RARE sequence. T_1 relaxation times were measured using a RARE T_1-map pulse sequence (RARE-VTR), with static echo time (6.5 ms) and variable repetition time (100, 200, 400, 800, 1500, 3000, and 6500 ms). Imaging parameters were as follows: RARE factor = 2, FOV = 30 × 30 mm^2, MTX = 128 × 128, NS = 3, slice SI = 0.7 mm, and NEX = 1 (total scan time = 11 min).

T_1 analysis was carried out using JIM 6.0 (Xinapse Systems, Essex, UK) with monoexponential curve-fitting of image intensities. JIM 6.0 was also used to draw ROIs in each tumor and surrounding muscle in the T_1-weighted image obtained at Day 26 of each mouse. T_1-maps obtained in each ROI were overlaid on a T_2-weighted anatomical reference image from the same time point.

2.4.19. In Vivo Fluorescence Imaging: Immediately prior to each MRI time point, fluorescence images of mice were obtained an IVIS Spectrum (PerkinElmer, Waltham, MA, U.S.A.). Mice held under 3% inhaled isoflurane anesthesia for the duration of imaging. Mice were placed on their right or left side to image the NDG tumor or unlabeled tumor respectively. For m-Cherry fluorescence readouts, an excitation wavelength of 580 nm and emission wavelength of

620 nm were used. Mice were allowed to recover and ambulate for several minutes before MR imaging. Image data was processed using Living Image software. ROIs were defined corresponding to each tumor and used to determine background subtracted radiant efficiency.

2.4.20. Organ Analysis for Gd(III) content: At the end of the 26-day time point, mice were sacrificed and organs were digested and analyzed for Gd(III) content by ICP-MS. The tumors, proximal leg muscles, spleen and kidneys were placed into preweighed Teflon tubes, weighed, and dissolved in 9:1 ACS reagent grade nitric acid/hydrogen peroxide to a total volume of 1 mL. The livers, stomachs and bowels were placed into preweighed TFM vessels, weighed, and dissolved in 9:1 ACS reagent grade nitric acid: hydrogen peroxide (10 mL). The solutions were digested using an EthosEZ microwave digestion system (Milestone, Shelton, CT, U.S.A.) with a 120 °C ramp for 30 min followed by a 30 min hold and a 45 min exhaust cycle. The resultant solutions were weighed and an aliquot was transferred to a preweighed 15 mL conical tube. The final ICP-MS sample was prepared as described above in section 2.4.8.

2.4.21. Laser ablation ICP-MS: Laser ablation ICP-MS was accomplished using a NuWave UP213 Nd:Yag Laser (Elemetnal Scientific Inc., Portlan, OR) coupled to a computer-controlled (QTEGRA v. 2.6.2) Thermo iCapQ ICP-MS (Thermo Fisher Scientific, Waltham, MA) of NDG-labelled and unlabeled tumor cross sections. Laser ablation performance was optimized prior to ample runs using a NIST 612 glass standard using an 80 um spot size, 10 Hz rep rate, and 100% laser power (%He was optimized at 5% with nebulizer Ar pressure at 1). Tissue sections were ablated using a 100 um spot size, 20 Hz rep rate, 100 um/sec laser passes and laser output of 39-42% (Laser power was adjusted to a fluence of 0.2-0.3 mJ for accurate tissue ablation). Additionally, the method was setup with a 40 second laser warm-up time prior to each line pass

and a 20 second washout time at the end of each line pass. The isotopes selected or analysis were ^{64}Zn, ^{66}Zn, ^{57}Fe, ^{156}Gd, and ^{157}Gd with a 10 ms dwell time for each isotope. Following ablation, data was analyzed using MATLAB (Version R2016a) to produce 2D color maps of signal intensities of the selected isotopes.

2.4.22. Statistics: Structural and chemical characterization results of NDG aggregates and Gd-C5-COOH report on the average and standard deviation of a minimum of three independently synthesized batches. NMRD profiles were obtained for two independently synthesized batches of NDG and Gd-C5-COOH. Results of cell studies represent averages of three separate experiments, each in triplicate wells. Five mice were used for *in vivo* MRI, each bearing two tumors (NDG-labeled and unlabeled). This setup requires no randomization and investigators were not blinded. MR and fluorescence images of a single representative mouse are shown. After the final imaging time point, three subjects were used for Gd(III) biodistribution analysis, while two subjects were used for histological analysis. All bar graphs indicate averages while error bars represent standard deviations.

Chapter 3:

Theranostic Nanodiamonds for Targeted Breast Cancer Imaging and Chemotherapy

Rammohan, N.; McLeod, S.; Moore, L.K.; MacRenaris, K.W.; Waters, E.A.; Preslar, A.T.; Ho, D.; Meade, T.J. Theranostic Nanodiamond-Gd(III)-Doxorubicin Nanoconjugates for Efficient Chemotherapy Monitored by MR Imaging. **2016.** *In Preparation.*

3.1. Introduction

Breast cancer is the second most common malignancy and leading cause of cancer death among women worldwide.[1] In 2013, it is estimated that there will be 232,340 new cases of invasive breast cancer among women in the United States.[2] It exceeds all other cancers in terms of healthcare costs in the US; in 2010, the disease burden was $16.2 billion.[3] Historically women have been taught to use a monthly self-breast exam in combination with clinical exams and screening mammography to monitor for the development of breast cancer. However the utility of any of these screening measures is questionable.[4-6] Even in women over 50 years of age annual screening mammography provides only a modest reduction in mortality, along with a significant increase in the number of unnecessary biopsies and false positive diagnoses.[3] In younger patients and in hormone receptor-negative tumors, mammography is often inconclusive due to soft tissue changes and decreased incidence of tumor calcifications.[7] The shortcomings of the currently available techniques for breast cancer detection make it clear that a better diagnostic modality is desperately needed.

Breast cancer treatment is not lacking for challenges. Current breast cancer treatment regimens typically involve a combination of surgery, radiation and chemotherapy.[8] Depending on the tumor size, type and location, surgical treatment of breast cancer may involve either a lumpectomy or a complete mastectomy. However, even with the aid of modern imaging systems it can be difficult for a surgeon to determine exactly where the tumor ends and healthy tissue begins. Failure to remove all of the cancerous tissue can result in tumor recurrence and treatment failure. Delivery of a targeted contrast agent prior to surgery could facilitate pre-operative surgical planning and improve breast cancer treatment. Furthermore, cell-targeted imaging could aid in the

detection of both local and distant metastases. Finally, studies have shown that both chemotherapy and radiation improve breast cancer survival rates when given after either breast conserving or radical surgery.[8,9] Although researchers have demonstrated that breast cancer responds to a wide variety of chemotherapeutic and hormone modulating agents, selection of the proper chemotherapeutic agents can prove challenging, especially when resistance is involved.[8,9] The response to treatment is currently assessed by gross changes in tumor volume that can take 6-8 weeks to appear.[10] More detailed non-invasive imaging, such as with targeted MRI contrast agents, could allow physicians to monitor changes in tumor size and receptor expression over the course of treatment thereby facilitating earlier detection of non-ideal treatment responses.

Since the emergence of hormone modulatory therapies, such as selective estrogen receptor modulators, selective progesterone receptor modulators, and Trastuzumab (anti-Her2), breast cancer treatment can now be tailored to each patient based on hormone receptor expression. Although these hormone modulators have greatly improved breast cancer treatment, cancers that do not express estrogen, progesterone or epidermal growth factor type 2 receptors (ER, PR and Her2/neu respectively) do not benefit from these therapies. Of all the subsets of breast cancer, these triple negative breast cancers (TNBCs) are the most aggressive and have the worst prognosis.[11] However, TNBCs present an interesting treatment paradox - they are associated with an aggressive clinical course and poor survival rates, but are relatively responsive to chemotherapy.[12] Additionally, although TNBCs do not express ER, PR and Her2/neu, they are known to overexpress CD44.[13-16] Therefore, CD44-targeted therapies have the potential to revolutionize the treatment of TNBC.

Nanoscale diamond particles, or nanodiamonds (NDs), represent one of several classes of carbon nanoparticles that have great potential for a variety of biological applications.[17-20] NDs are 4-6nm, spherical, carbon particles with a diamond crystal structure. NDs meet the requirements for being an efficient bioagent delivery platform: they are biocompatible, can carry a broad range of therapeutics, are dispersible in water and allow uniform, scalable production.[17] A range of cargos have been delivered using NDs, including covalently attached drugs[18,21-23], proteins[18,24], small molecules under acidic conditions (commonly observed in tumors)[18,20,25] and siRNA for specific cancers.[23,26,27]

One feature that sets NDs apart from other particles is its faceted surface shape that provides unique physical properties. The faceted surface of NDs allows electrostatic attachment of a variety of small molecules. For example, doxorubicin (Dox) adsorbed onto the faceted surface of NDs was used to treat drug-resistant breast cancer & liver cancer.[28,29] This sequestration of Dox onto the ND surface produced a delayed release profile, which in turn decreased systemic toxicity and the capacity of the tumors to expel Dox; furthermore, it increased the circulation half-time 10-fold over unmodified Dox and allowed for higher dosages of Dox in mice without affecting survivability.

ND-based conjugates have provided numerous breakthroughs for molecular imaging.[30-37] In particular, the Meade group developed NDs for magnetic resonance imaging (MRI) by covalently coupling Gd(III)-based contrast agents to the ND surface.[38] These ND-Gd(III) conjugates provided approximately a 12-fold enhancement in ability to produce contrast with respect to the uncoupled Gd(III) contrast agent.

Given the success of NDs in both imaging and therapy applications, a significant advance would be the simultaneous ND-mediated delivery of both MRI contrast agents and chemotherapy *in vivo*.

Here we seek to build on the success achieved with ND conjugates, such as ND-Dox and ND-Gd(III), by combining the imaging and therapeutic features onto the same ND platform (**Figure 3.1**). In addition, molecular targeting will be accomplished by further conjugating the NDs to hyaluronic acid (HA) - the targeting ligand of CD44. While some passive targeting of ND conjugates is observed in animal models due to the enhanced permeability of tumor vasculature, it is not optimal for selective tumor targeting. The addition of HA to the ND platform would enable selective targeting to the tumor and not to healthy tissue. A project workflow is presented in **Figure 3.2**.

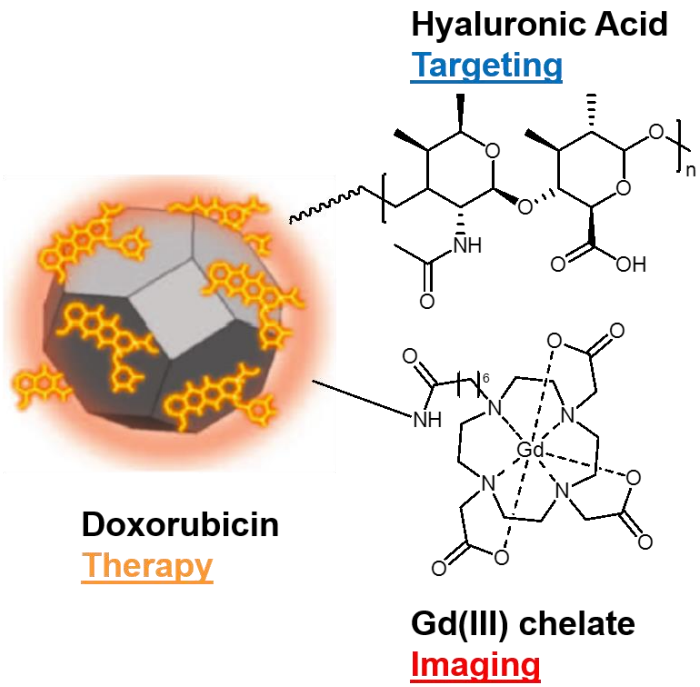

Figure 3.1. Theranostic NDs for targeted imaging & therapy. Gd(III) chelates enable MR imaging, Dox enable chemotherapy and HA enables molecular targeting to CD44.

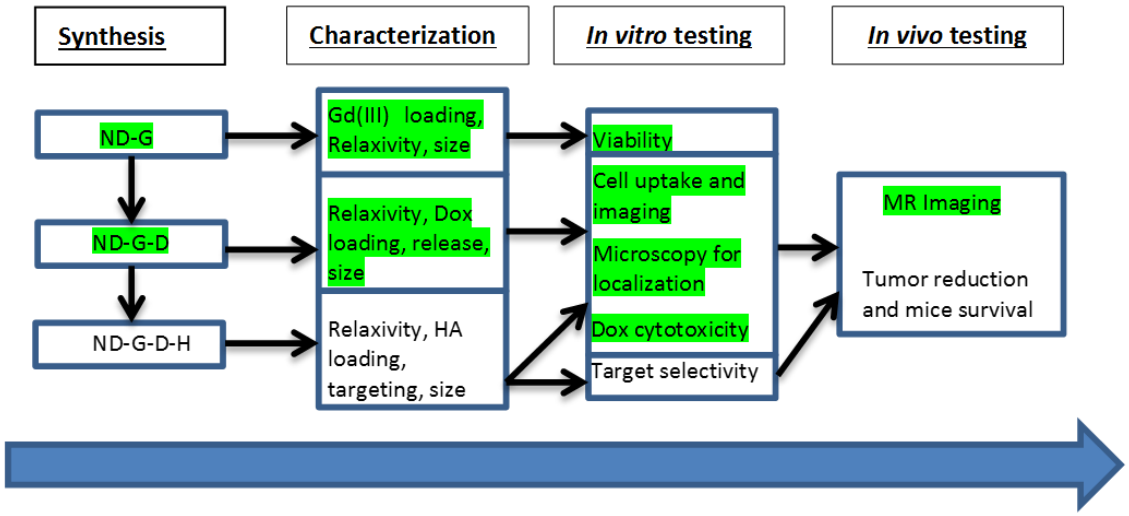

Figure 3.2. Project workflow and experimental progression. Completed steps highlighted in green.

3.2. Results and Discussion

3.2.1. Synthesis and Characterization of Nanodiamond-Gd(III)-Dox-HA (ND-G-D-H):

NDs for MR imaging: ND-Gd(III) (ND-G) conjugates were synthesized as described in Chapter 2, section 2.2.1. Briefly, nanodiamond powders were provided by our collaborator Dr. Dean Ho from Univ. of California, Los Angeles. The NDs were reduced using boron tetrahydride in tetrahydrofuran, followed by silanization with (3-aminopropyl)-trimethoxysilane as previously described.[39] Silanization provides an abundance of primary amine groups on the ND surface. Then, carboxylate-functionalized Gd(III) chelates were peptide-coupled to the amine groups on the ND surface, using 1-Ethyl-3-[3-dimethylaminopropyl] carbodiimide hydrochloride (EDC) and N-hydroxysuccinimide (NHS). ND-Gd(III) (ND-G) conjugates were purified by centrifugation, and covalent coupling was confirmed by inductively-coupled plasma-mass spectroscopy (ICP-MS) for Gd(III) content of NDs and supernatants. For characterization purposes, the T_1 and T_2 relaxivity of ND-G were measured. For summary of results, see ***Table 2.1.***

Targeted NDs: HA (average molecular weight of 10-100 kDa) was purchased from Lifecore Biomedical (Chaska, MN, USA). HA was covalently-coupled to the aminated NDs using the same peptide coupling chemistry as described above, exploiting the free carboxylate on the HA monomers, to form ND-HA (ND-H) conjugates.

Theranostic NDs: ND-G or ND-H conjugates were mixed with doxorubicin in varying ratios by mass (5:1, 3:1, 1:1, 1:3 and 1:5 ND:Dox) and spun down to produce ND-Gd(III)-Dox (ND-G-D) or ND-Gd(III)-Dox-HA (ND-G-D-H) conjugates (**Figure 3.3**). The solution will be adjusted with 3 mM NaOH to promote drug complexing.

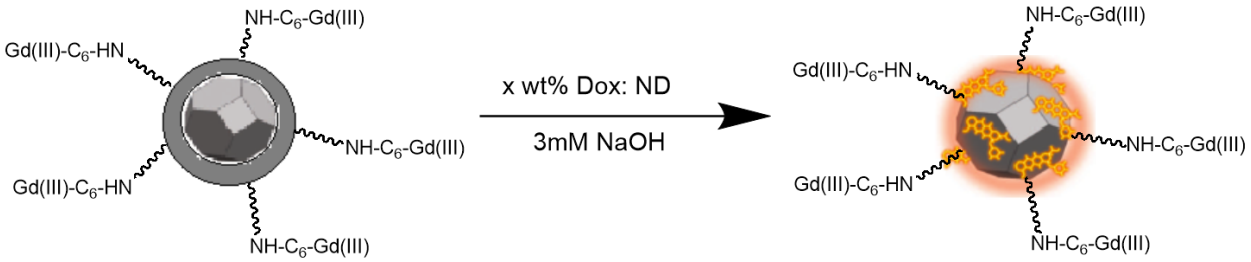

Figure 3.3. ND-G (or ND-H) was mixed with Dox in varying mass ratios (5:1, 3:1, 1:1, 1:3 and 1:5 ND:Dox) in 3 mM NaOH. The reagents were vortexed for at least one minute and allowed to mix overnight. The mixture was then spun down at 21,000g for 30 minutes at 4 ºC.

Loading was assessed by absorbance (Dox) intensity of supernatant and purified NDs. A standard curve was used to estimate Dox concentration in the supernatant (**Figure 3.4**). Based on Dox remaining in supernatant, efficiency of Dox loading onto ND-G was determined (**Figure 3.5**). Dox loading efficiency was determined for a range of ND:Dox mixing ratios by mass, where Dox loading decreases when more Dox is added to the ND:Dox mixture (**Figure 3.6**). Dox elution over time was assessed by absorbance intensity in supernatants after periodic particle spin-down (**Figure 3.7**). Dox leeched from ND-G-D suspended in media gradually over a period of 72 hours, but remained relatively stable in PBS and water.

3.2.2. Cellular studies using ND-G-D:

ND-G-D was tested in human triple-negative breast cancer MDA-MB-231 m-Cherry cells. These cells overexpress CD44 and are a reliable model for assessment of HA-mediated targeting.[13,14,40,41] Cells were incubated with ND-G, ND-G-D, ND-D or Dox alone 24 hours (**Figure 3.8**) or 72 hours (**Figure 3.9**) and then assayed by a flow cytometric live/dead assay. The number of live vs. dead cells served as an indicator of therapeutic efficacy. ND-G-D is the most potent agent with an EC50 at least two-fold better than free Dox after 24 hours and 72 hours. For assessment of *in vitro* theranostics, we set up the following experiment. Cells were treated with various Dox-equivalent concentrations of ND-G-D. After 4 hours, the doses were washed away and replaced with fresh media. After 72 hours, for each Dox-equivalent dose, cells were separated into live and dead cells by flow cytometry. Cellular Gd(III) was measured in the live cells at each dose and plotted along with cell viability (**Figure 3.10**). Increasing cell death is associated with increasing Gd(III) in remaining live cells, demonstrating that therapeutic efficacy can be tracked by Gd(III) uptake.

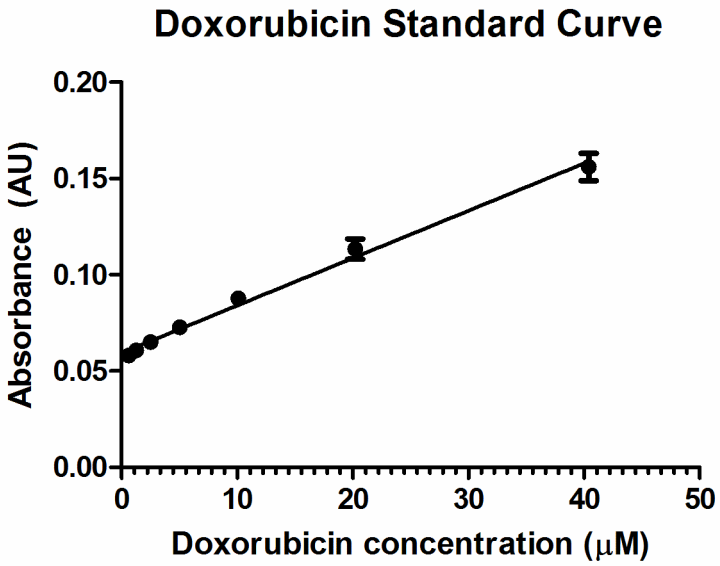

Figure 3.4. Dox-HCl was dissolved in 3 mM NaOH, 0.02% w/v Acetic Acid at serially diluted concentrations to form the standard curve. Absorbance reading was fit to curve and concentration of unbound Dox was determined.

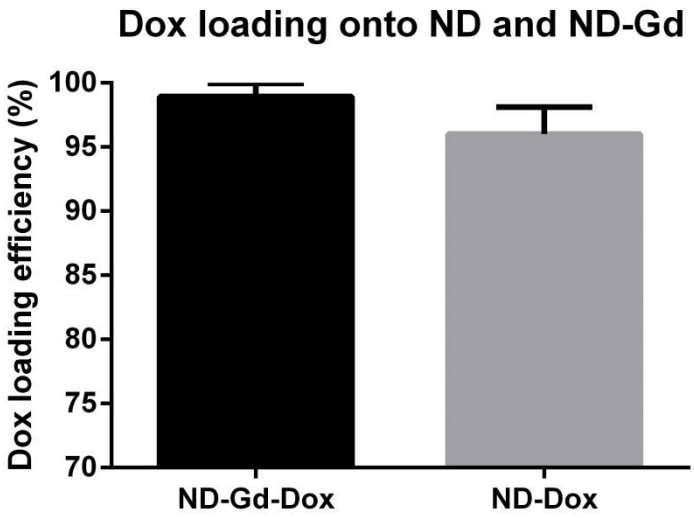

Figure 3.5. Based on Dox remaining in supernatant, efficiency of Dox loading onto ND-G and ND was determined. For 5:1 ND:Dox, loading efficiency in excess of 90% was achieved.

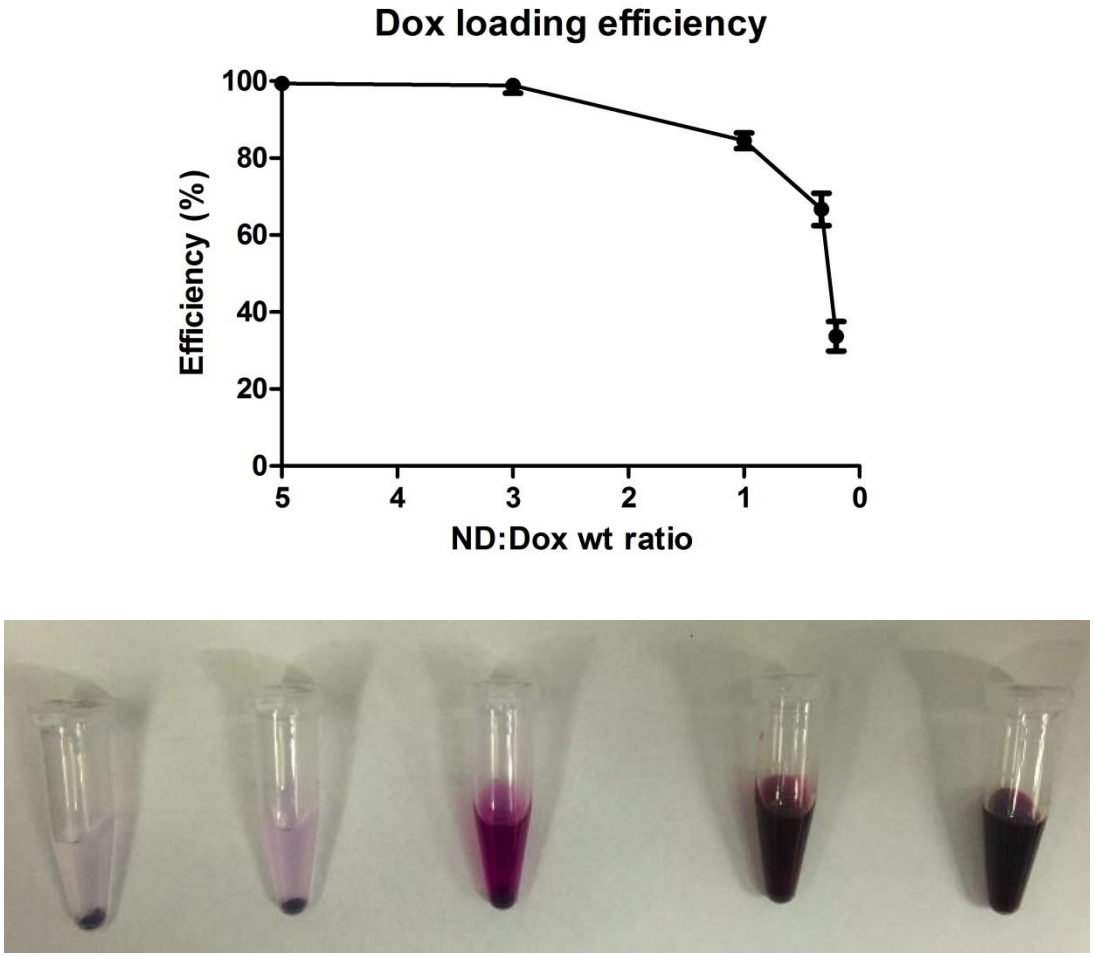

Figure 3.6. Dox loading efficiency for different ND:Dox mixing ratios by mass. (Top) Dox loading efficiency decreases with increasing mixing quantities of Dox, and loading amount can be chosen depending on dose requirement. (Bottom) With increasing Dox quantities, more Dox remains in the supernatant, decreasing loading efficiency.

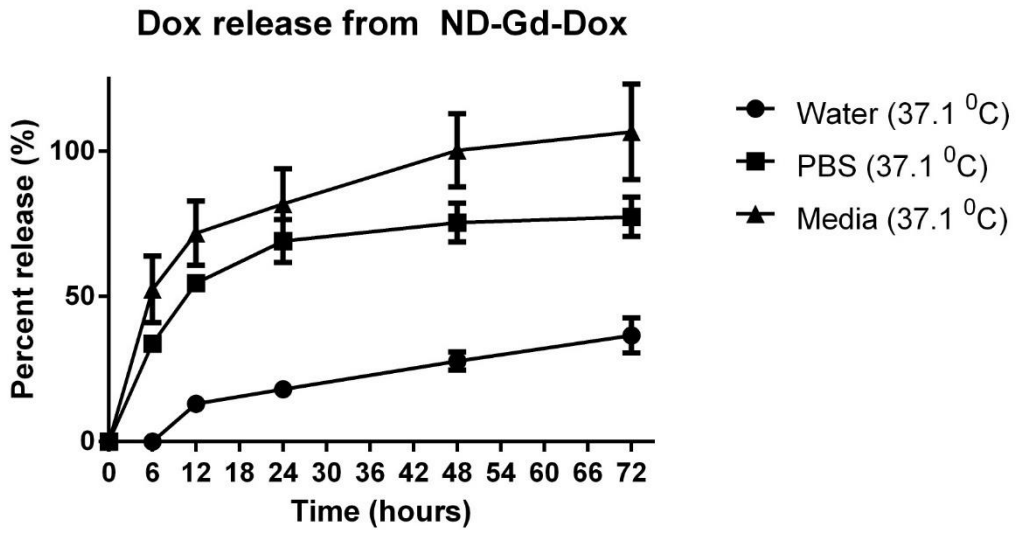

Figure 3.7. Dox elution from ND-G-D, demonstrating gradual leeching into media over 72 hours, with relative stability in water and PBS.

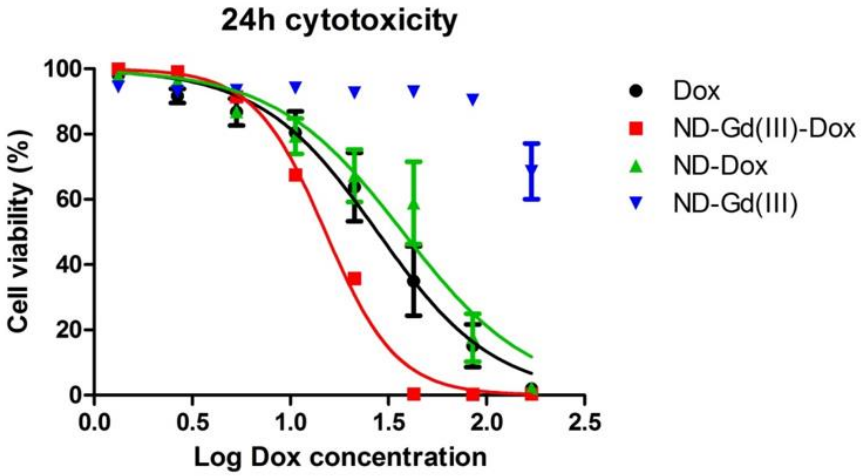

EC50:

Dox – 27.8 μM

ND-Dox – 37.5 μM

ND-Gd(III)-Dox – 15.1 μM

$p < 0.0001$

Figure 3.8. MDA-MB-231 m-Cherry cells were treated with ND-G-D, ND-D, ND-G or Dox alone for 24 hours. ND-G-D is the most potent agent, where its EC50 is nearly two-fold better than that of free Dox.

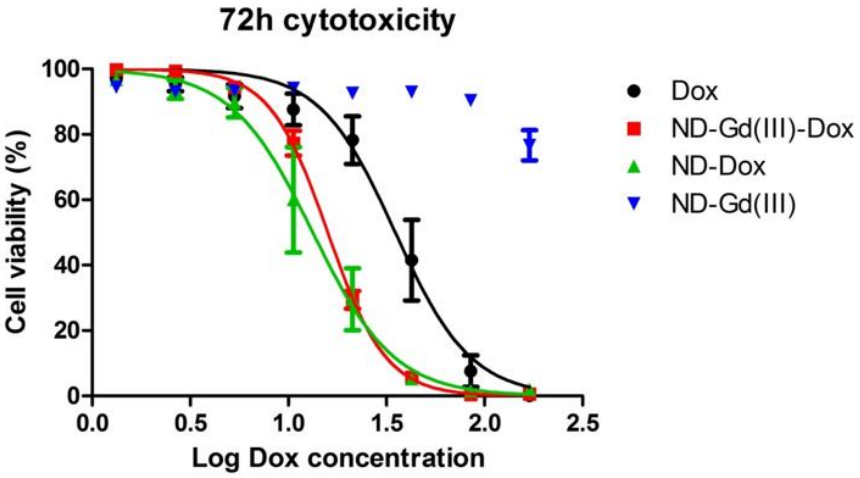

EC50:

Dox – 35.1 μM

ND-Dox – 13.3 μM

ND-Gd(III)-Dox – 15.9 μM

$p < 0.0001$

Figure 3.9. MDA-MB-231 m-Cherry cells were treated with ND-G-D, ND-D, ND-G or Dox alone for 72 hours. ND-G-D is the most potent agent, where its EC50 is nearly 2.5-fold better than that of free Dox.

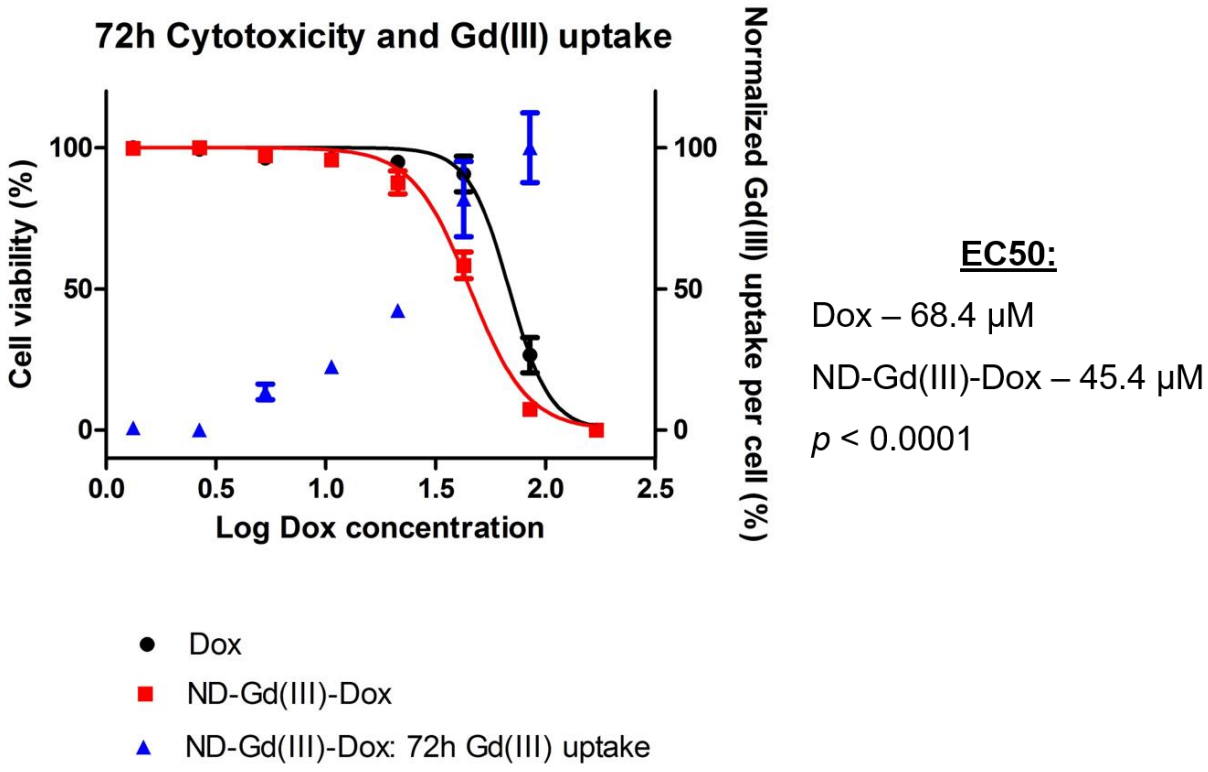

Figure 3.10. In vitro theranostics. Cellular Gd(III) was measured along with cellular viability across a wide dox-equivalent dose range of ND-G-D. Increasing cell death is associated with increasing Gd(III) in remaining live cells, demonstrating that therapeutic efficacy can be tracked by Gd(III) uptake.

3.2.3. Cellular Studies Using ND-G-H

ND-H and ND-G were mixed 1:1 to form ND-G-H, a targeted imaging agent. Since NDs spontaneously aggregate in solution, we generated ND-G-H as a mixture of NDs with heterogeneous expression of Gd(III) or HA on the surface (**Figure 3.11**). MDA-MB-231 cells were incubated with either ND-G or ND-G-H at the same concentration, and ND-G-H had 30% increased uptake over ND-G ($p < 0.001$) (**Figure 3.12**). This suggests that HA-mediated targeting to CD44 can further boost contrast enhancement. When increasing ND-H was added to the mixture in 2:1 and 5:1 ratios to ND-G, the targeting effect was diminished (**Figure 3.13**). This suggests that at higher ND-H mixing concentrations, CD44 receptors become saturated, limiting efficiency of molecular targeting.

3.2.4. Preliminary In Vivo studies

ND-G-D was selected for preliminary studies of in vivo theranostics. The efficacy of ND-Dox in vivo was established by Chow *et al*.[28] and therefore the focus of this preliminary study was establishing the imaging efficacy of ND-G-D. The setup for the study is shown in **Figure 3.14**. Mice were inoculated with right flank xenografts of MDA-MB-231 m-Cherry cells. MR imaging was performed in a Bruker PharmaScan 7 T magnet. 6 mice were imaged at baseline (pre-injection) and then after intraperitoneal injection of ND-G-D (5 mg/mL, [Gd(III)] of 8 mM, and [Dox] of 0.22 mM) at 15 minutes and 24h post-injection. 3 mice were eliminated from the study due to incorrect injection into the subcutaneous fascia as opposed to peritoneal cavity. Images from Mouse 1, Mouse 2 and Mouse 3 are shown in **Figure 3.15**, **Figure 3.16**, and **Figure 3.17** respectively.

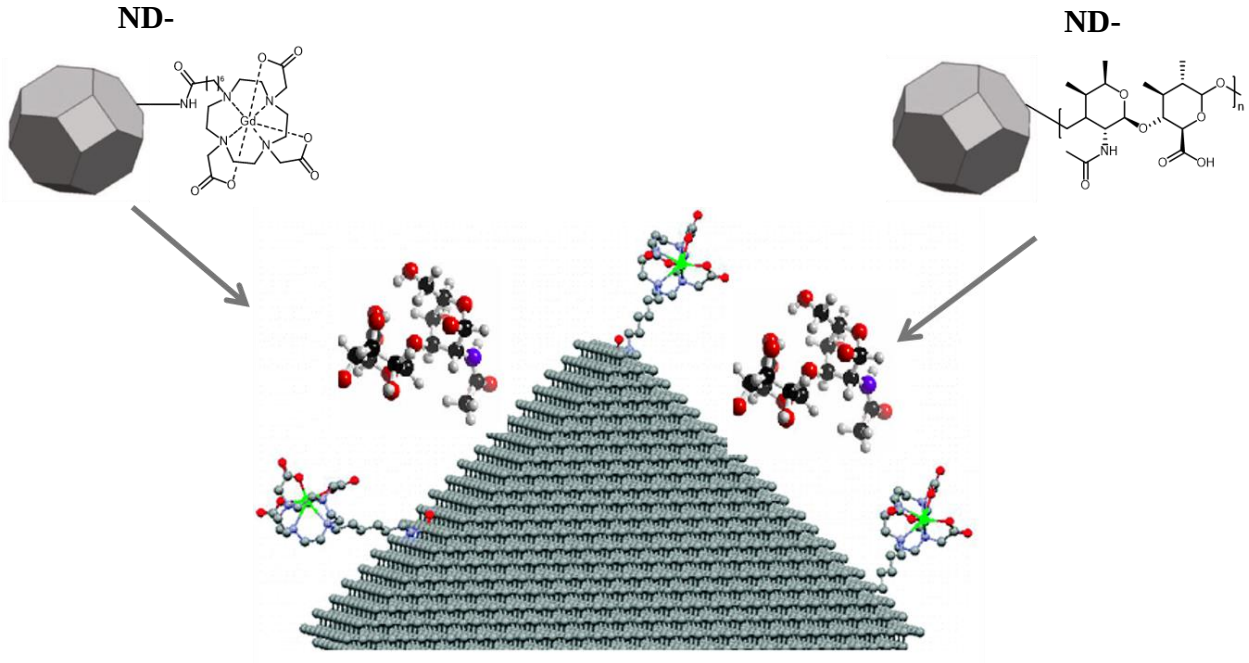

Figure 3.11. Heterogeneous mixture of ND-G and ND-H yield ND-G-H.

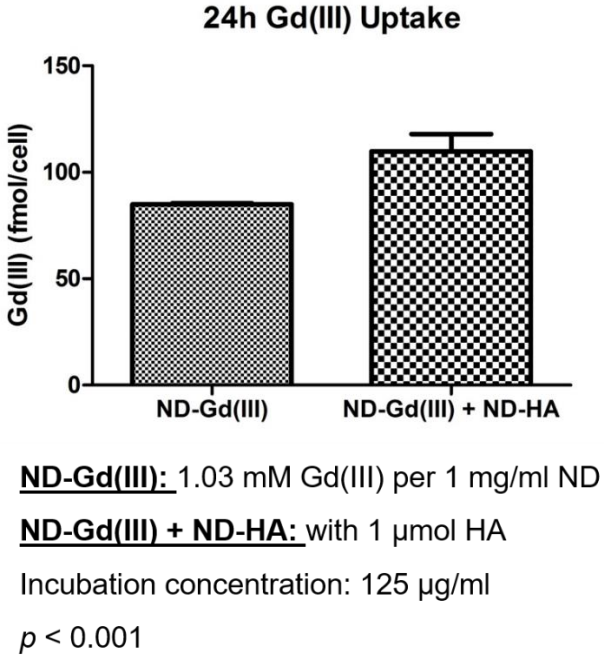

Figure 3.12. 24h Gd(III) uptake after incubation with ND-G or ND-G-H. ND-G-H affords 30% greater uptake showing promise for CD44 targeting.

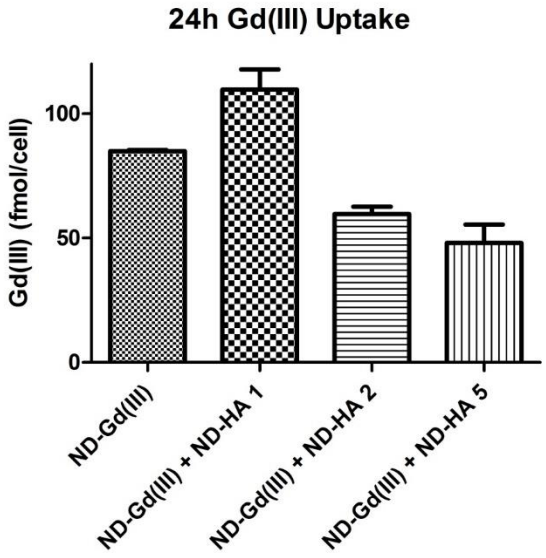

Figure 3.13. 24h Gd(III) uptake after incubation with ND-G or ND-G-H, with ND-G-H in 1:1, 2:1 and 5:1 compared to ND-G. ND-G-H only affords greater uptake when mixed 1:1, and decreased uptake compared to ND-G at higher ratios. This suggests saturation of CD44 receptors.

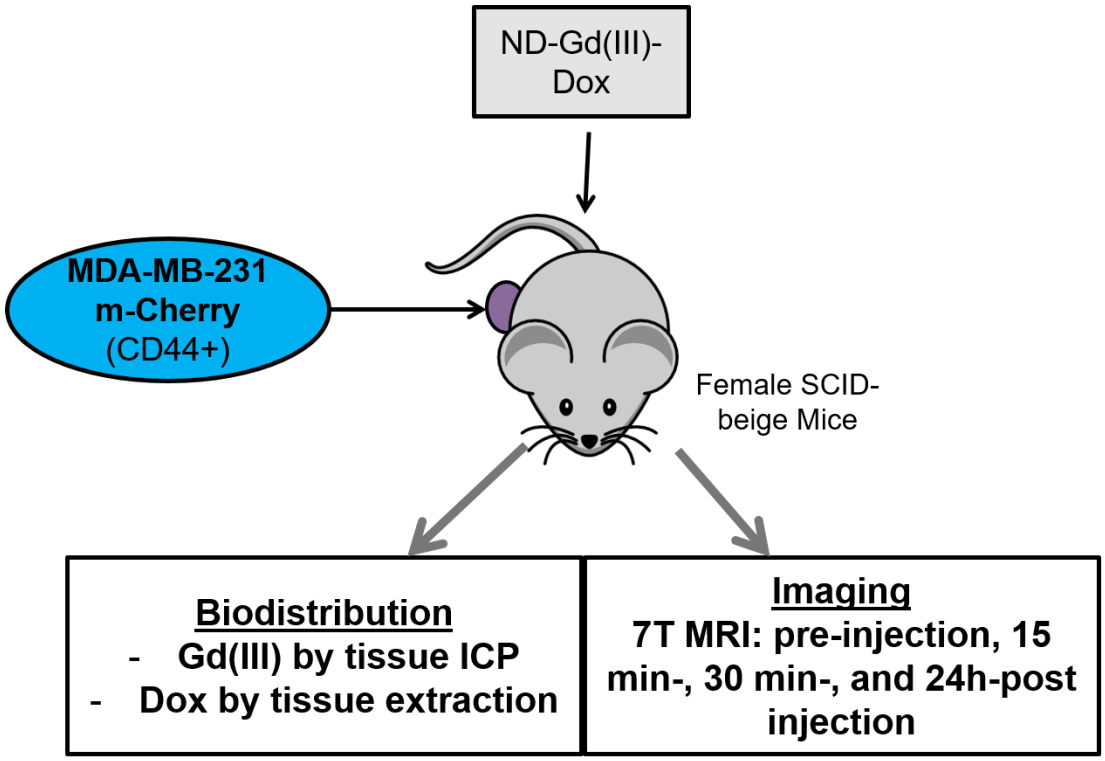

Figure 3.14. Preliminary in vivo study setup using ND-G-D. Mice were injected IP with ND-G-D and imaged by MR pre-injection, 15 min, 30 min and 24h post injection. After 24h, mice were euthanized and organs were collected for biodistribution of Gd(III) and Dox.

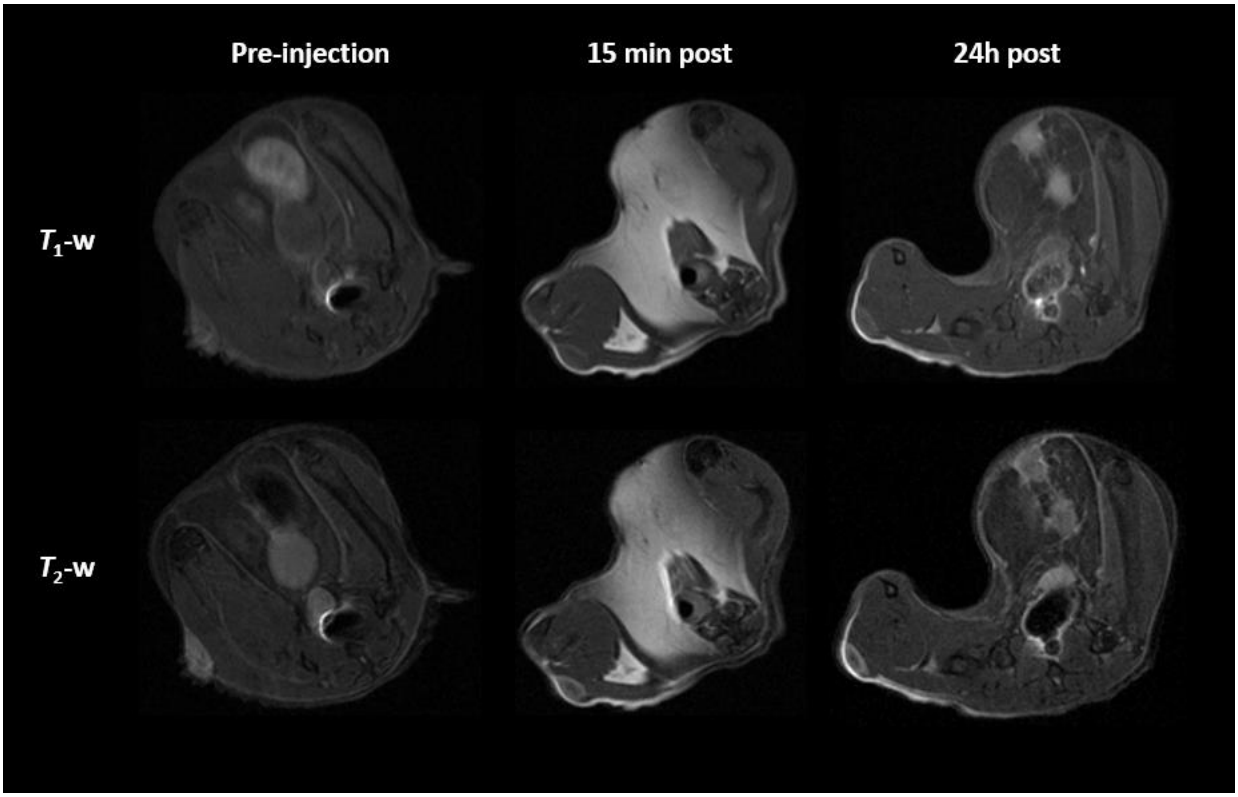

Figure 3.15. T_1- and T_2-weighted images pre-, 15 min post-, and 24h post-injection of Mouse 1

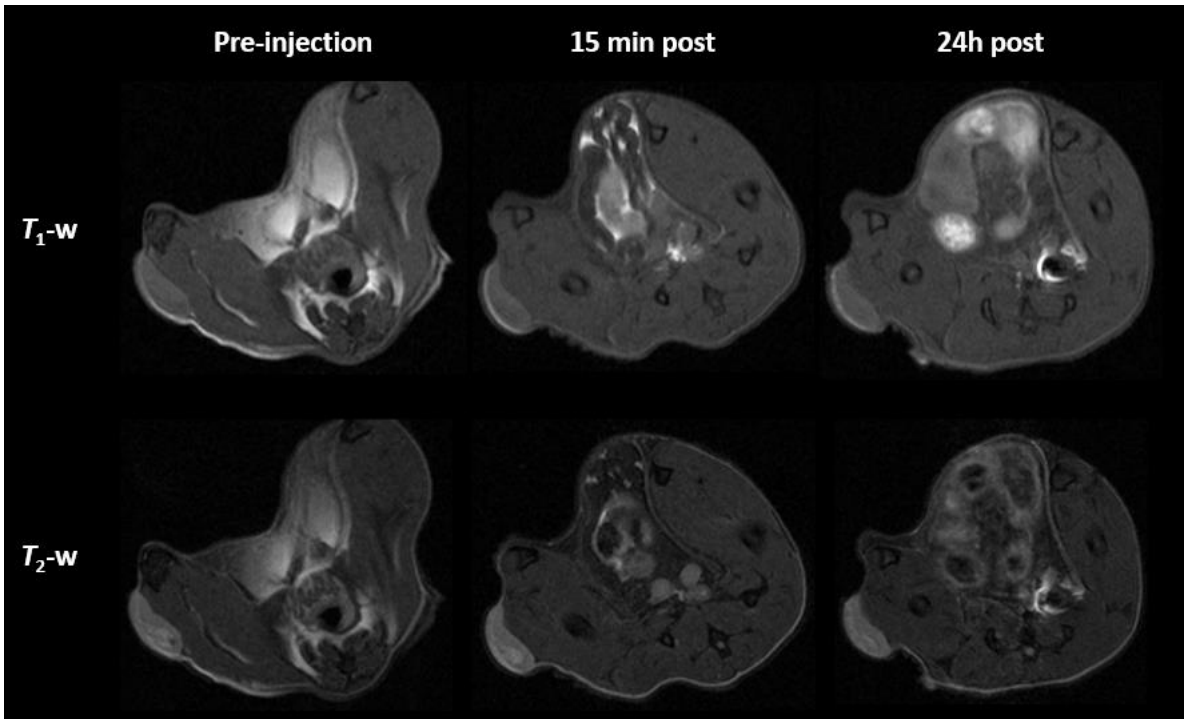

Figure 3.16. T_1- and T_2-weighted images pre-, 15 min post-, and 24h post-injection of Mouse 2

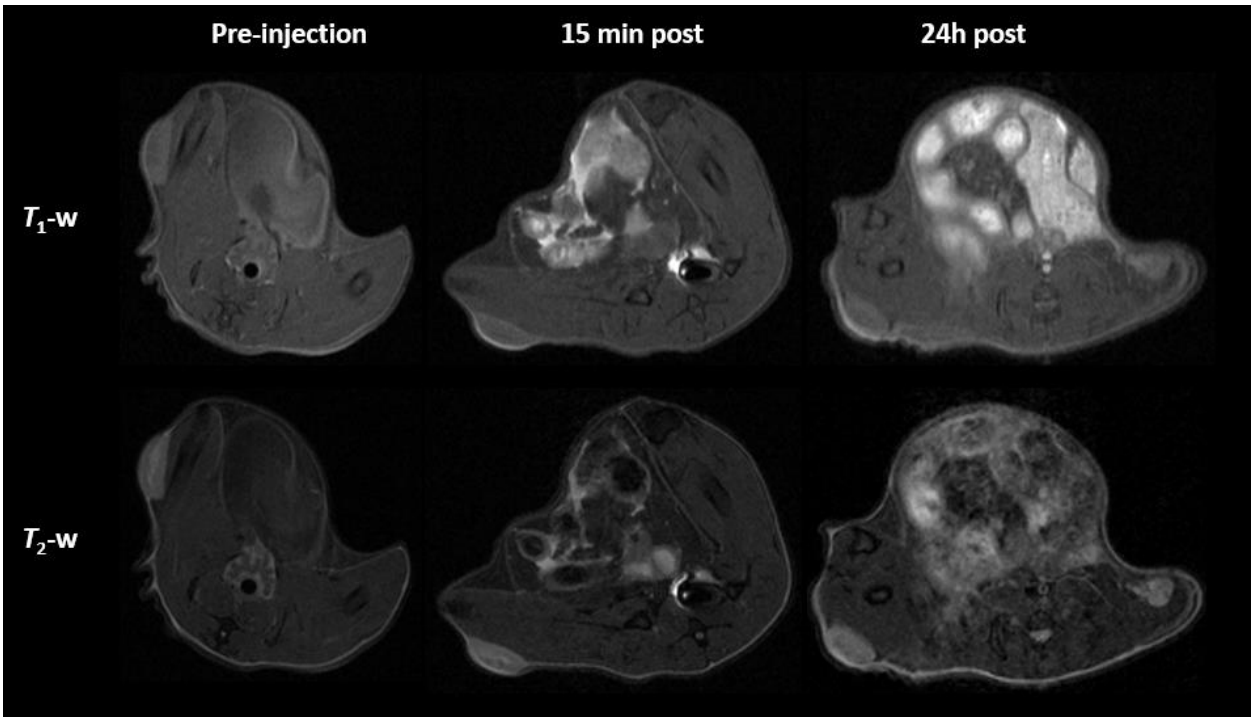

Figure 3.17. T_1- and T_2-weighted images pre-, 15 min post-, and 24h post-injection of Mouse 3

Based on **Figure 3.15**, **Figure 3.16**, and **Figure 3.17**, no contrast enhancement is observed after IP administration of ND-G-D. There are several reasons for this. Firstly, it is possible that ND-G-D did not distribute adequately to the tumor by the EPR effect as expected. Based on contrast enhancement observed in the gastrointestinal tract, it is likely that most of the agent pooled in that region and did not accumulate in the tumor. Biodistribution studies to assess organ accumulation of Gd(III) and Dox are currently underway.

3.3. Conclusions

We have developed theranostic ND-Gd(III)-Dox (ND-G-D) conjugates capable for therapeutic efficacy and cellular imaging. ND-G-D demonstrated excellent cell uptake by Gd(III) and cytotoxicity of MDA-MB-231 m-Cherry via Dox. These promising *in vitro* results unfortunately did not translate into observable contrast of tumor xenografts *in vivo*.

One concern is that optimal concentrations of Gd(III) chelates and Dox for *in vitro* studies did not translate for *in vivo* experiments. That is, a majority of the injection concentration of Gd(III) and Dox may have cleared by GI or renal routes limiting tumor accumulation. Biodistribution studies, looking at organ accumulation of Gd(III) and Dox, will reveal whether this was the case. Depending on the results, it may be necessary to re-tune the synthesis in terms of Gd(III) and Dox loading to ensure optimal imaging and tumor targeting.

Another possibility for the lack of observable contrast is the xenograft model itself. One limitation of orthotopic xenografts of cell lines passaged *in vitro* is that they fail to recapitulate the full extent of tumor development seen in the human breast. While these tumor models are an important first step to understand biodistribution, metabolism and clearance, they may be inconclusive for determining bioagent efficacy *in vivo*, largely because they are poorly

vascularized limiting agent access to the tumor. Patient-derived tumor xenografts (PDX) may be a better alternative. The Developmental Therapeutics Core at Northwestern University has developed several PDX models, including TNBC. These PDX more accurately represent the global gene-expression patterns, mutational status, metastatic potential, drug responsiveness and tumor architecture of endogenous tumors.[42-49]

In summary, ND-G-D is a valuable theranostic construct to combine T_1-weighted molecular MRI and targeted chemotherapy. Furthermore, this ND platform is highly versatile. A different chemotherapeutic (e.g., taxols), imaging agent (e.g., near IR fluorophore), or targeting molecule (e.g., antibody), could be conjugated to produce NDs that can be used to image or treat any number of different disease states.

3.4. Materials and Methods

3.4.1. Nanodiamonds (NDs), Aminated nanodiamonds (NDA) and Nanodiamond-Gadolinium(III) aggregates (NDG): Nanodiamond (ND) powders were acquired from the Nanocarbon Research Institute (Nagano, Japan). Amine modified NDs were produced according to the protocols from Kruger *et a*l[50], Zhang *et al*[23] and Chow *et al*[28]. Briefly, after reduction of the ND surface (2.5g) with BH3•THF (25mL, 1M) for 3 days, the ND surface (1g) was functionalized with (3-aminopropyl)trimethoxysilane (100mL, 5%), purified by centrifugation and dried by lyophlization. NDA powder was then re-suspended to a concentration of 10 mg/ml in 0.2% w/v acetic acid. 1 mL of this NDA suspension (10 mg of NDA) was dissolved in 0.5 mL of diisopropylethyl amine and 3.5 mL of DMSO, following by vigorous sonication. In a separate vessel, 0.5, 5 or 50 mg of Gd-C5-COOH was combined with five equivalents of NHS and EDC in 5 mL of 3:1 DMSO:Millipore water and vigorously sonicated. NDA and Gd-C5-COOH mixtures

were combined in a 15 mL Falcon tube and shaken overnight at room temperature. The mixture was purified first by 3 rounds of centrifugation with milli-Q water at 10000 x g for 20 minutes. At the end of the third round, the pellet was resuspended in 1 mL of milli-Q water and transferred to a 1.5 mL eppendorf tube. This mixture is purified by a further 3 rounds of centrifugation at 21000 x g for 20 minutes. The final pellet is re-suspended in 1 mL of 0.2% w/v acetic acid resulting in the NDG aggregates at 10 mg/mL.

3.4.2. ND-Gd(III)-Dox (ND-G-D) synthesis: ND-Gd(III) (ND-G) was dispersed in 0.2% HAc, and diluted to 10 mg/ml. A solution (10 mg/ml) of aqueous Dox was prepared. The ND-G was mixed with Dox to produce an ND-G-D conjugate solution with ND-G:D mass ratios of either 5:1, 3:1, 1:1, 1:2, or 1:5, with net diamond concentration ranging from 5 mg/ml–1 mg/ml. The solution was adjusted with 3 mM NaOH to promote drug complexing, resulting in a pH of ~7.74 followed by vortex for 1 min.

3.4.3. General Cell Culture: DPBS, media, and dissociation reagents were purchased from Life Technologies (Carlsbad, CA). CorningBrand® cell culture consumables (flasks, plates, etc.) and sera were purchased from VWR Scientific (Radnor, PA). MDA-MB-231 m-Cherry (ATCC® HTB-26TM) cells were purchased from the American Type Culture Collection (ATCC, Manassas, VA) and cultured in phenol red-free minimum essential media-alpha (α-MEM) supplemented with 10% fetal bovine serum (FBS), 1% non-essential amino acids, 1% sodium pyruvate, and 1% 100mM L-glutamate. Cells were confirmed free of mycoplasma contamination by MycoAlert™ Mycoplasma Detection Kit (Lonza Group Ltd., Switzerland). Prior to all experiments, cells were plated and allowed to incubate for 24 hours before dosing. Cells were harvested with 0.25%

TrypLE for 5 minutes at 37 °C in a 5.0% CO2 incubator. Cells were grown in a humidified incubator operating at 37°C and 5.0% CO_2.

3.4.4. Guava ViaCount Assay for Cell Counting: Cell counting was conducted using a Guava EasyCyte Mini Personal Cell Analyzer (EMD Millipore, Billerica, MA). After cell harvesting, an aliquot (50 μL) of the cell suspensions was mixed with Guava ViaCount reagent (150 μL) and allowed to stain at room temperature for at least 5 minutes (dilution factor of 4 and cell density between 20-150 cells/μL). After gently vortexing for 10 seconds, stained cells were counted using a Guava EasyCyte Mini Personal Cell Analyzer (PCA) using the ViaCount software module. For each sample, 500-1000 events were acquired. Gating of live/dead and cell/debris classifications were performed manually by the operator. Instrument performance was validated biweekly using GuavaCheck Beads following the software module "Daily Check".

3.4.5. Cellular Viability Studies. Cellular viability studies were performed with MDA-MB-231 m-Cherry cells. MDA-MB-231 m-Cherry cells were plated at a cell density of approximately 25,000 per well for 24-hour uptake in a 24-well plate as counted by a hemocytometer. Stock solutions of ND-G-D were prepared by resuspending a pellet of known mass of ND-G-D in fresh media. Gd(III) concentration ranged from 5 – 1500 μM (0.005 – 1 mg/ml diamond concentration), and Dox concentration ranged from 1 – 200 μM. To harvest, cells were rinsed in-plate three times with 500 μL PBS and trypsinized using 100 μL 0.25% TrypLE. Following trypsin treatment, 150 μL of media was added to each well and mixed by a pipette to ensure that all cells were lifted into suspension. Washes and cells were collected together in the same tube. From the final cell suspension, 50 μL was used for cell counting and viability.

3.4.6. In vivo studies. All mice were handled and processed according to a protocol approved by Northwestern University Animal Care and Use Committee in accordance with current guidelines from the National Institutes of Health Model Procedure of Animal Care and Use. Six female, SCID-beige mice aged 6-8 weeks at initiation were used for the length of the study. Mice were imaged by MRI on a Bruker PharmaScan 7 T magnet (Bruker Biospin, Billerica, MA, U.S.A.). Six 75 cm^2 flasks containing approximately 5 x 10^6 MDA-MB-231 m-Cherry cells were washed repeatedly, re-suspended in sterile phosphate buffered saline to a volume of 0.1 mL, and injected into the right rear flank of the mice (n = 6). Mice were imaged at baseline after two weeks of tumor growth. On Day 14, all mice were administered ND-G-D (5 mg/mL, [Gd(III)] of 8 mM, and [Dox] of 0.22 mM) by intraperitoneal injection. 3 mice underwent failed injection into the subcutaneous fat and were eliminated from the analysis. The remaining mice were imaged at 15-min, 30-min, and 24h post-injection using both T_1- and T_2-weighted sequences. During imaging, mice were held under 1−2% inhaled isoflurane anesthesia and respiration was monitored using an SA Instruments MR compatible monitoring system (SA Instruments, Stonybrook, NY, U.S.A.).

T_1-weighted images were acquired using a rapid acquisition rapid echo (T_1-RARE) sequence with imaging parameters as follows: RARE factor = 4, repetition time (TR)/echo time (TE) = 750 ms/6.2 ms, field of view (FOV) = 30 x 30 mm^2, matrix size (MTX) = 200 x 200, number of axial slices (NS) = 3, slice thickness (SI) = 0.7 mm, and averages (NEX) = 1. T_2-weighted images were acquired using an accelerated TurboRARE sequence with imaging parameters as follows: RARE factor = 4, TR/TE = 800 ms/17 ms, NEX=4, and identical geometry to the T_1-RARE sequence. T_1 relaxation times were measured using a RARE T_1-map pulse sequence (RARE-VTR), with static echo time (6.5 ms) and variable repetition time (100, 200, 400,

800, 1500, 3000, and 6500 ms). Imaging parameters were as follows: RARE factor = 2, FOV = 30 × 30 mm^2, MTX = 128 × 128, NS = 3, slice SI = 0.7 mm, and NEX = 1 (total scan time = 11 min).

T_1 analysis was carried out using JIM 6.0 (Xinapse Systems, Essex, UK) with monoexponential curve-fitting of image intensities. JIM 6.0 was also used to draw ROIs in each tumor and surrounding muscle in the T_1-weighted image obtained at Day 26 of each mouse. T_1-maps obtained in each ROI were overlaid on a T_2-weighted anatomical reference image from the same time point.

Chapter 4:

Gd(III)-Gold Nanoconjugates for Cell Labeling and High Field MR Imaging of the Pancreas

Rammohan, N.[¥] ; Holbrook, R.[¥]; Rotz, M.; MacRenaris, K.; Preslar, A.T.; Carney, C.; Reichova, V.; Meade, T.J. Gd(III)-Gold Nanoconjugates Provide Remarkable Cell Labeling for High Field MR Imaging. *Bioconjugate Chemistry.* **2016.** *In Press.* DOI: 10.1021/acs.bioconjchem.6b00389. (¥=equal contribution).

Holbrook, R. J.; **Rammohan, N.**; Rotz, M. W.; MacRenaris, K. W.; Preslar, A. T.; Meade, T. J. Gd(III)-Dithiolane Gold Nanoparticles for T1-Weighted Magnetic Resonance Imaging of the Pancreas. *Nano Letters.* **2016**, *16*, 3202-3209. PMCID in process.

4.1. Introduction

In vivo cell tracking is a burgeoning field of research because it is considered the crucial technology for the advancement of cell-based therapy.[1-4] Cell therapy has implications for a variety of diseases and disorders such as cancer[5-7], cardiovascular disease[8,9], neurodegenerative diseases[10,11], and musculoskeletal[12] disorders by providing unique opportunities for tissue regeneration, targeted therapy and drug delivery. In the context of cancer, cell tracking technology would elucidate the behavior of cancer cells at the molecular level, and further understanding of their metastatic potential. However, the outcomes of cell therapy have been variable as the fate of transplanted cells remains indeterminate.

Magnetic resonance (MR) imaging is ideally suited for non-invasive clinical diagnosis, molecular imaging and cell tracking.[2,13-17] MR imaging can visualize live specimen, and benefits from high spatiotemporal resolution and excellent soft-tissue contrast while avoiding radiolabels or ionizing radiation. However, MR imaging suffers from lower sensitivity compared to competing modalities such as fluorescence, bioluminescence, positron emission tomography, or single-photon emission computed tomography, all of which have little or no background. Paramagnetic or superparamagnetic contrast agents are used to enhance the sensitivity of MR imaging. Paramagnetic gadolinium(III) [Gd(III)]–based agents are the most frequently used MR contrast agents.[1,18,19] These agents are typically chelated Gd(III) which reduce the longitudinal relaxation time of nearby water protons, aided by the high magnetic moment and symmetrical *S* state of the Gd(III) ion.[1,18,20,21] Regions which incorporate Gd(III) appear brighter on a T_1-weighted image.

Most clinical and pre-clinical magnets now operate at higher field strengths (3T or higher) in order to increase resolution, signal-to-noise ratio, and contrast-to-noise ratio. However, the

benefits of high-field MRI must outweigh the resulting susceptibility artifacts and altered relaxation kinetics. These factors must be taken into account when designing a new contrast agent for high-field performance. Additionally, clinical Gd(III)-based MRI contrast agents are not effectively internalized by cells.[22,23]

To address these issues, Gd(III) chelates have been conjugated to nanoparticles, including gold nanoparticles, for improved relaxivity along with increased agent permeability and retention within cellular compartments.[18,20,21,24] Our group previously devised cell permeable, Gd(III)-enriched DNA–gold nanoparticle conjugates (DNA-Gd(III)@AuNPs) for cellular T_1-weighted MR imaging.[21] These constructs demonstrated high stability, cellular uptake, and surface loading of Gd(III). DNA-Gd(III)@AuNPs were used to successfully track the implantation of neural stem cells into rat brain regions affected by stroke.[4] However, apart from being a carrier for the Gd(III) chelates and optical dyes, it is likely that the presence of DNA limits the amount of Gd(III) that can be loaded onto the AuNP surface.

Herein, we report the synthesis of a series of DNA-free Gd(III)-Au nanoconjugates (Gd@AuNPs) for cancer cell labeling. Four different Gd(III)-based chelates were modified with lipoic acid generating a terminal dithiolane, which was in turn coupled to thiols on the AuNP surface (**Figure 4.1**).

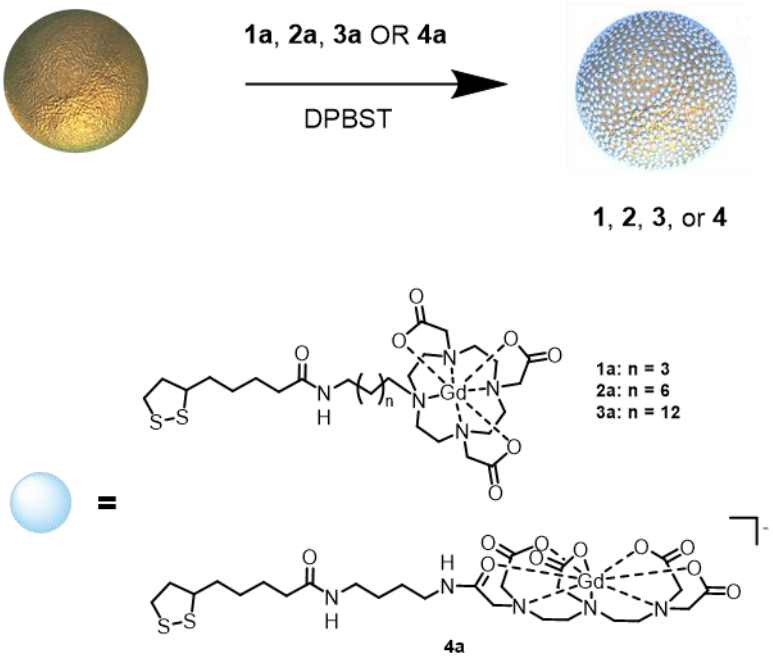

Figure 4.1. Synthetic scheme for facile, DNA-free, Gd@AuNPs with varying linker lengths conjugating Gd(III) chelates to the AuNP surface. Gd-Au surface conjugation is accomplished in the absence of reducing agents. By modifying the linkers lengths and coordination chemistry of the Gd(III) chelates, we demonstrate that surface loading and cellular delivery of Gd(III) can be optimized for highly efficient labeling of cancer cells.

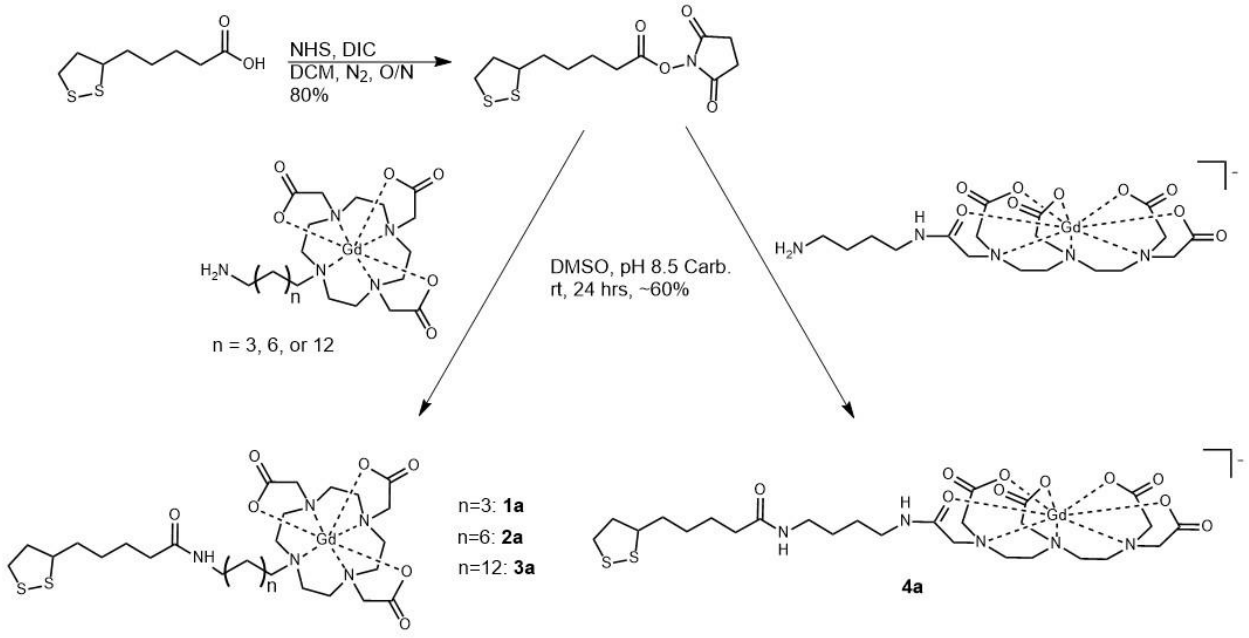

Figure 4.2. Synthetic scheme for lipoic acid-modified Gd(III) chelates.

4.2. Results and Discussion

4.2.1. Synthesis and Characterization of Gadolinium-Gold Nanoconjugates:

Synthesis of Gd@AuNP constructs: The overall synthetic scheme for the Gd@AuNPs is presented in **Figure 4.1** and **Figure 4.2**. To investigate the role of surface chemistry on our AuNP system and optimize cellular delivery of Gd(III), we studied four different Gd(III) chelates coupled to AuNPs.

Three amine-functionalized Gd(III)-tetraazacyclododecanetriacetic acid (DO3A) complexes of varying linker lengths (3-, 6- and 12-carbons), and an amine-functionalized Gd(III)-diethylene triaminepentaacetic acid (DTPA) with a four-carbon linker were synthesized according to previously reported protocols.[25,26] The DTPA complex is negatively charged, while the DO3A complexes are neutral. The four different chelates were peptide-coupled to lipoic acid-NHS ester in 1:1 DMSO: pH 8.5 carbonate buffer, and purified by reverse-phase high performance liquid chromatography (HPLC) with yield ranging from 60% generating **1a-4a** respectively (**Figure 4.2**).

The synthesis of citrate-stabilized AuNPs was carried out by literature procedures.[25] The diameter of the AuNPs was 18.0 ± 2.1 nm as determined by analysis of transmission electron microscopy (TEM) images. The hydrodynamic radius of the AuNPs suspended in water was 26.1 ± 0.2 nm with a polydispersity index of 0.08 ± 0.01 as determined by dynamic light scattering (DLS). Four, separate 10 nM AuNP suspensions in in Dubecco's Phosphate Buffered Saline (DPBST) in 0.01% Tween20 were aliquoted. To each of these AuNP suspensions was added either **1a**, **2a**, **3a**, or **4a**, dissolved in 1:1 MeOH:water. The AuNP mixtures were agitated overnight at ambient temperature. The crude mixtures were purified by four rounds of ultra-centrifugation, and the final particles were suspended in DPBST as 1 mL stocks at a gold concentration of 250 nM

yielding four, distinct, DNA-free Gd(III)@AuNP complexes **1-4** (**Figure 4.1**). It is notable that the coupling occurs without the aid of any reducing agents.

Characterization of Gd@AuNP constructs: Inductively-coupled plasma mass spectrometry (ICP-MS) was used to measure Gd(III) and Au content of complexes **1-4** (**Table 4.2**). Taking into account the Gd(III) and gold ratios from ICP-MS, the average diameter of AuNPs and the spherical packing of gold atoms, the loading of Gd(III) per AuNP was calculated. Similarly, the coverage density of Gd(III) was determined by assuming a spherical surface area of AuNPs. Hydrodynamic size and polydispersity of AuNPs in solution were measured using DLS, and are not significantly different between complexes **1-4**. It is evident that complex **3** has the greatest surface loading and coverage of Gd(III), following by complexes **1-2** (which have comparable levels) and lastly by complex **4** which has lowest surface loading of Gd(III).

This trend suggests the 12-carbon alkyl chain in complex **3a** confers greater packing efficiency on the AuNP surface, while the negative charge of **4a** may prevent the same level of surface coverage. It is likely complexes **1a-2a** have linker lengths that are suboptimal compared to complex **2** but their neutral surface charge confers better packing on AuNP than complex **4**. Overall, these results suggest that DO3A-based Gd(III) chelates are able to pack more efficiently on the AuNP surface compared to DTPA-based Gd(III) chelates, most likely due to charge on DTPA ligand and steric differences between the two chelates. Specifically, **1a-3a** are neutral while **4a** bears a negative charge, and the latter would be unable to pack as efficiently due to electrostatic repulsion. Notably, each of **1-4** demonstrate greater Gd(III) loading than previously reported DNA-Gd(III)@AuNPs, suggesting that polyvalent DNA bearing smaller Gd(III) chelates do not pack as efficiently.[21]

	Loading (Gd/AuNP)	***Surface Coverage (Gd/nm^2)***	***Hydrodynamic radius (nm)***	***Polydispersity Index***
1	1979 ± 370	1.94 ± 0.36	27.2 ± 1.4	0.16 ± 0.01
2	1715 ± 75	1.69 ± 0.07	28.7 ± 1.5	0.08 ± 0.01
3	2308 ± 291	2.27 ± 0.29	30.7 ± 2.6	0.13 ± 0.01
4	1114 ± 116	1.09 ± 0.11	27.8 ± 1.2	0.13 ± 0.01

Table 4.1. Characterization of AuNP constructs, specifically Gd(III) loading, surface coverage, hydrodynamic size, and polydispersity index. Complex **4** has significantly decreased loading and surface coverage of Gd(III) compared to complexes **1-3** ($p < 0.05$ for two-tailed t-test). The hydrodynamic radii and polydispersity indices are not significantly different between complexes **1-4**.

We investigated the ability of **1-4** to decrease the T_1 relaxation time, referred to as longitudinal relaxivity (r_1). r_1 is the slope of the linear plot of $1/T_1$ versus Gd(III) ion concentration (**Table 4.2**). Measurements were made at 1.4 T and 7 T. The ionic relaxivity r_1 of **1-4** at 1.4 T is comparable to the value reported for DNA-Gd@AuNPs.[21] The ionic r_1 values of **1-4** at 1.4 T are higher than small-molecule clinically used Gd(III) chelates, whose r_1 values range between 3.3 – 4.0 $mM^{-1}s^{-1}$.[27] This can be explained by an increase in the rotational correlation time, τ_r, mediated by conjugation to the AuNP surface. A longer τ_r corresponds to a slower tumbling rate that ultimately elongates the longitudinal relaxation of the Gd(III) ion. At 7 T, we observe a drop in ionic relaxivity for all complexes, which is expected of Gd(III)-based contrast agent behavior at higher field strengths.[28]

The particle relaxivity is computed by multiplying the number of Gd(III) ions per particle and the ionic relaxivity. This is a useful parameter to compare the efficiencies of AuNPs with different surface chemistries as realized in complexes **1-4**. For example, while the ionic relaxivity for complex **3** is lower than that for complex **2**, the particle relaxivity is greater since complex **3** confers greater packing density of Gd(III) ions.

Notably, complex **1** posed a challenge for further characterization as it demonstrated low colloidal stability in DPBST, suggestive of shorter linker lengths of the Gd(III) chelates conferring less salt stability than complexes **2** and **3**. As such, complex **1** was omitted from further analysis and not utilized for subsequent cellular studies.

	$r_{1,ionic}$ ($mM^{-1}s^{-1}$) @ 1.4 T	$r_{1,particle}$ ($mM^{-1}s^{-1}$) @ 1.4 T	$r_{1,ionic}$ ($mM^{-1}s^{-1}$) @ 7 T	$r_{1,particle}$ ($mM^{-1}s^{-1}$) @ 7 T
1*	15.6 ± 1.0	30872 ± 1979	3.4 ± 0.1	6728 ± 198
2	14.6 ± 0.7	25039 ± 1201	4.0 ± 0.1	6860 ± 172
3	12.9 ± 0.7	29773 ± 1616	3.5 ± 0.2	8078 ± 462
4	13.7 ± 0.8	15262 ± 891	4.7 ± 0.2	5236 ± 223

Table 4.2. Longitudinal relaxivity (r_1) of AuNP constructs, measured at 1.4 T and 7 T. The relaxivities of complexes **1-4** are not significantly different for measurements at both field strengths. *Complex **1** was not stable in DPBST so relaxivity of Complex **1** was measured in 25% DPBST in water.

4.2.2. Cancer Cell Labeling Using Gd(III)@AuNP constructs:

A majority of clinically utilized Gd(III)-based contrast agents do not accumulate in cells.[22,23] As a first step in evaluating the efficacy of cell-permeable contrast agents, it is vital to determine their cellular uptake and general biocompatibility *in vitro*. MDA-MB-231 m-Cherry human triple-negative breast cancer (TNBC) cells were treated with various Gd(III)-equivalent concentrations of complexes **2, 3** or **4** and incubated for 24 hours at 37 °C. The treated cells were harvested and counted through a flow cytometric live/dead assay. Cell viability and counts indicated that Gd@AuNPs were well-tolerated across a wide dose range (**Figure 4.3**). The cellular Gd(III) concentration per cell was quantified through ICP-MS (**Figure 4.4*A***). Significant differences in the cell uptake of Gd(III) were observed. Complexes **2** demonstrated the greatest overall uptake of Gd(III), and achieved approximately four times greater Gd(III) uptake over complex **3** and 20-fold greater than complex **4**. Cells incubated with the unbound chelates **2a**, **3a** and **4a** resulted in negligible Gd(III) uptake per cell ().

These results suggest that while **3a** conferred the greatest packing density of Gd(III) on the AuNP surface, the longer alkyl linker prevented cellular internalization to the same extent as complex **2**. For complex **4,** it appears that the negative surface charge in addition to the relatively poor surface loading confers the least favorable conditions for cellular penetration in this particular cell line. Notably, for the same dosing concentration, all formulations of Gd@AuNP are superior in terms of cellular Gd(III) delivery compared to the previously synthesized DNA-Gd(III)@AuNP.[21] In addition, time-dependent uptake for the cellular delivery of Gd@AuNPs was performed with MDA-MB-231 m-Cherry cells (**Figure 4.4*B***). Cells were incubated with 50 μM Gd(III)-equivalent concentration of either complex **2**, **3** or **4** for 1, 2, 4, 8, and 24 hours at 37 °C.

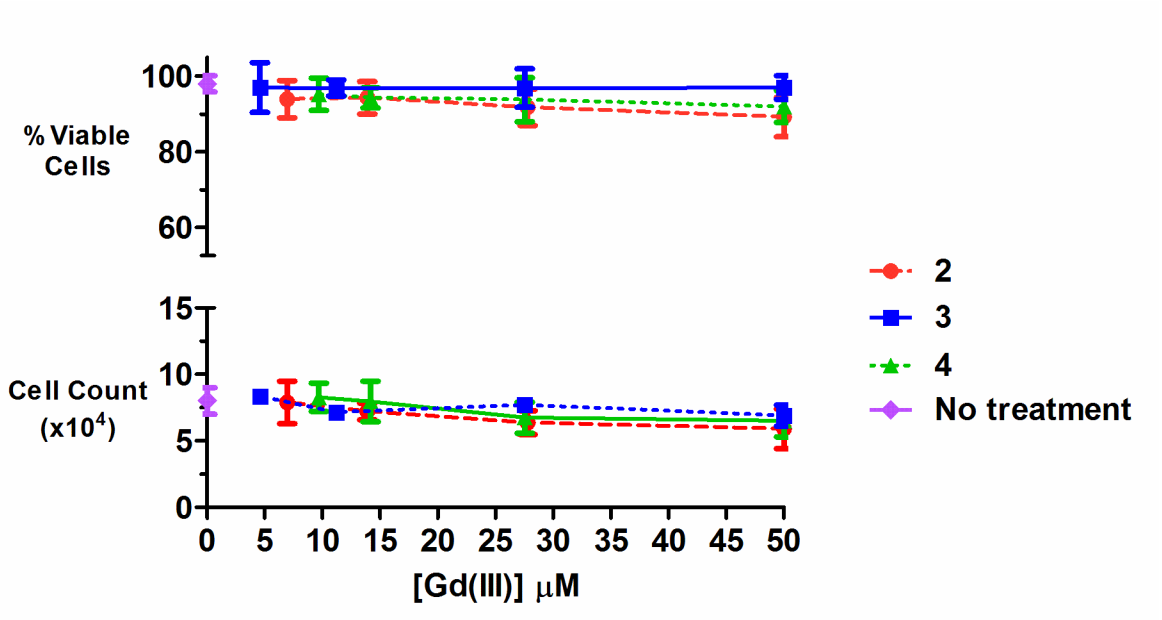

Figure 4.3. Viability and counts of MDA-MB-231 m-Cherry cells after no treatment or 24 hour incubation with various Gd(III)-equivalent concentrations of complexes **2, 3,** or **4**.

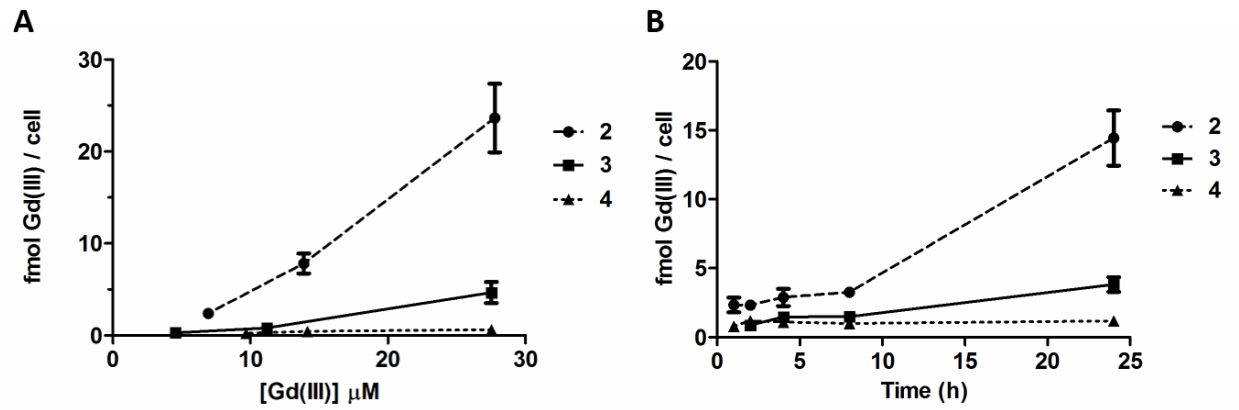

Figure 4.4. (A) MDA-MB-231 m-Cherry cell uptake of Gd(III) after incubation with either complex **2**, **3** or **4**. Complex 2 demonstrates the best overall uptake, and approximately 4-fold greater than complex 2 and 20-fold greater than complex 4. **(B)** Time course of MDA-MB-231 m-Cherry cell uptake over a 24 hour period after 50 μM incubation with either complex **2**, **3** or **4**. Complexes **2** and **3** demonstrate a significant increase in uptake between 8-24 hours post-incubation, while complex **4** achieves maximal uptake within 2 hours.

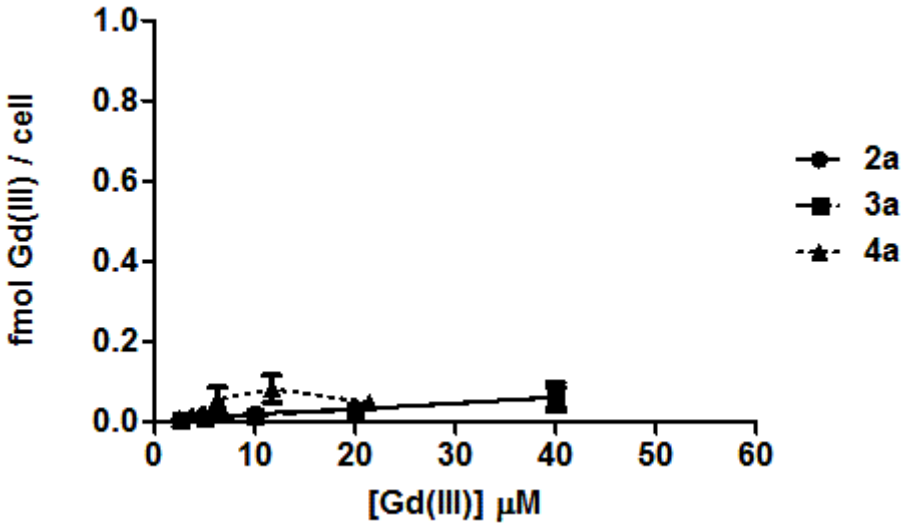

Figure 4.5. MDA-MB-231 m-Cherry cell uptake of Gd(III) after 24h incubation with **2a**, **3a** or **4a**. The free chelates do not significantly accumulate in cells.

After each time point, cells were harvested, counted and the Gd(III) content was quantified. The similar trend of cell uptake of Gd(III) between complexes **2**, **3** and **4** was observed. However, the uptake of complex **4** did not appear to be time-dependent. Maximum cell uptake of complex **4** was achieved within one hour. This suggests that complex **4** behaves similar to clinical Gd(III) chelates where extracellular and intracellular Gd(III) concentrations equilibrate quickly resulting in insignificant cellular uptake of Gd(III). Conversely, the cell uptake of complex **2** and **3** was time dependent. Significant increase in cell uptake of **2** and **3** was observed between 8 and 24 h incubation, suggesting uptake occurs concurrently with cell division. This pattern of time-dependent uptake corroborates that surface charge and linker length significantly contribute to degree of particle internalization by MDA-MB-231 m-Cherry cells.

To visualize AuNP uptake, MDA-MB-231 m-Cherry cells were incubated with 50 μM Gd(III)-equivalent concentration of complexes **2**, **3** or **4** for 24 hours and subsequently harvested for TEM. The intrinsic contrast afforded by the gold core of Gd@AuNPs enables the visualization of all three complexes in the intracellular space. In particular, complex **2** appeared in more abundance relative to complexes **3** and **4**, and appear to undergo phagocytosis in large aggregate form (**Figure 4.6*A, D***). Furthermore, the phagosomes appear to merge together and sequester the AuNPs in a single, large vesicle (**Figure 4.6*A, D***). In similar fashion, this behavior is observed for complexes **3** and **4** (**Figure 4.6*B, C, E, F***). This further corroborates the differences in cell uptake between complex **2** compared to complexes **3** and **4**. In general, these studies reveal that complexes **2-4** undergo a form of endocytosis (or phagocytosis) and accumulate inside the cell for Gd(III) cell labeling.

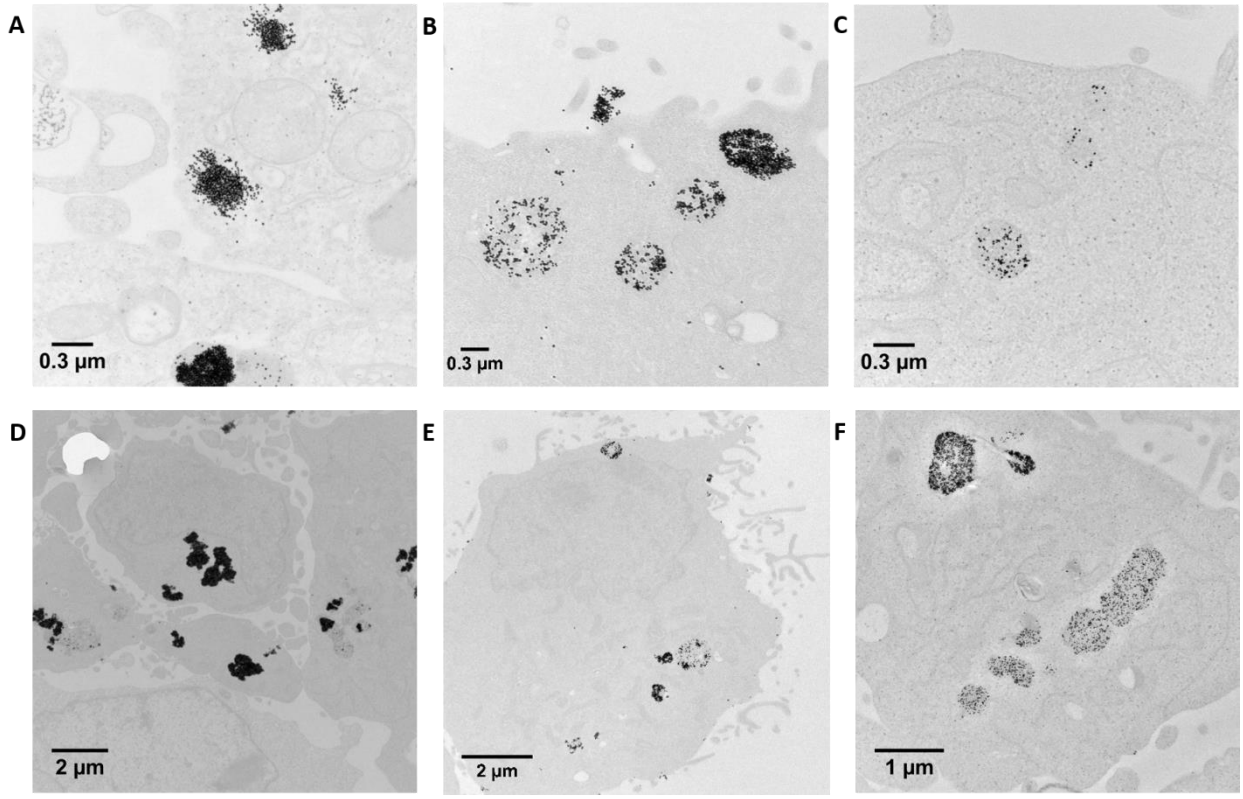

Figure 4.6. TEM images of MDA-MB-231 m-Cherry cells following 24 h incubation with complex **2** (A, D), complex **3** (B, E), or complex **4** (C, F). Complex **2** is present in large (0.5 µm) lysosomes as particle aggregates (A, D). Complexes **3** and **4** are more sparsely distributed within the cell (B, C, E and F).

4.2.3. MRI of MDA-MB-231 m-Cherry cell pellets labeled with Gd@AuNPs:

We investigated the ability of the various Gd@AuNPs to produce contrast enhancement via MRI. MDA-MB-231 m-Cherry cells were labeled with complexes **2**, **3**, or **4** for 24 hours, after which the cells were harvested and concentrated to a pellet. MR images of the cell pellets were acquired at 7 T. The cells were incubated with either complex **2**, **3**, or **4** at a normalized Gd(III) concentration of approximately 15 μM (***Figure 4.7***).

As observed in the ***Figure 4.7***, cells incubated with complex **2** demonstrated the shortest T_1 relaxation time and greatest positive (bright) contrast, and this was significantly shorter and brighter than demonstrated by cells incubated with complexes **3** and **4** ($p < 0.05$ for one-way ANOVA). Finally, for a relatively low dose of complex **2,** there is marked contrast enhancement compared to unlabeled cells, and when compared to DNA-Gd(III)@AuNP.[21]

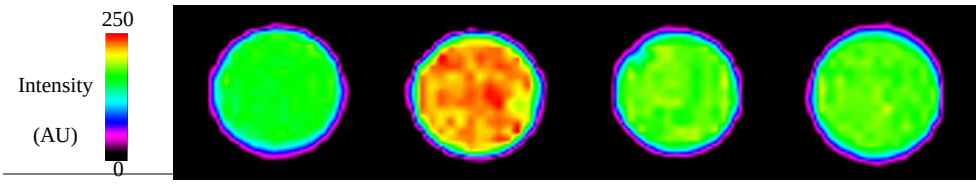

	Cells only	*Complex **2***	*Complex **3***	*Complex **4***
***T*₁ (ms)**	2126 ± 129	975 ± 73	1838 ± 105	1770 ± 103
Gd(III)/cell (fmoles)	0	2.060	0.246	0.333

Figure 4.7. MR images of MDA-MB-231 m-Cherry cell pellets treated with Gd@AuNPs acquired at 7 T. Cells labeled with Complex **2** demonstrate the greatest contrast enhancement and shortest T_1 relaxation time. Cells labeled with complexes **3** and **4** are indistinguishable from unlabeled cells.

4.2.4. Preliminary In Vivo Studies:

Complex **2**, the most promising agent from the cellular studies, was selected for preliminary *in vivo* MR imaging. Mice were IV injected with 4.0 nmol/kg body weight of complex **2** (approximately 9.0 μmol/kg body weight of Gd(III)). Immediately after injection, a series of fast FLASH MR images were acquired on Bruker Biospin 9.4T magnet to visually observe the distribution of the agent over 10 minutes (

Figure **4.8*A*-*B***). In the T_2 weighted image (

Figure **4.8*A***), the aorta and vena cava are dark and easily seen. The left kidney and stomach are easily identifiable.

Figure **4.8*B*** represents the subtraction of the post-contrast T_1 weighted image from the corresponding pre-contrast image, termed the Area-Under-Curve (AUC). The AUC image is displayed to demonstrate net contrast enhancement, and the T_2-weighted image is shown as an anatomical reference. In the AUC image, part of the interior of the kidney is starting to enhance. The AUC image suggests that Complex **2** is still in circulation during the FLASH image acquisition, as evidenced by the bright vessels. As expected, clearance is relatively slow. Therefore the AUC image does not show accumulation in the kidney or liver in the first 10 minutes. After 3 h, organs were harvested, and quantification of Gd(III) was performed using ICP-MS (n = 3) and reported as total μg of Gd(III) per gram of tissue (

Figure **4.8*C***). There is significant accumulation of complex **2** in clearance organs but negligible accumulation in other vital organs. These results indicate that complex **2** is well-tolerated by mice in the short-term and shows promise for future *in vivo* longitudinal imaging studies in mice.

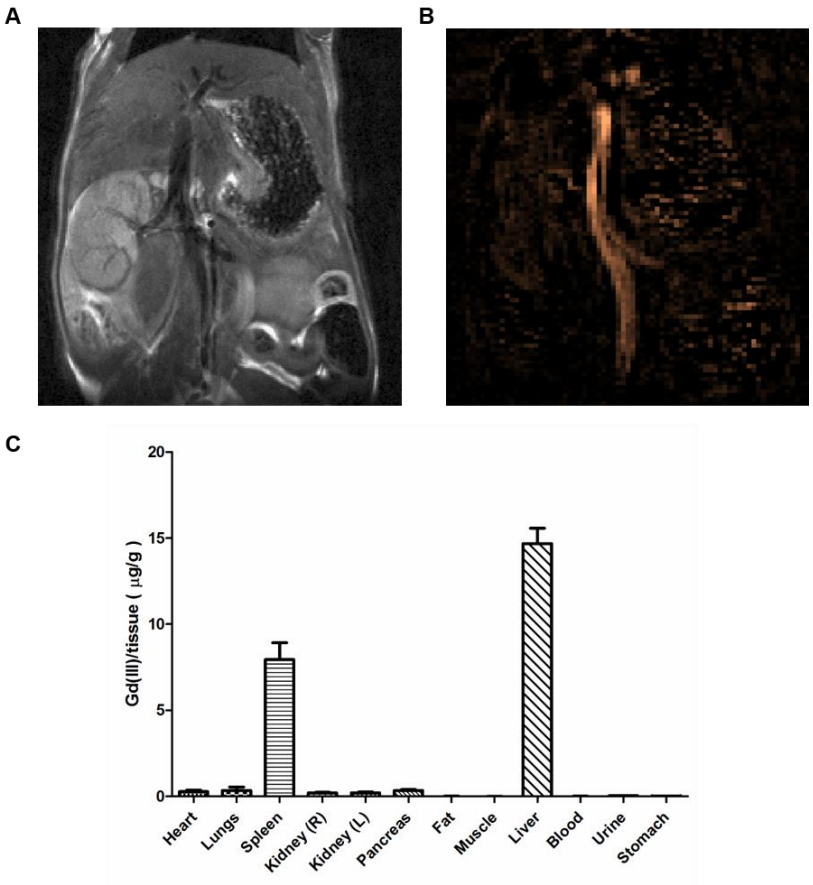

Figure 4.8. (A-B) FLASH MR Images post-IV injection of complex **2**. (A) T2-weighted image 10 minutes post-IV injection. The great vessels are dark and easily seen. The left kidney and stomach are also easily identifiable. (B) AUC image obtained by subtracting post-contrast image from pre-contrast image. Part of the interior of the kidney is starting to enhance. As evidenced by the bright great vessels, complex **2** is still in circulation during the FLASH image acquisition. Clearance is relatively slow, as expected. Therefore the AUC does not show accumulation in the kidney or liver in the first 10 minutes post-injection. (C) Organ accumulation of Complex **2** in C57 mice 3 hours after IV injection (n = 3). Significant accumulation is seen in the liver and spleen while accumulation in other organs is negligible.

4.2.5. Gd@AuNPs for in vivo MR imaging of the pancreas:

Pancreatic cancer is a leading cause of cancer death worldwide and bears the poorest prognosis of any major malignancy.[29] With a 5-year survival of approximately 3% and median survival of six months, it has among the most dismal of all prognoses in medicine. While outcomes for other cancer types have improved steadily in the past few decades, results for pancreatic cancer have not changed significantly. The poor prognosis is largely due to delayed diagnosis where 80% of patients remain asymptomatic until affected by local or distant metastases. Furthermore, at this late stage, only 20% of patients can benefit from surgery and adjuvant chemotherapy, which extends 5-year survival to 20%.[30] The first-line imaging techniques used for diagnosis and preoperative staging of pancreatic cancer are abdominal ultrasound and computed tomography, but these modalities have diagnostic value at only an advanced disease stage.[31] The shortcomings of the currently available techniques for pancreatic cancer detection make it clear that new diagnostic approaches are needed.

The newly synthesized Gd@AuNPs demonstrated greater Gd(III) loading, surface coverage, cellular Gd(III) delivery and MR imaging efficacy than previously reported DNA-Gd(III)@AuNPs. We explored whether these Gd@AuNPs can be used to image the mouse pancreas *in vivo*. Previous studies by Mukherjee *et al.* have shown the surface charge of AuNPs using small molecule PEG surface ligands can fine tune the circulation time and biodistribution through the systemic intravenous (IV) and intraperitoneal (IP) administration of AuNPs.[32] Interestingly, these AuNPs were observed to accumulate predominately in the pancreas of athymic nude mice through IP administration, due to intraperitoneal circulation and altered lymphatic

clearance. We hypothesized that surface functionalization of AuNPs with Gd(III) chelates may have a similar effect and result in pancreatic localization.

In vivo imaging of animals incubated with Gd@AuNPs (complexes **2** and **4**) was conducted to measure enhanced MR image contrast in pancreatic tissue. In particular, pancreatic imaging in rodents can be challenging since the organ is not a well-defined solid retroperitoneal organ, but rather a thin membrane, spread throughout the upper abdomen and lying immediately adjacent to the gut.[33] Furthermore, the low intrinsic T_1-weighted contrast of the pancreas, motion artifacts, and intestinal gas makes MR detection of the pancreas notoriously difficult.

In an effort to evaluate the performance of Gd@AuNPs for pancreatic imaging, animals were injected with 4.0 nmol/kg body weight of AuNPs through IP administration. For complex **2**, this equates to 8.8 μmol/kg body weight of Gd(III). For complex **4**, this equates to 5.5 μmol/kg body weight of Gd(III). Following IP injection and 24 h incubation, MR images were acquired of the peritoneal cavity at 9.4 T (n = 3 for complex **2** and complex **4**, respectively) using standard T_1-weighted FLASH scans. Significantly increased contrast enhancement was observed for mice treated with Gd@AuNPs, allowing obvious identification of the pancreas, with high contrast-to-noise ratios (CNRs) in all subjects (**Figure 4.9**). The muscle signal was subtracted from each pixel in the pancreas ROI, and divided by the standard deviation of the noise to generate the CNR map. The resulting CNR maps were set to a threshold at a value of 35 and the number of pixels in the pancreas ROI of each mouse was counted (see **Figure 4.10**, **Figure 4.11**). The number of pixels with a CNR greater than 35 ranged from 343 to 805 for complex **2**, and from 178 to 364 for complex **4**. Furthermore, the two control mice were observed to have 27 and 174 pixels with CNRs greater than 35.

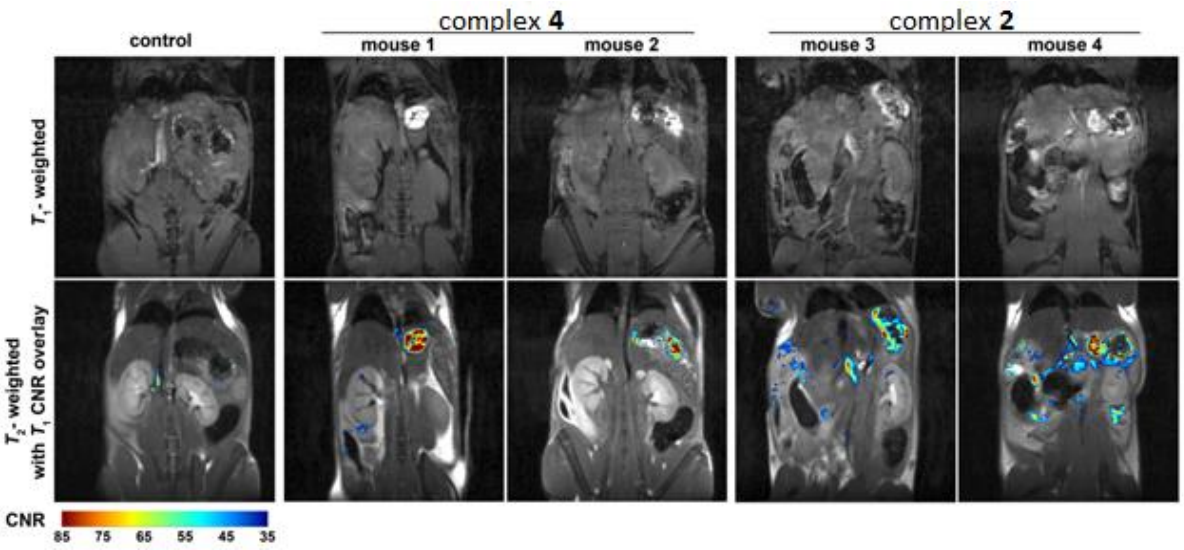

Figure 4.9. T_1-weighted FLASH images were obtained at 9.4 T to assess contrast after injection of complexes **2** and **4** (n = 3; 2 images are displayed; see supplementary figure 2). Contrast-to-noise ratio (CNR) relative to muscle, computed from T_1-weighted FLASH images, were overlaid on TurboRARE T_2-weighted anatomical images at 9.4 T after administration of complex **2**, complex **4**, and no agents (control) following 24 h incubation. Upon administration of both complex 2 and 4, significant contrast enhancement is observed in the region of the pancreas.

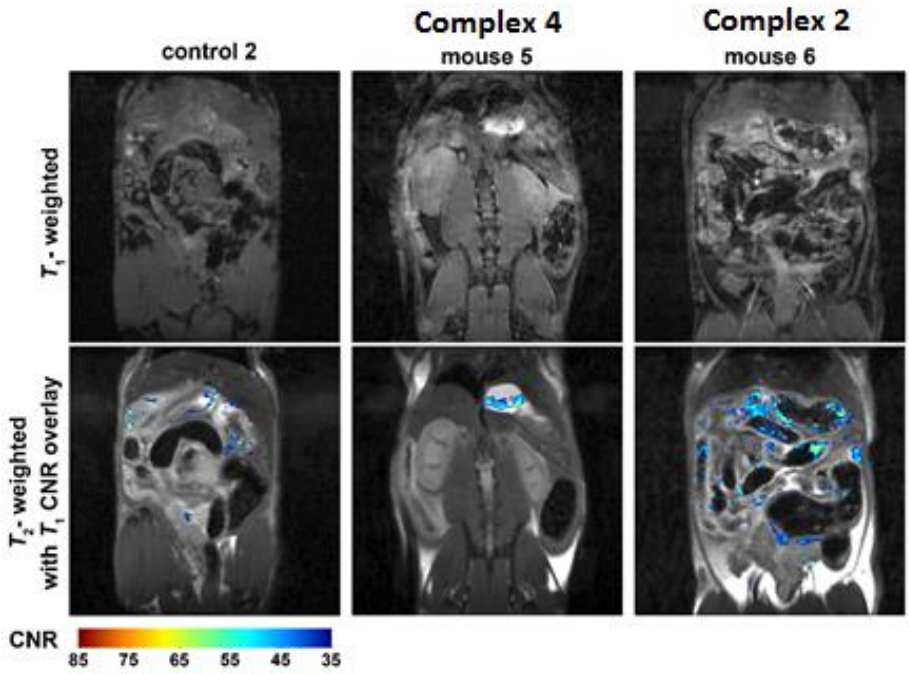

Figure 4.10. T_1-weighted FLASH images of mice after IP injection of complexes **2** and **4** were obtained at 9.4 T (for the second of two controls, and the third mouse of each nanoconjugate injection, shown here). Contrast-to-noise ratio (CNR) relative to muscle, computed from T_1-weighted FLASH images, were overlaid on TurboRARE T_2-weighted anatomical images at 9.4 T after administration of complex **2**, complex **4**, and no agents (control) following 24 h incubation.

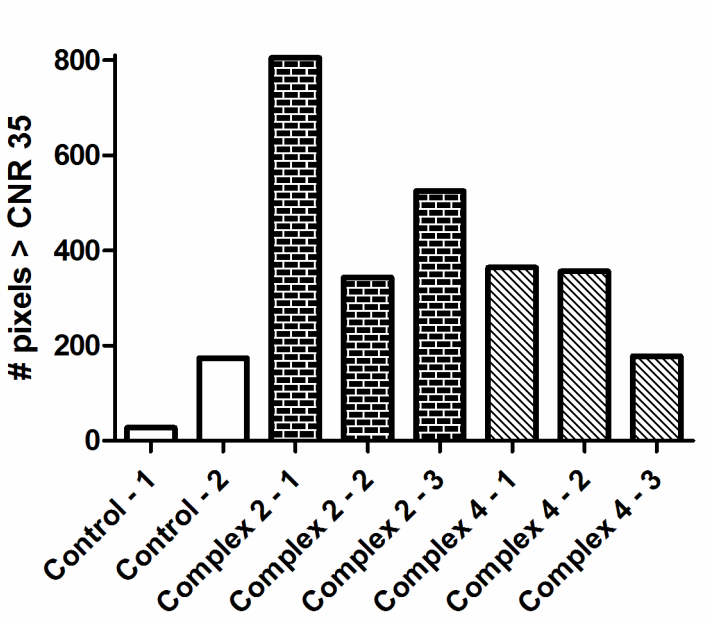

Figure 4.11. Graph depicting number of pixels in pancreas ROI above CNR of 35 relative to muscle in each mouse tested. CNR maps were measured by placing a single region of interest around the pancreas, in leg skeletal muscle, the bladder, and a noise region in the corner of the image. The muscle signal was subtracted from each pixel in the pancreas ROI, and divided by the standard deviation of the noise. CNR maps were set to a threshold at a value of 35, and the number of pixels in the pancreas ROI of each mouse was counted.

The marked increase in CNR of the T_1-weighted images of mice dosed with Gd@AuNPs indicates the localization of particles within the pancreas and subsequent contrast enhancement.

To investigate the performance observed in MR imaging, biodistribution of complex **2** and **4** was conducted. Animals were sacrificed and organs were harvested for quantification of Gd(III) and Au using ICP-MS (n = 5 for complex **2** and **4**, respectively; **Figure 4.12**). Significant accumulation in the liver and spleen was observed (~700 and ~400 μg of Au per g of tissue, respectively, for both complex **2** & **4**). The high levels of AuNPs found in the liver and spleen suggest that the reticuloendothelial system (RES) is the dominant mode of clearance for these particles.[34,35] However, despite this high accumulation, no significant MR contrast enhancement is observed in these organs when compared to the pancreas. This phenomenon may be attributed to organ density and differences in contrast agent diffusion rates within the tissues.[36] Importantly, significant localization to the pancreas was observed (~550 μg of Au per g of tissue for both complex **2** & **4**). Indeed, the levels of Gd(III) relative to Au in all tissues reflect the Gd(III) loading observed for complex **2** & **4** and not the differences in charge of the two chelates. In general, the biodistribution of Gd@AuNPs through IP administration reflects previously reported behavior of small molecule, PEGylated AuNPs.[32,37,38] These results validate our approach toward accumulation to the pancreas through AuNP surface modification with hydrophilic, small molecule Gd(III) CAs.

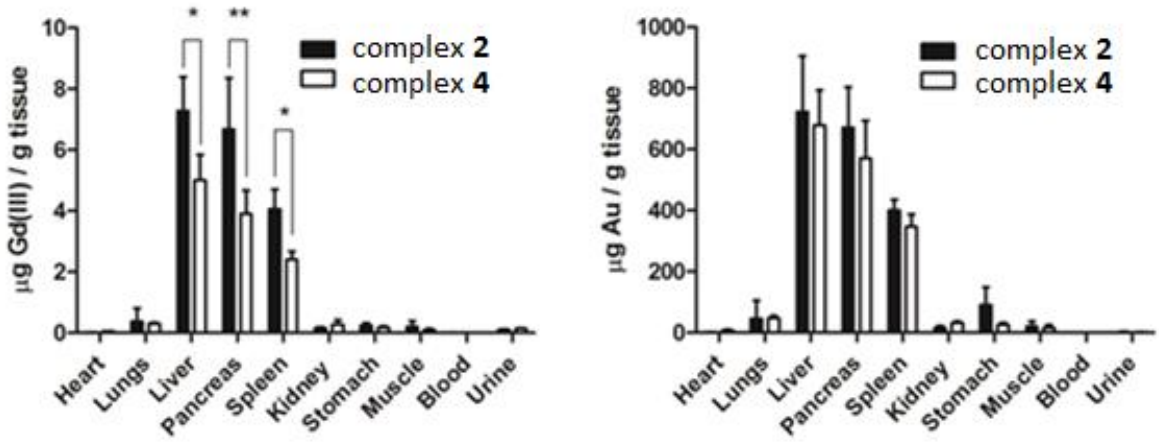

Figure 4.12. Biodistribution of complexes **2** and **4** in C-57 mice. Following IP administration and 24 h incubation, organs were harvested and metal analysis was conducted via ICP-MS to determine the amount of Gd and Au per g of organ. Gd@AuNPs accumulate in the clearance organs, liver and spleen, and accumulates in the pancreas. Similar amounts of Au per g of organ were observed for both complexes **2** and **4**. However, complex **2** was observed to have a greater amount of Gd per g of organ, reflecting the higher Gd(III) loading onto the particle. Two-tailed T-test: * $p < 0.01$, ** $p < 0.05$.

In an effort to validate the accumulation of Gd@AuNPs to the pancreas, TEM and histology of the pancreas were performed following 24 h incubation with complexes **2** & **4**, respectively. Immediately following harvesting of the pancreas, the tissue was divided in two and fixed in formalin. The tissue was separately prepared for sectioning for TEM and histology. TEM images of pancreatic tissue slices revealed the presence of AuNPs in mice incubated with both Lip-Gd@AuNP constructs (**Figure 4.13*A***). Significant presence of particles was observed to be encapsulated in large particle aggregates in lysosomes (~1 μm) of macrophages and located in the interstitial spaces between acinar cells of the pancreatic tissue. The identification of the acinar cells was based on the presence of extensive endoplasmic reticulum (ER) organelles because they are indicative of this particular pancreatic cell type.

Further confirmation of pancreatic tissue labeling by Gd@AuNPs was obtained through histological analysis. The presence of AuNP aggregates is observed in hematoxylin and eosin stained pancreatic tissue sections for animals incubated with complex **2** and **4**, respectively (**Figure 4.13*B***). No structural and morphological abnormalities were noted in either of the two pancreases. However, slight inflammation was noted in the adjacent fatty tissues. Under high power magnification (100×), black AuNP aggregates are diffusely distributed in the surrounding fatty tissue of the pancreas. The inflammatory cells include lymphocytes and histiocytes and nanoparticle-laden phagocytes. Furthermore, the tissue contained nanoparticle aggregates directly in the pancreatic tissue among acinar cells. While we have not established a mechanism of organ localization, we hypothesize that Gd@AuNPs (when delivered by IP administration) can elicit an immune response that drives accumulation to the pancreas through sequestration by macrophages.[32,39]

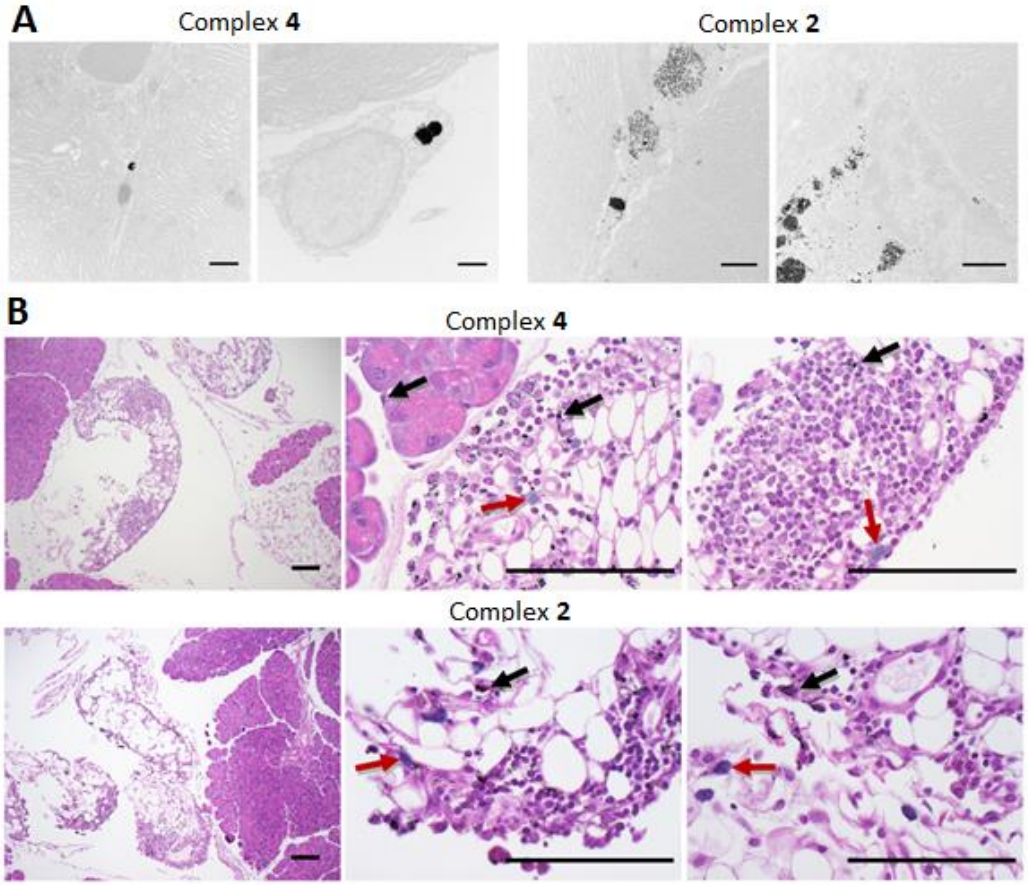

Figure 4.13. (**a**) TEM images of pancreatic tissue from mice treated with complex **2** and **4**. Particles are present (as black spheres) in a lysosome as particle aggregates (< 1 μm) in the macrophage. The labeled cell is present in the interstitial spaces of acrine cells as identified by the extensive ER organelles (scale bars are 1 μm). (**b**) Histology reveals mild inflammatory foreign material reaction in the adjacent tissue of the pancreas. The low magnification images (10x) show Gd@AuNP-labeled pancreatic tissue and the adjacent fatty tissues. No structural or morphological abnormalities were noted in either of the two pancreases. Under the high power magnification (100x), black nanoparticles are diffusely distributed in the fatty and pancreatic tissue (black arrows) of both pancreas slices. The inflammatory cells include lymphocytes and histocytes, some with phagocytic nanoparticles (red arrows) (scale bars are 100 μm).

4.3. Conclusions

We have reported the facile synthesis of Gd@AuNPs with four unique surface chemistries. Specifically, complexes **1**-**3** were synthesized bearing DO3A-based Gd(III) chelates with alkyl linkers of different lengths, while complex **4** was negatively charged LipGdDTPA@AuNP as previously reported.[25] Complexes **2-3** were stable in DPBST, whereas complex **1** was not, suggesting that the shorter alkyl linkers confer less salt stability than longer linkers. The newly synthesized Gd@AuNPs demonstrated greater Gd(III) loading, surface coverage, cellular Gd(III) delivery and MR imaging efficacy than previously reported DNA-Gd(III)@AuNPs. Interestingly, complex **2** was significantly better at delivering a Gd(III) payload to MDA-MB-231 m-Cherry breast cancer cells compared to complexes **3** and **4.** It is likely that the longer linker of **3a** and the negative charge of **4a** limit the cellular penetration of complexes **3** and **4** respectively, as evidenced by lower Gd(III) uptake and sparse intracellular localization observed in TEM images. Therefore, while complexes **2** and **4** showed unprecedented performance as T_1-weighted CAs of the pancreas[25], only complex **2** is optimal for cell labeling.

Further, Gd@AuNPs described here provide the first methods for using T_1-weighted MRI CAs for imaging the pancreas. The functionalization of AuNPs and increased surface loading of Gd(III) were demonstrated by ICP-MS during the synthesis and development of the Gd@AuNP system. Biodistribution experiments showed that both complex **2** and complex **4** accumulate to the pancreas. Furthermore, by TEM and histological analysis we found that significant nanoparticle labeling occurs through uptake by macrophages within the pancreatic tissue. As a result, unprecedented MR image contrast enhancement of the pancreas was observed.

Gd@AuNPs are the first MRI contrast agents of any type - either paramagnetic or superparamagnetic - to effectively image the pancreas. Targeting to the pancreas is a significant challenge since the organ is hypovascular and surrounded by abundant fibrous stroma and fatty tissue.[40,41] Other CA formulations utilizing iron oxide[42,43], manganese[44,45], or gadolinium[46,47] for MR imaging of the pancreas have been unconvincing. In this context, the efficacy of Gd@AuNPs for pancreatic MRI is compelling, but several features of this platform need further exploration.

Firstly, the lack of appreciable contrast in the liver and spleen is surprising, given the nearly equal Gd(III) content in those tissues compared to the pancreas (**Figure 4.12**). This may be due to differences in tissue density and contrast agent diffusion within tissue between the three organs. The mouse pancreas is a thin, membranous organ[33] where localized particle accumulation was observed by TEM and histology and resulted in high image contrast in T_1-weighted imaging. However, the mouse liver and spleen are dense organs, where diffusely distributed Gd(III) may not result in similar image contrast. Further study is required to understand and correlate particle diffusion and behavior within different tissue types and the image contrast produced in T_1-weighted imaging.

While the accumulation of Gd@AuNPs in the liver and spleen can be explained by their function as clearance organs, the mechanism by which Gd@AuNPs accumulate specifically in the pancreas is currently unknown. Studies are underway to explore which features of the nanoparticle construct i.e., size, shape, charge or gadolinium-gold surface chemistry, contribute toward pancreatic localization. We hypothesize, based on significant accumulation of Gd@AuNPs in macrophages in pancreatic tissue, that targeting to the pancreas is achieved via macrophage uptake by tissue-resident and peritoneal macrophages that home to the pancreas. Accordingly, the recruitment,

phenotype and inflammatory response of macrophages during administration and action of Gd@AuNPs should be evaluated.

In conclusion, Gd@AuNPs provide a robust platform for the development of pancreas-specific MR imaging agents, which may prove invaluable in the diagnosis and treatment of pancreatic disease. Further, the short-term *in vivo* pilot study reported herein suggests that the material is biocompatible and suitable for long-term studies in mice bearing tumor xenografts of human cancer cells. Gd@AuNPs label cancer cells *ex vivo* with high efficiency and can be used to track transplanted cells *in vivo* thereby enabling the success of cell therapy.

4.4. Materials and Methods

4.4.1 General Synthesis Protocols and Characterization Techniques: Reagents and solvents were purchased from Sigma Aldrich Chemical Co. (St. Louis, MO, USA). For flash chromatography, standard grade silica gel was purchased from Sorbent Technologies (Norcross, GA, USA). For NMR and mass spectroscopy, a Bruker 500 MHz Avance III NMR spectrometer and a Bruker Amazon X LC-MS Ion Trap Mass Spectrometer (Billerica, MA, USA) were used respectively. Final purification was accomplished using a Varian Prostar 500 HPLC (Santa Clara, CA, USA) using a Waters 4.6 × 250 mm 5 µm Atlantis C18 column (Milford, MA, USA). Mobile phases consisted of Millipore water, 0.05% trifluoroacetic acid in Millipore water, and acetonitrile. Gd@AuNP particles were assessed for hydrodynamic size by dynamic light scattering using a Brookhaven ZetaPals particle size analyzer. For structural characterization of Gd@AuNPs, TEM images were acquired using a JEOL 1230 microscope.

4.4.2 Synthesis of lipoic acid N-hydroxysuccinimidyl ester (Lip-NHS). To a 100 mL round bottom flask containing a magnetic stir bar and (±)-lipoic acid (0.500 g, 2.4 mmol) and *N*-

hydroxysuccinimide (0.418 g, 3.6 mmol) was added 20 mL of chloroform. The mixture was stirred at room temperature until dissolution of the NHS, at which time was added *N*, *N*'-diisopropylcarbodiimmide (0.563 mL, 3.6 mmol) dropwise at room temperature. Complete formation of the coupled NHS ester was assessed by the appearance of product by TLC (R*f* = 0.4) in diethyl ether and was visualized by CAM stain. Purification of the product was achieved by silica gel chromatography in 100% diethyl ether resulting in an 80% yield. Proton and carbon NMR spectra are shown in **Figure 4.14** and **Figure 4.15** respectively. ^{1}H NMR (500 MHz, Chloroform-*d*) δ 3.64 – 3.53 (m, 1H), 3.24 – 3.07 (m, 2H), 2.84 (s, 4H), 2.63 (t, *J* = 7.3 Hz, 2H), 2.47 (q, *J* = 12.3, 6.6 Hz, 1H), 1.92 (q, *J* = 13.5, 6.9 Hz, 1H), 1.85 – 1.43 (m, 7H). ^{13}C NMR (126 MHz, $CDCl_3$) δ 169.10, 168.40, 56.09, 40.15, 38.52, 34.42, 30.79, 28.32, 25.59, 24.37. ESI-MS (m/z) observed: 617.1, calculated 617.1 $[M]^-$.

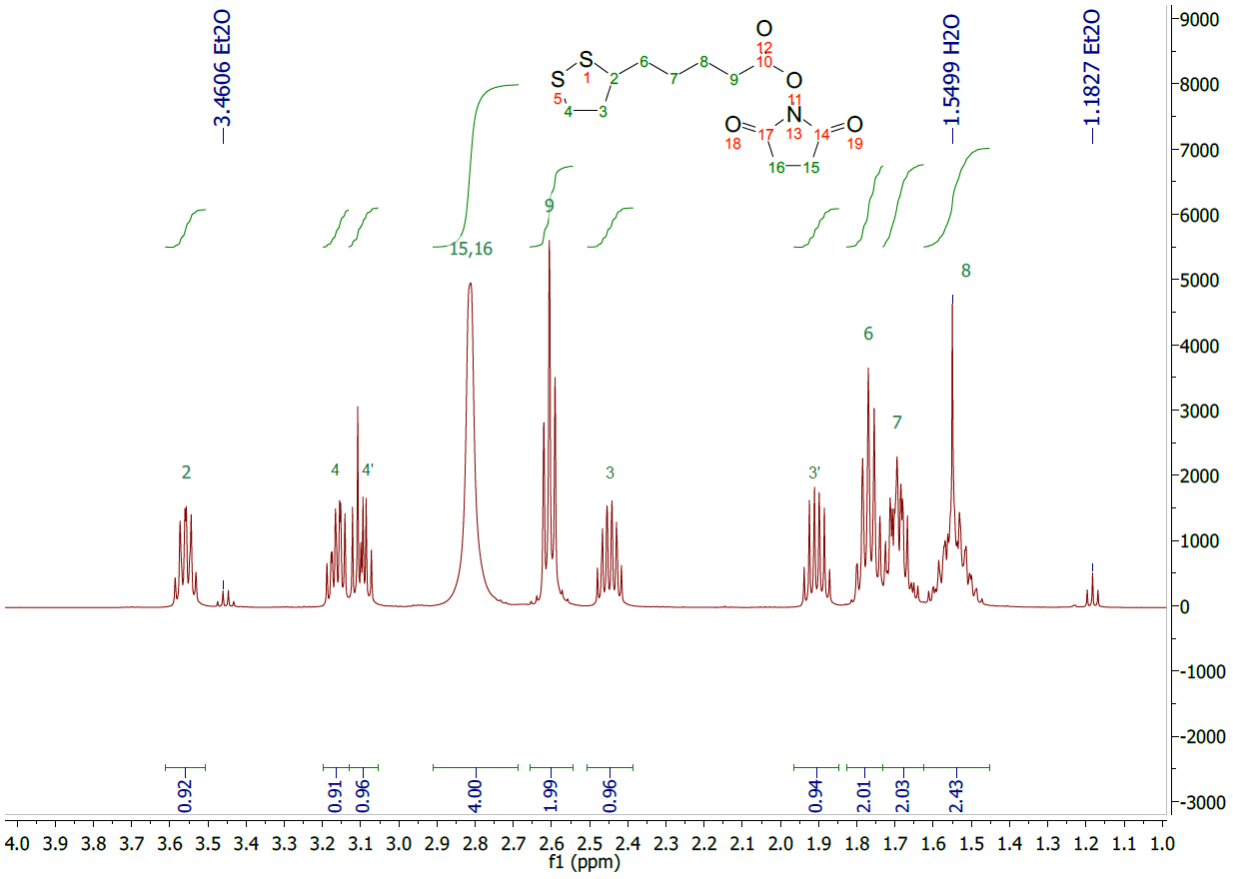

Figure 4.14. Proton NMR spectrum of Lip-NHS.

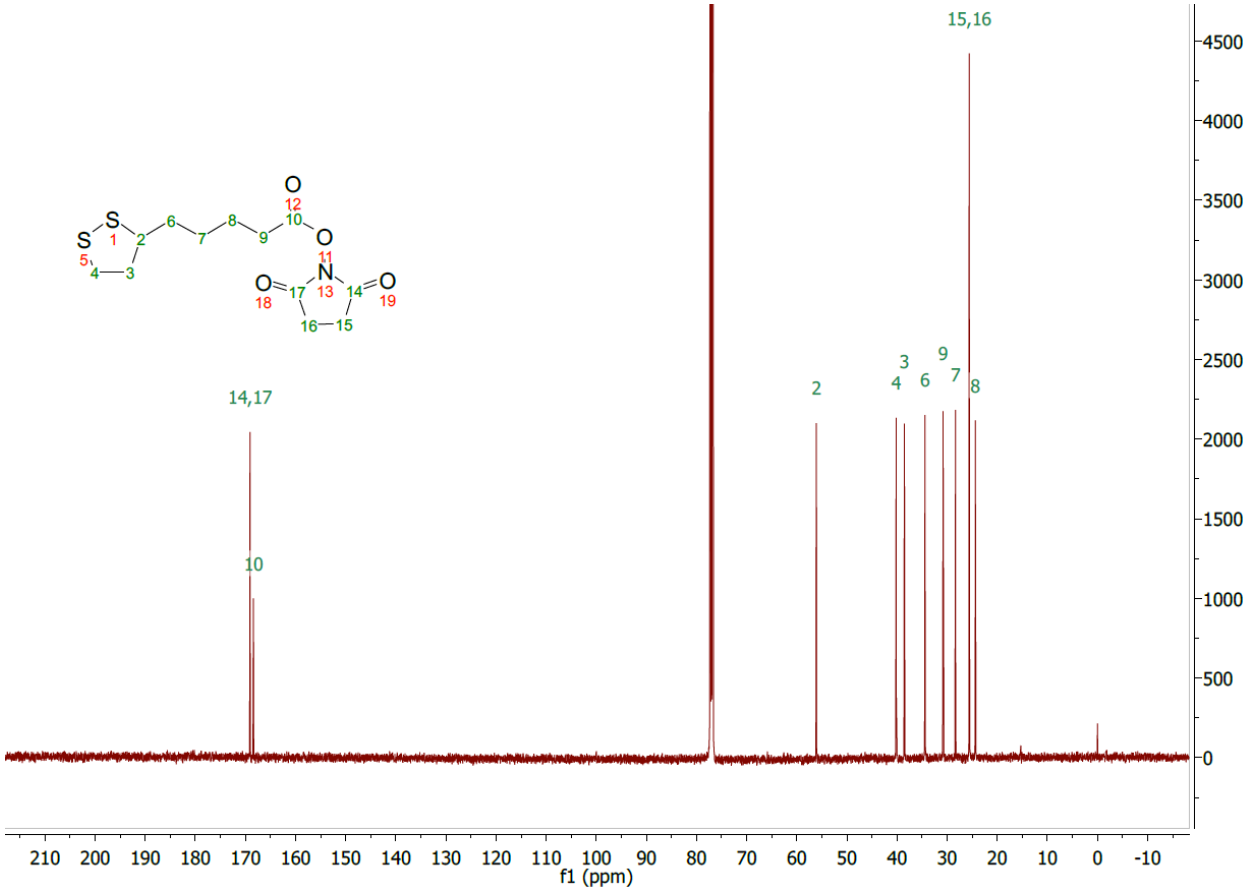

Figure 4.15. Carbon-13 NMR spectrum of Lip-NHS.

*4.4.3. Synthesis of **1a**.* Gd-DO3A-C3 amine (0.050 g, 0.091 mmol) and 2 mL of 100 mM carbonate buffer pH 8.5 were added to a 10 mL round bottom flask. Lip-NHS (0.030 g, 0.099 mmol), synthesized according to published procedure[25], and 3 mL DMSO were added in a separate glass vial. After Lip-NHS was dissolved, the solution was added to the Gd-DO3A-C3 amine solution, and stirred at room temperature for 12 hours. Reaction was monitored by ESI-MS for the disappearance of starting material. Final product was purified by semipreparative HPLC. The mobile phase comprised of Millipore water and HPLC grade acetonitrile (ACN). Initial conditions of 0% ACN were held constant for 5 min, then gradually increased to 32% ACN between 5–17 min, followed by a further increase to 40% ACN at 31 min. The product peak eluted between 21 and 23 minutes, as monitored by UV absorption at 210 nm. The product was collected, and lyophilized to a fluffy pale yellow solid. (m/z) observed: 747.1, calculated: 747.01 $[M + H]^+$.

*4.4.4. Synthesis of **2a***: To a 10 mL round bottom flask containing a magnetic stir bar was added previously reported Gd-DO3A-C6 amine (0.100 g, 0.17 mmol) in 1 mL of carbonate buffer pH 9.2. In a separate vial was added Lip-NHS (0.08 g, 0.20 mmol) and 2 mL DMSO. Upon complete dissolution of lipoic acid NHS-ester, the solution was added to the stirring solution of Gd-DO3A-C6 amine at room temperature, and left to stir for 12 hours. Purification of final product was achieved by semipreparative HPLC. The crude mixture was injected directly, eluting via the use of the following method, where the mobile phase consisted of Millipore water and HPLC grade acetonitrile (ACN): initial conditions of 0 % ACN were held constant for 5 min, then ramped to 32 % ACN between 5–17 min, followed by a gradual ramp to 40% ACN at 31 min. The product peak eluted between 23 and 26 minutes, as monitored by UV absorption at 210 nm. The product

was collected, and lyophilized to a fluffy pale yellow solid. ESI-MS spectrum is shown in **Figure 4.16**. (*m/*z) observed: 811.0, calculated: 811.1 $[M + Na]^+$.

*4.4.5. Synthesis of **3a**.* **3a** was synthesized by an analogous procedure to **1a** and **2a**. Specifically, Gd-DO3A-C12 amine (0.047 g, 0.069 mmol) and 2 mL of 100 mM carbonate buffer pH 8.5 were added to a 10 mL round bottom flask. Lip-NHS (0.025 g, 0.08 mmol), synthesized according to published procedure[25], and 3 mL DMSO were added to a separate glass vial. After Lip-NHS was dissolved, the solution was added to the Gd-DO3A-C12 amine solution, and stirred at room temperature for 12 hours. Reaction was monitored by ESI-MS for the disappearance of starting material. Final product was purified by semipreparative HPLC. The mobile phase comprised of Millipore water and HPLC grade acetonitrile (ACN). Initial conditions of 0% ACN were held constant for 5 min, then increased to 5% ACN between 5–10 min, and held constant at 5% CAN until 20 min. ACN was then gradually increased to 100% through 25 min and held constant at 100% ACN until 40 min. The product peak eluted between 32 and 35 minutes, as monitored by UV absorption at 210 nm. The product is collected, and lyophilized to a fluffy pale yellow solid. (m/z) observed: 873.23, calculated: 873.01 $[M + H]^+$.

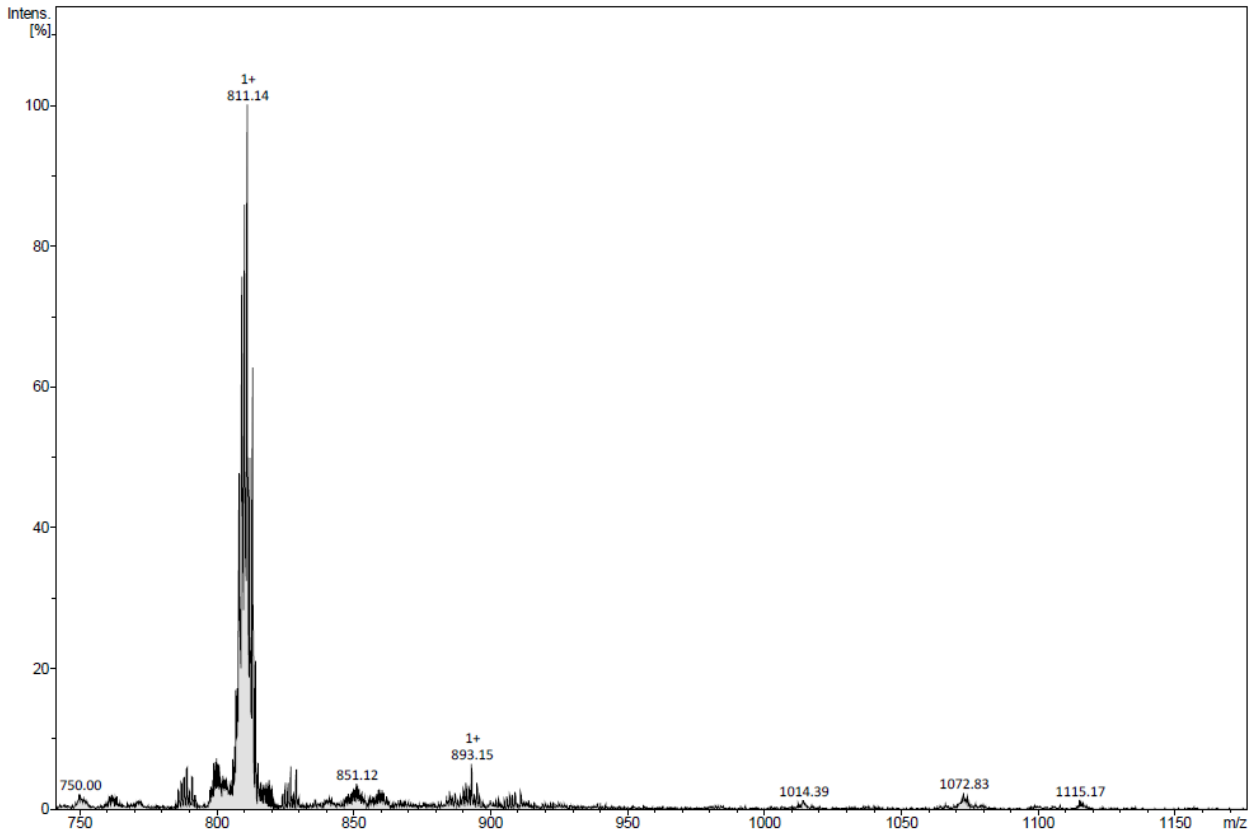

Figure 4.16. ESI-MS spectrum of **2a**.

*4.4.6. Synthesis of **4a***. **4a** was synthesized by an analogous procedure to **1a**-**3a**. Specifically, a 10 mL round bottom flask was charged with a magnetic stir bar and previously reported Gd-DTPA-C4 amine (0.100 g, 0.16 mmol) in 1 mL of carbonate buffer pH 9.2. In a separate vial was added lipoic acid NHS-ester (0.08 g, 0.20 mmol) and 2 mL DMSO. Upon complete dissolution of Lip-NHS, the solution was added to the stirring solution of Gd-DTPA-C4 amine at room temperature, and left to stir for 12 hours. Reaction completeness was monitored by ESI-MS for the disappearance of starting material. Purification of final product was achieved by semipreparative HPLC. The crude mixture was injected directly, eluting via the use of the following method, where the mobile phase consisted of Millipore water and HPLC grade acetonitrile (ACN): initial conditions of 0 % ACN were held constant for 5 min, then ramped to 5 % ACN between 5–10 min, and held constant at 5 % CAN until 20 min. Acetonitrile was then ramped to 100 % through 25 min and held constant at 100 % ACN until 30 min. The product peak eluted between 26.0 and 26.9 minutes, as monitored by UV absorption at 210 nm (chromatogram of pure product shown in **Figure 4.18**). ESI-MS spectrum is shown in **Figure 4.17**. (*m*/z) observed: 805.02, calculated:805.2 [M^-].

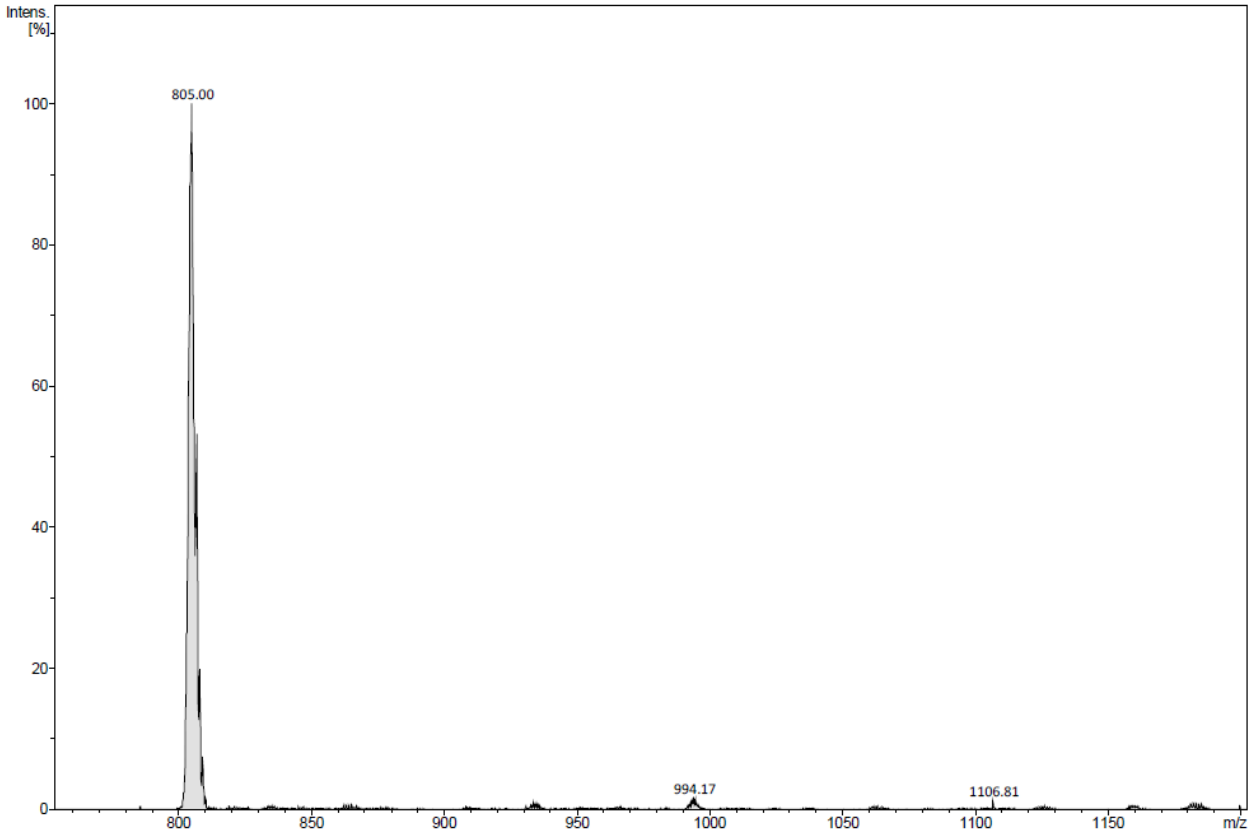

Figure 4.17. ESI-MS spectrum of **4a**.

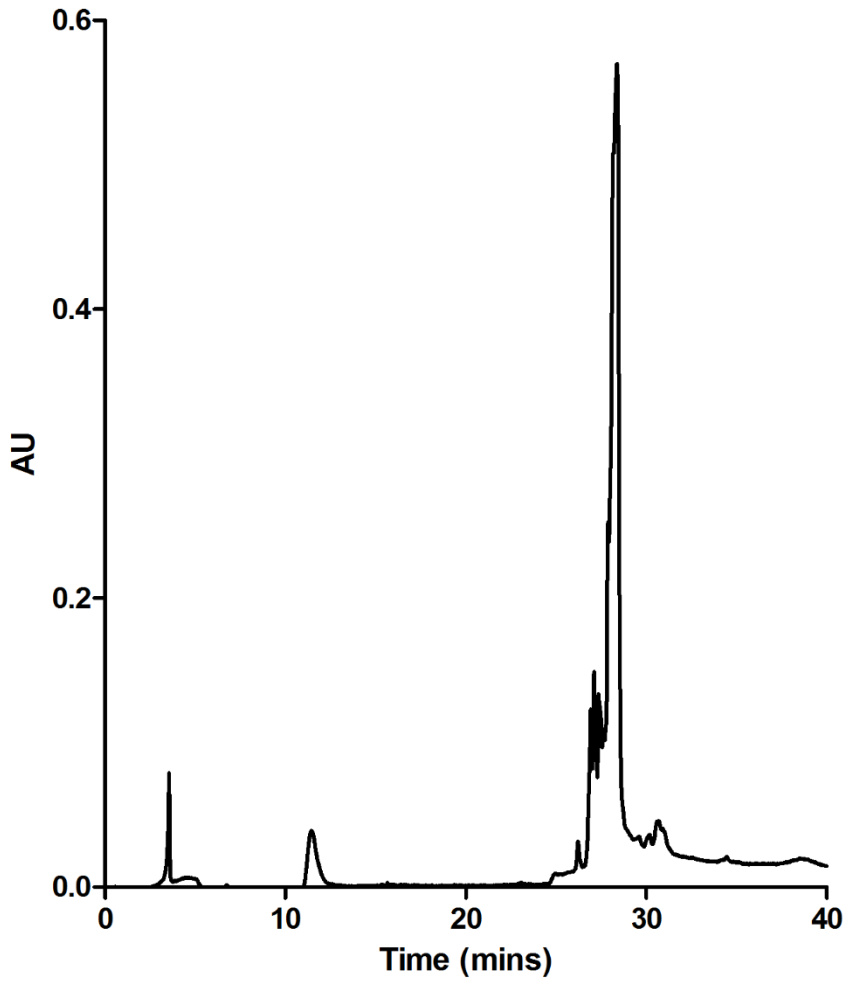

Figure 4.18. HPLC chromatogram of pure **4a** measured by UV absorption at 210 nm. Sample was suspended in 0.01% w/v TCEP buffer (TCEP peak visualized at approximately 12 minutes).

4.4.7. Synthesis of citrate-stabilized AuNP. Gold nanoparticles were synthesized by citrate reduction of gold chloride. Specifically, $HAuCl_4$ trihydrate (0.197 g) was dissolved in 498 mL of Millipore water in an acid washed two necked round bottom flask and brought to reflux. To the boiling mixture was added trisodium citrate (0.509 g) in 2 mL of water, and the solution was left to boil for 30 minutes. Particles were filtered using a 200 nm filter, and the plasmon resonance wavelength was observed by UV/Vis spectroscopy, and size was confirmed by DLS and TEM. Final particle concentration was determined using ICP-MS. Particle size was determined by examination of over 100 particles using ImageJ, and volume and total gold content approximations were made by using the geometric formula for the volume of a sphere and the density of bulk gold (59.01 Au/nm^3).

4.4.8. Synthesis of Gd@AuNPs. Functionalization of the citrate stabilized AuNPs with Lip-DO3A or Lip-DTPA were performed using 25 mL of 10 nM AuNPs with 0.01 % Tween 20 (v/v). The complexes **1a-4a** were dissolved in 500 μL of methanol and 500 μL of Millipore water, added to the AuNP solution, and shaken overnight for the formation of complexes **1-4**, respectively. Notably, functionalization of the AuNP surface was achieved without the addition of a reducing agent. The functionalized AuNPs were purified and concentrated using ultra-centrifugation. Five rounds of centrifugation at 21.1 × g (20 min, 7 °C) were performed to sediment the particles. Following each round of centrifugation, the top solution was subsequently decanted, and the particles were resuspended in Dulbecco's phosphate buffered saline (DPBS) with 0.01% Tween 20. The particles were concentrated down to 250 nM AuNPs as a 1 mL stock solution in DPBS 0.01% Tween 20. When not in use, particles were stored at 4 °C.

4.4.9. Low-field relaxivity (r_1): Stock solution of complexes **1-4** (approximately 500 μM Gd(III)) was serially diluted four times for five total samples in 150 μL volumes. Solutions were heated to 37 °C and 150 μL of each concentration was used for measurement of T_1 relaxation time via a Bruker minispec mq60 NMR spectrometer (60 MHz). An inversion recovery pulse sequence, with a repetition time of 15 seconds, 10 data points and 4 averages, was used to acquire data. The remaining solutions were used to prepare samples for ICP analysis of Gd(III) concentration (see *3.4.11*). The slope of the linear fit of the relaxation rate ($1/T_1$, s^{-1}) plotted against the Gd(III) concentration (mM) yields the relaxivity of the agent ($mM^{-1}\ s^{-1}$).

4.4.10. High Field Relaxivity (7 T): A Bruker Pharmscan 7 T (Billerica, MA, USA) imaging scanner fitted with shielded gradient coils at 25 °C was used. Samples of complexes **1-4** were prepared by serial dilution, and Gd(III) concentration was measured by ICP-MS. Solutions were placed in glass capillary tubes of approximate diameter = 1 mm, and the tubes containing the samples were taped around a larger tube containing water. For acquisition of T_1 relaxation times, a rapid-acquisition rapid-echo (RARE-VTR) pulse sequence was used. The following parameter values were utilized: static echo time = 11 ms, variable repetition time = 150, 250, 500, 750, 1000, 2000, 4000, 6000, 8000, and 10000 ms, field of view = 25 × 25 mm^2, matrix size = 256 × 256, number of axial slices = 4, slice thickness = 1.0 mm, and averages = 3. Paravision 6.0 software (Bruker, Billerica, MA, USA) was used for T_1 analysis, by monoexponential curve-fitting of image intensities of selected regions of interest (ROIs) from each axial slice.

4.4.11. Metals Analysis by ICP-MS: A computer-controlled (QTEGA v. 2.6) Thermo (Thermo Fisher Scientific, Waltham, MA) iCapQ ICP-MS equipped with an ESI SC-2DX autosampler/autodilution system (Elemental Scientific Inc., Omaha, NE) was utilized for metal

quantification. ICP-MS analysis was preceded by acid digestion of Gd@AuNPs samples. Specifically, for Gd analyses 20 µL of Gd@AuNPs sample was added into 120 µL of 1:1 concentrated nitric acid: concentrated hydrochloric acid (TraceSelect Nitric acid, >69%; TraceSelect HCl, fuming 37%) and mixed thoroughly. Similarly, for Au analyses, 5 µL of Gd@AuNPs sample was added to 500 µL of 1:1 HNO_3:HCl as above, and mixed thoroughly. Sample:acid mixtures were heated at 65 °C for at least 2 hours. Then, ultra-pure H_2O (18.2 Ω·m) was added up to 10 mL total sample volume. For cells labeled with Gd@AuNPs, 150 µL of labeled cells suspended in PBS or media were added to 100 µL 70% nitric acid and heated at 65 °C for at least 4 hours. Following digestion, ultra-pure water was added for a final sample volume of 3 mL. Individual Au and Gd elemental standards were prepared at 0, 0.78125, 1.5625, 3.125, 6.25, 12.5, 25.0, 50.0, 100, and 200 ng/mL concentrations with 2% nitric acid (v/v), 2% HCl (v/v) and 5.0 ng/mL internal standards up to a total sample volume of 5 mL. Each sample was acquired using 1 survey run (10 sweeps) and 3 main (peak jumping) runs (100 sweeps). The isotopes selected were ^{197}Au, ^{156,157}Gd and ^{115}In, ^{165}Ho, and ^{209}Bi (as internal standards for data interpolation and machine stability).

4.4.12. General Cell Culture. All reagents used for cell culture, such as Dulbecco's modified phosphate buffered saline (DPBS), media, and dissociation reagents, were purchased from Life Technologies (Carlsbad, CA). Only CorningBrand® (VWR Scientific, Radnor, PA) cell culture flasks, plates, and sera were used. MDA-MB-231 m-Cherry cells were purchased from the American Type Culture Collection (Manassas, VA). Cells were cultured in phenol red-free alpha minimum essential media (α-MEM) supplemented with 10% fetal bovine serum (FBS), 1% nonessential amino acids, and 1% sodium pyruvate. Cells were grown in a humidified incubator

operating at 37 °C and 5.0% CO_2. Cells were allowed to incubate for 24 hours before all experiments. For harvesting cells, 0.25% TrypLE was added and cells were incubated for 5 minutes at 37 °C in a 5.0% CO_2 incubator. For sterilization, Gd@AuNPs suspensions in media were filtered with 0.2 μm sterile filters prior to concentration determination and dosing.

4.4.13. Guava ViaCount Assay for Cell Counting and Viability. A Guava EasyCyte Mini Personal Cell Analyzer (EMD Millipore, Billerica, MA) was utilized to count cells and determine viability by a flow cytometric live/dead assay. 50 μL of cell suspension (from each well of 24-well plate) was mixed with 150 μL of Guava ViaCount reagent for 5 minutes to facilitate cell staining. Stained cells were counted using the ViaCount software module. For each sample, 1000 sampling counts were acquired and gated manually by the operator for live versus dead cells. Number of live cells and percentage of live cells were recorded. Instrument reproducibility was assessed biweekly using GuavaCheck Beads and following the manufacturer's suggested protocol using the Daily Check software module.

4.4.14. Cellular Delivery Studies. Cellular delivery studies were performed with MDA-MB-231 Cherry cells. Cells were plated at a cell density of approximately 25,000 cells per well for 24-hour uptake in a 24-well plate as counted by a hemocytometer. Stock solutions of complexes **2-4** (500 μM Gd(III)) were prepared. Samples from stock solution were diluted with media to 50 μM Gd(III) or less to prepare incubating solutions of 180 μL per well. Cells were incubated with complexes **2, 3** or **4** for 24 hours. Time-dependent uptake for cellular delivery studies were performed with MDA-MB-231 m-Cherry cells. Cells were plated at a cell density of approximately 35,000 cells per well in a 24-well plate as counted by a hemocytometer. Cells were incubated with 50 μM Gd(III)-equivalent concentration of complexes **2, 3,** or **4** for 1, 2, 4, 8, and

24 hours. To harvest, cells were rinsed in-plate three times with 500 μL PBS and trypsinized using 100 μL 0.25% TrypLE. Following trypsin treatment, 150 μL of media was added to each well and mixed by a pipette to ensure that all cells were lifted into suspension. 50 μL of the cell suspension was used for cell counting and 150 μL was used for Gd content analysis via ICP-MS.

4.4.15. Cell pellet imaging: Approximately 7.5×10^5 MDA-MB-231 m-Cherry cells were incubated in 25-cm^2 T-flasks with complexes **2**, **3**, or **4** suspended in media or plain media for 24 h, rinsed with DPBS (2 × 1 mL/flask), and harvested with 500 μL of trypsin. After addition of 500 μL of fresh complete media, cells were transferred to 1.5-mL microcentrifuge tubes and centrifuged at 1000 x *g* at 4.0 °C for 5 minutes. The supernatant was removed; the cell pellets were re-suspended in 1 mL of complete media, added to 5¾″ flame-sealed Pasteur pipets, and centrifuged at 100 x *g* at 4.0 °C for 5 minutes. The bottom sections of the flame-sealed pipets were then scored with a glass scribe, broken into small capillaries, and imaged using a RF RES 300 1H 089/023 quadrature transmit receive 23-mm volume coil (Bruker BioSpin, Billerica, MA, USA). A rapid acquisition with refocused echoes (RARE) pulse sequence was used. For T_1-weighting, the following parameters were used: TR = 500 ms, TE =10 ms, flip angle = 90°, NEX = 3, FOV = 20 x 20 mm^2, slice thickness = 1 mm, and matrix size = 256 x 256.

*4.4.16. In vivo studies. (a) Short-term distribution of complex **2*** - All mice were handled and processed according to a protocol approved by Northwestern University Animal Care and Use Committee in accordance with current guidelines from the National Institutes of Health Model Procedure of Animal Care and Use. Male C-57 black mice (wild type) were acquired from Charles River (Wilminton, MA), and were housed under pathogen free conditions. Mice (n = 3) were injected IV 4.0 nmol/kg body weight of Complex **2** through IV administration which equates to

9.0 μmol/kg body weight of Gd(III). Mice were imaged by MRI on a Bruker Biospin 9.4T magnet (Bruker Biospin, Billerica, MA, U.S.A.) within the first 10 minutes of injection using a standard FLASH sequence. Mice were kept warm using a heated pad and maintained under 1−2% inhaled isoflurane anesthesia. Respiration was monitored using an SA Instruments MR compatible monitoring system (SA Instruments, Stonybrook, NY, U.S.A.) for appropriate gating. After 3 hours, mice were euthanized and organs were analyzed for Gd(III) content by ICP-MS. The heart, lungs, liver, spleen, kidneys, muscle, pancreas, fat, stomach, blood, and urine were placed into preweighed Teflon tubes, weighed, and dissolved in 9:1 ACS reagent grade nitric acid/hydrogen peroxide (10 mL for livers and spleens, 1 mL for kidneys, 500 μL for remaining organs). Organ digestion was accomplished using an EthosEZ microwave digestion system (Milestone, Shelton, CT, U.S.A.). Solutions were heated to 120 °C ramp over 30 min followed by a 30 min hold and a 45 min exhaust cycle. The resultant solutions were weighed and an aliquot was transferred to a preweighed 15 mL conical tube. The final ICP-MS samples were prepared as described in section 4.4.11. (b) *Pancreas imaging - In vivo* MR images (n = 3) were acquired 24 hours post injection of Lip-Gd@AuNPs on a 9.4T Bruker Biospec (Bruker Biospin, Billerica, MA, USA) using a 38 mm quadrature mouse body volume coil. For anatomical reference, T_2 weighted accelerated spin echo (TurboRARE) images were acquired with TR/TE = 570 ms / 24ms, RARE factor 8, field of view 4 cm x 4 cm, matrix 256 x 256, 1 mm slice thickness, 7 slices, 0.3 mm slice gap, and 9 averages. To measure contrast enhancement, T_1 weighted gradient echo FLASH images were acquired with TR/TE/α = 100 ms/2.2 ms/45° and 2 averages. Slice geometry was identical to the T_2 weighted images except for a matrix of 192 x 192. During imaging, mice were held under 1-2 % inhaled isoflurane anesthesia and respiration was monitored using an SA Instruments MR

compatible monitoring system (SA Instruments, Stonybrook, NY, USA). Images were processed using JIM 6 software (Xinapse Systems, Essex, United Kingdom). Contrast to noise ratio (CNR) maps were measured by placing a signal region of interest in leg skeletal muscle and the bladder, and a noise region in the corner of the image, subtracting muscle signal from each pixel in the image, and dividing by the standard deviation of the noise. For visualization, CNR maps were set to a threshold at a value of 35, a color lookup table was applied, and the map was overlaid on the T_2 weighted anatomical reference image.

4.4.17. Statistics: Characterization results of Gd@AuNPs are reported as the average and standard deviation of at least three independently synthesized batches. Hydrodynamic radii, polydispersity indices and relaxivities of complexes **1-4** were compared by one-way ANOVA. Results from *in vitro* experiments are expressed as the average of three separate experiments, each performed in triplicate. Three mice were used for *in vivo* MRI and biodistribution analyses. MR images from a single representative experiment are shown. Bar graphs represent averages while error bars represent standard deviations.

Chapter 1 References

(1) Glasser, O.: *Wilhelm Conrad Röntgen and the early history of the Roentgen rays*; Norman Pub.: San Francisco, 1993.

(2) Hildebrandt, C.; Raschner, C.; Ammer, K. An overview of recent application of medical infrared thermography in sports medicine in Austria. *Sensors (Basel)* **2010**, *10*, 4700-4715.

(3) Lin, Y.; Chen, Z.-Y.; Yang, F.; Zhang, J.-S.; Wang, Y.-X.; Liu, J.-B.; Liao, J.-Y.; Liao, Y.-Y.; Zhou, Q.-L.; Li, B.-C.; Liang, H.-Y. Application of Molecular Imaging Technologies in Antitumor Drug Development and Therapy. *Curr. Pharm. Des.* **2015**, *21*, 2136-2146.

(4) Wolf, G.; Abolmaali, N. Preclinical Molecular Imaging Using PET and MRI. *Recent Results Cancer Res.* **2013**, *187*, 257-310.

(5) Zeng, W.; Wang, X.; Xu, P.; Liu, G.; Eden, H. S.; Chen, X. Molecular imaging of apoptosis: from micro to macro. *Theranostics* **2015**, *5*, 559-582.

(6) Reilly, R. M.; Lam, K.; Chan, C.; Levine, M. Advancing Novel Molecular Imaging Agents from Preclinical Studies to First-in-Humans Phase I Clinical Trials in Academia-A Roadmap for Overcoming Perceived Barriers. *Bioconjugate Chem.* **2015**, *26*, 625-632.

(7) Rudin, M.: *Molecular Imaging: Basic Principles and Applications in Biomedical Research, 2nd Edition*; World Sci., 2013.

(8) Mankoff, D. A. A definition of molecular imaging. *Journal of Nuclear Medicine* **2007**, *48*, 18N-21N.

(9) Meir, R.; Shamalov, K.; Betzer, O.; Motiei, M.; Horovitz-Fried, M.; Yehuda, R.; Popovtzer, A.; Popovtzer, R.; Cohen, C. J. Nanomedicine for Cancer Immunotherapy: Tracking Cancer-Specific T-Cells in vivo with Gold Nanoparticles and CT Imaging. *ACS Nano* **2015**, Ahead of Print.

(10) Farwell, M. D.; Pryma, D. A.; Mankoff, D. A. PET/CT imaging in cancer: Current applications and future directions. *Cancer (Hoboken, NJ, U. S.)* **2014**, *120*, 3433-3445.

(11) Schirra, C. O.; Brendel, B.; Anastasio, M. A.; Roessl, E. Spectral CT: a technology primer for contrast agent development. *Contrast Media Mol. Imaging* **2014**, *9*, 62-70.

(12) George, N.; Gean, E. G.; Nandi, A.; Frolov, B.; Zaidi, E.; Lee, H.; Brasic, J. R.; Wong, D. F. Advances in CNS Imaging Agents: Focus on PET and SPECT Tracers in Experimental and Clinical Use. *CNS Drugs* **2015**, *29*, 313-330.

(13) Differding, S.; Hanin, F.-X.; Gregoire, V. PET imaging biomarkers in head and neck cancer. *Eur. J. Nucl. Med. Mol. Imaging* **2015**, *42*, 613-622.

(14) Sun, X.; Cai, W.; Chen, X. Positron Emission Tomography Imaging Using Radiolabeled Inorganic Nanomaterials. *Acc. Chem. Res.* **2015**, *48*, 286-294.

(15) Fuchigami, T.; Ogawa, A.; Yamashita, Y.; Haratake, M.; Watanabe, H.; Ono, M.; Kawasaki, M.; Yoshida, S.; Nakayama, M. Development of alkoxy styrylchromone derivatives for imaging of cerebral amyloid-β plaques with SPECT. *Bioorg. Med. Chem. Lett.* **2015**, Ahead of Print.

(16) Rangacharyulu, C.; Roh, C. K. Isotopes for combined PET/SPECT imaging. *J. Radioanal. Nucl. Chem.* **2015**, Ahead of Print.

(17) Zhu, L.; Ploessl, K.; Kung, H. F. PET/SPECT imaging agents for neurodegenerative diseases. *Chem. Soc. Rev.* **2014**, *43*, 6683-6691.

(18) Borden, M.; Sirsi, S. Ultrasound imaging. Better contrast with vesicles. *Nat. Nanotechnol.* **2014**, *9*, 248-249.

(19) Kiessling, F.; Fokong, S.; Bzyl, J.; Lederle, W.; Palmowski, M.; Lammers, T. Recent advances in molecular, multimodal and theranostic ultrasound imaging. *Adv. Drug Delivery Rev.* **2014**, *72*, 15-27.

(20) Sakadzic, S.; Lee, J.; Boas, D. A.; Ayata, C. High-resolution in vivo optical imaging of stroke injury and repair. *Brain Res.* **2015**, Ahead of Print.

(21) Botz, B.; Bolcskei, K.; Kemeny, A.; Sandor, Z.; Tekus, V.; Setalo, G., Jr.; Csepregi, J.; Mocsai, A.; Pinter, E.; Kollar, L.; Helyes, Z. Hydrophobic cyanine dye-doped micelles for optical in vivo imaging of plasma leakage and vascular disruption. *J. Biomed. Opt.* **2015**, *20*, 016022/016021-016022/016029.

(22) Byrne, W. L.; DeLille, A.; Kuo, C.; de Jong, J. S.; van Dam, G. M.; Francis, K. P.; Tangney, M. Use of optical imaging to progress novel therapeutics to the clinic. *J. Controlled Release* **2013**, *172*, 523-534.

(23) Kneuer, R.; Gremlich, H.-U.; Beckmann, N.; Jetzfellner, T.; Ntziachristos, V. In vivo fluorescence optical and multi-modal imaging in pharmacological research: from chemistry to therapy monitoring. *RSC Drug Discovery Ser.* **2012**, *15*, 343-370.

(24) Brown, R. W.; Cheng, Y. C. N.; Haacke, E. M.; Thompson, M. R.; Venkatesan, R.; Editors: *Magnetic Resonance Imaging: Physical Properties and Sequence Design, 2nd Edition*; Wiley-Blackwell, 2014.

(25) Rocchi, L.; Niccolini, F.; Politis, M. Recent imaging advances in neurology. *J. Neurol.* **2015**, Ahead of Print.

(26) Hwang, J.-H.; Choi, C. S. Use of in vivo magnetic resonance spectroscopy for studying metabolic diseases. *Exp. Mol. Med.* **2015**, *47*, e139.

(27) Siegel, R. L.; Miller, K. D.; Jemal, A. Cancer statistics, 2016. *CA Cancer J Clin* **2016**, *66*, 7-30.

(28) Weissleder, R. Scaling down imaging: molecular mapping of cancer in mice. *Nature Reviews Cancer* **2002**, *2*, 11-18.

(29) Weissleder, R. Molecular imaging in cancer. *Science* **2006**, *312*, 1168-1171.

(30) Heyn, C.; Ronald, J. A.; Ramadan, S. S.; Snir, J. A.; Barry, A. M.; MacKenzie, L. T.; Mikulis, D. J.; Palmieri, D.; Bronder, J. L.; Steeg, P. S.; Yoneda, T.; MacDonald, I. C.; Chambers, A. F.; Rutt, B. K.; Foster, P. J. In vivo MRI of cancer cell fate at the single-cell level in a mouse model of breast cancer metastasis to the brain. *Magn Reson Med* **2006**, *56*, 1001-1010.

(31) Srivastava, A. K.; Kadayakkara, D. K.; Bar-Shir, A.; Gilad, A. A.; McMahon, M. T.; Bulte, J. W. Advances in using MRI probes and sensors for in vivo cell tracking as applied to regenerative medicine. *Dis Model Mech* **2015**, *8*, 323-336.

(32) Bulte, J. W. In vivo MRI cell tracking: clinical studies. *AJR Am J Roentgenol* **2009**, *193*, 314-325.

(33) Vuu, K.; Xie, J.; McDonald, M. A.; Bernardo, M.; Hunter, F.; Zhang, Y.; Li, K.; Bednarski, M.; Guccione, S. Gadolinium-rhodamine nanoparticles for cell labeling and tracking via magnetic resonance and optical imaging. *Bioconjug Chem* **2005**, *16*, 995-999.

(34) Manus, L. M.; Mastarone, D. J.; Waters, E. A.; Zhang, X.-Q.; Schultz-Sikma, E. A.; MacRenaris, K. W.; Ho, D.; Meade, T. J. Gd(III)-Nanodiamond Conjugates for MRI Contrast Enhancement. *Nano Letters* **2009**, *10*, 484-489.

(35) Bull, S. R.; Guler, M. O.; Bras, R. E.; Meade, T. J.; Stupp, S. I. Self-assembled peptide amphiphile nanofibers conjugated to MRI contrast agents. *Nano Letters* **2005**, *5*, 1-4.

(36) Hung, A. H.; Holbrook, R. J.; Rotz, M. W.; Glasscock, C. J.; Mansukhani, N. D.; MacRenaris, K. W.; Manus, L. M.; Duch, M. C.; Dam, K. T.; Hersam, M. C.; Meade, T. J. Graphene Oxide Enhances Cellular Delivery of Hydrophilic Small Molecules by Co-incubation. *ACS Nano* **2014**, *8*, 10168-10177.

(37) Jensen, S. A.; Day, E. S.; Ko, C. H.; Hurley, L. A.; Luciano, J. P.; Kouri, F. M.; Merkel, T. J.; Luthi, A. J.; Patel, P. C.; Cutler, J. I.; Daniel, W. L.; Scott, A. W.; Rotz, M. W.; Meade, T. J.; Giljohann, D. A.; Mirkin, C. A.; Stegh, A. H. Spherical Nucleic Acid Nanoparticle Conjugates as an RNAi-Based Therapy for Glioblastoma. *Science Translational Medicine* **2013**, *5*, 209ra152.

(38) Manus, L. M.; Mastarone, D. J.; Waters, E. A.; Zhang, X. Q.; Schultz-Sikma, E. A.; Macrenaris, K. W.; Ho, D.; Meade, T. J. Gd(III)-nanodiamond conjugates for MRI contrast enhancement. *Nano Lett* **2010**, *10*, 484-489.

(39) Tóth, É.; Bolskar, R. D.; Borel, A.; González, G.; Helm, L.; Merbach, A. E.; Sitharaman, B.; Wilson, L. J. Water-Soluble Gadofullerenes: Toward High-Relaxivity, pH-Responsive MRI Contrast Agents. *Journal of the American Chemical Society* **2005**, *127*, 799-805.

(40) Richard, C.; Doan, B.-T.; Beloeil, J.-C.; Bessodes, M.; Tóth, É.; Scherman, D. Noncovalent Functionalization of Carbon Nanotubes with Amphiphilic Gd3+ Chelates: Toward Powerful T1 and T2 MRI Contrast Agents. *Nano Letters* **2008**, *8*, 232-236.

(41) Moore, L.; Yang, J.; Lan, T. T.; Osawa, E.; Lee, D. K.; Johnson, W. D.; Xi, J.; Chow, E. K.; Ho, D. Biocompatibility Assessment of Detonation Nanodiamond in Non-Human Primates and Rats Using Histological, Hematologic, and Urine Analysis. *ACS Nano* **2016**, *10*, 7385-7400.

(42) Chaudhary, H. M.; Duttagupta, A. S.; Jadhav, K. R.; Chilajwar, S. V.; Kadam, V. J. Nanodiamonds as a New Horizon for Pharmaceutical and Biomedical Applications. *Curr Drug Deliv* **2015**, *12*, 271-281.

(43) Vaijayanthimala, V.; Lee, D. K.; Kim, S. V.; Yen, A.; Tsai, N.; Ho, D.; Chang, H. C.; Shenderova, O. Nanodiamond-mediated drug delivery and imaging: challenges and opportunities. *Expert Opin Drug Deliv* **2015**, *12*, 735-749.

(44) Chow, E. K.; Zhang, X.-Q.; Chen, M.; Lam, R.; Robinson, E.; Huang, H.; Schaffer, D.; Osawa, E.; Goga, A.; Ho, D. Nanodiamond therapeutic delivery agents mediate enhanced chemoresistant tumor treatment. *Science Translational Medicine* **2011**, *3*, 73ra21.

(45) Merkel, T. J.; DeSimone, J. M. Dodging Drug-Resistant Cancer with Diamonds. *Science Translational Medicine* **2011**, *3*, 73ps78.

(46) Rotz, M. W.; Culver, K. S. B.; Parigi, G.; MacRenaris, K. W.; Luchinat, C.; Odom, T. W.; Meade, T. J. High Relaxivity Gd(III)–DNA Gold Nanostars: Investigation of Shape Effects on Proton Relaxation. *ACS Nano* **2015**, *9*, 3385-3396.

(47) Alric, C.; Taleb, J.; Duc, G. L.; Mandon, C.; Billotey, C.; Meur-Herland, A. L.; Brochard, T.; Vocanson, F.; Janier, M.; Perriat, P.; Roux, S.; Tillement, O. Gadolinium Chelate Coated Gold Nanoparticles As Contrast Agents for Both X-ray Computed Tomography and Magnetic Resonance Imaging. *Journal of the American Chemical Society* **2008**, *130*, 5908-5915.

(48) Debouttière, P. J.; Roux, S.; Vocanson, F.; Billotey, C.; Beuf, O.; Favre-Réguillon, A.; Lin, Y.; Pellet-Rostaing, S.; Lamartine, R.; Perriat, P.; Tillement, O. Design of Gold Nanoparticles for Magnetic Resonance Imaging. *Advanced Functional Materials* **2006**, *16*, 2330-2339.

(49) Song, Y.; Xu, X.; MacRenaris, K. W.; Zhang, X.-Q.; Mirkin, C. A.; Meade, T. J. Multimodal Gadolinium-Enriched DNA–Gold Nanoparticle Conjugates for Cellular Imaging. *Angewandte Chemie International Edition* **2009**, *48*, 9143-9147.

(50) Qin, H.; Zhou, T.; Yang, S.; Chen, Q.; Xing, D. Gadolinium(III)-gold nanorods for MRI and photoacoustic imaging dual-modality detection of macrophages in atherosclerotic inflammation. *Nanomedicine* **2013**, *8*, 1611-1624.

(51) Sun, H.; Yuan, Q.; Zhang, B.; Ai, K.; Zhang, P.; Lu, L. GdIII functionalized gold nanorods for multimodal imaging applications. *Nanoscale* **2011**, *3*, 1990-1996.

(52) Park, J.-A.; Reddy, P. A. N.; Kim, H.-K.; Kim, I.-S.; Kim, G.-C.; Chang, Y.; Kim, T.-J. Gold nanoparticles functionalised by Gd-complex of DTPA-bis(amide) conjugate of glutathione as an MRI contrast agent. *Bioorganic & Medicinal Chemistry Letters* **2008**, *18*, 6135-6137.

(53) Chen, Q.; Wang, H.; Liu, H.; Wen, S.; Peng, C.; Shen, M.; Zhang, G.; Shi, X. Multifunctional Dendrimer-Entrapped Gold Nanoparticles Modified with RGD Peptide for Targeted Computed Tomography/Magnetic Resonance Dual-Modal Imaging of Tumors. *Anal. Chem. (Washington, DC, U. S.)* **2015**, *87*, 3949-3956.

(54) Zeng, Y.; Zhang, D.; Wu, M.; Liu, Y.; Zhang, X.; Li, L.; Li, Z.; Han, X.; Wei, X.; Liu, X. Lipid-AuNPs@PDA Nanohybrid for MRI/CT Imaging and Photothermal Therapy of Hepatocellular Carcinoma. *ACS Appl. Mater. Interfaces* **2014**, *6*, 14266-14277.

(55) Coughlin, A. J.; Ananta, J. S.; Deng, N.; Larina, I. V.; Decuzzi, P.; West, J. L. Gadolinium-Conjugated Gold Nanoshells for Multimodal Diagnostic Imaging and Photothermal Cancer Therapy. *Small* **2014**, *10*, 556-565.

(56) Marradi, M.; Alcantara, D.; de la Fuente, J. M.; Garcia-Martin, M. L.; Cerdan, S.; Penades, S. Paramagnetic Gd-based gold glyconanoparticles as probes for MRI: tuning relaxivities with sugars. *Chemical Communications* **2009**, 3922-3924.

(57) Irure, A.; Marradi, M.; Arnaiz, B.; Genicio, N.; Padro, D.; Penades, S. Sugar/gadolinium-loaded gold nanoparticles for labelling and imaging cells by magnetic resonance imaging. *Biomaterials Science* **2013**, *1*, 658-668.

(58) Chen, Q.; Li, K.; Wen, S.; Liu, H.; Peng, C.; Cai, H.; Shen, M.; Zhang, G.; Shi, X. Targeted CT/MR dual mode imaging of tumors using multifunctional dendrimer-entrapped gold nanoparticles. *Biomaterials* **2013**, *34*, 5200-5209.

(59) Li, K.; Wen, S.; Larson, A. C.; Shen, M.; Zhang, Z.; Chen, Q.; Shi, X.; Zhang, G. Multifunctional dendrimer-based nanoparticles for in vivo MR/CT dual-modal molecular imaging of breast cancer. *Int. J. Nanomed.* **2012**, *8*, 2589-2600.

(60) Beija, M.; Li, Y.; Duong, H. T.; Laurent, S.; Elst, L. V.; Muller, R. N.; Lowe, A. B.; Davis, T. P.; Boyer, C. Polymer-gold nanohybrids with potential use in bimodal MRI/CT: enhancing the relaxometric properties of Gd(iii) complexes. *Journal of Materials Chemistry* **2012**, *22*, 21382-21386.

(61) Nicholls, F. J.; Rotz, M. W.; Ghuman, H.; MacRenaris, K. W.; Meade, T. J.; Modo, M. DNA-gadolinium-gold nanoparticles for in vivo T1 MR imaging of transplanted human neural stem cells. *Biomaterials* **2016**, *77*, 291-306.

(62) Suetens, P.: *Fundamentals of medical imaging*; Cambridge university press, 2009.

(63) Herman, G. T.: *Fundamentals of computerized tomography: image reconstruction from projections*; Springer Science & Business Media, 2009.

(64) Brenner, D. J.; Hall, E. J. Computed Tomography — An Increasing Source of Radiation Exposure. *New England Journal of Medicine* **2007**, *357*, 2277-2284.

(65) Hainfeld, J.; Slatkin, D.; Focella, T.; Smilowitz, H. Gold nanoparticles: a new X-ray contrast agent. *The British journal of radiology* **2014**.

(66) Kim, D.; Park, S.; Lee, J. H.; Jeong, Y. Y.; Jon, S. Antibiofouling polymer-coated gold nanoparticles as a contrast agent for in vivo X-ray computed tomography imaging. *Journal of the American Chemical Society* **2007**, *129*, 7661-7665.

(67) Cai, Q.-Y.; Kim, S. H.; Choi, K. S.; Kim, S. Y.; Byun, S. J.; Kim, K. W.; Park, S. H.; Juhng, S. K.; Yoon, K.-H. Colloidal gold nanoparticles as a blood-pool contrast agent for X-ray computed tomography in mice. *Investigative Radiology* **2007**, *42*, 797-806.

(68) Hainfeld, J.; O'connor, M.; Dilmanian, F.; Slatkin, D.; Adams, D.; Smilowitz, H. Micro-CT enables microlocalisation and quantification of Her2-targeted gold nanoparticles within tumour regions. *The British journal of radiology* **2014**.

(69) Das, B.: Positron Emission Tomography: An Overview. In *Positron Emission Tomography*; Das, B. K., Ed.; Springer India, 2015; pp 1-6.

(70) Cherry, S.; Dahlbom, M.: PET: Physics, Instrumentation, and Scanners. In *PET*; Phelps, M., Ed.; Springer New York, 2006; pp 1-117.

(71) Gambhir, S. S. Molecular imaging of cancer with positron emission tomography. *Nature Reviews Cancer* **2002**, *2*, 683.

(72) Som, P.; Atkins, H. L.; Bandoypadhyay, D.; Fowler, J. S.; MacGregor, R. R.; Matsui, K.; Oster, Z. H.; Sacker, D. F.; Shiue, C. Y.; Turner, H.; Wan, C.-N.; Wolf, A. P.; Zabinski, S. V. A Fluorinated Glucose Analog, 2-fluoro-2-deoxy-D-glucose (F-18): Nontoxic Tracer for Rapid Tumor Detection. *Journal of Nuclear Medicine* **1980**, *21*, 670-675.

(73) Warburg, O. On the Origin of Cancer Cells. *Science* **1956**, *123*, 309-314.

(74) Schultz, M. K.; Parameswarappa, S. G.; Pigge, F. C. Synthesis of a DOTA− biotin conjugate for radionuclide chelation via Cu-free click chemistry. *Organic Letters* **2010**, *12*, 2398-2401.

(75) Simecek, J.; Zemek, O. e.; Hermann, P.; Notni, J.; Wester, H.-J. r. Tailored gallium (III) chelator NOPO: synthesis, characterization, bioconjugation, and application in preclinical Ga-68-PET imaging. *Molecular pharmaceutics* **2013**, *11*, 3893-3903.

(76) Ikotun, O. F.; Lapi, S. E. The rise of metal radionuclides in medical imaging: copper-64, zirconium-89 and yttrium-86. *Future Med Chem* **2011**, *3*, 599-621.

(77) Banerjee, S. R.; Pomper, M. G. Clinical applications of gallium-68. *Applied Radiation and Isotopes* **2013**, *76*, 2-13.

(78) Shokeen, M.; Anderson, C. J. Molecular Imaging of Cancer with Copper-64 Radiopharmaceuticals and Positron Emission Tomography (PET). *Accounts of Chemical Research* **2009**, *42*, 832-841.

(79) Luehmann, H. P.; Pressly, E. D.; Detering, L.; Wang, C.; Pierce, R.; Woodard, P. K.; Gropler, R. J.; Hawker, C. J.; Liu, Y. PET/CT Imaging of Chemokine Receptor CCR5 in Vascular Injury Model Using Targeted Nanoparticle. *Journal of Nuclear Medicine* **2014**, *55*, 629-634.

(80) Feger, S.; Rief, M.; Zimmermann, E.; Richter, F.; Roehle, R.; Dewey, M.; Schönenberger, E. Patient satisfaction with coronary CT angiography, myocardial CT perfusion, myocardial perfusion MRI, SPECT myocardial perfusion imaging and conventional coronary angiography. *European radiology* **2015**, 1-10.

(81) Rangacharyulu, C.; Roh, C. K. Isotopes for combined PET/SPECT imaging. *Journal of Radioanalytical and Nuclear Chemistry* **2015**, 1-6.

(82) Black, K. C. L.; Akers, W. J.; Sudlow, G.; Xu, B.; Laforest, R.; Achilefu, S. Dual-radiolabeled nanoparticle SPECT probes for bioimaging. *Nanoscale* **2015**, *7*, 440-444.

(83) Haidekker, M.: Ultrasound Imaging. In *Medical Imaging Technology*; SpringerBriefs in Physics; Springer New York, 2013; pp 97-110.

(84) Berg, W. A.; Zhang, Z.; Lehrer, D.; et al. DEtection of breast cancer with addition of annual screening ultrasound or a single screening mri to mammography in women with elevated breast cancer risk. *JAMA* **2012**, *307*, 1394-1404.

(85) Klibanov, A. L. Targeted delivery of gas-filled microspheres, contrast agents for ultrasound imaging. *Advanced Drug Delivery Reviews* **1999**, *37*, 139-157.

(86) Willmann, J. K.; Kimura, R. H.; Deshpande, N.; Lutz, A. M.; Cochran, J. R.; Gambhir, S. S. Targeted Contrast-Enhanced Ultrasound Imaging of Tumor Angiogenesis with Contrast Microbubbles Conjugated to Integrin-Binding Knottin Peptides. *Journal of Nuclear Medicine* **2010**, *51*, 433-440.

(87) Massoud, T. F.; Gambhir, S. S. Molecular imaging in living subjects: seeing fundamental biological processes in a new light. *Genes & development* **2003**, *17*, 545-580.

(88) Quan, L.; Liu, S.; Sun, T.; Guan, X.; Lin, W.; Xie, Z.; Huang, Y.; Wang, Y.; Jing, X. Near-Infrared Emitting Fluorescent BODIPY Nanovesicles for in Vivo Molecular Imaging and Drug Delivery. *ACS Applied Materials & Interfaces* **2014**, *6*, 16166-16173.

(89) Badr, C.: Bioluminescence Imaging: Basics and Practical Limitations. In *Bioluminescent Imaging*; Badr, C. E., Ed.; Methods in Molecular Biology; Humana Press, 2014; Vol. 1098; pp 1-18.

(90) Zhao, D.; Richer, E.; Antich, P. P.; Mason, R. P. Antivascular effects of combretastatin A4 phosphate in breast cancer xenograft assessed using dynamic bioluminescence imaging and confirmed by MRI. *The FASEB Journal* **2008**, *22*, 2445-2451.

(91) Lauterbur, P. C. Image formation by induced local interactions. Examples employing nuclear magnetic resonance. 1973. *Clinical orthopaedics and related research* **1989**, 3-6.

(92) Damadian, R. Tumor detection by nuclear magnetic resonance. *Science* **1971**, *171*, 1151-1153.

(93) Shellock, F. G.; Spinazzi, A. MRI Safety Update 2008: Part 2, Screening Patients for MRI. *American Journal of Roentgenology* **2008**, *191*, 1140-1149.

(94) Shellock, F. G.; Spinazzi, A. MRI Safety Update 2008: Part 1, MRI Contrast Agents and Nephrogenic Systemic Fibrosis. *American Journal of Roentgenology* **2008**, *191*, 1129-1139.

(95) Caravan, P.; Ellison, J. J.; McMurry, T. J.; Lauffer, R. B. Gadolinium(III) Chelates as MRI Contrast Agents: Structure, Dynamics, and Applications. *Chemical Reviews* **1999**, *99*, 2293-2352.

(96) L. Villaraza, A. J.; Bumb, A.; Brechbiel, M. W. Macromolecules, Dendrimers, and Nanomaterials in Magnetic Resonance Imaging: The Interplay between Size, Function, and Pharmacokinetics. *Chemical Reviews* **2010**, *110*, 2921-2959.

(97) Magnetic Resonance Imaging. In *Magnetic Resonance Imaging*; John Wiley & Sons Ltd, 2014; pp 1-17.

(98) Raymond, K. N.; Pierre, V. C. Next Generation, High Relaxivity Gadolinium MRI Agents. *Bioconjugate Chemistry* **2005**, *16*, 3-8.

(99) Caravan, P.; Ellison, J. J.; McMurry, T. J.; Lauffer, R. B. Gadolinium(III) Chelates as MRI Contrast Agents: Structure, Dynamics, and Applications. *Chem Rev* **1999**, *99*, 2293-2352.

(100) Helm, L.; Merbach, A. E.; Tóth, É.; ebrary Inc.: The chemistry of contrast agents in medical magnetic resonance imaging. 2nd ed.; John Wiley & Sons Inc.,: Hoboken, N.J., 2013; pp xvi, 496 p. ill. (some col.).

(101) Winter, P. M.; Caruthers, S. D.; Wickline, S. A.; Lanza, G. M. Molecular imaging by MRI. *Curr Cardiol Rep* **2006**, *8*, 65-69.

(102) Villaraza, A. J.; Bumb, A.; Brechbiel, M. W. Macromolecules, dendrimers, and nanomaterials in magnetic resonance imaging: the interplay between size, function, and pharmacokinetics. *Chem Rev* **2010**, *110*, 2921-2959.

(103) Helm, L.; Merbach, A. E.; Tóth, É.; ebrary Inc.: *The chemistry of contrast agents in medical magnetic resonance imaging*; 2nd ed.; John Wiley & Sons Inc.: Hoboken, N.J., 2013.

(104) Claes, A.; Gambarota, G.; Hamans, B.; van Tellingen, O.; Wesseling, P.; Maass, C.; Heerschap, A.; Leenders, W. Magnetic resonance imaging-based detection of glial brain tumors in mice after antiangiogenic treatment. *International journal of cancer. Journal international du cancer* **2008**, *122*, 1981-1986.

(105) Wang, Y. X. Superparamagnetic iron oxide based MRI contrast agents: Current status of clinical application. *Quantitative imaging in medicine and surgery* **2011**, *1*, 35-40.

(106) Manus, L. M.; Strauch, R. C.; Hung, A. H.; Eckermann, A. L.; Meade, T. J. Analytical Methods for Characterizing Magnetic Resonance Probes. *Analytical Chemistry* **2012**, *84*, 6278-6287.

(107) Caravan, P.; Farrar, C. T.; Frullano, L.; Uppal, R. Influence of molecular parameters and increasing magnetic field strength on relaxivity of gadolinium- and manganese-based T1 contrast agents. *Contrast media & molecular imaging* **2009**, *4*, 89-100.

(108) Aime, S.; Calabi, L.; Cavallotti, C.; Gianolio, E.; Giovenzana, G. B.; Losi, P.; Maiocchi, A.; Palmisano, G.; Sisti, M. [Gd-AAZTA]-: A New Structural Entry for an Improved Generation of MRI Contrast Agents. *Inorganic Chemistry* **2004**, *43*, 7588-7590.

(109) Costa, J.; Tóth, É.; Helm, L.; Merbach, A. E. Dinuclear, Bishydrated GdIII Polyaminocarboxylates with a Rigid Xylene Core Display Remarkable Proton Relaxivities. *Inorganic Chemistry* **2005**, *44*, 4747-4755.

(110) Costa, J.; Ruloff, R.; Burai, L.; Helm, L.; Merbach, A. E. Rigid MIIL2Gd2III (M = Fe, Ru) Complexes of a Terpyridine-Based Heteroditopic Chelate: A Class of Candidates for MRI Contrast Agents. *Journal of the American Chemical Society* **2005**, *127*, 5147-5157.

(111) Livramento, J. B.; Tóth, É.; Sour, A.; Borel, A.; Merbach, A. E.; Ruloff, R. High Relaxivity Confined to a Small Molecular Space: A Metallostar-Based, Potential MRI Contrast Agent. *Angewandte Chemie International Edition* **2005**, *44*, 1480-1484.

(112) Cohen, S. M.; Xu, J.; Radkov, E.; Raymond, K. N.; Botta, M.; Barge, A.; Aime, S. Syntheses and Relaxation Properties of Mixed Gadolinium Hydroxypyridinonate MRI Contrast Agents. *Inorganic Chemistry* **2000**, *39*, 5747-5756.

(113) Xu, J.; Churchill, D. G.; Botta, M.; Raymond, K. N. Gadolinium(III) 1,2-Hydroxypyridonate-Based Complexes: Toward MRI Contrast Agents of High Relaxivity1. *Inorganic Chemistry* **2004**, *43*, 5492-5494.

(114) Mastarone, D. J.; Harrison, V. S. R.; Eckermann, A. L.; Parigi, G.; Luchinat, C.; Meade, T. J. A Modular System for the Synthesis of Multiplexed Magnetic Resonance Probes. *Journal of the American Chemical Society* **2011**, *133*, 5329-5337.

(115) Casali, C.; Janier, M.; Canet, E.; Obadia, J. F.; Benderbous, S.; Corot, C.; Revel, D. Evaluation of Gd-DOTA-labeled dextran polymer as an intravascular MR contrast agent for myocardial perfusion. *Academic Radiology* **1998**, *5, Supplement 1*, S214-S218.

(116) Paris, J.; Gameiro, C.; Humblet, V.; Mohapatra, P. K.; Jacques, V.; Desreux, J. F. Auto-Assembling of Ditopic Macrocyclic Lanthanide Chelates with Transition-Metal Ions. Rigid Multimetallic High Relaxivity Contrast Agents for Magnetic Resonance Imaging. *Inorganic Chemistry* **2006**, *45*, 5092-5102.

(117) Song, Y.; Kohlmeir, E. K.; Meade, T. J. Synthesis of Multimeric MR Contrast Agents for Cellular Imaging. *Journal of the American Chemical Society* **2008**, *130*, 6662-6663.

(118) Gløgård, C.; Stensrud, G.; Hovland, R.; Fossheim, S. L.; Klaveness, J. Liposomes as carriers of amphiphilic gadolinium chelates: the effect of membrane composition on incorporation efficacy and in vitro relaxivity. *International Journal of Pharmaceutics* **2002**, *233*, 131-140.

(119) André, J. P.; Tóth, É.; Fischer, H.; Seelig, A.; Mäcke, H. R.; Merbach, A. E. High Relaxivity for Monomeric Gd (DOTA)-Based MRI Contrast Agents, Thanks to Micellar Self-Organization. *Chemistry-A European Journal* **1999**, *5*, 2977-2983.

(120) Hovland, R.; Glogard, C.; Aasen, A. J.; Klaveness, J. Gadolinium DO3A derivatives mimicking phospholipids; preparation and in vitro evaluation as pH responsive MRI contrast agents. *Journal of the Chemical Society, Perkin Transactions 2* **2001**, 929-933.

(121) Preslar, A. T.; Parigi, G.; McClendon, M. T.; Sefick, S. S.; Moyer, T. J.; Haney, C. R.; Waters, E. A.; MacRenaris, K. W.; Luchinat, C.; Stupp, S. I.; Meade, T. J. Gd(III)-Labeled Peptide Nanofibers for Reporting on Biomaterial Localization in Vivo. *ACS Nano* **2014**, *8*, 7325-7332.

(122) Caravan, P.; Cloutier, N. J.; Greenfield, M. T.; McDermid, S. A.; Dunham, S. U.; Bulte, J. W. M.; Amedio, J. C.; Looby, R. J.; Supkowski, R. M.; Horrocks, W. D.; McMurry, T. J.; Lauffer, R. B. The Interaction of MS-325 with Human Serum Albumin and Its Effect on Proton Relaxation Rates. *Journal of the American Chemical Society* **2002**, *124*, 3152-3162.

(123) Caravan, P.; Parigi, G.; Chasse, J. M.; Cloutier, N. J.; Ellison, J. J.; Lauffer, R. B.; Luchinat, C.; McDermid, S. A.; Spiller, M.; McMurry, T. J. Albumin Binding, Relaxivity, and Water Exchange Kinetics of the Diastereoisomers of MS-325, a Gadolinium(III)-Based Magnetic Resonance Angiography Contrast Agent. *Inorganic Chemistry* **2007**, *46*, 6632-6639.

(124) Prasuhn, J. D. E.; Yeh, R. M.; Obenaus, A.; Manchester, M.; Finn, M. G. Viral MRI contrast agents: coordination of Gd by native virions and attachment of Gd complexes by azide-alkyne cycloaddition. *Chemical Communications* **2007**, 1269-1271.

(125) Pokorski, J. K.; Breitenkamp, K.; Liepold, L. O.; Qazi, S.; Finn, M. G. Functional Virus-Based Polymer–Protein Nanoparticles by Atom Transfer Radical Polymerization. *Journal of the American Chemical Society* **2011**, *133*, 9242-9245.

(126) Soto, C. M.; Ratna, B. R. Virus hybrids as nanomaterials for biotechnology. *Current Opinion in Biotechnology* **2010**, *21*, 426-438.

(127) Allen, M.; Bulte, J. W. M.; Liepold, L.; Basu, G.; Zywicke, H. A.; Frank, J. A.; Young, M.; Douglas, T. Paramagnetic viral nanoparticles as potential high-relaxivity magnetic resonance contrast agents. *Magnetic Resonance in Medicine* **2005**, *54*, 807-812.

(128) Liepold, L.; Anderson, S.; Willits, D.; Oltrogge, L.; Frank, J. A.; Douglas, T.; Young, M. Viral capsids as MRI contrast agents. *Magnetic Resonance in Medicine* **2007**, *58*, 871-879.

(129) Caravan, P. Strategies for increasing the sensitivity of gadolinium based MRI contrast agents. *Chemical Society Reviews* **2006**, *35*, 512-523.

(130) Driehuys, B. Toward Molecular Imaging with Xenon MRI. *Science* **2006**, *314*, 432-433.

(131) Schwanhausser, B.; Busse, D.; Li, N.; Dittmar, G.; Schuchhardt, J.; Wolf, J.; Chen, W.; Selbach, M. Global quantification of mammalian gene expression control. *Nature* **2011**, *473*, 337-342.

(132) Anelli, Pier L.; Bertini, I.; Fragai, M.; Lattuada, L.; Luchinat, C.; Parigi, G. Sulfonamide-Functionalized Gadolinium DTPA Complexes as Possible Contrast Agents for MRI: A Relaxometric Investigation. *European Journal of Inorganic Chemistry* **2000**, *2000*, 625-630.

(133) De León-Rodríguez, L. M.; Ortiz, A.; Weiner, A. L.; Zhang, S.; Kovacs, Z.; Kodadek, T.; Sherry, A. D. Magnetic Resonance Imaging Detects a Specific Peptide−Protein Binding Event. *Journal of the American Chemical Society* **2002**, *124*, 3514-3515.

(134) Botnar, R. M.; Perez, A. S.; Witte, S.; Wiethoff, A. J.; Laredo, J.; Hamilton, J.; Quist, W.; Parsons, E. C.; Vaidya, A.; Kolodziej, A.; Barrett, J. A.; Graham, P. B.; Weisskoff, R. M.; Manning, W. J.; Johnstone, M. T. In Vivo Molecular Imaging of Acute and Subacute Thrombosis Using a Fibrin-Binding Magnetic Resonance Imaging Contrast Agent. *Circulation* **2004**, *109*, 2023-2029.

(135) Overoye-Chan, K.; Koerner, S.; Looby, R. J.; Kolodziej, A. F.; Zech, S. G.; Deng, Q.; Chasse, J. M.; McMurry, T. J.; Caravan, P. EP-2104R: A Fibrin-Specific Gadolinium-Based MRI Contrast Agent for Detection of Thrombus. *Journal of the American Chemical Society* **2008**, *130*, 6025-6039.

(136) De León-Rodríguez, L. M.; Kovacs, Z. The Synthesis and Chelation Chemistry of DOTA−Peptide Conjugates. *Bioconjugate Chemistry* **2008**, *19*, 391-402.

(137) Karfeld, L. S.; Bull, S. R.; Davis, N. E.; Meade, T. J.; Barron, A. E. Use of a Genetically Engineered Protein for the Design of a Multivalent MRI Contrast Agent. *Bioconjugate Chemistry* **2007**, *18*, 1697-1700.

(138) Strauch, R. C.; Mastarone, D. J.; Sukerkar, P. A.; Song, Y.; Ipsaro, J. J.; Meade, T. J. Reporter Protein-Targeted Probes for Magnetic Resonance Imaging. *Journal of the American Chemical Society* **2011**, *133*, 16346-16349.

(139) Gustafsson, B.; Youens, S.; Louie, A. Y. Development of Contrast Agents Targeted to Macrophage Scavenger Receptors for MRI of Vascular Inflammation. *Bioconjugate Chemistry* **2006**, *17*, 538-547.

(140) Dirksen, A.; Langereis, S.; de Waal, B. F. M.; van Genderen, M. H. P.; Hackeng, T. M.; Meijer, E. W. A supramolecular approach to multivalent target-specific MRI contrast agents for angiogenesis. *Chemical Communications* **2005**, 2811-2813.

(141) Jung, H.-i.; Kettunen, M. I.; Davletov, B.; Brindle, K. M. Detection of Apoptosis Using the C2A Domain of Synaptotagmin I. *Bioconjugate Chemistry* **2004**, *15*, 983-987.

(142) Neves, A. A.; Krishnan, A. S.; Kettunen, M. I.; Hu, D.-e.; de Backer, M. M.; Davletov, B.; Brindle, K. M. A Paramagnetic Nanoprobe To Detect Tumor Cell Death Using Magnetic Resonance Imaging. *Nano Letters* **2007**, *7*, 1419-1423.

(143) Sperling, R. A.; Parak, W. J.: *Surface modification, functionalization and bioconjugation of colloidal inorganic nanoparticles*, 2010; Vol. 368.

(144) Anglin, E. J.; Cheng, L.; Freeman, W. R.; Sailor, M. J. Porous silicon in drug delivery devices and materials. *Advanced Drug Delivery Reviews* **2008**, *60*, 1266-1277.

(145) Vallet-Regí, M.; Balas, F.; Arcos, D. Mesoporous Materials for Drug Delivery. *Angewandte Chemie International Edition* **2007**, *46*, 7548-7558.

(146) Rieter, W. J.; Kim, J. S.; Taylor, K. M. L.; An, H.; Lin, W.; Tarrant, T.; Lin, W. Hybrid Silica Nanoparticles for Multimodal Imaging. *Angewandte Chemie International Edition* **2007**, *46*, 3680-3682.

(147) Taylor, K. M. L.; Kim, J. S.; Rieter, W. J.; An, H.; Lin, W.; Lin, W. Mesoporous Silica Nanospheres as Highly Efficient MRI Contrast Agents. *Journal of the American Chemical Society* **2008**, *130*, 2154-2155.

(148) Carniato, F.; Tei, L.; Cossi, M.; Marchese, L.; Botta, M. A Chemical Strategy for the Relaxivity Enhancement of GdIII Chelates Anchored on Mesoporous Silica Nanoparticles. *Chemistry – A European Journal* **2010**, *16*, 10727-10734.

(149) Davis, J. J.; Huang, W.-Y.; Davies, G.-L. Location-tuned relaxivity in Gd-doped mesoporous silica nanoparticles. *Journal of Materials Chemistry* **2012**, *22*, 22848-22850.

(150) Liu, Y.; Chen, Z.; Liu, C.; Yu, D.; Lu, Z.; Zhang, N. Gadolinium-loaded polymeric nanoparticles modified with Anti-VEGF as multifunctional MRI contrast agents for the diagnosis of liver cancer. *Biomaterials* **2011**, *32*, 5167-5176.

(151) Ratzinger, G.; Agrawal, P.; Körner, W.; Lonkai, J.; Sanders, H. M. H. F.; Terreno, E.; Wirth, M.; Strijkers, G. J.; Nicolay, K.; Gabor, F. Surface modification of PLGA nanospheres with Gd-DTPA and Gd-DOTA for high-relaxivity MRI contrast agents. *Biomaterials* **2010**, *31*, 8716-8723.

(152) Courant, T.; Roullin, V. G.; Cadiou, C.; Callewaert, M.; Andry, M. C.; Portefaix, C.; Hoeffel, C.; de Goltstein, M. C.; Port, M.; Laurent, S.; Elst, L. V.; Muller, R.; Molinari, M.; Chuburu, F. Hydrogels Incorporating GdDOTA: Towards Highly Efficient Dual T1/T2 MRI Contrast Agents. *Angewandte Chemie International Edition* **2012**, *51*, 9119-9122.

(153) Langereis, S.; Dirksen, A.; Hackeng, T. M.; van Genderen, M. H. P.; Meijer, E. W. Dendrimers and magnetic resonance imaging. *New Journal of Chemistry* **2007**, *31*, 1152-1160.

(154) Menjoge, A. R.; Kannan, R. M.; Tomalia, D. A. Dendrimer-based drug and imaging conjugates: design considerations for nanomedical applications. *Drug Discovery Today* **2010**, *15*, 171-185.

(155) Adam, G.; Neuerburg, J.; Spüntrup, E.; Mühler, A.; Surg, K. S. V.; Günther, R. W. Gd-DTPA-cascade-polymer: Potential blood pool contrast agent for MR imaging. *Journal of Magnetic Resonance Imaging* **1994**, *4*, 462-466.

(156) Langereis, S.; de Lussanet, Q. G.; van Genderen, M. H. P.; Meijer, E. W.; Beets-Tan, R. G. H.; Griffioen, A. W.; van Engelshoven, J. M. A.; Backes, W. H. Evaluation of Gd(III)DTPA-terminated poly(propylene imine) dendrimers as contrast agents for MR imaging. *NMR in Biomedicine* **2006**, *19*, 133-141.

(157) Boswell, C. A.; Eck, P. K.; Regino, C. A. S.; Bernardo, M.; Wong, K. J.; Milenic, D. E.; Choyke, P. L.; Brechbiel, M. W. Synthesis, Characterization, and Biological Evaluation of Integrin αvβ3-Targeted PAMAM Dendrimers. *Molecular pharmaceutics* **2008**, *5*, 527-539.

(158) Han, L.; Li, J.; Huang, S.; Huang, R.; Liu, S.; Hu, X.; Yi, P.; Shan, D.; Wang, X.; Lei, H.; Jiang, C. Peptide-conjugated polyamidoamine dendrimer as a nanoscale tumor-targeted T1 magnetic resonance imaging contrast agent. *Biomaterials* **2011**, *32*, 2989-2998.

(159) Rudovsky, J.; Hermann, P.; Botta, M.; Aime, S.; Lukes, I. Dendrimeric Gd(iii) complex of a monophosphinated DOTA analogue: optimizing relaxivity by reducing internal motion. *Chemical Communications* **2005**, 2390-2392.

(160) Kojima, C.; Turkbey, B.; Ogawa, M.; Bernardo, M.; Regino, C. A. S.; Bryant Jr, L. H.; Choyke, P. L.; Kono, K.; Kobayashi, H. Dendrimer-based MRI contrast agents: the effects of PEGylation on relaxivity and pharmacokinetics. *Nanomedicine: Nanotechnology, Biology and Medicine* **2011**, *7*, 1001-1008.

(161) Floyd, W. C.; Klemm, P. J.; Smiles, D. E.; Kohlgruber, A. C.; Pierre, V. C.; Mynar, J. L.; Fréchet, J. M. J.; Raymond, K. N. Conjugation Effects of Various Linkers on Gd(III) MRI Contrast Agents with Dendrimers: Optimizing the Hydroxypyridinonate (HOPO) Ligands with Nontoxic, Degradable Esteramide (EA) Dendrimers for High Relaxivity. *Journal of the American Chemical Society* **2011**, *133*, 2390-2393.

(162) Israelachvili, J. N.; Mitchell, D. J.; Ninham, B. W. Theory of self-assembly of hydrocarbon amphiphiles into micelles and bilayers. *Journal of the Chemical Society, Faraday Transactions 2: Molecular and Chemical Physics* **1976**, *72*, 1525-1568.

(163) Jones, M.-C.; Leroux, J.-C. Polymeric micelles – a new generation of colloidal drug carriers. *European Journal of Pharmaceutics and Biopharmaceutics* **1999**, *48*, 101-111.

(164) Torchilin, V. P. Recent advances with liposomes as pharmaceutical carriers. *Nat Rev Drug Discov* **2005**, *4*, 145-160.

(165) Devoisselle, J. M.; Vion-Dury, J.; Galons, J. P.; Confort-Gouny, S.; Coustaut, D.; Canioni, P.; Cozzone, P. J. Entrapment of Gadolinium-DTPA in Liposomes: Characterization of Vesicles by P-31 NMR Spectroscopy. *Investigative Radiology* **1988**, *23*.

(166) Unger, E.; Shen, D. K.; Wu, G.; Fritz, T. Liposomes as MR contrast agents: Pros and cons. *Magnetic Resonance in Medicine* **1991**, *22*, 304-308.

(167) Accardo, A.; Tesauro, D.; Aloj, L.; Pedone, C.; Morelli, G. Supramolecular aggregates containing lipophilic Gd(III) complexes as contrast agents in MRI. *Coordination Chemistry Reviews* **2009**, *253*, 2193-2213.

(168) Lee, S.-M.; Song, Y.; Hong, B. J.; MacRenaris, K. W.; Mastarone, D. J.; O'Halloran, T. V.; Meade, T. J.; Nguyen, S. T. Modular Polymer-Caged Nanobins as a Theranostic Platform with Enhanced Magnetic Resonance Relaxivity and pH-Responsive Drug Release. *Angewandte Chemie* **2010**, *122*, 10156-10160.

(169) Gianolio, E.; Giovenzana, G. B.; Longo, D.; Longo, I.; Menegotto, I.; Aime, S. Relaxometric and Modelling Studies of the Binding of a Lipophilic Gd-AAZTA Complex to Fatted and Defatted Human Serum Albumin. *Chemistry – A European Journal* **2007**, *13*, 5785-5797.

(170) Briley-Saebo, K. C.; Geninatti-Crich, S.; Cormode, D. P.; Barazza, A.; Mulder, W. J. M.; Chen, W.; Giovenzana, G. B.; Fisher, E. A.; Aime, S.; Fayad, Z. A. High-Relaxivity Gadolinium-Modified High-Density Lipoproteins as Magnetic Resonance Imaging Contrast Agents. *The Journal of Physical Chemistry B* **2009**, *113*, 6283-6289.

(171) Dresselhaus, M. S.; Dresselhaus, G.; Eklund, P. C.: *Science of fullerenes and carbon nanotubes: their properties and applications*; Academic press, 1996.

(172) Mehra, N. K.; Mishra, V.; Jain, N. A review of ligand tethered surface engineered carbon nanotubes. *Biomaterials* **2014**, *35*, 1267-1283.

(173) Compton, O. C.; Nguyen, S. T. Graphene Oxide, Highly Reduced Graphene Oxide, and Graphene: Versatile Building Blocks for Carbon-Based Materials. *Small* **2010**, *6*, 711-723.

(174) Kato, H.; Kanazawa, Y.; Okumura, M.; Taninaka, A.; Yokawa, T.; Shinohara, H. Lanthanoid Endohedral Metallofullerenols for MRI Contrast Agents. *Journal of the American Chemical Society* **2003**, *125*, 4391-4397.

(175) Shu, C.; Corwin, F. D.; Zhang, J.; Chen, Z.; Reid, J. E.; Sun, M.; Xu, W.; Sim, J. H.; Wang, C.; Fatouros, P. P.; Esker, A. R.; Gibson, H. W.; Dorn, H. C. Facile Preparation of a New Gadofullerene-Based Magnetic Resonance Imaging Contrast Agent with High 1H Relaxivity. *Bioconjugate Chemistry* **2009**, *20*, 1186-1193.

(176) Zhang, J.; Fatouros, P. P.; Shu, C.; Reid, J.; Owens, L. S.; Cai, T.; Gibson, H. W.; Long, G. L.; Corwin, F. D.; Chen, Z.-J.; Dorn, H. C. High Relaxivity Trimetallic Nitride (Gd3N) Metallofullerene MRI Contrast Agents with Optimized Functionality. *Bioconjugate Chemistry* **2010**, *21*, 610-615.

(177) Sitharaman, B.; Kissell, K. R.; Hartman, K. B.; Tran, L. A.; Baikalov, A.; Rusakova, I.; Sun, Y.; Khant, H. A.; Ludtke, S. J.; Chiu, W.; Laus, S.; Toth, E.; Helm, L.; Merbach, A. E.; Wilson, L. J. Superparamagnetic gadonanotubes are high-performance MRI contrast agents. *Chemical Communications* **2005**, 3915-3917.

(178) Hartman, K. B.; Laus, S.; Bolskar, R. D.; Muthupillai, R.; Helm, L.; Toth, E.; Merbach, A. E.; Wilson, L. J. Gadonanotubes as Ultrasensitive pH-Smart Probes for Magnetic Resonance Imaging. *Nano Letters* **2008**, *8*, 415-419.

(179) Hung, A. H.; Duch, M. C.; Parigi, G.; Rotz, M. W.; Manus, L. M.; Mastarone, D. J.; Dam, K. T.; Gits, C. C.; MacRenaris, K. W.; Luchinat, C.; Hersam, M. C.; Meade, T. J. Mechanisms of Gadographene-Mediated Proton Spin Relaxation. *The Journal of Physical Chemistry C* **2013**, *117*, 16263-16273.

(180) Chang, I. P.; Hwang, K. C.; Chiang, C. S. Preparation of fluorescent magnetic nanodiamonds and cellular imaging. *J. Am. Chem. Soc.* **2008**, *130*, 15476.

(181) Hegyi, A.; Yablonovitch, E. Molecular Imaging by Optically Detected Electron Spin Resonance of Nitrogen-Vacancies in Nanodiamonds. *Nano letters* **2013**.

(182) Li, J.; Zhu, Y.; Li, W.; Zhang, X.; Peng, Y.; Huang, Q. Nanodiamonds as intracellular transporters of chemotherapeutic drug. *Biomaterials* **2010**, *31*, 8410-8418.

(183) Mochalin, V. N.; Shenderova, O.; Ho, D.; Gogotsi, Y. The properties and applications of nanodiamonds. *Nature Nanotechnology* **2012**, *7*, 11-23.

(184) Puzyr, A. P.; Baron, A. V.; Purtov, K. V.; Bortnikov, E. V.; Skobelev, N. N.; Mogilnaya, O. A.; Bondar, V. S. Nanodiamonds with novel properties: A biological study. *Diamond and Related Materials* **2007**, *16*, 2124-2128.

(185) Tisler, J.; Reuter, R.; Lämmle, A.; Jelezko, F.; Balasubramanian, G.; Hemmer, P. R.; Reinhard, F.; Wrachtrup, J. Highly Efficient FRET from a Single Nitrogen-Vacancy Center in Nanodiamonds to a Single Organic Molecule. *ACS Nano* **2011**, *5*, 7893-7898.

(186) Xing, Y.; Xiong, W.; Zhu, L.; Osawa, E.; Hussin, S.; Dai, L. DNA Damage in Embryonic Stem Cells Caused by Nanodiamonds. *ACS Nano* **2011**.

(187) Yuan Y, C. Y., Liu J H, Wang H; Y, L. Biodistribution and fate of nanodiamonds in vivo. *Diamond and Related Materials* **2009**, *18*, 95.

(188) Zhang, X. Q.; Chen, M.; Lam, R.; Xu, X.; Osawa, E.; Ho, D. Polymer-functionalized nanodiamond platforms as vehicles for gene delivery. *ACS Nano* **2009**, *3*, 2609-2616.

(189) Zhang, X.-Q.; Lam, R.; Xu, X.; Chow, E. K.; Kim, H.-J.; Ho, D. Multimodal Nanodiamond Drug Delivery Carriers for Selective Targeting, Imaging, and Enhanced Chemotherapeutic Efficacy. *Advanced Materials* **2011**, 4770–4775.

(190) Krueger, A. Diamond Nanoparticles: Jewels for Chemistry and Physics. *Advanced Materials* **2008**, *20*, 2445-2449.

(191) Bradac, C.; Gaebel, T.; Naidoo, N.; Rabeau, J. R.; Barnard, A. S. Prediction and measurement of the size-dependent stability of fluorescence in diamond over the entire nanoscale. *Nano letters* **2009**, *9*, 3555-3564.

(192) Fu, C.-C.; Lee, H.-Y.; Chen, K.; Lim, T.-S.; Wu, H.-Y.; Lin, P.-K.; Wei, P.-K.; Tsao, P.-H.; Chang, H.-C.; Fann, W. Characterization and application of single fluorescent nanodiamonds as cellular biomarkers. *Proceedings of the National Academy of Sciences* **2007**, *104*, 727-732.

(193) Igarashi, R.; Yoshinari, Y.; Yokota, H.; Sugi, T.; Sugihara, F.; Ikeda, K.; Sumiya, H.; Tsuji, S.; Mori, I.; Tochio, H.; Harada, Y.; Shirakawa, M. Real-time background-free selective imaging of fluorescent nanodiamonds in vivo. *Nano letters* **2012**, *12*, 5726-5732.

(194) Liu, K.-K.; Cheng, C.-L.; Chang, C.-C.; Chao, J.-I. Biocompatible and detectable carboxylated nanodiamond on human cell. *Nanotechnology* **2007**, 325102.

(195) Liu, K.-K.; et al. Alpha-bungarotoxin binding to target cell in a developing visual system by carboxylated nanodiamond. *Nanotechnology* **2008**, *19*, 205102.

(196) Mkandawire, M.; Pohl, A.; Gubarevich, T.; Lapina, V.; Appelhans, D.; Rodel, G.; Pompe, W.; Schreiber, J.; Opitz, J. Selective targeting of green fluorescent nanodiamond conjugates to mitochondria in HeLa cells. *Journal of biophotonics* **2009**, *2*, 596-606.

(197) Tisler, J.; Balasubramanian, G.; Naydenov, B.; Kolesov, R.; Grotz, B.; Reuter, R.; Boudou, J.-P.; Curmi, P. A.; Sennour, M.; Thorel, A.; Börsch, M.; Aulenbacher, K.; Erdmann, R.; Hemmer, P. R.; Jelezko, F.; Wrachtrup, J. r. Fluorescence and Spin Properties of Defects in Single Digit Nanodiamonds. *ACS Nano* **2009**, *3*, 1959-1965.

(198) Zhang, B.; Li, Y.; Fang, C. Y.; Chang, C. C.; Chen, C. S.; Chen, Y. Y.; Chang, H. C. Receptor-mediated cellular uptake of folate-conjugated fluorescent nanodiamonds: a combined ensemble and single-particle study. *Small* **2009**, *5*, 2716-2721.

(199) Chang, Y.-R.; Lee, H.-Y.; Chen, K.; Chang, C.-C.; Tsai, D.-S.; Fu, C.-C.; Lim, T.-S.; Tzeng, Y.-K.; Fang, C.-Y.; Han, C.-C.; Chang, H.-C.; Fann, W. Mass production and dynamic imaging of fluorescent nanodiamonds. *Nat Nano* **2008**, *3*, 284-288.

(200) Dreaden, E. C.; Alkilany, A. M.; Huang, X.; Murphy, C. J.; El-Sayed, M. A. The golden age: gold nanoparticles for biomedicine. *Chemical Society Reviews* **2012**, *41*, 2740-2779.

(201) Ferreira, M. F.; Mousavi, B.; Ferreira, P. M.; Martins, C. I. O.; Helm, L.; Martins, J. A.; Geraldes, C. F. G. C. Gold nanoparticles functionalised with stable, fast water exchanging Gd3+ chelates as high relaxivity contrast agents for MRI. *Dalton Transactions* **2012**, *41*, 5472-5475.

(202) Moriggi, L. c.; Cannizzo, C.; Dumas, E.; Mayer, C. d. R.; Ulianov, A.; Helm, L. Gold Nanoparticles Functionalized with Gadolinium Chelates as High-Relaxivity MRI Contrast Agents. *Journal of the American Chemical Society* **2009**, *131*, 10828-10829.

(203) Cutler, J. I.; Auyeung, E.; Mirkin, C. A. Spherical Nucleic Acids. *Journal of the American Chemical Society* **2012**, *134*, 1376-1391.

(204) Song, Y.; Xu, X.; MacRenaris, K. W.; Zhang, X. Q.; Mirkin, C. A.; Meade, T. J. Multimodal gadolinium-enriched DNA-gold nanoparticle conjugates for cellular imaging. *Angewandte Chemie* **2009**, *48*, 9143-9147.

(205) Barnholtz-Sloan, J. S.; Sloan, A. E.; Davis, F. G.; Vigneau, F. D.; Lai, P.; Sawaya, R. E. Incidence proportions of brain metastases in patients diagnosed (1973 to 2001) in the Metropolitan Detroit Cancer Surveillance System. *J Clin Oncol* **2004**, *22*, 2865-2872.

(206) Tsukada, Y.; Fouad, A.; Pickren, J. W.; Lane, W. W. Central nervous system metastasis from breast carcinoma. Autopsy study. *Cancer* **1983**, *52*, 2349-2354.

(207) Weil, R. J.; Palmieri, D. C.; Bronder, J. L.; Stark, A. M.; Steeg, P. S. Breast cancer metastasis to the central nervous system. *Am J Pathol* **2005**, *167*, 913-920.

(208) Ahrens, E. T.; Bulte, J. W. Tracking immune cells in vivo using magnetic resonance imaging. *Nat Rev Immunol* **2013**, *13*, 755-763.

(209) Guenoun, J.; Koning, G. A.; Doeswijk, G.; Bosman, L.; Wielopolski, P. A.; Krestin, G. P.; Bernsen, M. R. Cationic Gd-DTPA liposomes for highly efficient labeling of mesenchymal stem cells and cell tracking with MRI. *Cell Transplant* **2012**, *21*, 191-205.

(210) Baetke, S. C.; Lammers, T.; Kiessling, F. Applications of nanoparticles for diagnosis and therapy of cancer. *Br J Radiol* **2015**, *88*, 20150207.

(211) Brigger, I.; Dubernet, C.; Couvreur, P. Nanoparticles in cancer therapy and diagnosis. *Adv Drug Deliv Rev* **2002**, *54*, 631-651.

(212) Juang, J. H.; Wang, J. J.; Shen, C. R.; Kuo, C. H.; Chien, Y. W.; Kuo, H. Y.; Tsai, Z. T.; Yen, T. C. Magnetic resonance imaging of transplanted mouse islets labeled with chitosan-coated superparamagnetic iron oxide nanoparticles. *Transplant Proc* **2010**, *42*, 2104-2108.

(213) Rogers, W. J.; Meyer, C. H.; Kramer, C. M. Technology insight: in vivo cell tracking by use of MRI. *Nat Clin Pract Cardiovasc Med* **2006**, *3*, 554-562.

(214) Lamprianou, S.; Immonen, R.; Nabuurs, C.; Gjinovci, A.; Vinet, L.; Montet, X. C.; Gruetter, R.; Meda, P. High-resolution magnetic resonance imaging quantitatively detects individual pancreatic islets. *Diabetes* **2011**, *60*, 2853-2860.

(215) Crich, S. G.; Biancone, L.; Cantaluppi, V.; Duo, D.; Esposito, G.; Russo, S.; Camussi, G.; Aime, S. Improved route for the visualization of stem cells labeled with a Gd-/Eu-chelate as dual (MRI and fluorescence) agent. *Magn Reson Med* **2004**, *51*, 938-944.

(216) Evans, A. J.; Rakha, E. A.; Pinder, S. E.; Green, A. R.; Paish, C.; Ellis, I. O. Basal phenotype: a powerful prognostic factor in small screen-detected invasive breast cancer with long-term follow-up. *J Med Screen* **2007**, *14*, 210-214.

(217) Green, A. R.; Burney, C.; Granger, C. J.; Paish, E. C.; El-Sheikh, S.; Rakha, E. A.; Powe, D. G.; Macmillan, R. D.; Ellis, I. O.; Stylianou, E. The prognostic significance of steroid receptor co-regulators in breast cancer: co-repressor NCOR2/SMRT is an independent indicator of poor outcome. *Breast Cancer Res Treat* **2008**, *110*, 427-437.

(218) Hutchinson, L. Breast cancer: challenges, controversies, breakthroughs. *Nature reviews. Clinical oncology* **2010**, *7*, 669-670.

(219) Lippman, M. E.: Breast Cancer. In *Harrison's Principles of Internal Medicine*; Anthony S. Fauci, E. B., Dennis L. Kasper, Stephen L. Hauser, Dan L. Longo, J. Larry Jameson, and Joseph Loscalzo, Ed. 86; McGraw Hill, 2008; Vol. 17.

(220) Carlson, R. W.: NCCN Clinical Guidelines in Oncology: Breast Cancer. . ed.; National Comprehensive Cancer Network: Fort Washington, PA, 2012; Vol. Version 2.

(221) Andreetta, C.; Minisini, A. M.; Miscoria, M.; Puglisi, F. First-line chemotherapy with or without biologic agents for metastatic breast cancer. *Critical Reviews in Oncology/Hematology* **2010**, *76*, 99-111.

(222) Carey, L. A.; Rugo, H. S.; Marcom, P. K.; Mayer, E. L.; Esteva, F. J.; Ma, C. X.; Liu, M. C.; Storniolo, A. M.; Rimawi, M. F.; Forero-Torres, A.; Wolff, A. C.; Hobday, T. J.; Ivanova, A.; Chiu, W. K.; Ferraro, M.; Burrows, E.; Bernard, P. S.; Hoadley, K. A.; Perou, C. M.; Winer, E. P. TBCRC 001: randomized phase II study of cetuximab in combination with carboplatin in stage IV triple-negative breast cancer. *J Clin Oncol* **2012**, *30*, 2615-2623.

(223) Nogi, H.; Kobayashi, T.; Suzuki, M.; Tabei, I.; Kawase, K.; Toriumi, Y.; Fukushima, H.; Uchida, K. EGFR as paradoxical predictor of chemosensitivity and outcome among triple-negative breast cancer. *Oncology Reports* **2009**, *21*, 413-417.

(224) ICRF-187 and doxorubicin-induced cardiac toxicity. *N Engl J Med* **1989**, *320*, 399-400.

(225) Ahaus, E. A.; Couto, C. G.; Valerius, K. D. Hematological toxicity of doxorubicin-containing protocols in dogs with spontaneously occurring malignant tumors. *Journal of the American Animal Hospital Association* **2000**, *36*, 422-426.

(226) Aiken, M. J.; Suhag, V.; Garcia, C. A.; Acio, E.; Moreau, S.; Priebat, D. A.; Chennupati, S. P.; Van Nostrand, D. Doxorubicin-induced cardiac toxicity and cardiac rest gated blood pool imaging. *Clinical nuclear medicine* **2009**, *34*, 762-767.

(227) Alshabanah, O. A.; Hafez, M. M.; Al-Harbi, M. M.; Hassan, Z. K.; Al Rejaie, S. S.; Asiri, Y. A.; Sayed-Ahmed, M. M. Doxorubicin toxicity can be ameliorated during antioxidant L-carnitine supplementation. *Oxidative medicine and cellular longevity* **2010**, *3*, 428-433.

(228) Bielack, S. S.; Erttmann, R.; Kempf-Bielack, B.; Winkler, K. Impact of scheduling on toxicity and clinical efficacy of doxorubicin: what do we know in the mid-nineties? *Eur J Cancer* **1996**, *32A*, 1652-1660.

(229) Kelkar, S. S.; Reineke, T. M. Theranostics: combining imaging and therapy. *Bioconjugate chemistry* **2011**, *22*, 1879-1903.

(230) Ho, D.; Sun, X.; Sun, S. Monodisperse Magnetic Nanoparticles for Theranostic Applications. *Accounts of Chemical Research* **2011**, *44*, 875-882.

(231) Yoo, D.; Lee, J.-H.; Shin, T.-H.; Cheon, J. Theranostic Magnetic Nanoparticles. *Accounts of Chemical Research* **2011**, *44*, 863-874.

(232) Albanese, A.; Chan, W. C. Effect of gold nanoparticle aggregation on cell uptake and toxicity. *ACS Nano* **2011**, *5*, 5478-5489.

(233) Schrand, A. M.; Huang, H.; Carlson, C.; Schlager, J. J.; Ōsawa, E.; Hussain, S. M.; Dai, L. Are Diamond Nanoparticles Cytotoxic? *The Journal of Physical Chemistry B* **2006**, *111*, 2-7.

(234) Wrachtrup, J. Nanoparticles: Switching blinking on and off. *Nat Nano* **2010**, *5*, 314-315.

(235) Xiao, Z.; Levy-Nissenbaum, E.; Alexis, F.; Lupták, A.; Teply, B. A.; Chan, J. M.; Shi, J.; Digga, E.; Cheng, J.; Langer, R.; Farokhzad, O. C. Engineering of Targeted Nanoparticles for Cancer Therapy Using Internalizing Aptamers Isolated by Cell-Uptake Selection. *ACS Nano* **2012**, *6*, 696-704.

(236) Lam, R.; Chen, M.; Pierstorff, E.; Huang, H.; Osawa, E.; Ho, D. Nanodiamond-embedded microfilm devices for localized chemotherapeutic elution. *ACS Nano* **2008**, *2*, 2095-2102.

(237) Purtov, K. V.; Petunin, A. I.; Burov, A. E.; Puzyr, A. P.; Bondar, V. S. Nanodiamonds as Carriers for Address Delivery of Biologically Active Substances. *Nanoscale Res Lett* **2010**, *5*, 631-636.

(238) Liu, Y.; Sun, K. Protein functionalized nanodiamond arrays. *Nanoscale Res Lett* **2010**, *5*, 1045-1050.

(239) C, H. L.; C, C. H. Adsorption and immobilization of cytochrome c on nanodiamonds. *Langmuir* **2004**, *20*, 5879.

Chapter 2 References

(1) Banerjee, S. R.; Ngen, E. J.; Rotz, M. W.; Kakkad, S.; Lisok, A.; Pracitto, R.; Pullambhatla, M.; Chen, Z.; Shah, T.; Artemov, D.; Meade, T. J.; Bhujwalla, Z. M.; Pomper, M. G. Synthesis and Evaluation of Gd(III) -Based Magnetic Resonance Contrast Agents for Molecular Imaging of Prostate-Specific Membrane Antigen. *Angew Chem Int Ed Engl* **2015**, *54*, 10778-10782.

(2) Heffern, M. C.; Matosziuk, L. M.; Meade, T. J. Lanthanide probes for bioresponsive imaging. *Chem Rev* **2014**, *114*, 4496-4539.

(3) Manus, L. M.; Strauch, R. C.; Hung, A. H.; Eckermann, A. L.; Meade, T. J. Analytical methods for characterizing magnetic resonance probes. *Anal Chem* **2012**, *84*, 6278-6287.

(4) Haris, M.; Yadav, S. K.; Rizwan, A.; Singh, A.; Wang, E.; Hariharan, H.; Reddy, R.; Marincola, F. M. Molecular magnetic resonance imaging in cancer. *Journal of translational medicine* **2015**, *13*, 313.

(5) Nandwana, V.; De, M.; Chu, S.; Jaiswal, M.; Rotz, M.; Meade, T. J.; Dravid, V. P. Theranostic Magnetic Nanostructures (MNS) for Cancer. *Cancer Treat Res* **2015**, *166*, 51-83.

(6) Harney, A. S.; Meade, T. J. Molecular imaging of in vivo gene expression. *Future medicinal chemistry* **2010**, *2*, 503-519.

(7) Caravan, P. Strategies for increasing the sensitivity of gadolinium based MRI contrast agents. *Chemical Society reviews* **2006**, *35*, 512-523.

(8) Caravan, P.; Ellison, J. J.; McMurry, T. J.; Lauffer, R. B. Gadolinium(III) Chelates as MRI Contrast Agents: Structure, Dynamics, and Applications. *Chemical reviews* **1999**, *99*, 2293-2352.

(9) Helm, L.; Merbach, A. E.; Tóth, É.; ebrary Inc.: The chemistry of contrast agents in medical magnetic resonance imaging. 2nd ed.; John Wiley & Sons Inc.,: Hoboken, N.J., 2013; pp xvi, 496 p. ill. (some col.).

(10) Bulte, J. W. In vivo MRI cell tracking: clinical studies. *AJR. American journal of roentgenology* **2009**, *193*, 314-325.

(11) Guenoun, J.; Koning, G. A.; Doeswijk, G.; Bosman, L.; Wielopolski, P. A.; Krestin, G. P.; Bernsen, M. R. Cationic Gd-DTPA liposomes for highly efficient labeling of mesenchymal stem cells and cell tracking with MRI. *Cell transplantation* **2012**, *21*, 191-205.

(12) Rogers, W. J.; Meyer, C. H.; Kramer, C. M. Technology insight: in vivo cell tracking by use of MRI. *Nature clinical practice. Cardiovascular medicine* **2006**, *3*, 554-562.

(13) Zhang, F.; Xie, J.; Liu, G.; He, Y.; Lu, G.; Chen, X. In vivo MRI tracking of cell invasion and migration in a rat glioma model. *Molecular imaging and biology : MIB : the official publication of the Academy of Molecular Imaging* **2011**, *13*, 695-701.

(14) Frangioni, J. V.; Hajjar, R. J. In vivo tracking of stem cells for clinical trials in cardiovascular disease. *Circulation* **2004**, *110*, 3378-3383.

(15) Hoshino, K.; Ly, H. Q.; Frangioni, J. V.; Hajjar, R. J. In vivo tracking in cardiac stem cell-based therapy. *Progress in cardiovascular diseases* **2007**, *49*, 414-420.

(16) Crich, S. G.; Biancone, L.; Cantaluppi, V.; Duo, D.; Esposito, G.; Russo, S.; Camussi, G.; Aime, S. Improved route for the visualization of stem cells labeled with a Gd-/Eu-chelate as dual (MRI and fluorescence) agent. *Magn Reson Med* **2004**, *51*, 938-944.

(17) Juang, J. H.; Wang, J. J.; Shen, C. R.; Kuo, C. H.; Chien, Y. W.; Kuo, H. Y.; Tsai, Z. T.; Yen, T. C. Magnetic resonance imaging of transplanted mouse islets labeled with chitosan-coated superparamagnetic iron oxide nanoparticles. *Transplantation proceedings* **2010**, *42*, 2104-2108.

(18) Botsikas, D.; Terraz, S.; Vinet, L.; Lamprianou, S.; Becker, C. D.; Bosco, D.; Meda, P.; Montet, X. Pancreatic magnetic resonance imaging after manganese injection distinguishes type 2 diabetic and normoglycemic patients. *Islets* **2012**, *4*, 243-248.

(19) Lamprianou, S.; Immonen, R.; Nabuurs, C.; Gjinovci, A.; Vinet, L.; Montet, X. C.; Gruetter, R.; Meda, P. High-resolution magnetic resonance imaging quantitatively detects individual pancreatic islets. *Diabetes* **2011**, *60*, 2853-2860.

(20) Carney, C. E.; Lenov, I. L.; Baker, C. J.; MacRenaris, K. W.; Eckermann, A. L.; Sligar, S. G.; Meade, T. J. Nanodiscs as a Modular Platform for Multimodal MR-Optical Imaging. *Bioconjug Chem* **2015**, *26*, 899-905.

(21) Hung, A. H.; Holbrook, R. J.; Rotz, M. W.; Glasscock, C. J.; Mansukhani, N. D.; MacRenaris, K. W.; Manus, L. M.; Duch, M. C.; Dam, K. T.; Hersam, M. C.; Meade, T. J.

Graphene oxide enhances cellular delivery of hydrophilic small molecules by co-incubation. *ACS nano* **2014**, *8*, 10168-10177.

(22) Nicholls, F. J.; Rotz, M. W.; Ghuman, H.; MacRenaris, K. W.; Meade, T. J.; Modo, M. DNA-gadolinium-gold nanoparticles for in vivo T1 MR imaging of transplanted human neural stem cells. *Biomaterials* **2016**, *77*, 291-306.

(23) Vistain, L. F.; Rotz, M. W.; Rathore, R.; Preslar, A. T.; Meade, T. J. Targeted delivery of gold nanoparticle contrast agents for reporting gene detection by magnetic resonance imaging. *Chemical communications* **2015**, *52*, 160-163.

(24) Ananta, J. S.; Godin, B.; Sethi, R.; Moriggi, L.; Liu, X.; Serda, R. E.; Krishnamurthy, R.; Muthupillai, R.; Bolskar, R. D.; Helm, L.; Ferrari, M.; Wilson, L. J.; Decuzzi, P. Geometrical confinement of gadolinium-based contrast agents in nanoporous particles enhances T1 contrast. *Nature nanotechnology* **2010**, *5*, 815-821.

(25) Matson, M. L.; Wilson, L. J. Nanotechnology and MRI contrast enhancement. *Future medicinal chemistry* **2010**, *2*, 491-502.

(26) Sitharaman, B.; Tran, L. A.; Pham, Q. P.; Bolskar, R. D.; Muthupillai, R.; Flamm, S. D.; Mikos, A. G.; Wilson, L. J. Gadofullerenes as nanoscale magnetic labels for cellular MRI. *Contrast media & molecular imaging* **2007**, *2*, 139-146.

(27) Toth, E.; Bolskar, R. D.; Borel, A.; Gonzalez, G.; Helm, L.; Merbach, A. E.; Sitharaman, B.; Wilson, L. J. Water-soluble gadofullerenes: toward high-relaxivity, pH-responsive MRI contrast agents. *Journal of the American Chemical Society* **2005**, *127*, 799-805.

(28) Ciofani, G.; Raffa, V.; Vittorio, O.; Cuschieri, A.; Pizzorusso, T.; Costa, M.; Bardi, G. In vitro and in vivo biocompatibility testing of functionalized carbon nanotubes. *Methods in molecular biology* **2010**, *625*, 67-83.

(29) Mooney, E.; Dockery, P.; Greiser, U.; Murphy, M.; Barron, V. Carbon nanotubes and mesenchymal stem cells: biocompatibility, proliferation and differentiation. *Nano letters* **2008**, *8*, 2137-2143.

(30) Mochalin, V. N.; Shenderova, O.; Ho, D.; Gogotsi, Y. The properties and applications of nanodiamonds. *Nature Nanotechnology* **2012**, *7*, 11-23.

(31) Chen, M.; Pierstorff, E. D.; Lam, R.; Li, S.-Y.; Huang, H.; Osawa, E.; Ho, D. Nanodiamond-Mediated Delivery of Water-Insoluble Therapeutics. *ACS Nano* **2009**, *3*, 2016-2022.

(32) Chow, E. K.; Zhang, X.-Q.; Chen, M.; Lam, R.; Robinson, E.; Huang, H.; Schaffer, D.; Osawa, E.; Goga, A.; Ho, D. Nanodiamond therapeutic delivery agents mediate enhanced chemoresistant tumor treatment. *Science Translational Medicine* **2011**, *3*, 73ra21.

(33) Man, H. B.; Kim, H.; Kim, H. J.; Robinson, E.; Liu, W. K.; Chow, E. K.; Ho, D. Synthesis of nanodiamond-daunorubicin conjugates to overcome multidrug chemoresistance in leukemia. *Nanomedicine : nanotechnology, biology, and medicine* **2014**, *10*, 359-369.

(34) Moore, L.; Chow, E. K.; Osawa, E.; Bishop, J. M.; Ho, D. Diamond-Lipid Hybrids Enhance Chemotherapeutic Tolerance and Mediate Tumor Regression. *Advanced materials* **2013**.

(35) Moore, L.; Yang, J.; Lan, T. T.; Osawa, E.; Lee, D. K.; Johnson, W. D.; Xi, J.; Chow, E. K.; Ho, D. Biocompatibility Assessment of Detonation Nanodiamond in Non-Human Primates and Rats Using Histological, Hematologic, and Urine Analysis. *ACS nano* **2016**.

(36) Puzyr, A. P.; Baron, A. V.; Purtov, K. V.; Bortnikov, E. V.; Skobelev, N. N.; Mogilnaya, O. A.; Bondar, V. S. Nanodiamonds with novel properties: A biological study. *Diamond and Related Materials* **2007**, *16*, 2124-2128.

(37) Rej, E.; Gaebel, T.; Boele, T.; Waddington, D. E.; Reilly, D. J. Hyperpolarized nanodiamond with long spin-relaxation times. *Nature communications* **2015**, *6*, 8459.

(38) Purtov, K. V.; Petunin, A. I.; Burov, A. E.; Puzyr, A. P.; Bondar, V. S. Nanodiamonds as Carriers for Address Delivery of Biologically Active Substances. *Nanoscale Res Lett* **2010**, *5*, 631-636.

(39) Manus, L. M.; Mastarone, D. J.; Waters, E. A.; Zhang, X. Q.; Schultz-Sikma, E. A.; Macrenaris, K. W.; Ho, D.; Meade, T. J. Gd(III)-nanodiamond conjugates for MRI contrast enhancement. *Nano Lett* **2010**, *10*, 484-489.

(40) Kruger, A.; Liang, Y.; Jarre, G.; Stegk, J. Surface functionalisation of detonation diamond suitable for biological applications. *Journal of Materials Chemistry* **2006**, *16*, 2322-2328.

(41) Jarre, G.; Heyer, S.; Memmel, E.; Meinhardt, T.; Krueger, A. Synthesis of nanodiamond derivatives carrying amino functions and quantification by a modified Kaiser test. *Beilstein journal of organic chemistry* **2014**, *10*, 2729-2737.

(42) Caravan, P.; Farrar, C. T.; Frullano, L.; Uppal, R. Influence of molecular parameters and increasing magnetic field strength on relaxivity of gadolinium- and manganese-based T1 contrast agents. *Contrast media & molecular imaging* **2009**, *4*, 89-100.

(43) Bertini, I.; Kowalewski, J.; Luchinat, C.; Nilsson, T.; Parigi, G. Nuclear spin relaxation in paramagnetic complexes of S=1: Electron spin relaxation effects. *J Chem Phys* **1999**, *111*, 5795-5807.

(44) Hung, A. H.; Duch, M. C.; Parigi, G.; Rotz, M. W.; Manus, L. M.; Mastarone, D. J.; Dam, K. T.; Gits, C. C.; Macrenaris, K. W.; Luchinat, C.; Hersam, M. C.; Meade, T. J. Mechanisms of Gadographene-Mediated Proton Spin Relaxation. *The journal of physical chemistry. C, Nanomaterials and interfaces* **2013**, *117*.

(45) Rotz, M. W.; Culver, K. S.; Parigi, G.; MacRenaris, K. W.; Luchinat, C.; Odom, T. W.; Meade, T. J. High relaxivity Gd(III)-DNA gold nanostars: investigation of shape effects on proton relaxation. *ACS nano* **2015**, *9*, 3385-3396.

(46) Bertini, I.; Galas, O.; Luchinat, C.; Messori, L.; Parigi, G. A Theoretical-Analysis of the H-1 Nuclear Magnetic-Relaxation Dispersion Profiles of Diferric Transferrin. *J Phys Chem-Us* **1995**, *99*, 14217-14222.

(47) Preslar, A. T.; Parigi, G.; McClendon, M. T.; Sefick, S. S.; Moyer, T. J.; Haney, C. R.; Waters, E. A.; MacRenaris, K. W.; Luchinat, C.; Stupp, S. I.; Meade, T. J. Gd(III)-labeled peptide nanofibers for reporting on biomaterial localization in vivo. *ACS nano* **2014**, *8*, 7325-7332.

(48) Ma, Q.; Jebb, M.; Tweedle, M. F.; Wilson, L. J. The gadonanotubes: structural origin of their high-performance MRI contrast agent behavior. *J Mater Chem B* **2013**, *1*, 5791-5797.

(49) Korobov, M. V.; Avramenko, N. V.; Bogachev, A. G.; Rozhkova, N. N.; Ōsawa, E. Nanophase of Water in Nano-Diamond Gel. *Journal of Physical Chemistry C* **2007**, *111*, 7330-7334.

(50) Carney, C. E.; MacRenaris, K. W.; Mastarone, D. J.; Kasjanski, D. R.; Hung, A. H.; Meade, T. J. Cell labeling via membrane-anchored lipophilic MR contrast agents. *Bioconjugate chemistry* **2014**, *25*, 945-954.

(51) Harrison, V. S.; Carney, C. E.; MacRenaris, K. W.; Waters, E. A.; Meade, T. J. Multimeric Near IR-MR Contrast Agent for Multimodal In Vivo Imaging. *J Am Chem Soc* **2015**, *137*, 9108-9116.

(52) Hassan, A. A.; Chan, B. T.; Tran, L. A.; Hartman, K. B.; Ananta, J. S.; Mackeyev, Y.; Hu, L.; Pautler, R. G.; Wilson, L. J.; Lee, A. V. Serine-derivatized gadonanotubes as magnetic nanoprobes for intracellular labeling. *Contrast media & molecular imaging* **2010**, *5*, 34-38.

(53) Oudkerk, M.; Sijens, P. E.; Van Beek, E. J.; Kuijpers, T. J. Safety and efficacy of dotarem (Gd-DOTA) versus magnevist (Gd-DTPA) in magnetic resonance imaging of the central nervous system. *Investigative radiology* **1995**, *30*, 75-78.

(54) Smart, S. K.; Cassady, A. I.; Lu, G. Q.; Martin, D. J. The biocompatibility of carbon nanotubes. *Carbon* **2006**, *44*, 1034-1047.

(55) Christensen, J.; Vonwil, D.; Shastri, V. P. Non-Invasive In Vivo Imaging and Quantification of Tumor Growth and Metastasis in Rats Using Cells Expressing Far-Red Fluorescence Protein. *PloS one* **2015**, *10*, e0132725.

(56) Gao X, C. Y., Levenson R M, Chung L W; S, N. In vivo cancer targeting and imaging with semiconductor quantum dots. *Nat. Biotechnol.* **2004**, *22*, 969.

(57) Kershaw, M. H.; Westwood, J. A.; Darcy, P. K. Gene-engineered T cells for cancer therapy. *Nature reviews. Cancer* **2013**, *13*, 525-541.

(58) Brenner, M. K. CAR T cells for acute myeloid leukemia: the LeY of the land. *Molecular therapy : the journal of the American Society of Gene Therapy* **2013**, *21*, 1983-1984.

(59) Kruger, A.; Liang, Y. J.; Jarre, G.; Stegk, J. Functionalisation of Detonation Diamond Suitable for Biological Applications. *J. Mater. Chem.* **2006**, *16*, 2322.

(60) Zhang, X.-Q.; Lam, R.; Xu, X.; Chow, E. K.; Kim, H.-J.; Ho, D. Multimodal Nanodiamond Drug Delivery Carriers for Selective Targeting, Imaging, and Enhanced Chemotherapeutic Efficacy. *Advanced Materials* **2011**, 4770–4775.

Chapter 3 References

(1) Fletcher, J. I.; Haber, M.; Henderson, M. J.; Norris, M. D. ABC transporters in cancer: more than just drug efflux pumps. *Nature reviews. Cancer* **2010**, *10*, 147-156.

(2) Fitzgerald, S. P. Breast-cancer screening. *N Engl J Med* **2012**, *366*, 191; author reply 191-192.

(3) Gotzsche, P. C.; Nielsen, M. Screening for breast cancer with mammography. *Cochrane Database Syst Rev* **2009**, CD001877.

(4) Austoker, J. Breast self examination. *BMJ* **2003**, *326*, 1-2.

(5) Rosolowich, V. Breast self-examination. *J Obstet Gynaecol Can* **2006**, *28*, 728-730.

(6) Thomas, D. B.; Gao, D. L.; Ray, R. M.; Wang, W. W.; Allison, C. J.; Chen, F. L.; Porter, P.; Hu, Y. W.; Zhao, G. L.; Pan, L. D.; Li, W.; Wu, C.; Coriaty, Z.; Evans, I.; Lin, M. G.; Stalsberg, H.; Self, S. G. Randomized trial of breast self-examination in Shanghai: final results. *J Natl Cancer Inst* **2002**, *94*, 1445-1457.

(7) Gluz, O.; Liedtke, C.; Gottschalk, N.; Pusztai, L.; Nitz, U.; Harbeck, N. Triple-negative breast cancer--current status and future directions. *Annals of oncology : official journal of the European Society for Medical Oncology / ESMO* **2009**, *20*, 1913-1927.

(8) Lippman, M. E.: Breast Cancer. In *Harrison's Principles of Internal Medicine*; Anthony S. Fauci, E. B., Dennis L. Kasper, Stephen L. Hauser, Dan L. Longo, J. Larry Jameson, and Joseph Loscalzo, Ed. 86; McGraw Hill, 2008; Vol. 17.

(9) Kantarjian, H.; Koller, C. A.; Wolff, R. A.; University of Texas M.D. Anderson Cancer Center.: *The MD Anderson manual of medical oncology*; McGraw-Hill, Medical Pub.: New York, 2006.

(10) Therasse, P.; Arbuck, S. G.; Eisenhauer, E. A.; Wanders, J.; Kaplan, R. S.; Rubinstein, L.; Verweij, J.; Van Glabbeke, M.; van Oosterom, A. T.; Christian, M. C.; Gwyther, S. G. New guidelines to evaluate the response to treatment in solid tumors. European Organization for Research and Treatment of Cancer, National Cancer Institute of the United States, National Cancer Institute of Canada. *J Natl Cancer Inst* **2000**, *92*, 205-216.

(11) Nogi, H.; Kobayashi, T.; Suzuki, M.; Tabei, I.; Kawase, K.; Toriumi, Y.; Fukushima, H.; Uchida, K. EGFR as paradoxical predictor of chemosensitivity and outcome among triple-negative breast cancer. *Oncology Reports* **2009**, *21*, 413-417.

(12) Wu, J.; Li, S.; Jia, W.; Su, F. Response and prognosis of taxanes and anthracyclines neoadjuvant chemotherapy in patients with triple-negative breast cancer. *J Cancer Res Clin Oncol* **2011**, *137*, 1505-1510.

(13) Entwistle, J.; Hall, C. L.; Turley, E. A. HA receptors: regulators of signalling to the cytoskeleton. *Journal of cellular biochemistry* **1996**, *61*, 569-577.

(14) Lee, T.; Lim, E. K.; Lee, J.; Kang, B.; Choi, J.; Park, H. S.; Suh, J. S.; Huh, Y. M.; Haam, S. Efficient CD44-targeted magnetic resonance imaging (MRI) of breast cancer cells using hyaluronic acid (HA)-modified MnFe2O4 nanocrystals. *Nanoscale Res Lett* **2013**, *8*, 149.

(15) Ricardo, S.; Vieira, A. F.; Gerhard, R.; Leitao, D.; Pinto, R.; Cameselle-Teijeiro, J. F.; Milanezi, F.; Schmitt, F.; Paredes, J. Breast cancer stem cell markers CD44, CD24 and ALDH1: expression distribution within intrinsic molecular subtype. *Journal of clinical pathology* **2011**, *64*, 937-946.

(16) Yoon, H. Y.; Koo, H.; Choi, K. Y.; Lee, S. J.; Kim, K.; Kwon, I. C.; Leary, J. F.; Park, K.; Yuk, S. H.; Park, J. H.; Choi, K. Tumor-targeting hyaluronic acid nanoparticles for photodynamic imaging and therapy. *Biomaterials* **2012**, *33*, 3980-3989.

(17) Mochalin, V. N.; Shenderova, O.; Ho, D.; Gogotsi, Y. The properties and applications of nanodiamonds. *Nature Nanotechnology* **2012**, *7*, 11-23.

(18) Purtov, K. V.; Petunin, A. I.; Burov, A. E.; Puzyr, A. P.; Bondar, V. S. Nanodiamonds as Carriers for Address Delivery of Biologically Active Substances. *Nanoscale Res Lett* **2010**, *5*, 631-636.

(19) Puzyr, A. P.; Baron, A. V.; Purtov, K. V.; Bortnikov, E. V.; Skobelev, N. N.; Mogilnaya, O. A.; Bondar, V. S. Nanodiamonds with novel properties: A biological study. *Diamond and Related Materials* **2007**, *16*, 2124-2128.

(20) Yuan Y, C. Y., Liu J H, Wang H; Y, L. Biodistribution and fate of nanodiamonds in vivo. *Diamond and Related Materials* **2009**, *18*, 95.

(21) Lam, R.; Chen, M.; Pierstorff, E.; Huang, H.; Osawa, E.; Ho, D. Nanodiamond-embedded microfilm devices for localized chemotherapeutic elution. *ACS Nano* **2008**, *2*, 2095-2102.

(22) Li, J.; Zhu, Y.; Li, W.; Zhang, X.; Peng, Y.; Huang, Q. Nanodiamonds as intracellular transporters of chemotherapeutic drug. *Biomaterials* **2010**, *31*, 8410-8418.

(23) Zhang, X.-Q.; Lam, R.; Xu, X.; Chow, E. K.; Kim, H.-J.; Ho, D. Multimodal Nanodiamond Drug Delivery Carriers for Selective Targeting, Imaging, and Enhanced Chemotherapeutic Efficacy. *Advanced Materials* **2011**, 4770–4775.

(24) Liu, Y.; Sun, K. Protein functionalized nanodiamond arrays. *Nanoscale Res Lett* **2010**, *5*, 1045-1050.

(25) C, H. L.; C, C. H. Adsorption and immobilization of cytochrome c on nanodiamonds. *Langmuir* **2004**, *20*, 5879.

(26) Xing, Y.; Xiong, W.; Zhu, L.; Osawa, E.; Hussin, S.; Dai, L. DNA Damage in Embryonic Stem Cells Caused by Nanodiamonds. *ACS Nano* **2011**.

(27) Zhang, X. Q.; Chen, M.; Lam, R.; Xu, X.; Osawa, E.; Ho, D. Polymer-functionalized nanodiamond platforms as vehicles for gene delivery. *ACS Nano* **2009**, *3*, 2609-2616.

(28) Chow, E. K.; Zhang, X.-Q.; Chen, M.; Lam, R.; Robinson, E.; Huang, H.; Schaffer, D.; Osawa, E.; Goga, A.; Ho, D. Nanodiamond therapeutic delivery agents mediate enhanced chemoresistant tumor treatment. *Science Translational Medicine* **2011**, *3*, 73ra21.

(29) Merkel, T. J.; DeSimone, J. M. Dodging Drug-Resistant Cancer with Diamonds. *Science Translational Medicine* **2011**, *3*, 73ps78.

(30) Bradac, C.; Gaebel, T.; Naidoo, N.; Rabeau, J. R.; Barnard, A. S. Prediction and measurement of the size-dependent stability of fluorescence in diamond over the entire nanoscale. *Nano Letters* **2009**, *9*, 3555-3564.

(31) Fu, C.-C.; Lee, H.-Y.; Chen, K.; Lim, T.-S.; Wu, H.-Y.; Lin, P.-K.; Wei, P.-K.; Tsao, P.-H.; Chang, H.-C.; Fann, W. Characterization and application of single fluorescent nanodiamonds as cellular biomarkers. *Proceedings of the National Academy of Sciences* **2007**, *104*, 727-732.

(32) Igarashi, R.; Yoshinari, Y.; Yokota, H.; Sugi, T.; Sugihara, F.; Ikeda, K.; Sumiya, H.; Tsuji, S.; Mori, I.; Tochio, H.; Harada, Y.; Shirakawa, M. Real-time background-free selective imaging of fluorescent nanodiamonds in vivo. *Nano Letters* **2012**, *12*, 5726-5732.

(33) Liu, K.-K.; Cheng, C.-L.; Chang, C.-C.; Chao, J.-I. Biocompatible and detectable carboxylated nanodiamond on human cell. *Nanotechnology* **2007**, 325102.

(34) Liu, K.-K.; et al. Alpha-bungarotoxin binding to target cell in a developing visual system by carboxylated nanodiamond. *Nanotechnology* **2008**, *19*, 205102.

(35) Mkandawire, M.; Pohl, A.; Gubarevich, T.; Lapina, V.; Appelhans, D.; Rodel, G.; Pompe, W.; Schreiber, J.; Opitz, J. Selective targeting of green fluorescent nanodiamond conjugates to mitochondria in HeLa cells. *Journal of biophotonics* **2009**, *2*, 596-606.

(36) Tisler, J.; Balasubramanian, G.; Naydenov, B.; Kolesov, R.; Grotz, B.; Reuter, R.; Boudou, J.-P.; Curmi, P. A.; Sennour, M.; Thorel, A.; Börsch, M.; Aulenbacher, K.; Erdmann, R.; Hemmer, P. R.; Jelezko, F.; Wrachtrup, J. r. Fluorescence and Spin Properties of Defects in Single Digit Nanodiamonds. *ACS Nano* **2009**, *3*, 1959-1965.

(37) Zhang, B.; Li, Y.; Fang, C. Y.; Chang, C. C.; Chen, C. S.; Chen, Y. Y.; Chang, H. C. Receptor-mediated cellular uptake of folate-conjugated fluorescent nanodiamonds: a combined ensemble and single-particle study. *Small* **2009**, *5*, 2716-2721.

(38) Manus, L. M.; Mastarone, D. J.; Waters, E. A.; Zhang, X. Q.; Schultz-Sikma, E. A.; Macrenaris, K. W.; Ho, D.; Meade, T. J. Gd(III)-nanodiamond conjugates for MRI contrast enhancement. *Nano Lett* **2010**, *10*, 484-489.

(39) Kruger, A.; Liang, Y.; Jarre, G.; Stegk, J. Surface functionalisation of detonation diamond suitable for biological applications. *Journal of Materials Chemistry* **2006**, *16*, 2322-2328.

(40) Mizrahy, S.; Raz, S. R.; Hasgaard, M.; Liu, H.; Soffer-Tsur, N.; Cohen, K.; Dvash, R.; Landsman-Milo, D.; Bremer, M. G.; Moghimi, S. M.; Peer, D. Hyaluronan-coated nanoparticles: the influence of the molecular weight on CD44-hyaluronan interactions and on the immune response. *Journal of controlled release : official journal of the Controlled Release Society* **2011**, *156*, 231-238.

(41) Qhattal, H. S.; Liu, X. Characterization of CD44-mediated cancer cell uptake and intracellular distribution of hyaluronan-grafted liposomes. *Molecular pharmaceutics* **2011**, *8*, 1233-1246.

(42) Jin, K.; Teng, L.; Shen, Y.; He, K.; Xu, Z.; Li, G. Patient-derived human tumour tissue xenografts in immunodeficient mice: a systematic review. *Clinical & translational oncology : official publication of the Federation of Spanish Oncology Societies and of the National Cancer Institute of Mexico* **2010**, *12*, 473-480.

(43) Kabos, P.; Finlay-Schultz, J.; Li, C.; Kline, E.; Finlayson, C.; Wisell, J.; Manuel, C. A.; Edgerton, S. M.; Harrell, J. C.; Elias, A.; Sartorius, C. A. Patient-derived luminal breast cancer xenografts retain hormone receptor heterogeneity and help define unique estrogen-dependent gene signatures. *Breast cancer research and treatment* **2012**, *135*, 415-432.

(44) Kopetz, S.; Lemos, R.; Powis, G. The promise of patient-derived xenografts: the best laid plans of mice and men. *Clinical cancer research : an official journal of the American Association for Cancer Research* **2012**, *18*, 5160-5162.

(45) Landis, M. D.; Lehmann, B. D.; Pietenpol, J. A.; Chang, J. C. Patient-derived breast tumor xenografts facilitating personalized cancer therapy. *Breast cancer research : BCR* **2013**, *15*, 201.

(46) Marangoni, E.; Vincent-Salomon, A.; Auger, N.; Degeorges, A.; Assayag, F.; de Cremoux, P.; de Plater, L.; Guyader, C.; De Pinieux, G.; Judde, J. G.; Rebucci, M.; Tran-Perennou, C.; Sastre-Garau, X.; Sigal-Zafrani, B.; Delattre, O.; Dieras, V.; Poupon, M. F. A new model of patient tumor-derived breast cancer xenografts for preclinical assays. *Clinical cancer research : an official journal of the American Association for Cancer Research* **2007**, *13*, 3989-3998.

(47) Reyal, F.; Guyader, C.; Decraene, C.; Lucchesi, C.; Auger, N.; Assayag, F.; De Plater, L.; Gentien, D.; Poupon, M. F.; Cottu, P.; De Cremoux, P.; Gestraud, P.; Vincent-Salomon, A.; Fontaine, J. J.; Roman-Roman, S.; Delattre, O.; Decaudin, D.; Marangoni, E. Molecular profiling of patient-derived breast cancer xenografts. *Breast cancer research : BCR* **2012**, *14*, R11.

(48) Siolas, D.; Hannon, G. J. Patient-derived tumor xenografts: transforming clinical samples into mouse models. *Cancer research* **2013**, *73*, 5315-5319.

(49) Tentler, J. J.; Tan, A. C.; Weekes, C. D.; Jimeno, A.; Leong, S.; Pitts, T. M.; Arcaroli, J. J.; Messersmith, W. A.; Eckhardt, S. G. Patient-derived tumour xenografts as models for oncology drug development. *Nature reviews. Clinical oncology* **2012**, *9*, 338-350.

(50) Kruger, A.; Liang, Y. J.; Jarre, G.; Stegk, J. Functionalisation of Detonation Diamond Suitable for Biological Applications. *J. Mater. Chem.* **2006**, *16*, 2322.

Chapter 4 References

(1) Guenoun, J.; Koning, G. A.; Doeswijk, G.; Bosman, L.; Wielopolski, P. A.; Krestin, G. P.; Bernsen, M. R. Cationic Gd-DTPA liposomes for highly efficient labeling of mesenchymal stem cells and cell tracking with MRI. *Cell transplantation* **2012**, *21*, 191-205.

(2) Harney, A. S.; Meade, T. J. Molecular imaging of in vivo gene expression. *Future medicinal chemistry* **2010**, *2*, 503-519.

(3) Modo, M.; Mellodew, K.; Cash, D.; Fraser, S. E.; Meade, T. J.; Price, J.; Williams, S. C. Mapping transplanted stem cell migration after a stroke: a serial, in vivo magnetic resonance imaging study. *Neuroimage* **2004**, *21*, 311-317.

(4) Nicholls, F. J.; Rotz, M. W.; Ghuman, H.; MacRenaris, K. W.; Meade, T. J.; Modo, M. DNA-gadolinium-gold nanoparticles for in vivo T1 MR imaging of transplanted human neural stem cells. *Biomaterials* **2016**, *77*, 291-306.

(5) Banerjee, S. R.; Ngen, E. J.; Rotz, M. W.; Kakkad, S.; Lisok, A.; Pracitto, R.; Pullambhatla, M.; Chen, Z.; Shah, T.; Artemov, D.; Meade, T. J.; Bhujwalla, Z. M.; Pomper, M. G. Synthesis and Evaluation of Gd(III) -Based Magnetic Resonance Contrast Agents for Molecular Imaging of Prostate-Specific Membrane Antigen. *Angew Chem Int Ed Engl* **2015**, *54*, 10778-10782.

(6) Nandwana, V.; De, M.; Chu, S.; Jaiswal, M.; Rotz, M.; Meade, T. J.; Dravid, V. P. Theranostic Magnetic Nanostructures (MNS) for Cancer. *Cancer Treat Res* **2015**, *166*, 51-83.

(7) Patra, C. R.; Bhattacharya, R.; Wang, E.; Katarya, A.; Lau, J. S.; Dutta, S.; Muders, M.; Wang, S.; Buhrow, S. A.; Safgren, S. L.; Yaszemski, M. J.; Reid, J. M.; Ames, M. M.; Mukherjee, P.; Mukhopadhyay, D. Targeted Delivery of Gemcitabine to Pancreatic Adenocarcinoma Using Cetuximab as a Targeting Agent. *Cancer Research* **2008**, *68*, 1970-1978.

(8) Jokerst, J. V.; Khademi, C.; Gambhir, S. S. Intracellular aggregation of multimodal silica nanoparticles for ultrasound-guided stem cell implantation. *Science translational medicine* **2013**, *5*, 177ra135.

(9) Rickers, C.; Gallegos, R.; Seethamraju, R. T.; Wang, X.; Swingen, C.; Jayaswal, A.; Rahrmann, E. P.; Kastenberg, Z. J.; Clarkson, C. E.; Bianco, R.; O'Brian, T.; Verfaillie, C.; Bolman, R. M., 3rd; Wilke, N.; Jerosch-Herold, M. Applications of magnetic resonance imaging for cardiac stem cell therapy. *Journal of interventional cardiology* **2004**, *17*, 37-46.

(10) Massensini, A. R.; Ghuman, H.; Saldin, L. T.; Medberry, C. J.; Keane, T. J.; Nicholls, F. J.; Velankar, S. S.; Badylak, S. F.; Modo, M. Concentration-dependent rheological properties of ECM hydrogel for intracerebral delivery to a stroke cavity. *Acta biomaterialia* **2015**.

(11) Tang, Y.; Zhang, C.; Wang, J.; Lin, X.; Zhang, L.; Yang, Y.; Wang, Y.; Zhang, Z.; Bulte, J. W.; Yang, G. Y. MRI/SPECT/Fluorescent Tri-Modal Probe for Evaluating the Homing and Therapeutic Efficacy of Transplanted Mesenchymal Stem Cells in a Rat Ischemic Stroke Model. *Advanced functional materials* **2015**, *25*, 1024-1034.

(12) Skeoch, S.; Williams, H.; Cristinacce, P.; Hockings, P.; James, J.; Alexander, Y.; Waterton, J.; Bruce, I. Evaluation of carotid plaque inflammation in patients with active rheumatoid arthritis using (18)F-fluorodeoxyglucose PET-CT and MRI: a pilot study. *Lancet* **2015**, *385 Suppl 1*, S91.

(13) Heffern, M. C.; Matosziuk, L. M.; Meade, T. J. Lanthanide probes for bioresponsive imaging. *Chem Rev* **2014**, *114*, 4496-4539.

(14) Manus, L. M.; Strauch, R. C.; Hung, A. H.; Eckermann, A. L.; Meade, T. J. Analytical methods for characterizing magnetic resonance probes. *Anal Chem* **2012**, *84*, 6278-6287.

(15) Meade, T. J.; Aime, S. Chemistry of molecular imaging. *Acc Chem Res* **2009**, *42*, 821.

(16) Boros, E.; Gale, E. M.; Caravan, P. MR imaging probes: design and applications. *Dalton Trans* **2015**, *44*, 4804-4818.

(17) Pierre, V. C.; Allen, M. J.; Caravan, P. Contrast agents for MRI: 30+ years and where are we going? *Journal of biological inorganic chemistry : JBIC : a publication of the Society of Biological Inorganic Chemistry* **2014**, *19*, 127-131.

(18) Alric, C.; Taleb, J.; Duc, G. L.; Mandon, C.; Billotey, C.; Meur-Herland, A. L.; Brochard, T.; Vocanson, F.; Janier, M.; Perriat, P.; Roux, S.; Tillement, O. Gadolinium Chelate Coated Gold Nanoparticles As Contrast Agents for Both X-ray Computed Tomography and Magnetic Resonance Imaging. *Journal of the American Chemical Society* **2008**, *130*, 5908-5915.

(19) Shellock, F. G.; Spinazzi, A. MRI Safety Update 2008: Part 1, MRI Contrast Agents and Nephrogenic Systemic Fibrosis. *American Journal of Roentgenology* **2008**, *191*, 1129-1139.

(20) Irure, A.; Marradi, M.; Arnaiz, B.; Genicio, N.; Padro, D.; Penades, S. Sugar/gadolinium-loaded gold nanoparticles for labelling and imaging cells by magnetic resonance imaging. *Biomaterials Science* **2013**, *1*, 658-668.

(21) Song, Y.; Xu, X.; MacRenaris, K. W.; Zhang, X.-Q.; Mirkin, C. A.; Meade, T. J. Multimodal Gadolinium-Enriched DNA–Gold Nanoparticle Conjugates for Cellular Imaging. *Angewandte Chemie International Edition* **2009**, *48*, 9143-9147.

(22) Carney, C. E.; MacRenaris, K. W.; Mastarone, D. J.; Kasjanski, D. R.; Hung, A. H.; Meade, T. J. Cell labeling via membrane-anchored lipophilic MR contrast agents. *Bioconjugate chemistry* **2014**, *25*, 945-954.

(23) Endres, P. J.; MacRenaris, K. W.; Vogt, S.; Meade, T. J. Cell-permeable MR contrast agents with increased intracellular retention. *Bioconjugate chemistry* **2008**, *19*, 2049-2059.

(24) Patra, C. R.; Bhattacharya, R.; Mukhopadhyay, D.; Mukherjee, P. Fabrication of gold nanoparticles for targeted therapy in pancreatic cancer. *Advanced drug delivery reviews* **2010**, *62*, 346-361.

(25) Holbrook, R. J.; Rammohan, N.; Rotz, M. W.; MacRenaris, K. W.; Preslar, A. T.; Meade, T. J. Gd(III)-Dithiolane Gold Nanoparticles for T1-Weighted Magnetic Resonance Imaging of the Pancreas. *Nano Lett* **2016**, *16*, 3202-3209.

(26) Hung, A. H.; Holbrook, R. J.; Rotz, M. W.; Glasscock, C. J.; Mansukhani, N. D.; MacRenaris, K. W.; Manus, L. M.; Duch, M. C.; Dam, K. T.; Hersam, M. C.; Meade, T. J. Graphene oxide enhances cellular delivery of hydrophilic small molecules by co-incubation. *ACS nano* **2014**, *8*, 10168-10177.

(27) Rohrer, M.; Bauer, H.; Mintorovitch, J.; Requardt, M.; Weinmann, H. J. Comparison of magnetic properties of MRI contrast media solutions at different magnetic field strengths. *Invest Radiol* **2005**, *40*, 715-724.

(28) Caravan, P.; Farrar, C. T.; Frullano, L.; Uppal, R. Influence of molecular parameters and increasing magnetic field strength on relaxivity of gadolinium- and manganese-based T1 contrast agents. *Contrast media & molecular imaging* **2009**, *4*, 89-100.

(29) Klein, A. P. Identifying people at a high risk of developing pancreatic cancer. *Nat Rev Cancer* **2013**, *13*, 66-74.

(30) Abbruzzese, J. The challenge of pancreatic cancer. *Int J Gastrointest Canc* **2003**, *33*, 1-2.

(31) Hidalgo, M.; Cascinu, S.; Kleeff, J.; Labianca, R.; Löhr, J. M.; Neoptolemos, J.; Real, F. X.; Van Laethem, J.-L.; Heinemann, V. Addressing the challenges of pancreatic cancer: Future directions for improving outcomes. *Pancreatology*, *15*, 8-18.

(32) Arvizo, R. R.; Miranda, O. R.; Moyano, D. F.; Walden, C. A.; Giri, K.; Bhattacharya, R.; Robertson, J. D.; Rotello, V. M.; Reid, J. M.; Mukherjee, P. Modulating Pharmacokinetics, Tumor Uptake and Biodistribution by Engineered Nanoparticles. *PLoS ONE* **2011**, *6*, e24374.

(33) Grimm, J.; Potthast, A.; Wunder, A.; Moore, A. Magnetic resonance imaging of the pancreas and pancreatic tumors in a mouse orthotopic model of human cancer. *International Journal of Cancer* **2003**, *106*, 806-811.

(34) Lasagna-Reeves, C.; Gonzalez-Romero, D.; Barria, M. A.; Olmedo, I.; Clos, A.; Sadagopa Ramanujam, V. M.; Urayama, A.; Vergara, L.; Kogan, M. J.; Soto, C. Bioaccumulation and toxicity of gold nanoparticles after repeated administration in mice. *Biochemical and Biophysical Research Communications* **2010**, *393*, 649-655.

(35) Sadauskas, E.; Wallin, H.; Stoltenberg, M.; Vogel, U.; Doering, P.; Larsen, A.; Danscher, G. Kupffer cells are central in the removal of nanoparticles from the organism. *Particle and Fibre Toxicology* **2007**, *4*, 1-7.

(36) Koh, D.-M.; Collins, D. J. Diffusion-Weighted MRI in the Body: Applications and Challenges in Oncology. *American Journal of Roentgenology* **2007**, *188*, 1622-1635.

(37) Patra, C. R.; Bhattacharya, R.; Mukhopadhyay, D.; Mukherjee, P. Fabrication of gold nanoparticles for targeted therapy in pancreatic cancer. *Advanced drug delivery reviews* **2010**, *62*, 346-361.

(38) Patra, C. R.; Bhattacharya, R.; Wang, E.; Katarya, A.; Lau, J. S.; Dutta, S.; Muders, M.; Wang, S.; Buhrow, S. A.; Safgren, S. L.; Yaszemski, M. J.; Reid, J. M.; Ames, M. M.; Mukherjee, P.; Mukhopadhyay, D. Targeted delivery of gemcitabine to pancreatic adenocarcinoma using cetuximab as a targeting agent. *Cancer research* **2008**, *68*, 1970-1978.

(39) Bellingan, G. J.; Xu, P.; Cooksley, H.; Cauldwell, H.; Shock, A.; Bottoms, S.; Haslett, C.; Mutsaers, S. E.; Laurent, G. J. Adhesion Molecule–dependent Mechanisms Regulate the Rate of Macrophage Clearance During the Resolution of Peritoneal Inflammation. *The Journal of Experimental Medicine* **2002**, *196*, 1515-1521.

(40) Miller, F. H.; Rini, N. J.; Keppke, A. L. MRI of adenocarcinoma of the pancreas. *AJR. American journal of roentgenology* **2006**, *187*, W365-374.

(41) Tummala, P.; Junaidi, O.; Agarwal, B. Imaging of pancreatic cancer: An overview. *Journal of gastrointestinal oncology* **2011**, *2*, 168-174.

(42) Lee, G. Y.; Qian, W. P.; Wang, L.; Wang, Y. A.; Staley, C. A.; Satpathy, M.; Nie, S.; Mao, H.; Yang, L. Theranostic nanoparticles with controlled release of gemcitabine for targeted therapy and MRI of pancreatic cancer. *ACS nano* **2013**, *7*, 2078-2089.

(43) Torres, G. M.; Erquiaga, E.; Ros, P. R.; Burton, S. S.; Barreda, R.; Langmo, L. S.; Kennedy, S. J. Preliminary results of MR imaging with superparamagnetic iron oxide in pancreatic and retroperitoneal disorders. *Radiographics : a review publication of the Radiological Society of North America, Inc* **1991**, *11*, 785-791; discussion 792-783.

(44) Botsikas, D.; Terraz, S.; Vinet, L.; Lamprianou, S.; Becker, C. D.; Bosco, D.; Meda, P.; Montet, X. Pancreatic magnetic resonance imaging after manganese injection distinguishes type 2 diabetic and normoglycemic patients. *Islets* **2012**, *4*, 243-248.

(45) Diehl, S. J.; Lehmann, K. J.; Gaa, J.; McGill, S.; Hoffmann, V.; Georgi, M. MR imaging of pancreatic lesions. Comparison of manganese-DPDP and gadolinium chelate. *Investigative radiology* **1999**, *34*, 589-595.

(46) Schima, W. MRI of the pancreas: tumours and tumour-simulating processes. *Cancer Imaging* **2006**, *6*, 199-203.

(47) Birchard, K. R.; Semelka, R. C.; Hyslop, W. B.; Brown, A.; Armao, D.; Firat, Z.; Vaidean, G. Suspected pancreatic cancer: evaluation by dynamic gadolinium-enhanced 3D gradient-echo MRI. *AJR. American journal of roentgenology* **2005**, *185*, 700-703.

Appendix:

Curriculum Vitae

Nikhil Rammohan

(other names used for academic publications: Nikhil Ram Mohan, Nikhil R. Mohan)

UNIVERSITY ADDRESS

Northwestern University
Medical Scientist Training Program
303 E Chicago Ave, Morton Bldg 1-670
Chicago, IL, 60611
877-698-6787 *tel*
312-908-5253 *fax*
nikhil-rammohan@northwestern.edu *e-mail*

HOME ADDRESS

5945 N Campbell Ave, Apt 3
Chicago, IL, 60659
312-636-8753 *tel*

PERSONAL INFORMATION

Born April 25, 1987, Chennai, India

EDUCATION

Northwestern University, Chicago, IL

NIH Medical Scientist Training Program (MSTP), MD/PhD, July 2010 – May 2018 (expected)
Feinberg School of Medicine, Medical Student, July 2010 - September 2012
The Graduate School, Department of Interdisciplinary Biological Sciences, PhD Student, October 2012 – September 2016. PhD Thesis Adviser: Thomas J. Meade
Thesis topic: Modular Carbon- and Gold-nanoparticles for High Field MR Imaging and Theranostics
Overall GPA: 4.00/4.00

Johns Hopkins University, Baltimore, MD

B.S. (Honors), Applied Mathematics and Statistics, 2008
B.A. Psychological and Brain Sciences, 2008
M.S.E, Applied Mathematics and Statistics, 2009. Master's Thesis Adviser: Carey E. Priebe

Overall GPA: 3.89/4.00
Major GPA: 3.94/4.00 (Applied Math)
3.96/4.00 (Psych)

SCIENTIFIC EXPERIENCE:

Northwestern University, Department of Chemistry & Molecular Biosciences & Center for Advanced Molecular Imaging: Laboratory of Thomas J. Meade
Research Areas: Chemistry, Nanotechnology, Cancer, Magnetic Resonance Imaging.

Graduate Research Assistant (July 2011 – August 2011), PhD Candidate (October 2012 -)

- Nanodiamond-Gadolinium(III) Probes for Tracking Cancer Growth *In Vivo* Using High Field Magnetic Resonance Imaging. Adviser: Dr. Thomas J. Meade, Dr. Dean Ho

- Gadolinium(III)-Gold Nanoconjugates for Highly Efficient Cancer Cell Tracking. Adviser: Dr. Thomas J. Meade.
- Gadolinium(III)-Gold Nanoconjugates for MR Imaging of the Pancreas. Adviser: Dr. Thomas J. Meade.
- Multifunctional Theranostic Nanodiamonds for simultaneous non-invasive magnetic resonance imaging and targeted chemotherapy. Adviser: Dr. Thomas J. Meade, Dr. Dean Ho

Northwestern University Neuroimaging and Applied Computational Anatomy Laboratory:
Research Areas: Medical Imaging, Computational Statistics, Machine Learning, Data Mining.

Graduate Research Assistant (July 2010 – September 2010). Automated Labeled Cortical Depth Mapping (LCDM) pipeline for analyzing regional structures. Adviser: Dr. Lei Wang

Northwestern University, The Chemistry of Life Processes Institute: Laboratory of Thomas O'Halloran
Research Areas: Biochemistry, Fluorescence Imaging.

Graduate Research Assistant (June 2011 – July 2011). Understanding the Zinc Spark: the rapid extrusion of Zinc from the M2 phase mammalian oocyte. Adviser: Thomas O'Halloran

Johns Hopkins Center for Imaging Science (CIS): Laboratory of Carey E. Priebe
Research Areas: Medical Imaging, Computational Statistics, Machine Learning, Data Mining.

Undergraduate Research Assistant (March 2006 – May 2008), Graduate Research Assistant (July 2008 – May 2009), Research Technician (July 2009 – March 2010)

- Statistical image analysis of hippocampus shape differences between populations with Clinical Depression: March 2006-Nov 2007. Adviser: Dr. Carey Priebe.
- Development of a data-adaptive weighted generalized Mann-Whitney-Wilcoxon statistic for application in interpoint distance analysis: August 2007 – May 2009. Adviser: Dr. Carey Priebe.
- Improving the computational efficiency of a modified Mann-Whitney-Wilcoxon for use in medical imaging and olfactory classification: June 2009 – March 2010
- Examining structural and physiological changes in the Planum Temporale among patients with Schizophrenia: August 2008 – March 2010. Advisers: Dr. Patrick Barta, Dr. Carey Priebe.
- Localizing functional activation to cortical and subcortical regions during tinnitus: July 2009 – March 2010. Adviser: Dr. Tilak Ratnanather.

RECOGNITION & AWARDS

United World College (UWC) Shelby Davis Scholar: $10,000 award per year, September 2005 – May 2008.
Dean's List: Spring 2006, Fall 2006, Spring 2007, Fall 2007, Spring 2008
BS degree: General University Honors, and Departmental Honors in Applied Mathematics & Statistics, May 2008

Graduate Half-Tuition Fellowship: Department of Applied Mathematics & Statistics, September 2008 – May 2009
Medical Scientist Training Program MD/PhD Fellow

SOCIETIES & MEMBERSHIPS:

Professional Societies
American Medical Association
American Medical Students Association
American Physician-Scientists Association
Illinois State Medical Society
Chicago Medical Society

Leadership:
Founder and President: Radiation Oncology Society, November 2012-October 2014
I coordinated learning activities dedicated to informing and educating the Northwestern medical student body regarding the clinical discipline of Radiation Oncology. Mentor: Dr. William Small, Vice Chair of Department of Radiation Oncology at Northwestern Memorial Hospital.

Founder and President: NU Imaging, August 2014 – July 2015
I co-founded, along with MSTP fellow Andy Hung, the Northwestern University Imaging group. We received a Community Building Grant from NU to facilitate cross-campus activities dedicated to the understanding and application of medical imaging techniques. We have organized research seminars, faculty presentations and clinical experiences for graduate students interested in translational radiological research.

Lead Editor, The Beat, Newsletter of the Northwestern University Feinberg School of Medicine, August 2011-May 2012
I coordinated the publication of the main medical school newsletter by compiling articles from several student and faculty writers. I contributed articles on music and Chicago area cultural events.

THESES AND UNIVERSITY PUBLICATIONS:

Northwestern PhD Thesis: “Carbon and Gold Nanoparticles for High Field MR Imaging and Theranostics”. **2016**.
Adviser: Thomas J. Meade (tmeade@northwestern.edu)

JHU Master’s Thesis: “Hippocampus Shape Analysis of Clinically Depressed Twin Populations Using a Modified Mann-Whitney-Wilcoxon Statistic”. **2009**.
Adviser: Carey E. Priebe (cep@jhu.edu)

TEACHING EXPERIENCE:

Northwestern University –
Spring 2013: Graduate Teaching Assistant, Physiology Laboratory. Dr. Tracy Hodgson, Course Director.

Johns Hopkins University -

Fall 2006: Tutor, Organic Chemistry I. JHU Tutoring Program.
Fall 2008: Teaching Assistant at JHU, Probability and Statistics for Biological Sciences. Dr. Fred Torcaso, Course Director.
Fall 2009: Teaching Assistant at JHU, Probability and Statistics for Physical Sciences. Dr. Bruno Jedynak, Course Director.

SCIENTIFIC MEETINGS:

American Society of Therapeutic Radiology and Oncology (ASTRO), 58th Annual Meeting:
Boston, MA, September 2016. *Poster Presentation.*

Imaging in 2020 - 2016 Conference: The Future of Precision Medicine – Molecular Imaging for Diagnosis and Surgery/Therapy
Jackson Hole, WY, September 2016. *Poster Presentation*.

American Physician Scientists Association – American Academy of Physicians – American Society of Clinical Investigators (APSA-AAP-ASCI) Joint Meeting:
Chicago, IL, April 2016. *Poster Presentation.*

Gordon Research Conference – Cancer Nanotechnology:
Mt. Snow, West Dover, VT, June 2015. *Poster Presentation*.

International Conference on Bio-Science and Bio-Technology (BSBT):
Jeju Island, Republic of Korea, December 2009. *Oral Presentation*.

Joint Statistical Meetings (JSM):
Washington D.C., August 2009. *Oral Presentation.*

National Conference on Undergraduate Research (NCUR):
Dominican University of California, San Rafael, California, April 2007. *Oral Presentation*

BIBLIOGRAPHY: ORIGINAL JOURNAL ARTICLES

1) **Rammohan, N.;** MacRenaris, K.; Moore, L.; Parigi, G; Mastarone, D; Manus, L.; Lilley L; Preslar, A.T.; Waters, E.A.; Filicko, A; Luchinat, C; Ho, D.; Meade, T.J. Nanodiamond-Gadolinium(III) Aggregates for Tracking Cancer Growth *In Vivo* at High Field. *Nano Letters*. **2016**. *Under Revision.*
2) **Rammohan, N.¥**; Holbrook, R.¥; Rotz, M.; MacRenaris, K.; Preslar, A.T.; Carney, C.; Reichova, V.; Meade, T.J. Gd(III)-Gold Nanoconjugates Provide Remarkable Cell Labeling for High Field MR Imaging. *Bioconjugate Chemistry.* **2016.** *Article ASAP.* DOI: 10.1021/acs.bioconjchem.6b00389 (¥=equal contribution).
3) Holbrook, R. J.; **Rammohan, N.**; Rotz, M. W.; MacRenaris, K. W.; Preslar, A. T.; Meade, T. J. Gd(III)-Dithiolane Gold Nanoparticles for T1-Weighted Magnetic Resonance Imaging of the Pancreas. *Nano Letters.* **2016**, *16*, 3202-3209. PMCID in process.
4) **Rammohan, N.;** McLeod, S.**;** MacRenaris K.; Ho D.; Meade T.J. Theranostic Nanodiamond-Gadolinium(III)-Doxorubicin conjugates enable potent chemotherapy tracked by MRI. **2016**. *In Preparation*.

5) Moore, L.; Caldwell, M.; Townsend, T.; MacRenaris, K.; Moyle-Heyrman, G.; **Rammohan, N.**; Schonher, E.; Burdette, J.; Ho, D; Meade T.J. A Water-soluble Nanoconjugate for Enhanced Cellular Delivery of Steroid Receptor-targeted MR Contrast Agents. **2016.** *in preparation.*
6) **Ram Mohan N.,** Priebe C.E., Park Y., John M. (2011). "Statistical Analysis of Hippocampus Shape Using a Modified Mann-Whitney-Wilcoxon Test," *International Journal of Bio-Science and Bio-Technology (IJBSBT),* **2011**, Vol. 3, No. 1, pp. 19–26.
7) Park Y., Priebe C.E., Miller M.I., **Mohan N.R.,** Botteron K.B. (2008). Statistical Analysis of Twin Populations using Dissimilarity Measurements in Hippocampus Shape Space, *Journal of Biomedicine and Biotechnology.* **2008**;2008:694297. PMCID: PMC2246089

BIBLIOGRAPHY: CONFERENCE PROCEEDINGS – FULL ARTICLES

1) **Ram Mohan N.,** Priebe C.E., Park Y., John M. Hippocampus Shape Analysis of Clinically Depressed Twin Populations Using a Modified Mann-Whitney-Wilcoxon Statistic. **2009**. Proceedings of the Joint Statistical Meetings, Section on Nonparametric Statistics, pp 4976-4991, 2009.
2) **Ram Mohan N.,** Priebe C.E., Park Y., John M. Statistical Analysis of Hippocampus Shape Using a Modified Mann-Whitney-Wilcoxon Test. **2009**. Proceedings of the International Conference on Bio-Science and Bio-Technology, pp 45-53, 2009.
3) Park Y., Priebe C.E., Miller M.I., **Ram Mohan N.,** Botteron K.B. Hippocampus shape-space analysis of clinically depressed, high-risk, and control populations. **2007**. Proceedings of the Frontiers in the Convergence of Bioscience and Information Technology, pp 465-469

BIBLIOGRAPHY: CONFERENCE PROCEEDINGS – ABSTRACTS

1) **Rammohan N.**, Filicko A., MacRenaris K., Ho D., Meade T.J. Theranostic Nanodiamond-Gadolinium(III)-Doxorubicin Conjugates Improve Chemotherapy of Cancer Cells That Can Be Monitored by Magnetic Resonance Imaging. **2016**. American Society of Therapeutic Radiology and Oncology (ASTRO), 58th Annual Meeting, Boston, MA.
2) **Rammohan N.,** Holbrook R., Rotz M., Moore L., MacRenaris K., Parigi G., Preslar A., Luchinat C., Ho D., Meade T.J. Carbon and Gold Nanoparticles for Magnetic Resonance Imaging and Theranostics of Cancer. **2016**. Imaging in 2020 - 2016 Conference: The Future of Precision Medicine – Molecular Imaging for Diagnosis and Surgery/Therapy, Jackson Hole, WY.
3) **Rammohan N.,** Moore L., MacRenaris K., Parigi G., Preslar A., Luchinat C., Ho D., Meade T.J. Nanodiamond-Gadolinium(III) Probes for Tracking Cancer Growth *In Vivo* Using High Field Magnetic Resonance Imaging. **2016**. American Physician Scientists Association – American Academy of Physicians – American Society of Clinical Investigators (APSA-AAP-ASCI) Joint Meeting, Chicago, IL.
4) **Rammohan N.,** Moore L., MacRenaris K., Preslar A., Luchinat C., Ho D., Meade T.J. Nanodiamond-Gadolinium(III) Probes for Magnetic Resonance Imaging of Cancer. **2015**. Gordon Research Conference – Cancer Nanotechnology, Mt. Snow, West Dover, VT.

BIBLIOGRAPHY: ORAL PRESENTATIONS

1) **Rammohan N.** Statistical Analysis of Hippocampus Shape Using a Modified Mann-Whitney-Wilcoxon Test. **2009**. International Conference on Bioscience and Biotechnology, Jeju Island, Republic of Korea.
2) **Rammohan N.** Hippocampus Shape Analysis in Clinically Depressed Twin Populations Using a Modified Mann-Whitney-Wilcoxon Statistic. **2009**. Joint Statistical Meetings, Washington, D.C.
3) **Rammohan N.** Interpoint comparison analysis of hippocampus shape in the onset of Clinical Depression in twin populations. **2007**. National Conference on Undergraduate Research, San Rafael, CA.
4) **Rammohan N.,** Priebe CE. Computational anatomy - a mapping model to study hippocampus shape differences between twin populations with or without Clinical Depression. **2006**. JHU Whiting School of Engineering's Leadership & Alumni Symposium.